Investigation into the Surface Chemistry of Passivated Carbon Fiber/$LiMn_2O_4$ Electrodes for Lithium Ion Batteries

A Dissertation

Presented to

The Academic Faculty

by

Gordon Henry Waller

In Partial Fulfillment

of the Requirements for the Degree

Doctorate of Philosophy in the

School of School of Materials Science and Engineering

Georgia Institute of Technology

May 2016

Investigation into the Surface Chemistry of Passivated Carbon Fiber/$LiMn_2O_4$ Electrodes for Lithium Ion Batteries

Approved by:

Dr. Meilin Liu, Advisor
School of Materials Science and Engineering
Georgia Institute of Technology

Dr. Satish Kumar
School of Materials Science and Engineering
Georgia Institute of Technology

Dr. Lawrence Bottomley
School of Chemistry and Biochemistry
Georgia Institute of Technology

Dr. Kenneth Sandhage
School of Materials Science and Engineering
Georgia Institute of Technology

Dr. Thomas Fuller
School of Chemical and Biomolecular Engineering
Georgia Institute of Technology

Date Approved: [February 25, 2016]

This dissertation is dedicated to my wife, Danielle, and our parents. Thank you for your continued support and encouragement.

ACKNOWLEDGEMENTS

I would like to thank my friends and research colleagues, Dr. Philip Brooke, Dr. Samson Lai, Dongchang Chen, Benjamin Rainwater and Brian Doyle for their advice and comradery during my dissertation research. In particular, the experimental help from these individuals with characterization and fabrication techniques including Atomic Layer Deposition, X-ray Photoelectron Spectroscopy, synchrotron X-ray diffraction, and Raman spectroscopy has been critical to help me to complete my research. I would also like to acknowledge Dr. Yong Ding, Yolande Berta and David Tavoliki of the Georgia Tech Center for Nanostructure Characterization for their assistance with Transmission Electron Microscopy, Scanning Electron Microscopy and X-ray Diffraction, respectively.

I have had several mentors during my dissertation work that have been consistently available for fruitful discussions on various topics, both inside and outside of a classroom setting. These include my committee members Professor Lawrence Bottomley, Professor Thomas Fuller, Professor Kenneth Sandhage and Professor Satish Kumar, and my advisor Professor Meilin Liu. Professor Liu's leadership and sponsorship has enabled me to pursue topics and opportunities of interest to me, which has allowed me to gain exposure to a broad range of topics in materials science and electrochemistry. One opportunity of note is the TI:GER program at Georgia Tech, which allowed me to explore topics in technology entrepreneurship while working with an interdisciplinary group of graduate students. Other mentors important to acknowledge include MSE faculty Professor Faisal Alamgir, faculty in the TI:GER program Professor Marie Thursby, Professor Anne Rector, Ms. Margi Berbari and Ms. Nicole Morris, and visiting

scholar Dr. Renzong Hu. Thank you all for sharing your expertise, as well as your time, with me during my graduate studies.

Finally, I would like to acknowledge the staff of the Department of Materials Science and Engineering at Georgia Tech, in particular our academic advising manager Susan Bowman. I always knew who to turn to for accurate information and felt that the department was looking out for the best interests of me and my fellow graduate students. Thank you all for your diligence in managing the least-fun aspect of any graduate study: paperwork!

TABLE OF CONTENTS

LIST OF TABLES

Page

LIST OF FIGURES

Page

LIST OF ABBREVIATIONS AND SYMOBLS

ALD	Atomic Layer Deposition
CE	Counter Electrode
CFP	Carbon Fiber Paper
CPE	Constant Phase Element
CV	Cyclic Voltammetry/Voltammogram
DMC	Dimethyl Carbonate
DMF	Dimethyl Formamide
DSC	Differential Scanning Calorimetry
EC	Ethylene Carbonate
EDS	Energy Dispersive X-ray Spectroscopy
EIS	Electrochemical Impedance Spectroscopy
FCC	Face-centered Cubic
HOMO	Highest-occupied Molecular Orbital
LIB	Lithium-ion Battery
LMO@CFP	$LiMn_2O_4$ on Carbon Fiber Paper
LUMO	Lowest Unoccupied Molecular Orbital
NMP	N-methyl-2-pyrrolidone
PAN	Polyacrylonitrile
PVDF	Polyvinylidene Fluoride
SEI	Solid Electrolyte Interphase
SEM	Scanning Electron Microscopy
TEM	Transmission Electron Microscopy
TGA	Thermogravimetric Analysis

TOF-SIMS	Time-of-flight Secondary Ion Mass Spectroscopy
WE	Working Electrode
XPS	X-ray Photoelectron Spectroscopy
XRD	X-ray Diffraction
λ	X-ray wavelength

SUMMARY

Lithium-ion batteries are one of the most energy dense electrochemical energy storage systems available today and for the foreseeable future will be the dominant secondary battery type for applications needing large energy density and long operational lifetimes. Among the many varieties and applications of lithium-ion batteries, electrode design - and in particular the selection of active materials - is extremely influential in determining overall device specifications. Furthermore, the cathode plays a particularly important role in factors such as cell safety, lifetime, and cost. In applications which require low cost and high safety $LiMn_2O_4$ cathodes are an excellent choice; however, the well-known issue of rapid capacity fading has yet to be overcome.

In this dissertation, composite cathodes were fabricated by hydrothermal precipitation of a $LiMn_2O_4$ coating on carbon fiber paper substrate, producing an electrode with uninterrupted electronic and ionic pathways, thereby eliminating the need for toxic solvents, polymeric binders, and metal foil current collectors used in conventional tape-cast electrodes. The $LiMn_2O_4$ coated carbon fiber sheets were used directly as free-standing electrodes, demonstrating superior specific capacity and comparable rate capabilities to conventional tape-cast electrodes. A variety of phases of manganese-oxides were produced and evaluated in electrochemical cells, while only $LiMn_2O_4$ was found to have significant reversible capacity. Maximum $LiMn_2O_4$ mass loading, which determines the overall electrode gravimetric energy density, was found to be a major limitation when using commercially available carbon fiber paper.

Further improvements on this approach were achieved by replacing the commercially available carbon fiber paper substrates with lab-made carbon nanofiber

sheets via electrospinning. The decreased fiber diameter and void space of the electrospun nanofiber sheets allowed for oxide mass loadings of more than double the value achieved with carbon fiber paper, enabling the production of electrodes with total energy densities rivaling optimized tape cast electrodes. Two carbon fiber precursors were investigated, the commonly used polyacrylonitrile in dimethyl formamide as well as the bio-polymer lignin which was dissolved along with polyvinyl alcohol into distilled water. While the carbon nanofibers derived from the two polymer precursors showed similar overall morphologies, they displayed dramatically different electronic conductivity and graphitic content. These variations influenced not only the $LiMn_2O_4$ phases deposited on carbon nanofibers by hydrothermal precipitation but also their efficacy in electrochemical devices.

As expected, rapid capacity fading was observed while cycling the $LiMn_2O_4$ coated carbon fibers for extended numbers of charge and discharge cycles. To directly mitigate these issues, ultrathin (<5 nm) layers of Al_2O_3 were deposited onto the surface of the $LiMn_2O_4$ coated carbon fibers by atomic layer deposition. With Al_2O_3 coatings as thin as 1 nm, capacity retention was improved by >100% over 500 charge and discharge cycles. In addition, alumina coatings were found to decrease total electrochemical impedance and enhance apparent lithium ion diffusivity, thus enhancing efficiency and rate capability.

To better understand the mechanism through which ALD coatings enhanced electrochemical performance, surface chemistry and molecular structure were characterized using x-ray photoelectron spectroscopy and Raman spectroscopy, respectively, for both carbon-fiber supported and thin-film model electrodes. These

studies indicate that ALD coatings mitigate capacity loss and improve lithium-ion kinetics by formation of preferential surface phases, namely aluminum fluoride and aluminum oxy-fluoride, while inhibiting the formation of detrimental phases associated with electrolyte decomposition which lead to increased electrode polarization.

While this dissertation focuses on the methods to produce and characterize surface modified $LiMn_2O_4$ electrodes, the approaches used are general and applicable to a wide variety of electrochemical devices. Specific conclusions from this work will inform the development of low-cost lithium-ion batteries and support future research into this area.

1 INTRODUCTION

1.1 Motivation

In recent years, energy storage has been highlighted as a key limitation to advances in emerging large format applications, including hybrid and electric vehicles, broad incorporation of intermittent sources of renewable electricity, and overall improvements to grid-level energy efficiency through load shifting[1-4]. For these applications, cost, energy density, lifetime, and safety requirements are satisfied using various combinations of active materials, pack designs, and engineering controls. Lithium-ion batteries are becoming a dominant player in these application spaces, but other secondary battery chemistries, such as nickel-metal hydride, lead-acid, and sodium-sulfur, are still prevalent for certain applications[2]. In comparison, for the secondary cells found in small scale portable electronic devices, the incumbent lithium-ion chemistry of a $LiCoO_2$ cathode and graphite anode have largely reached an equilibrium between the same critical design factors influencing the large scale applications and the market realities of producing and distributing over one billion smartphones, laptops, and tablets annually.

For all of these metrics the cathode material plays a disproportionately large role in determining the properties of the cell. For example, cell safety is related to the thermal stability, oxygen evolution during thermal decomposition, and overcharge reactivity of the cathode material[5]. In general, $LiFePO_4$ and $LiMn_2O_4$ are the most stable cathode materials, with $LiFePO_4$ showing greater thermal stability and no oxygen release during decomposition, while $LiMn_2O_4$ has superior performance during overcharge. Cathode

materials also strongly influence total cell energy density and cost. Table 1.1 compares the capacities, voltages, and costs for various cathode materials relative to a natural graphite anode. The energy storage cost, as normalized by active material mass (e.g., only the cost of the electrode materials are considered), is calculated with Equation 1:

$$Energy\ Storage\ Cost = \left(\frac{\left(\frac{A_{mat}}{A_{cap}}\right) + \left(\frac{C_{mat}}{C_{cap}}\right)}{(V_{cath} - V_{an})} \right) \times 1000 \qquad \textbf{Eqn.1}$$

where A_{cap} and C_{cap} are the anode and cathode capacities, A_{mat} and C_{mat} are the anode and cathode materials costs, and V_{an} and V_{cath} are the anode and cathode half-cell voltages relative to a lithium metal reference.

Table 1.1 Comparison of various parameters for common lithium-ion electrode materials. Energy storage cost is calculated for each cathode material with a natural graphite anode.

Material	Material Cost ($/kg)	Capacity (Ah/kg)	Average Voltage (V vs. Li/Li+)	Energy Storage Cost ($/kWh)
$LiMn_2O_4$	10	110	4	30.6
$LiFePO_4$	20	150	3.45	48.3
$LiNi_{0.8}Co_{0.15}Al_{0.05}O_2$	33	191	3.7	55.9
$LiCoO_2$	36	145	3.9	70.7
Natural Graphite	10	350	0.1	N/A

It is apparent from Table 1 that there is a large discrepancy between both typical cathode and anode capacities and cost. Compared to the low cost and relatively high capacity of the graphite anode, the current cathode materials fall short. A recent study by Nelson, et al. (Argonne National Laboratory) reported that, for a 16 kWh battery pack using a $LiMn_2O_4$ cathode and graphite anode, about half of the total battery pack cost is associated with the cell materials (active materials, current collectors, binders and conductive carbon, separator and electrolyte), with a quarter of this total pack cost being

due to the cathode active material (i.e., the cathode active material is the largest single-component contribution to the total cost) [6].

Applications for which maximizing energy density is less critical than cost and safety (e.g., for hybrid vehicles and stationary storage), lithium-ion batteries utilizing $LiMn_2O_4$ make an excellent choice. However, the rapid capacity fade upon cycling for $LiMn_2O_4$ cathodes has prevented more widespread usage of this material[7, 8]. In this dissertation the focus will be the development of a high-performance and long-lasting $LiMn_2O_4$ based cathode.

1.2 Research Objectives

The objectives for the proposed thesis research are divided below into two categories: engineering and scientific. From a practical point of view, it is important to recognize the fact that lithium-ion batteries already exist in the marketplace. As a consequence, research into electrode materials must acknowledge the current commercial benchmarks for performance, cost, and safety. The main engineering objective is to develop an electrode structure and processing technique that does not have the limitations of the currently used tape cast electrodes. This design should be cheap, have acceptable energy and power density compared to commercially available cells, and have excellent capacity retention for many charge and discharge cycles. From a scientific point of view, this study will focus on enhancing understanding towards the scientific basis for rational design of efficient electrodes, especially the dynamic chemical changes that occur at the interface between the electrolyte and electrode in a lithium ion battery using a passivated $LiMn_2O_4$ positive electrode. To achieve this, the proposed research will leverage the available surface characterization tools applied to cells with well-designed electrode

architecture, directly probing the relationship between materials microscopic features (structure, composition, and morphology) and their electrochemical performance under service conditions.

1.2.1 Engineering objectives

1. Develop a cost-effective process to directly fabricate $LiMn_2O_4$ electrodes on carbon fibers of varying dimensions using a low temperature solution-precipitation reaction. These oxide-coated carbon fiber networks will be applied directly as the positive electrode in LIB test cells.
2. Passivate the as-prepared electrodes with appropriate materials (e.g. amphoteric oxides) through a second processing step to enhance capacity retention.
3. Optimize the carbon fiber/oxide heterostructured electrode for other electrode materials and electrochemical devices. This will be achieved by manipulating carbon fiber dimensions/architecture as well as the chemistry of the synthesis process.

1.2.2 Scientific objectives

1. Develop model cells with well-controlled geometry (e.g., thin- film electrodes) and characterize the interfacial layer composition and structure. Compare these results to passivated and bare carbon fiber supported electrodes.
2. Utilize in-situ techniques to analyze the chemistry, structure, and morphology of electrode surfaces under cycling conditions as a function of cell polarization and cycling rate, providing insights vital to the rational design of new electrode materials and structures.

3. Gain a fundamental understanding on the role of amphoteric oxides on the improved capacity retention for $LiMn_2O_4$ electrodes.

1.3 Dissertation Structure

Chapter 2 introduces fundamental concepts in electrochemistry that help to guide the experimental design and interpret results of electrochemical testing used in this dissertation. Relevant concepts from crystallography and thermodynamics are also discussed.

Chapter 3 covers the theory and operational technique behind all of the experimental methods used herein. This chapter is separated into sample preparation techniques and characterization methods. Details of each method in application are provided in subsequent chapters where appropriate.

Chapter 4 describes the fabrication and electrochemical testing of $LiMn_2O_4$ on carbon fiber paper (LMO@CFP) by the hydrothermal method. The techniques and results described in this chapter serve as a benchmark for subsequent chapter which investigate various aspects introduced in Chapter 4 in more depth.

Chapter 5 discusses the results of surface-modified LMO@CFP electrodes by atomic layer deposition (ALD). The electrodes modified by ALD in this chapter were prepared in an identical fashion to those described in Chapter 4.

Chapter 6 describes the use of electrospinning from various polymer solutions to produce carbon nanofibers. These fibers are in contrast to the micron-sized fibers found in CFP. Comparisons and made between both the physical properties of the fibers produced by

electrospinning with their CFP counterparts, as well as comparisons between the electrodes made by introducing oxide coatings onto the carbon fibers.

Chapter 7 expands on the conclusions drawn in Chapter 5 using model electrodes and *in situ* characterization of the modified electrode surface using Raman spectroscopy.

Chapter 8 concludes this dissertation and includes recommendations for future research in this area.

2 BACKGROUND

2.1 Fundamental Concepts

The theoretical specific capacity (in Ah/g) of an electrode material can be calculated from Equation 2 below [9],

$$Theoretical\ Capacity = \frac{zF}{M} \qquad \textbf{Eqn. 2}$$

where z is the moles of electrons associated with the reaction, F is Faraday's constant, and M is the molecular weight of the lithiated oxide. For a lithium-ion battery positive electrode, z is equal to the moles of Li^+ that can be removed from the lithiated oxide, as 1 e^- is needed for each Li^+ to maintain charge neutrality. When selecting a battery for any application, total capacity (usually expressed in amp-hours) will determine the operating time for the device. Because capacity is determined by the mass of active materials, this value can be manipulated by simply scaling the battery size. This is the reason why the commonly used primary "alkaline" cells (i.e. Zn/MnO_2 in KOH electrolyte) and others are sold in a variety of sizes. However, the operating potential of a cell is governed by thermodynamics. Indeed, the relatively large operating potential of lithium-ion batteries is the primary reason they are of technological interest. From a fundamental standpoint, the reactions that occur in an electrochemical cell are identical to a normal oxidation/reduction ("redox") chemical reaction. A minimum of two reactant species react to form at least one new product species which has lower total energy than the reactants. In this reaction, electrons are exchanged in such a way that the oxidized species loses an electron which is donated to the reduced species. The critical difference for

redox reactions in an electrochemical cell is that electrons cannot pass directly between reactant species. Instead, the reactants (the electrodes) are separated by an electrically insulating region (the electrolyte), and electrons must travel through an external conducing circuit. To maintain charge neutrality of each electrode positive ions pass through the electrolyte to match the electron flow. An example of this reaction is shown in Equation 3 where reactants A and B form a product AB [9].

$$A + B \rightarrow AB \qquad \textbf{Eqn. 3}$$

This reaction can also be expressed as a half reaction by arbitrarily designating reactant A as the reducing species and reactant B as the oxidizing species. Equations 4 and 5 describe the intermediate step of electron transfer between A and B before the final product AB is formed.

$$A \rightarrow A^{+} + e^{-} \qquad \textbf{Eqn. 4}$$

$$B + e^{-} \rightarrow B^{-} \qquad \textbf{Eqn. 5}$$

The reactions described in equation 3-5 are classified as "reconstitution" reactions in which a new produced phase is formed during the reaction. All commercially available lithium-ion batteries undergo an "insertion" type reaction at the positive electrode (i.e. the lithiated transition metal oxide). Several examples of such electrode materials are shown in Table 2.1. Table 2.1 also includes the most common negative electrode, graphite, which is also an insertion type electrode. In an insertion type reaction, the product phase

is a modified version of one of the reactants which has formed a solid solution with the other reactant through electrochemical means. This is illustrated for $LiMn_2O_4$ in Equation 6.

$$xLi + Mn_2O_4 \rightarrow Li_xMn_2O_4 \qquad \textbf{Eqn. 6}$$

Half reactions can also be written for each electrode. In a laboratory setting, lithium is used as the negative electrode and is oxidized to form Li^+ ions and electrons. The electrons cannot pass through the electrically insulating electrolyte, and thus travel through an external circuit driven by a potential gradient to the positive electrode. The half reaction for lithium metal is shown in Equation 7.

$$Li \rightarrow Li^+ + e^- \qquad \textbf{Eqn. 7}$$

At the positive electrode (shown here for the discharge reaction) lithium ions are introduced into the host structure and one of the Mn^{4+} cations is reduced to Mn^{3+} in a stoichiometric ratio with the extent of the reaction.

$$[Mn^{4+}]_2O_4 + xLi^+ + e^- \rightarrow xLi[xMn^{3+}][(2-x)Mn^{4+}]O_4 \qquad \textbf{Eqn. 8}$$

In order for the reaction which forms AB to occur spontaneously, the total free energy of the products must be less than that of the reactants. This energy difference referred to as the change in Gibbs free energy, ΔG, and is often expressed as the

difference in energy between reactants and products for reactants that existed prior to reaction in their standard states. This quantity is denoted $\Delta G°$. By introducing the Faraday constant, F, which is the electric charge of one mole of electrons, an expression relating the change in Gibbs free energy and electrical potential can be written. This is shown in Equation 9.

$$\Delta G° = -zFE° \qquad \textbf{Eqn. 9}$$

The potential "E°" expressed in Equation 10 applies only when current is not flowing through the cell, and for this reason is referred to as the "open circuit" potential. For reactions not involving reactants in their standard states, the Gibbs free energy change can be adjusted by considering the activities ($\alpha_{reactant/product}$) of the products and reactants. This is shown in Equation 9 for the example reaction from Equation 3.

$$\Delta G = \Delta G° + RT\ln\frac{\alpha_{AB}}{\alpha_A\alpha_B} \qquad \textbf{Eqn. 10}$$

By combining equations 9 and 10 we can produce the Nernst equation (Equation 11), which is used to express the open circuit potential for an electrochemical cell consisting of reactants not in their standard states.

$$E = E° - \frac{RT}{zF}\ln\frac{\alpha_{AB}}{\alpha_A\alpha_B} \qquad \textbf{Eqn. 11}$$

However, as soon as current flows from the electrochemical cell the potential will deviate from the equilibrium potential calculated in Equation 11. This deviation in expected and observed potential is called the overpotential which increases with current. The overpotential value is represented by η and is expressed in Equation 12.

$$\eta = E_{OCV} - E_{cell} \qquad \textbf{Eqn. 12}$$

E_{OCV} refers to the potential calculated using Equation 11 and E_{cell} is the potential observed during operation. The overpotential is due to a convolution of influences known as the cell polarization, which has contributions from electronic and ionic conductivities as well electrochemical kinetics [10]. These are referred to as ohmic, concentration and activation polarization respectively. Ohm's law can be used to describe the overpotential contribution from ohmic losses, shown in Equation 13. Thus, the ohmic potential increases linearly with current.

$$\eta_{ohmic} = IR \qquad \textbf{Eqn. 13}$$

Concentration polarization is due to the finite rate at which the electrochemical reactant can be delivered, via diffusion through the electrolyte, to the electrode surface. In the case of a lithium-ion battery this is the Li^+ ion. The limiting current is sometimes used in discussions of concentration polarization, and describes the scenario in which any reactant species which arrives at the electrode surface is instantaneously converted to a soluble product species. The product species then diffuses back into the electrolyte. In

this way a reactant concentration gradient is established with a depleted zone at the interface between electrode and electrolyte and a reactant concentration effectively equal to the bulk electrolyte value some characteristic distance away. The concentration overpotential increases with the fraction of the limiting current drawn from the cell. A notable difference between ohmic and concentration polarization is that while ohmic polarization reaches the maximum value for a given current density very quickly, concentration polarization gradually increases as the thickness of the concentration gradient, called the diffusion layer, reaches a steady state value. Equation 14 describes the concentration polarization, where C and C_o are the concentration of reactant at the electrode surface and in bulk solution (i.e. the nominal electrolyte concentration) respectively. An equivalent expression relating concentration polarization to limiting current i_l and applied current i is also given.

$$\eta_{concentration} = \left(\frac{RT}{z}\right)\ln\left(\frac{C}{C_o}\right) = \left(\frac{RT}{z}\right)\ln\left(\frac{i_l}{i_l - i}\right) \qquad \textbf{Eqn. 14}$$

Activation polarization is determined by electrochemical kinetics, and is related to the chemical kinetics for the related redox reaction. Equation 15, the Butler-Volmer equation, describes the expected current density (i=I/A) for a given value of overpotential. In Equation 15, α is known as the charge transfer coefficient which describes the symmetry of the electrochemical overpotential for forward and backward reactions, and i_o is the exchange current density ($i_o = k_o F(\alpha_A \alpha_B)$), where k_o is the chemical equilibrium constant) which describes the current flow at zero overpotential. The exchange current density is analogous to the thermodynamic equilibrium constant, as the

aforementioned current flow is assumed to be equal in both forward and reverse reactions, creating a net flux of zero.

$$i = i_o \exp\left(\frac{\alpha F \eta}{RT}\right) - \exp\left(\frac{(1-\alpha)(F\eta)}{RT}\right) \qquad \textbf{Eqn. 15}$$

The expression shown in Equation 15 is one commonly used limiting case for electrochemical kinetics which assumes that the electrolyte solution has a homogeneous concentration of active species, or that the current flow is so low that no significant concentration gradients are formed. This expression is obviously in contrast to Equation 14 in which overpotential is due to concentration gradients. The Tafel expression can be derived from Equation 15 which describes the activation polarization far from equilibrium, shown in Equation 16 where a and b are constants related to the charge transfer coefficient.

$$\eta_{activation} = a + \left(b * log\left(\frac{I}{I_o}\right)\right) \qquad \textbf{Eqn. 16}$$

Beyond choosing materials with high electrical and ionic conductivities, cell design can strongly influence overpotential. This is discussed in more detail in the next section.

2.2 Lithium-ion Battery Cell Design

The conventional cell design for a lithium-ion battery is shown in Figure 2.1. For each electrode, an active material is mixed into a solvent (usually N-methyl-2-

pyrrolidone, “NMP”) with a binder material soluble in NMP (usually Polyvinylidene fluoride, “PVDF”) and tape cast onto a metal foil current collector. For reasons of electrochemical corrosion, aluminum is used at the oxidizing potentials of the positive electrode and copper is used in the negative electrode. Aluminum is mutually inapplicable at the negative electrode, because it would undergo an alloying reaction with Li^+ at the very reducing potentials of the negative electrode. In Figure 2.1, the negative electrode active material is depicted as porous carbon, shown as black hexagons, which is also present as a conducting additive in the positive electrode to compensate for the relatively low electronic conductivity of the transition metal oxide active materials. The positive electrode active material is shown as blue circles, and the PVDF binder is assumed to be homogenously dispersed through each electrode. The separator must meet the criterion of high electrolyte permeability to maintain ionic contact between the electrodes and very low electrical conductivity. Separators are usually a porous sheet of polymer or glass fibers.

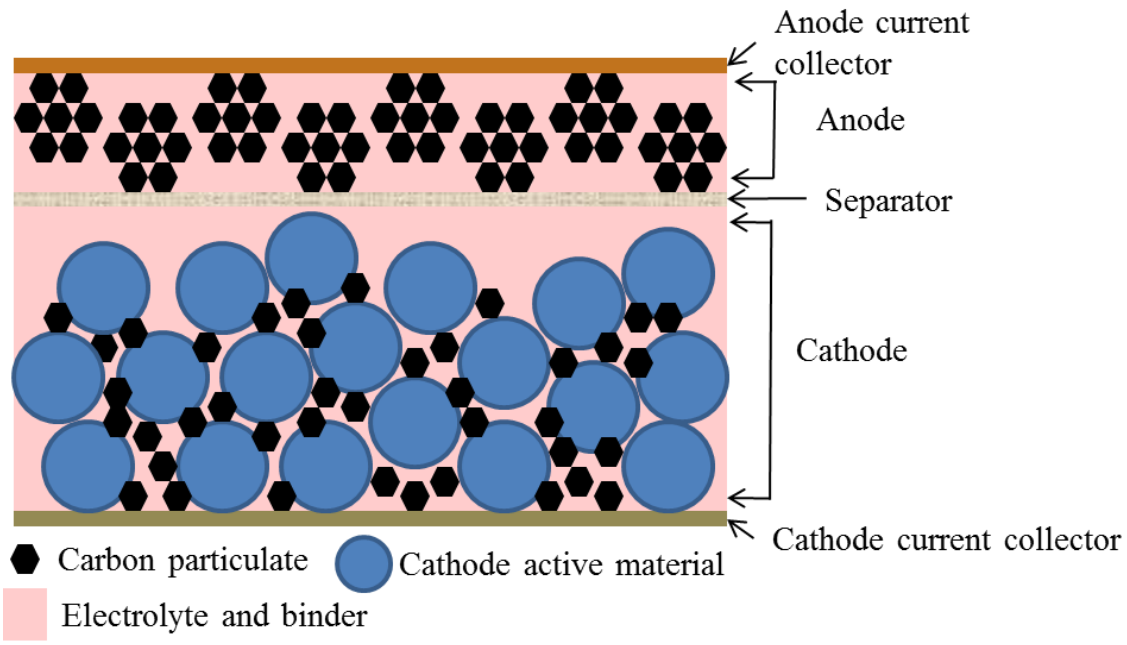

Figure 2.1 Conventional lithium-ion battery construction by tape casting.

Because of the large difference in specific capacity between carbon and the lithium transition metal oxide positive electrode materials, Figure 2.1 depicts a thicker positive electrode. In practical cells the maximum thickness of either electrode is roughly 150-200 microns. Increasing the tape cast thickness requires more polymer binder to maintain mechanical integrity, which decreases the cell energy density. Furthermore, increasing a composite film thickness leads to an increase in joule heating due to contact resistance between discrete particles [11]. Finally, the rate of electrolyte penetration into a composite electrode, which is related to the electrode thickness, limits processing speeds in thick electrodes [12]. Research activity focused on improving cell design utilizes interconnected networks of electrode and current collector as well as completely interdigitated electrodes to maximize electrical and ionic conductivity [13-15].

The polarization sources described in the previous section are influenced by cell design in the following ways. Increasing the content of conductive additive in the positive electrode and reducing the electrode or separator thickness will reduce ohmic polarization. Creating a porous electrode which maximizes electrolyte penetration and increasing electrode surface area by using very small active materials decreases concentration polarization. Increasing surface area will also reduce the current density for a fixed current value, and thus lower the activation polarization. A tradeoff between cells with very high energy density (i.e. minimal amounts of inactive materials) or very high rate capability (i.e. lots of conductive additive and thin electrodes to support large current densities) determines the desired cell design for a given application.

With the exception of thin film or otherwise monolithic oxide positive electrodes, a conductive agent must always be added to a working cell. The reason for this is quite clear when observing the low electrical conductivities for lithiated transition-metal oxides, which are in fact wide-bandgap semiconductors, used in lithium-ion batteries shown in Table 2.1. Carbon is an excellent choice for this additive because of its acceptably high electrical conductivity (compared to oxide positive electrodes), good electrochemical stability, very low weight and myriad of microstructures available[16, 17]. In some cases, carbon has been used to completely replace the conventional aluminum foil current collector allowing for electrodes not limited by tape casting[18-20]. Carbon fibers, with dimensions ranging from nanometers to microns, are a particularly active area for improved LIB cell design[21-24].

Table 2.1 Conductivities of lithium-ion battery electrode materials.

Material	Li^+ Diffusivity (cm^2/s)	Electrical Conductivity (S/cm)	Band Gap (eV)
$LiCoO_2$	$10^{-10} – 10^{-8}$	10^{-4}	0.5-2.7
$LiMn_2O_4$	$10^{-11} – 10^{-9}$	10^{-6}	0.28-2.2
$LiFePO_4$	$10^{-14} – 10^{-15}$	10^{-9}	0.3-1
Graphite	$10^{-7} – 10^{-12}$	$10^{3} – 10^{4}$	-

2.3 Positive Electrode Materials

Three structures stand out amongst the research into lithium-ion battery positive electrodes. Two are lithiated transition metal oxides, with the first being the layered structure $LiMO_2$ where M is mixtures of Co, Mn, Ni or Al. The second oxide is $LiMn_2O_4$ where Mn is sometimes partially replaced with Ni. The third is a lithiated transition metal phosphate $LiFePO_4$. All of them conduct Li^+ ions through a network of interconnecting pathways or "tunnels" formed by the interstitial voids of the unit cell. When Li^+ enters a structure, one of the transition metal atoms in the host structure of which there can be more than one species, will be reduced in a stoichiometric ratio to maintain charge neutrality. All of the structures exhibit a slight anisotropic volume change during lithiation and de-lithiation but the total volume change is typically less than about 5% [25]. Each electrode material has various pros and cons. The layered transition metal oxides ($LiMO_2$) type have the highest specific capacity, exceeding 200 mAh/g with mixtures of transition metal cations, but as shown in Table 2.1 typically high costs [26]. When considering operating voltage, $LiMO_2$ compounds and $LiMn_2O_4$ have open-circuit potentials at the beginning of discharge exceeding 4 V vs. Li/Li^+. $LiFePO_4$ has a discharge potential below 3.5 V vs. Li/Li^+ but has a higher specific capacity than

$LiMn_2O_4$. These are commonly used metrics to compare various lithium-ion battery electrode chemistries but ignore the influence of chemical stability, rate capabilities and safety. This section will focus on the properties of $LiMn_2O_4$, and compare these to the other common electrode chemistries when appropriate.

2.3.1 Structure of $LiMn_2O_4$

$LiMn_2O_4$ has a spinel structure with an FCC lattice formed by O atoms, half of the octahedral sites filled by Mn cations, and one eighth of the tetrahedral sites filled by Li^+. Figure 2.2 shows this structure, where Li is represented as orange, O as teal, and Mn as red within the green octahedrons [27].

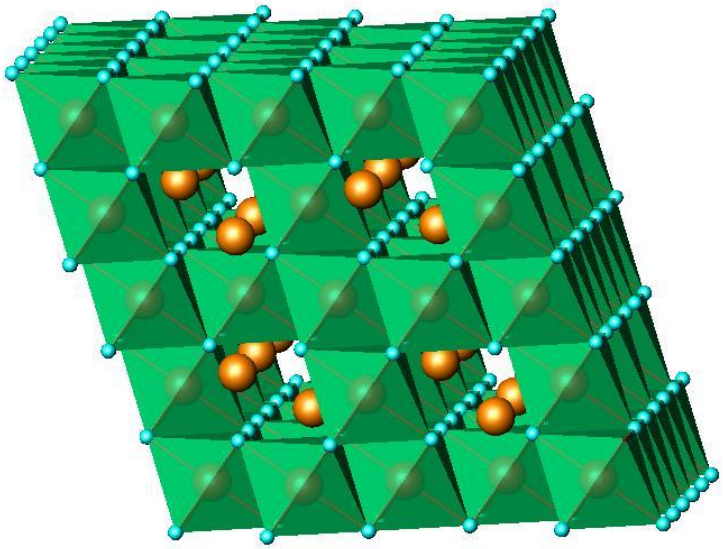

Figure 2.2 Crystallographic structure of Spinel $LiMn_2O_4$ with orange tetrahedrally coordinated Li atoms, red octahedral coordinate Mn atoms, and teal oxygen atoms at the corners of the green octahedrons.

Manganese exists in both the +3 and +4 states in the above mentioned stoichiometry and lithium can either be inserted up maximum of $Li_2Mn_2O_4$ (all Mn^{3+}) or

removed to form Mn_2O_4 (all Mn^{4+}), which is sometimes referred to as λ-MnO_2 [28, 29]. In the case of the extra-lithiated $LiMn_2O_4$, a significant impact on capacity retention from the Jahn-Teller effect is observed. This is related to the concentration of Mn^{3+} in the host structure, as the octahedrally coordinated d^4 electrons of Mn^{3+} induce a distortion of the Mn coordination polyhedron [30]. As the Li fraction of the host structure exceeds 1 atom per formula unit the crystal structure is distorted from the cubic spinel to tetragonal. Repeated cycling in this region is a known source of severe capacity degradation in the extra-lithiated spinel and for this reason only Li contents ≤ 1 ($Li_{(0-1)}Mn_2O_4$) will be discussed further.

2.3.2 Theoretical Capacity and Potential

When considering a maximum of 1 Li atom per mole of host spinel Mn oxide the theoretical capacity is 148 mAh/g using Equation 2. In the layered type ($LiMO_2$) metal oxides, the maximum accessible Li content is limited due to significant structural re-arrangement. When charging beyond some fraction of Li (about 50% for $LiCoO_2$), removal of Li^+ ions filling the inner-layer space between [MO_6] octahedra causes this re-arrangement. The consequence is that while $LiCoO_2$ has a theoretical capacity of 273 mAh/g, it can only demonstrate about 160 mAh/g associated with 58% of the total lithium extraction. However, the accessible lithium content is enhanced by doping with multiple cations. The three-dimensional tunnels or "gallery space" which accommodate Li^+ in the spinel structure are relatively invariant with lithium extraction and thus $LiMn_2O_4$ can be completely stripped of Li^+. The operating voltage for $LiMn_2O_4$ is usually in the range of 4.5 to 3.5 V vs. Li/Li^+ with two distinct plateaus occurring at about 4.1 and 3.9 V vs. Li/Li^+. Similarly to the layered oxides, Mn can be replaced with other

transition metal cations to shift operating voltage. For example, Ni and Fe substituted $LiMn_2O_4$ ($LiMn_{1.5}Ni_{.42}Fe_{.008}O_4$) has an operating voltage of over 4.8 V vs. Li/Li^+ [31]. It is also possible to formed a mixed spinel in which some amount of the normally tetrahedrally coordinated Li atoms occupy octahedral sites displacing Mn ($Li_{1+x}Mn_{2-x}O_4$) which can yield a greater initial discharge capacity [8]. Table 1.1 compares includes typical voltages and obtainable specific capacities for several positive electrode materials.

2.3.3 Rate Capabilities

From a fundamental standpoint, the rate capability, which is the maximum current density that a battery can demonstrate with the desired voltage and capacity outputs, is governed by the ability of the electrode active material to conduct electrons and lithium ions. In a full cell the various contributions to overpotential described earlier must also be considered. Electrical conductivity and lithium ion diffusivity for the three positive electrode materials discussed are listed in Table 2.1. Values presented in Table 2.1 are from a review article written by M. Park et. Al. on the subject [32]. Graphite is the only negative electrode included in Table 2.1 for comparison. It is interesting to note that all of the positive electrode materials discussed are considered semiconductors by the presence of a band gap, but conduct via hopping conduction between neighboring atoms.

From the same article, ionic conductivities for several salt/solvent electrolyte pairs range from 3-10 S/cm. A typically used electrolyte, 1 M $LiPF_6$ in a 50/50 mixture of Ethylene Carbonate and Dimethyl Carbonate (EC/DMC), has a reported ionic conductivity of 10.7 S/cm – five orders of magnitude higher than the electrical conductivity of $LiCoO_2$. Furthermore, the Li^+ diffusivity in all of the listed electrode materials is smaller still. For this reason, the rate capability of a lithium-ion battery is

limited by the insertion of Li^+ ions into the host electrodes, except for at very high current densities when ohmic losses become significant.

The assumption could be made based on the data presented Table 2.1 that only the layered type electrode materials are suitable for high rate applications. However, many reports have shown that nanostructured electrode materials can exhibit extremely high rate capabilities – each chemistry discussed has been shown to be capable of charge and discharges of rates greater than 10 C [26, 33-37]. The "c-rate" is defined as 1C corresponding to a complete discharge or charge in one hour. Thus a rate of 10C means complete charge or discharge takes place in 6 minutes. This is typically reported as an impact of greatly reduced diffusion distances, but it should be noted that these values are almost always reported for cells which contain high amounts of carbon additive to increase electrical conductivity (and minimize ohmic polarization) and have laboratory scale dimensions. At extremely high rates of charge and discharge, joule heating in external cell hardware (e.g. metal wiring connecting cells within a battery pack) can become significant.

2.3.4 Capacity Retention

It is insufficient to compare batteries based on their short term cycling ability alone. Battery electrodes should be capable of cycling many times while maintaining all of their original capacity – to be more precise, they should exhibit complete electrochemical reversibility. In reality, all battery materials exhibit slight capacity fade during cycling. One fundamental contribution to this capacity fade that influences all battery insertion type electrodes is known as "electrochemical shock" which is analogous to thermal shock [25]. Electrochemical shock occurs when the active materials expand and contract anisotropically during insertion and extraction of Li^+ ions. The effect is rate

independent and leads to micro-cracking, which introduces discontinuities in ionic and electronic conduction pathways and opens up previously unexposed regions to form SEI layers. This cracking phenomenon is particularly problematic for negative electrode materials like graphite which can experience exfoliation of graphene layers or alloy type electrodes which show expansion of several times their original volume.

In positive electrode materials SEI formation is due to electrochemical decomposition of the electrolyte during cycling and contributes to increased overall cell impedance[38]. The potential range within which formation of an SEI due to decomposition of the electrolyte is not thermodynamically possible is constrained by the highest occupied molecular orbital (HOMO) and lowest unoccupied molecular orbital (LUMO) of the electrolyte [39]. For carbonate based electrolytes, like the ethylene carbonate/dimethyl carbonate mixture described in the previous section, this range is about 1 V to < 5 V vs. Li/Li^+. If an electrode potential travels outside this region decomposition of the electrolyte is possible but often becomes kinetically retarded when a passivating SEI is formed. In the case of $LiMn_2O_4$, it is clear from the reported increase in electrode impedance and loss in total capacity that some irreversible reactions are occurring. However the nature of these reactions and their effect on the surface chemistry of an $LiMn_2O_4$ electrode are difficult to attribute to one mechanism.

Most discussions of the $LiMn_2O_4$ capacity fade focus on two mechanisms: dissolution of Mn and the Jahn-Teller distortion. Both of these mechanisms are related to the cathode state of charge (and thus, the Mn oxidation state) and are most prominent when the Mn^{3+} content in the cathode is relatively high. While the Jahn-Teller distortion is possible for $LiMn_2O_4$ in the discharged state, it has been reported to have a relatively

minor contribution to capacity fade for cathodes cycled above 3 V vs. Li/Li^{+}[40]. Mn dissolution is often associated with the reaction proposed by J.C. Hunter in the early 1980's, in which $LiMn_2O_4$ spinel was exposed to acidic, water-based solutions to produce the isostructural λ-MnO_2 phase[41]. Since then, the "Hunter Reaction" has become synonymous with Mn dissolution.

Early work studying Mn dissolution in lithium-ion batteries suggested that at potentials near the charge cutoff (~4.5 V vs. Li/Li^{+}) the electrolyte could be oxidized on the surface of carbon additives in composite electrodes [42]. This observation could be due both to the electrolyte stability window discussed above, as well an inhomogeneous current density at the surface of the electrode leading to regions of slightly higher electrochemical potential. These oxidized species from the electrolyte can contribute to the dissolution of the $LiMn_2O_4$ by functioning as Lewis acids, in contrast to the protons in the classical Hunter reaction mechanism. Later works showed that this dissolution was also influenced by the electrolyte solvent and salt types and that the dissolution does not become exothermic except for in acidic pH solutions, which were caused by formation of acids during chemical decomposition of the electrolyte salts themselves [38, 43]. In particular fluorine containing electrolyte salts, most importantly $LiPF_6$ which is the commercially used salt, is said to react with trace water impurities to form HF which accelerates this process. In fact, because of the prevalence of $LiPF_6$ as a standard salt in studies involving positive electrode materials formation of HF is usually assigned as the sole culprit for capacity loss. However, it is important to recognize that while electrolyte salt choice does influence the specifics of electrode degradation, for instance which compounds are formed in the SEI, these reactions also depend on solvent, temperature, and state of

charge[44-48]. Because of the influence of decomposed solvent species and other factors Mn dissolution is also observed for non-$LiPF_6$ electrolyte salts, although the effect is not as severe[42, 49]. Capacity loss with cycling is a major impediment to the use of $LiMn_2O_4$ positive electrodes which otherwise are considered promising because of the high operating voltage and relative low cost compared to Co based electrodes. As Amatucci and Tarascon summarized, the combined electrolyte decomposition and Mn dissolution further exacerbate capacity fade in $LiMn_2O_4$ vs. graphite full cells by destroying the solid electrolyte interphase layer formed on the anode [8].

Several avenues have been pursued to enhance the capacity retention of $LiMn_2O_4$ positive electrodes. One approach investigated early in the development of $LiMn_2O_4$ electrodes is cation doping of the spinel host structure. Replacing some of the Mn cations with mono or bi-valent (e.g. Li^+ or Al^{2+}) dopant species raises the average Mn oxidation state above the stoichiometric $Mn^{3.5+}$, reducing the amount Mn^{3+} available to disproportionate. Alternatively or in conjunction with cationic doping, anionic doping of atoms in the FCC oxygen lattice with F can also reduce Mn dissolution. This is achieved by limiting Mn ion mobility due to an increased electronegativity in the Mn-anion bond[8, 50]. While effective, the doping approach decreases electrochemical performance and requires precise control of dopant placement within the unit cell, presumably negating the cost advantage of the relatively lower capacity $LiMn_2O_4$ compared to derivatives of $LiCoO_2$ (e.g. $Li(Ni_xCo_yAl_z)O_2$) used today.

More recently introducing surface coatings has been shown to enhance the cycling ability of $LiMn_2O_4$ electrodes. Several oxides have demonstrated this effect, including amphoteric oxides of Zn, Zr, Al and Ti synthesized with a variety of

techniques[40, 51, 52]. It is typically reported that these oxide coatings, which are usually discrete nanoparticles nucleated on the surface of a previously formed oxide (i.e. not produced simultaneously with the active components), are "scavenging" the residual acids like HF formed chemically in the electrolyte. Contributions to mechanical stability such as enhanced resistance to the aforementioned micro cracking and physical separation between active material and electrolyte which has also been demonstrated with Li^+ conducting glass are also cited as contributing to enhanced capacity retention[53]. For these reasons, it is also often reported that any remaining capacity loss from introducing these protective oxides is due to inhomogeneous surface coverage. However, at least one demonstration of amphoteric oxides contrary to this assumption was produced by S.B. Park et. Al. who reported that simply introducing ZrO_2 into the tape cast slurry could enhance capacity retention to a greater extent than their demonstration of a ZrO_2 coating[54].

While coatings of amphoteric oxides have been utilized in several studies to greatly enhance capacity retention of $LiMn_2O_4$ electrodes, very little has been reported on the exact mechanism of this enhancement. The generally accepted explanation is that by removing HF from the electrolyte $LiMn_2O_4$ will not undergo the aforementioned disproportionation reaction leading to Mn dissolution [41]. The detailed role of the amphoteric oxide is still unknown, although neutralizing electrolyte pH and smaller Mn concentrations for electrolytes containing amphoteric oxides have both been observed experimentally[54, 55].

2.3.5 Safety of Lithium-ion Batteries

When comparing cathode materials, the most commonly discussed parameters are those mentioned in the previous sections which pertain directly to battery performance. Considering the fact lithium-ion batteries already exist in the marketplace, additional criteria beyond performance metrics are needed. These criteria are the relative production costs and safety issues which are occasionally, but not often, considered in academic literature[12, 56].

Safety can be subdivided into two categories [39]. First, the likelihood of the battery to exhibit catastrophic failure, particularly under abusive conditions such as high current densities, elevated temperature or mechanical degradation. Second, environmental safety or toxicity can be considered. This is especially important when developing large format batteries for grid level energy storage or electric vehicles which represent potentially large concentrations of hazardous materials. In the case of catastrophic failure, battery manufactures refer to a risk of "venting with flame" and "rapid disassembly". In most cases these events are brought on by cell abuse – for example overcharge by not using an appropriate charge management system, cycling or storing at high temperatures, and mechanical failure can cause the kinetically limited, exothermic reactions associated with SEI formation to progress spontaneously [57]. When reactions at either electrode generate sufficient heat to overcome the activation energy barrier for these destructive reactions, they are collectively termed "thermal runaway" [58]. Several reactions contribute to these events such as decomposition of a the passivating SEI on the negative electrode, melting of a polymer separator causing an internal short circuit, vaporization of the electrolyte, or thermal decomposition of the oxide positive electrode. Some reactions such as the

evolution of oxygen from a de-lithiated layered type positive electrode are dependent on the state of charge of the electrode. While selection of positive electrode obviously does not reduce the risk associated with other cell components it can limit the degree to which thermal runaway presents a serious safety risk. For example, the aforementioned oxygen evolution from de-lithiated electrodes does not occur in $LiMn_2O_4$ which reduces the likelihood of electrolyte combustion during failure [59]. In a review article reporting the stability of oxide positive electrodes in a 1 M $LiPF_6$ ethylene carbonate/diethyl carbonate electrolyte, it was reported that an exothermic reaction between partially lithiated $LiCoO_2$ began at 130 °C with thermal runaway occurring above 155 °C, whereas $LiMn_2O_4$ did not experience thermal runaway until 180 °C [57]. $LiFePO_4$, which is considered the most intrinsically safe positive electrode material, did not experience thermal runaway up to 200 °C. These concepts are illustrated in Figure 2.3, which highlight that the majority of heat generated during a thermal runaway event is attributed to the positive electrode (2.3A), as well as the significantly lower heat rate for cathode materials like $LiMn_2O_4$ and $LiFePO_4$ during decomposition (2.3B) [60].

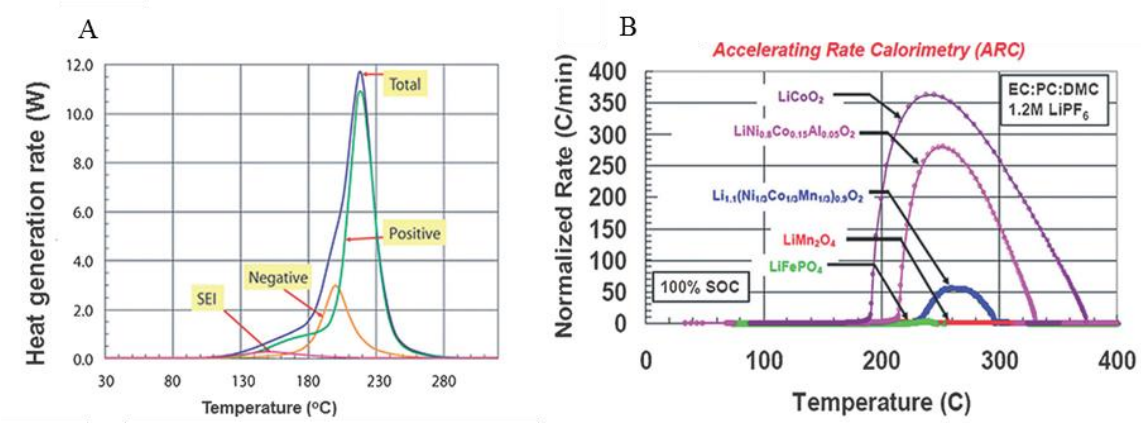

Figure 2.3 Heat generation rate for LIB full-cell, which initiates due to decomposition of the SEI but is dominated by the eventual decomposition of the positive electrode (A), and normalized heat rate for LIB cathode materials which shows that the spinel structure $LiMn_2O_4$ and olivine $LiFePO_4$ have the smallest normalized heat rates during thermal decomposition (B) (From Ref. 60).

When considering safety of positive electrode materials from a health or toxicity standpoint, consulting the MSDS for compounds of $LiCoO_2$, $LiMn_2O_4$ and $LiFePO_4$ shows that while all compounds receive a "0" for both flammability and reactivity according to the Hazardous Materials Identification System (HMIS) only $LiCoO_2$ does not receive a 0 for health, which indicates no known toxicity. $LiCoO_2$ is ranked as a "2", denoting a risk of temporary or minor lasting injury resulting from contact.

3 TECHNICAL APPROACH

3.1 Sample Preparation

3.1.1 Hydrothermal Precipitation

Hydothermal precipitation was used to deposit oxides onto the surface of carbon fibers in the current work. Also commonly referred to as hydrothermal synthesis or the hydrothermal method, hydrothermal precipitation involves the formation of solid particulates from an aqueous solution under conditions of elevated temperature. Hydrothermal experiments are frequently conducted above the 1 atmosphere boiling point of water and for this reason are contained inside of pressure vessels to prevent solvent evaporation. In these cases a void space is included in the pressure vessel which becomes saturated with water vapor during the experiment. The resulting steam pressure can significantly raise the pressure of the reaction vessel. Typical laboratory experiments utilize temperatures of <200 °C with corresponding autogenous pressures of a few MPa[61]. Because of the relatively low synthesis temperatures, as well as the kinetic factors that govern the solution nucleation and growth processes, powders formed by hydrothermal precipitation are frequently on the sub-micron scale. The hydrothermal method has been used to fabricate an impressive variety of compounds, crystal structures, and morphologies including metals, oxides and semiconductors[62-64]. A multitude of academic works have also demonstrated to applicability of hydrothermal processes in producing nanostructured electrode materials for lithium-ion batteries, including $LiMn_2O_4$ [65-67], $LiFePO_4$ [68, 69], and many other transition metal compounds [70-73].

In a typical experiment water-soluble compounds (frequently including transition-metal salts) are dissolved into water at a known molarity, sealed inside a pressure vessel, and then heated up to a temperature at which a chemical reaction will occur between the reactants resulting in an insoluble product species. Many variations on this exist, for

example the reaction may begin with an insoluble template precursor (i.e. an already formed metal-oxide), or the precipitation reaction could occur immediately under ambient conditions, whereupon the hydrothermal step is used to modify the crystallinity or morphology of the rapidly formed precipitate. A schematic of a Teflon lined, stainless steel autoclave used for hydrothermal experiments is shown in Figure 3.1 [74]. Teflon (or glass) liners prevent reaction of the hydrothermal solution with the pressure vessel, and reduce thermal gradients within the solution.

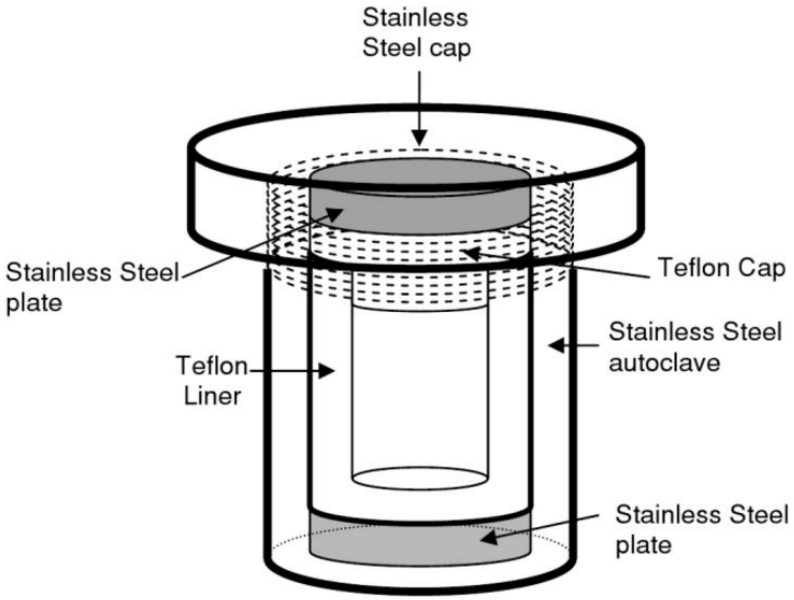

Figure 3.1 Schematic diagram of a Teflon lined stainless steel autoclave used for hydrothermal precipitation (From Ref. 74).

In the simplest sense, all hydrothermal experiments involve some precipitation event due to a thermodynamic driving force, which is usually that the concentration of the product species has exceeded the equilibrium concentration in the solvent. This driving force is expressed for a homogenous nucleation as the change in Gibbs free energy per unit volume (ΔG_v)

$$\Delta G_v = -\frac{kT}{\Omega}\ln(\frac{C}{C_0}) \qquad \textbf{Eqn. 17}$$

where k is the Boltzmann constant, T is the solution temperature, Ω is the atomic volume, C is the solute concentration and C_0 is the equilibrium solute concentration[75, 76]. For a spherical particle with radius r, the change in chemical potential associated with the change in free volume energy $\Delta\mu_v$ is given by the expression

$$\Delta\mu_v = \frac{4}{3}\pi r^3 \Delta G_v \qquad \textbf{Eqn. 18}$$

where ΔG_v is as defined in equation 17.

While introducing a volume energy by nucleating a particle in a supersaturated ($C > C_o$) solution will reduce the overall Gibbs free energy, and is thus favorable thermodynamically, particle nucleation introduces new surfaces with associated change in chemical potential associated with surface energy, $\Delta\mu_s$, defined for a spherical particle as

$$\Delta\mu_s = 4\pi r^2 \gamma \qquad \textbf{Eqn. 19}$$

where γ is the surface energy per unit area. Particles nucleate when the sum of two competing chemical potential changes, which are reducing total free energy by introducing a solid volume into a super saturated solution vs. raising the total free energy by creating new surface area, become negative (spontaneous). The total change in chemical potential is expressed below as

$$\Delta G = \Delta\mu_v + \Delta\mu_s = \frac{4}{3}\pi r^3 \Delta G_v + 4\pi r^2 \gamma \qquad \textbf{Eqn. 20}$$

where the change in chemical potential associated with the volume ($\Delta\mu_v$) and surface ($\Delta\mu_s$) for a spherical particle are defined in equations 18 and 19.

For equations 19 and 20 the surface energy per unit area (γ) is assumed to be homogenous, and can be generally defined at constant number of moles, temperature and pressure as

$$\gamma = (\frac{\partial G}{\partial A})_{n_i,T,P} = \frac{1}{2} N_b \varepsilon \rho_a \qquad \textbf{Eqn. 21}$$

where A is the surface area, n_i is the number of moles, T is temperature, P is pressure, N_b is the number of broken bonds on a particle surface, ε is the bond strength, and ρ_a is the surface atomic density. In reality, bond strength (ε) and surface atomic density (ρ_a) vary as a function of crystal structure or crystallographic plane (different packing densities) and chemical composition (different bond character). This discrepancy provides a thermodynamic driving force for faceted crystal formation. Meanwhile, amorphous nuclei which should have relatively isotropic bond strength and packing density would favor spherical particle formation.

For hydrothermal reactions which utilize a substrate as a nucleation site, the driving force for nucleation is still the supersaturation of the solute species however the surface energy component (which resists nucleation) is split into three factors. The nuclei-liquid interfacial surface energy (solid nuclei and liquid hydrothermal solution), which is the only factor for the homogeneous nucleation case, is expressed as γ_{NL}, the nuclei-substrate interface (solid nuclei and solid substrate), which is expressed as γ_{NS} and the liquid-substrate interface (liquid hydrothermal solution and solid substrate), which is expressed as γ_{LS}.Thus the driving force for a heterogenous nucleation (ΔG_{het}) can be expressed as

$$\Delta G_{het} = V_s \Delta G_v + A_{NL}\gamma_{NL} + A_{NS}\gamma_{NS} - A_{NS}\gamma_{LS} \qquad \textbf{Eqn. 22}$$

where V_s is the volume of the solid nuclei (no longer spherical as in equation 20), A_{NL} and A_{NS} are the areas of the nuclei-liquid and nuclei-substrate respectively. It is apparent from equation 22 that the surface energy changes are negative (favored by thermodynamics) for the liquid-substrate interfaces (γ_{LS}), as they are related to the area of the nuclei-substrate interface (A_{NS}) which becomes covered during the nucleation process. This factor tends to make heterogeneous nucleation favored over homogeneous nucleation, however both processes can occur simultaneously. Instead of a spherical particle, a hemispherical "cap" can be defined with a wetting angle θ and used to define an expression very similar in appearance to equation 20

$$\Delta G_{het} = \left(\frac{4}{3}\pi r^3 \Delta G_v + 4\pi r^2 \gamma_{NL}\right) S(\theta) \qquad \textbf{Eqn. 23}$$

where S(θ) is a geometrical relation as follows

$$S(\theta) = (2 + cos\theta)(1 - cos\theta)^2/4 \quad \textbf{Eqn. 24}$$

which describes the shape of the semispherical nuclei cap as a function of the wetting angle.

In both homogenous and heterogeneous nucleation cases, the rate at which nuclei form is described by an Arrhenius type equation below

$$nucleation\ rate = Ne^{\left(\frac{-\Delta G}{kT}\right)} \quad \textbf{Eqn. 25}$$

where the pre-exponential factor N, which describes the quantity and distribution of nucleation sites, is also dependent on the nucleation type. A rapid nucleation rate for a given solute concentration generally means the final particle size will be smaller, however after nucleation particles can grow through a number of mechanisms. For high temperature synthesis, crystallographic domains are expected to grow through the migration of grain boundaries by sintering, resulting in larger crystallite sizes. In a hydrothermal experiment temperatures are significantly below the rule of thumb estimation of a sintering onset temperature (~ 70% $T_{melting}$), thus particulate growth through sintering is unlikely. Still, nanosized nuclei have large surface areas and thus some driving force to reduce the total system energy, and as a result grain growth does occur. The two mechanisms available to low temperature synthesis of particulates to reduce overall surface energy are Ostwald ripening and agglomeration. Ostwald ripening occurs due to a chemical potential gradient produced by nuclei with dissimilar radii (and therefore, different surface curvatures), shown below

$$\Delta\mu = 2\gamma\Omega\left(\frac{1}{R_1} - \frac{1}{R_2}\right) \quad \textbf{Eqn. 26}$$

where surface energy and atomic volume are again represented by γ and Ω respectively, while R_1 and R_2 are the radii of two neighboring nuclei. Equation 26 is related to, but distinct from, the Young-Laplace equation (Equation 27) which describes the chemical potential gradient between a curved surface with radius R and an infinitely flat surface

$$\Delta\mu = 2\gamma\frac{\Omega}{R} \quad \textbf{Eqn. 27}$$

which shows that for smaller nuclei radius the change in chemical potential increases, thereby favoring the removal of atoms from the curved surface. As the curvature of a

small particle is higher relative to a large particle, the change in chemical potential is higher for the smaller particle and thus atoms will diffuse through the liquid solution to the larger particles. Meanwhile, particles are assumed to maintain their shape and size during agglomeration but will re-arrange themselves relative to each other to decrease total surface energy.

3.1.2 Electrospinning

Electrospinning is a method which allows for the production of nanoscale polymer filaments with controllable diameters, lengths, and interconnectivity from a viscous solution. Such solutions are typically obtained by dissolving a polymer in an appropriate solvent, and solvents utilized are frequently organic compounds like ethanol, acetone and dimethyl formamide which can dissolve a wide variety of polymers. This technique is used in the present work to prepare interconnected polymer-fiber mats which are subsequently pyrolized to produce carbon fibers.

During the electrospinning experiment a computer controlled pump regulates the flow of the viscous polymer solution from a syringe until a small droplet is formed from a needle tip. A large DC electric field (i.e. kV) is applied between the needle tip with polymer droplet and a grounded collector. The droplet is warped into a characteristic "Taylor cone" due to repulsion between surface charges incurred by the electric field until the surface tension of the viscous solution is overcome to produce a filament. The filament is elongated and whipped in the direction of the collector, and this whipping action both reduces the filament diameter as well as removes solvent from the thinning filament [77]. Depending on the magnitude of the electric field (controlled by needle to collector distance and applied DC bias), the viscosity of the polymer solution (a function of solvent and polymer type, solution temperature, and the rheological properties of the

solution), as well as the position and geometry of the collector a non-woven mat of polymer fibers will be produced. A schematic of the electrospinning process is shown in Figure 3.2[77]. In the case that the polymer solution and experimental parameters cannot maintain a continuous filament during the spinning process, the filament may break into small droplets in transit to the collector and result in discrete particles. This process is referred to as "electrospraying" and can also be utilized to create nano-scale materials. One drawback of the electrospinning process is that on the laboratory scale building up a suitably thick non-woven mat is very slow. Typical laboratory setups like the one depicted in Figure 3.2 use a single spinneret, though demonstrations of "needleless" systems can reportedly produce non-woven mats hundreds of micrometers thick at a rate of 10s of meters per minute [78, 79].

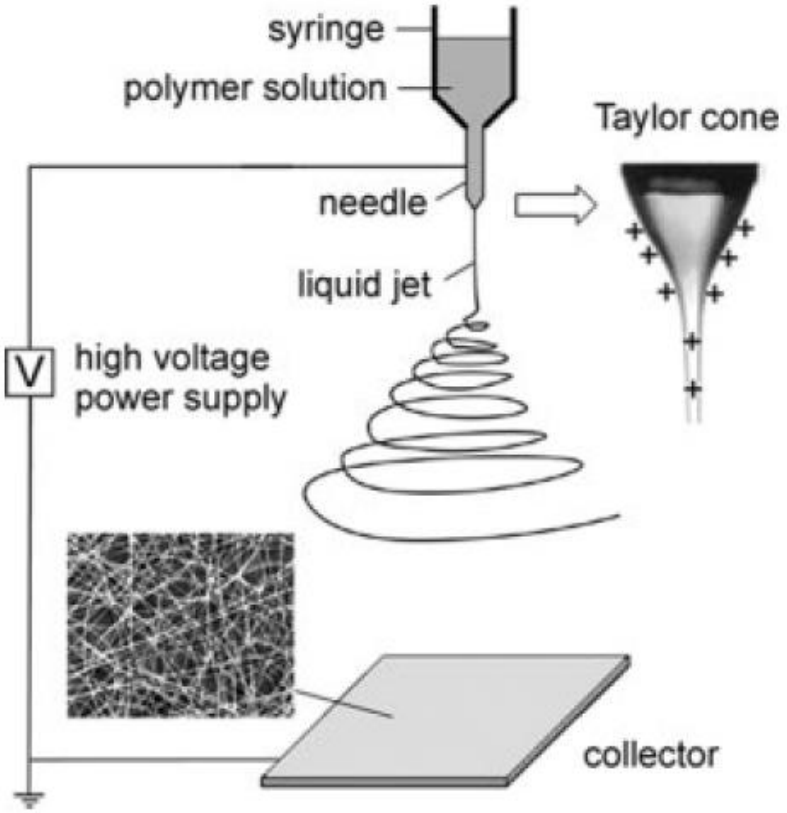

Figure 3.2 Schematic depiction of electrospinning experiment. Solution variables include solvent type, solute type and temperature. Needle variables include diameter, arrangement of multiple needles and needle-hole geometry. Collector variables include collector movement and geometry (drum, plate or mesh) (From Ref. 77).

3.1.3 Sol-gel Films

Sol-gel process refers to the general process in which a solution of precursor's compounds (usually metal salts) in a suitable solvent is converted into a viscous gel by controlled evaporation of said solvent. This approach ensures good homogeneity of precursor compounds prior to a calcination step to form oxides, which can be difficult to achieve by mechanical mixing of powders. In the current work, drop-coating of sol-gel solutions was used to produce dense $LiMn_2O_4$ coatings on metal current collectors. These dense films were used as model electrodes without any organic additives (e.g. carbon or binders) to study interfacial effects in surface-modified electrodes. In a typical procedure,

a solution containing a known concentration of metal-oxide precursors is placed onto a substrate with a micropipette. The sol is then allowed to dry in a controlled manner, usually involving increased temperatures, to form a gel. Depending on solution properties (e.g. solvent vapor pressure, viscosity and solute concentration) a crack-free and uniform gel can be produced. This gel can be calcined to produce dense oxide. While in this dissertation a simple drop-coating approach is used, a common variation to produce uniform films on larger substrate is spin-coating, which can be iterated to achieve relatively thick films.

3.1.4 Atomic Layer Deposition

Atom layer deposition (ALD) allows for the coating of porous samples with a conformal film, making it ideal for application in composite electrodes used in lithium-ion batteries. In theory, ALD is a self-limiting process due to reactions of a precursor molecule with functional groups on the sample surface. The deposition of Al_2O_3 onto Si is depicted in Figure 3.3[80]. In this case, hydroxyl groups on the surface of Si (or the native SiO_2 layer) react with incoming trimethyl alumina (TMA) molecules, releasing methane in the process. The reaction chamber is then purged of excess TMA and pulsed with a second precursor, in this case water, to re-functionalize the now methyl terminated aluminum surface with hydroxyl groups. This process can be repeated indefinitely to build up thicker layers of oxide layer-by-layer. Another advantage of ALD is the relatively gentle conditions required for deposition. Reaction temperatures usually do not exceed 200 °C and vacuum levels of approximately 10^{-2} Torr. Thus, carbons and even some polymers can be easily coated provided they have the correct functionalization.

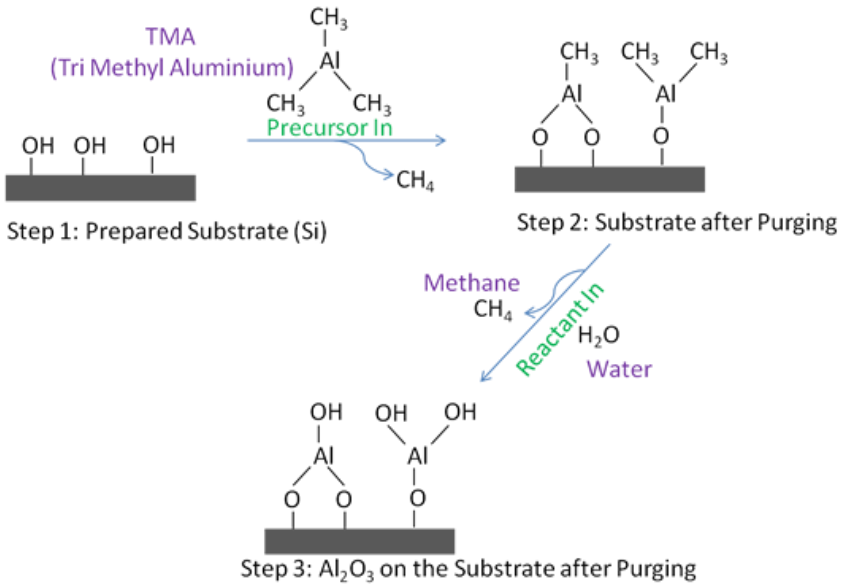

Figure 3.3 Schematic depiction of atomic layer deposition process for Al_2O_3 on Si (From Ref. 80)

3.2 Physical and Chemical Characterization Techniques

3.2.1 Electron Microscopy

Two variations of electron microscopy are utilized in this dissertation, scanning electron microscopy (SEM) and transmission electron microscopy (TEM), however SEM was implemented to a much greater extent. Electron microscopes are ubiquitous tools for materials characterization, in particular for nanoscale materials, as they are capable of achieving lateral resolutions on the order of a few nanometers. All electron microscopes utilize high-energy electrons to interrogate the sample. Electrons are extracted from the tip of a charged (and sometimes heated) filament and accelerated towards the sample by electromagnets. A series of apertures and electromagnetic "lenses" are used to shape the electron spot to control flux and focus of the electron beam. For SEM systems, electrons have typical energies of 5-25 keV, while TEM systems utilize much higher energies in excess of 100 keV. As the name implies, the higher energy electrons utilized by TEM enable electrons to transmit through sufficiently thin samples, while the lower energy

electrons of an SEM interact only with the outer surface of the sample to some limited depth. Thus, images are collected in TEM by analyzing the primary electron beam after it interacts with the sample, which produces a contrast image where the electron beam is blocked. Diffraction of the electron beam can also be utilized in TEM for crystalline samples. Imaging in SEM is achieved by collecting both backscattered primary electrons, which interact with the sample surface nearly elastically and maintain a high energy, and secondary electrons which are released from ionization events within the sample. Primary electrons can be used to analyze regions of a sample with high discrepancies in atomic density and appear as regions of differing contrast. Secondary electrons are typically very low energy, and thus come from near the sample surface. The ionization events which produce secondary electrons can also release a number of other valuable signals, most notably characteristic x-rays, which are discussed in the next section. The electron interaction volume, which has a tear-drop shape relating to the energy of both incoming energies (electrons) and exiting signals, is depicted in Figure 3.4 [81].

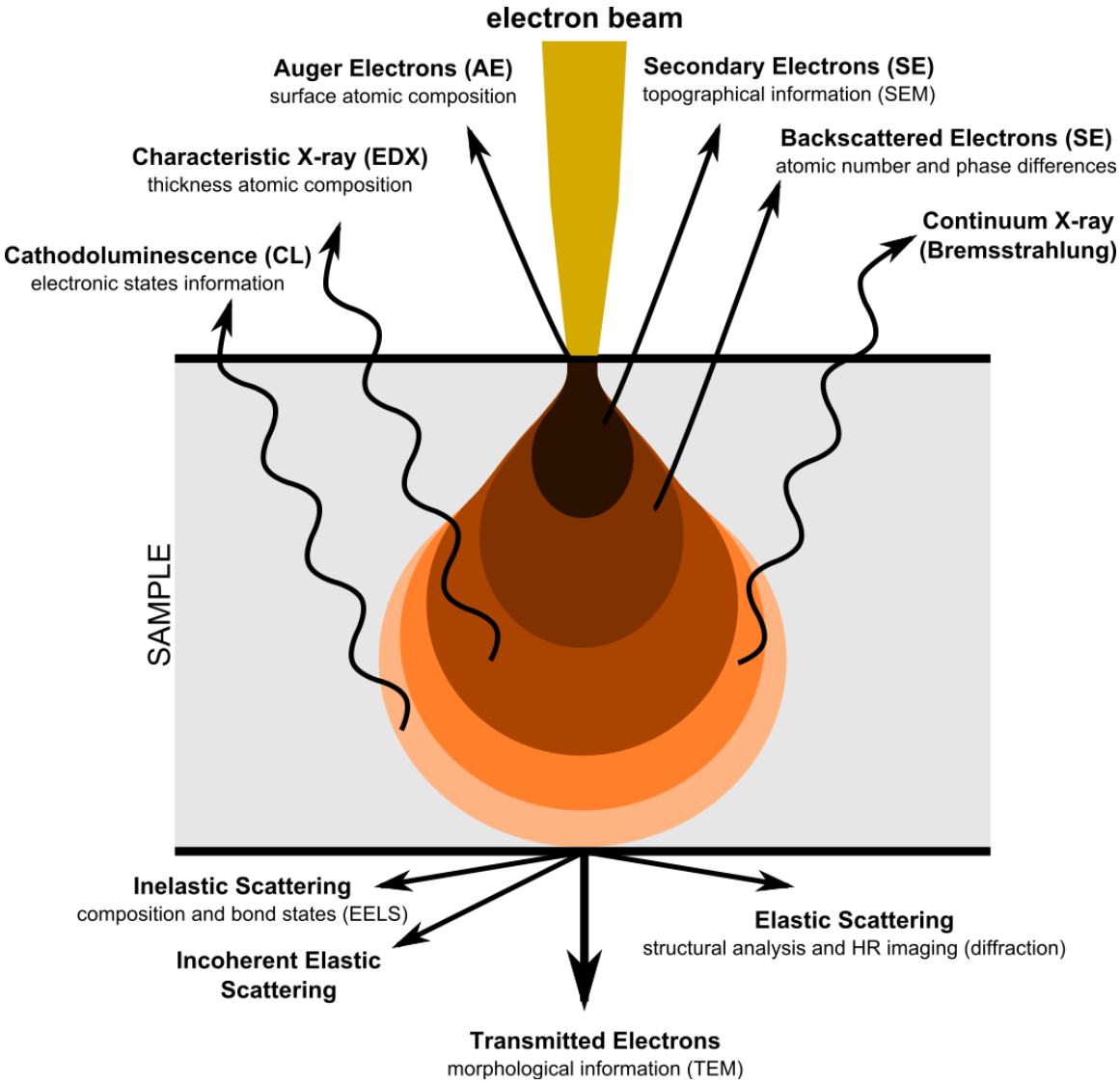

Figure 3.4 Schematic depiction of the electron interaction volume occurring during electron microscopy analysis. Multiple processes occur in the sample, including both elastic and inelastic processes (From Ref. 81).

One limitation of electron microscopes is that because the probe used for characterization is charged, this charge can be imparted to insulating samples. Charge buildup will warp the incoming electron beam and thus manipulate the apparent surface morphology observed. For this reason, insulating samples are frequently coated with thin conductive layers or gold or carbon to provide a conductive pathway away from the

sample surface. At very high magnifications these conductive coatings can be observed, thus inhibiting the observation of ultra-fine surface details.

3.2.2 Energy Dispersive X-ray Spectroscopy

As shown in the previous section, a variety of emissions are produced when a material interacts with high energy electron. While transmitted, scattered or generated electrons are useful for characterizing the morphology of a material, the x-rays produced during electron microscopy are a powerful tool to characterize the elemental composition of the sample by a technique known as Energy Dispersive X-ray Spectroscopy (EDS). Characteristic x-rays are released from the sample when a high energy primary electron removes an electron from an inner atomic orbital of an atom in the sample being analyzed. The electron hole left behind is then filled by an electron from a higher-energy outer shell, and an x-ray with a wavelength related to the energy difference between the electron-hole shell and donor shell is emitted from the sample. Because the x-ray emission process involves core electrons, the energy levels are fixed and thus the x-rays are unique fingerprints for a given element. Electrons must have sufficiently high energy to stimulate emission of an x-ray, and for the electron energies used during SEM emissions from the Kα, Kβ, Lα and Lβ transitions depicted in Figure 3.5 are most common[82].

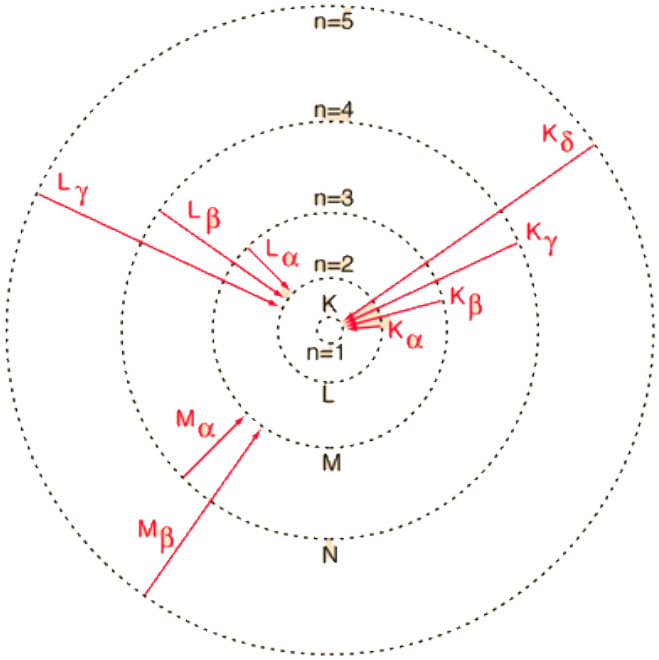

Figure 3.5 Core-hole electron transitions leading to x-ray emissions observed by EDS. K and L transitions involve core-hole generation in the two innermost electron shells (From Ref. 82).

One limitation of EDS is that because the interaction volume extends to some significant depth into the sample, EDS does not have the same lateral resolution as SEM or TEM can achieve for imagining. A rule of thumb is that x-rays can escape from approximately 1 micron of depth from the electron beam, even if the beam spot-size is only a few nanometers in diameter. Related to this escape depth are matrix effects, meaning that x-rays of different energies will absorb differently within samples of differing compositions or phases. As a result EDS is often considered a qualitative technique, useful for identifying elemental composition but not reliably reporting elemental stoichiometry. An additional limitation for lithium-ion battery electrodes is that elements with atomic weights below Boron, which includes Lithium, cannot be detected using the commonly available laboratory EDS systems which use a Be window and Si-Li detector.

3.2.3 X-ray Photoelectron Spectroscopy

Like EDS, X-ray Photoelectron Spectroscopy (XPS) can be used to identify the elemental content of a sample. However, unlike EDS the XPS signal can be used to determine bonding information and oxidation state from the elemental signals. X-rays are used as the probe signal during XPS, which ionize core-level electrons such that they are ejected into the vacuum beyond the sample surface. These electrons are called "photoelectrons" because they are produced by interactions of the sample with high-energy photons, and have kinetic energies described as follows

$$E_{kinetic} = h\nu - (E_{binding} + \varphi_{sample}) \qquad \textbf{Eqn. 28}$$

where $E_{kinetic}$ is the kinetic energy of the photoelectron at the vacuum level, h is Plank's constant, ν is the photon frequency (ν=speed of light divided by the photon wavelength) $E_{binding}$ is the binding energy of the photoelectron, and φ_{sample} is the work function of the sample being analyzed which varies from sample to sample. The kinetic energy of the photoelectrons is measured by a spectrometer, while the binding energy is a quantized value independent of the work function or photon energy. While the spectrometer has a different work function than the sample, which would complicate the calculation of binding energies, the Fermi level of the spectrometer and sample surface are identical. Thus, the following relation applies

$$E_{kinetic\_sp} + \varphi_{spectrometer} = E_{kinetic\_s} + \varphi_{sample} \quad \textbf{Eqn. 29}$$

where $E_{kinetic\_s}$ is the kinetic energy of the photoelectron relative to the sample, $E_{kinetic\_sp}$ is the kinetic energy of the photoelectron relative to the spectrometer, and $\varphi_{spectrometer}$ is the work function of the spectrometer. Thus equations 28 and 29 can be combined as

$$E_{binding} = h\nu - E_{kinetic_{sp}} - \varphi_{spectrometer}$$ **Eqn. 30**

and because ν and $\varphi_{spectrometer}$ are constant for a given spectrometer, the binding energy of photoelectrons in any sample can be determined (by measuring $E_{kinetic_{sp}}$) without measuring the work function of each sample. Accurate determination of the photoelectron binding energy is particularly useful because binding energies are influenced by the bonding environment and oxidation state of the atom from which they are derived. Higher oxidation states or stronger bonds (i.e. a metal cation bound to a more electronegative anion) will lead to a greater amount of energy needed to remove the photoelectron, and thus a higher observed binding energy. These so-called "chemical shifts" are utilized to further characterize the sample.

Soft x-rays (<5 keV, and typically 1-2 keV for laboratory XPS x-ray sources) have relatively shallow penetration depths due to the short mean-free path for photoelectrons produced by soft x-rays. Typical sampling depths are estimated to be less than 10 nm for laboratory XPS systems, giving this technique a high degree of surface specificity. Sputtering the sample with Ar ions can be utilized to mill into the sample surface either to remove unwanted surface contamination or develop a depth-profile of elemental content or chemical states. Peak fitting can be used to quantify relative photoelectron yield between both different elements, as well as for electrons from atoms with different bonding environments or oxidation states, making XPS more quantitative than EDS. Still, many elements have asymmetrical peaks or various ancillary signal sources such as shake-up peaks that can complicate analysis. Instrumental factors can also influence the observed peak shape. Whenever possible, reference samples should be used for quantitative analysis.

3.2.4 X-ray Diffraction

X-ray diffraction (XRD) is utilized extensively in this dissertation to characterize crystalline materials. XRD measurements produce a pattern of diffraction peaks related to the crystal structure and composition of the sample being analyzed. In order for diffraction to occur, the spacing between crystallographic planes (d) must satisfy the Bragg condition below

$$n\lambda = 2dsin\theta \quad \textbf{Eqn. 31}$$

where n is an integer of the x-ray wavelength λ and θ is the diffraction angle. Diffraction of x-rays is an inelastic process, but the intensity produced during diffraction is highly dependent on the sample crystallinity and density. Loosely packed, highly amorphous or polycrystalline samples will diffract relatively weakly and can be difficult to analyze.

While satisfying the Bragg condition is required for any set of planes to diffract, not all planes which meet this condition will diffract. For crystal structures containing only one type of atom, or for structures containing multiple atoms, complete or partial destructive interference will occur during diffraction. This interaction between planes results in peaks with reduced intensity or "absent" peaks which satisfy the Bragg condition but are not observed in the diffraction pattern. Equation 32 describes this effect known as the structure factor as a sum of influence for N atoms,

$$F_{hkl} = \sum_{i=1}^{N} f_i e^{2\pi i(hu_i+kv_i+lw_i)} \qquad \textbf{Eqn. 32}$$

where u_i, v_i and w_i are the lattice positions for each atom i in a given plane described by the miller indices (hkl) and f_i is the intrinsic scattering factor for that atom. Other structural features influence the intensity of individual diffraction peaks as well. For example, planes which have a high multiplicity (multiple planes with identical lattice

constant and therefore Bragg angle) will have a large intensity relative to those with few planes. In cubic system, low index planes such as (100) or (111) will have the highest multiplicity and therefore highest intensity. Intensity can also be influenced by non-structural factors, such as relative degree of crystallinity as mentioned earlier, as well as x-ray absorption (dependent on elemental composition) and crystallite size. Very small crystallites (<100 nm) will lead to a broadened peak shape which can be interpreted by the Scherrer equation

$$\tau = \frac{0.9\lambda}{B\cos\theta_B} \qquad \textbf{Eqn. 33}$$

where τ is the crystallite size, λ is the x-ray wavelength, B is the full-width at half-max of the peak being analyzed, and θ_B is the position of the peak being analyzed. For crystallites on the order of >100 nm, the Scherer equation does not provide accurate estimation of crystallite size.

3.2.5 Raman Spectroscopy

Raman spectroscopy utilizes photons, usually within the visible spectrum, to characterize the molecular structure of a material through the inelastic Raman scattering processes. During the Raman experiment, a small fraction of incident photons impart some energy to the molecules in the sample and return to a photodetector with less energy than the incident photons. The difference is energy is observed as a change in wavelength between the incident and scattered photons and is expressed in "wavenumbers" with units of Δcm^{-1}. Raman scattering is associated with molecular vibrational modes with the theoretical number of modes defined a non-linear molecule with N atoms as

$$Total\ Vibrational\ Modes = 3N - 6 \qquad \textbf{Eqn. 34}$$

which is derived from the available degrees of freedom in molecular motion, with the exception of translation in three directions or rotation about three axis (total of 6 "missing" modes). Further restrictions apply for different crystal structures, meaning that some of the vibrational modes predicted for a molecule by equation 34 are "forbidden". For centrosymmetric space groups, which includes the space group to which $LiMn_2O_4$ belongs ($Fd\bar{3}m$) only molecular vibrations which are symmetrical after an inversion operation are Raman active, while all other modes are active during infrared spectroscopy.

The Raman signal is generated regardless of whether a material is crystalline or amorphous, however this can influence the observed spectrum. Furthermore, Raman spectroscopy can be conducted under ambient or even *in situ* conditions, giving it a distinct advantage over laboratory scale XPS, EDS and XRD. The lateral resolution of Raman spectroscopy can be enhanced by using an optical microscope objective, with a laser spot size on the order of a few microns. A significant drawback however is the variability between the Raman spectrum produced for chemically or structurally similar samples, for this reason the lack of a comprehensive database of Raman spectra. This limitation requires significant prior knowledge of the materials being analyzed. Thus, Raman is a suitable complimentary technique to the techniques previous introduced. Figure 3.6 shows a schematic representation of the electrochemical cell utilized for *in situ* characterization of $LiMn_2O_4$ electrodes. In order to make electrical contact to the electrode, metal foils are used as the substrate and the electrode active material is a relatively thin film without binders or conductive additives. To produce an optical pathway for Raman analysis, both the separator and counter electrode (lithium metal) are prepared with an annulus shape. This means that the portion of the working electrode being analyzed has a more tortuous ionic pathway compared to the working electrode

region directly below the counter electrode. Careful cell assembly and electrochemical testing is required to prevent this from being a significant issue.

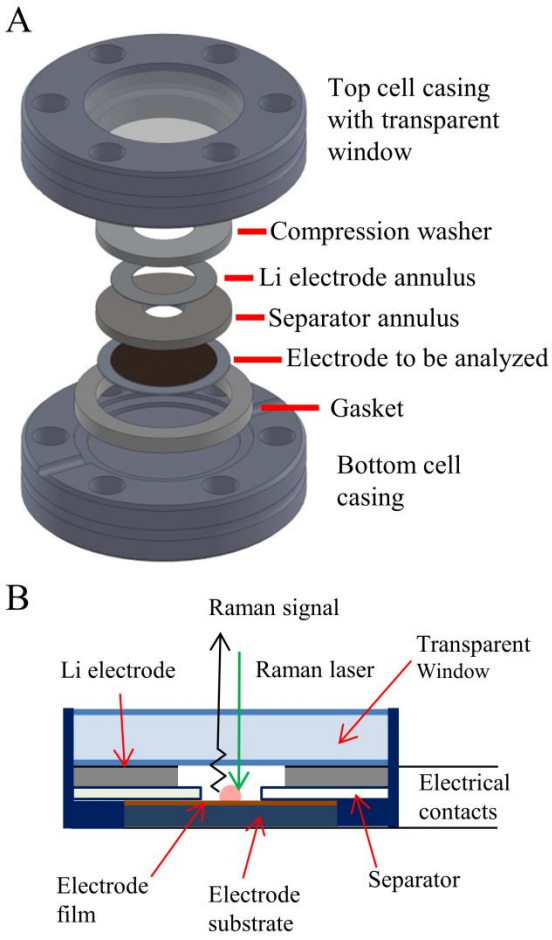

Figure 3.6 Schematic of in situ Raman cell showing cell hardware (A) and internal cross-section (B).

3.2.6 TGA/DSC

Thermal analysis is conducted in this dissertation to determine both reaction temperatures and to determine the weight content of carbon fibers in composite electrodes produced by coating oxides onto carbon fiber by hydrothermal precipitation. Thermogravimetric analysis (TGA) and differential scanning calorimetry (DSC) were conducted in this dissertation simultaneously by heating an alumina crucible filled with a

sample of interest in a controlled fashion under pure, dry air. As the sample heats, fluctuations in mass and heat flow relative to an empty reference crucible are monitored to identify chemical reactions. For samples containing carbon fibers, oxidation of the carbon fibers is associated with a large exothermic heat flow and mass loss. When heated to a suitably high temperature all of the carbon in a sample will oxidize leaving behind only incombustible components and alloying for precise identification of the mass of the coatings added during hydrothermal precipitation. In some cases, the oxidation of carbon fibers is influenced by the oxide coating, which can also be observed by TGA/DSC.

3.3 Electrochemical Testing

3.3.1 Electrochemical Cell Assembly

Electrochemical testing was conducted for all electrodes using "Swagelok" type cell hardware, excluding those electrode tested with the *in situ* Raman cell shown in Figure 3.6. Swagelok cells are constructed from off the shelf hardware from the company Swagelok originally intended as tube fittings. Stainless steel is used for all points of electrical contact inside the cell, while the rest of the unit is made of chemical resistant perfluoroalkoxy alkane (PFA). The working electrode (WE) is either an oxide coated carbon fiber paper or drop-coated sol-gel electrode on stainless steel, with typical diameters of 0.25 to 0.438 inches. The lithium metal counter electrode (CE), electrolyte soaked separator, stainless steel spacer and stainless steel plungers are all 0.5". The Swagelok cells are assembled inside an Ar filled glovebox and tightened to compress the stainless steel spring and seal the internal components from the atmosphere. Once sealed, the cells can be cycled using a computer controlled potentiostat outside the glovebox.

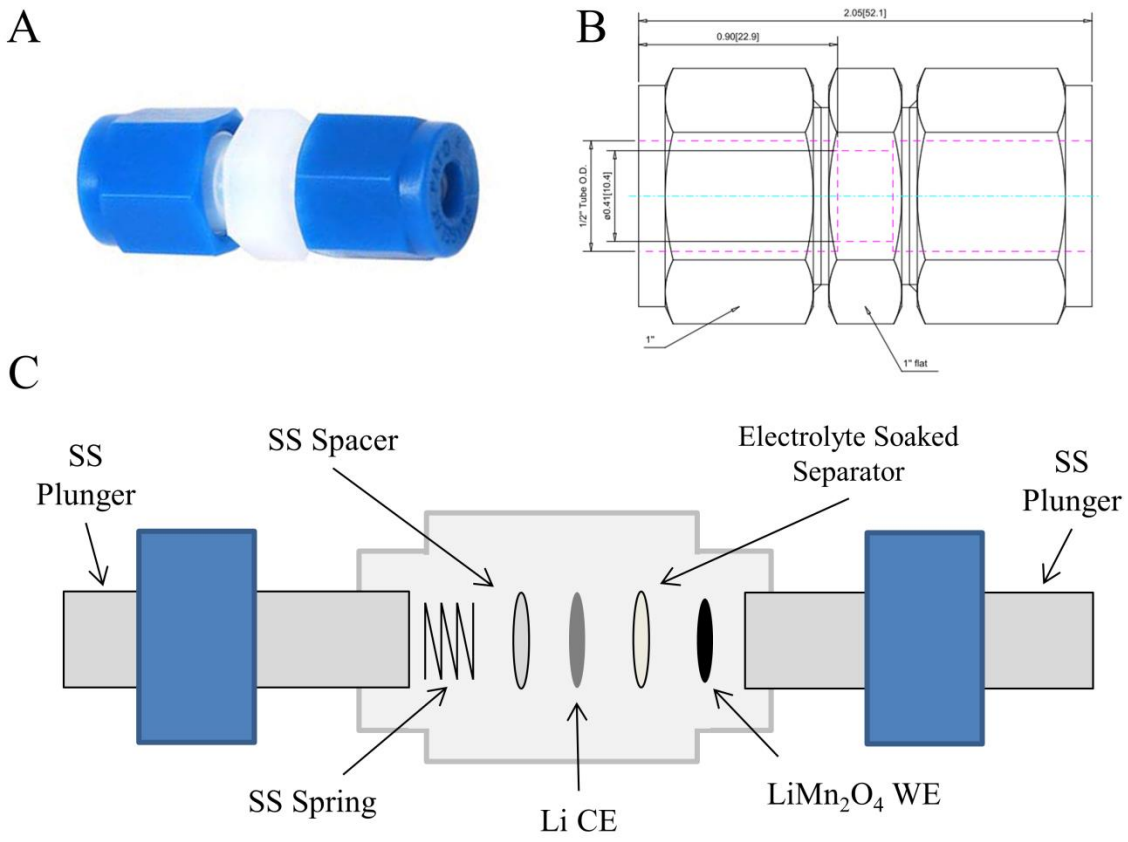

Figure 3.7 Swagelok cell hardware showing digital photograph of actual Swagelok fitting (A), technical drawing showing cell interior (B) and schematic identifying features of assembled cell (C).

3.3.2 Cyclic Voltammetry

Cyclic Voltammetry (CV) involves sweeping the cell potential at fixed rate between a starting and final potential, and then reversed. This technique was used to identify the position of reduction and oxidation (Faradaic) reactions relative to a reference electrode, which in all cases for this dissertation was lithium metal. Multiple cycles are typically collected to monitor changes in the electrochemical behavior of the electrode. Redox activity for Faradaic reactions is observed during a CV experiment as an increase in current to a maximum in the vicinity of the equilibrium redox potential, as defined by the Nernst equation (Chapter 2, Equation 11), followed by a decaying current to a constant diffusion controlled value. For a faradaic reaction the peak current, i_p, can be described by the Randles-Sevchick equation at room temperature with Equation 35

$$i_p = (2.69x10^5)n^{3/2}AD^{1/2}Cv^{1/2} \quad \textbf{Eqn. 35}$$

where *n* is the number of electrons transferred per molecule of reactant, A is the electrode surface area in cm^2, D is the diffusion coefficient of the reactant species in cm^2/s, *C* is the concentration of the same species at the electrode surface in mol/cm^3, and *v* is the sweep rate in V/s [83]. For a completely reversible reaction, an identical current magnitude is expected during the reverse sweep, while the potential observed will be separated from the forward sweep reaction by a value of approximately 59/*n* mV.

As can be seen in equation 35, the peak current observed for a redox peak during a CV experiment is related to the square root of the sweep rate. For a set of known electrode conditions, unknown factors such as the diffusion coefficient (D) can be determined by conducting CV sweeps at various rates. In some cases, capacitive current may also be observed, especially for high surface-area electrodes in which the current associated with forming an electrochemical double-layer is large. For an ideal capacitor, the current is described as

$$I_{cap} = C\frac{dV}{dT} \quad \textbf{Eqn. 36}$$

where I_{cap} is the purely capacitive current, C is the capacitance, and dV/dT is the change in voltage with respect to time (i.e. the sweep rate). Thus, a relatively constant current associated with a capacitor may be imbedded in the observed current response from a Faradaic reaction during a CV experiment.

3.3.3 Galvanostatic Cycling

Most battery testing is conducted under galvanostatic, or constant current, conditions between a voltage maximum and minimum. Upper and lower cutoff conditions are

defined by the theoretical potential of the active material, but also the working range of the electrolyte. In most cases the active materials potential will be well within the working range of the electrolyte. Currents are typically presented as a normalized value, either by the area of the electrode or the mass of the active material. In the latter case a "C rate" is used, where 1C is defined as the current required to consume the entire theoretical capacity of the active material in one hour. In an example for $LiMn_2O_4$, with a theoretical capacity of 148 mAh/g, a rate of 1C corresponds to 148 mA/g. C rate are useful when comparing batteries with identical active materials but dissimilar amounts of inactive components or cell construction. In this dissertation, galvanostatic testing is used to determine the life time of electrodes during repeated charge and discharge cycling. While the observed capacity may decrease with each subsequent cycle, the amount of active material is assumed to be constant and thus the C rate defined for the starting condition is maintained throughout the testing.

3.3.4 Electrochemical Impedance Spectroscopy

Electrochemical Impedance Spectroscopy (EIS) utilizes a small AC voltage perturbation on a cell under open circuit conditions. The frequency of the AC signal is varied with time and the current response is recorded. The result of this testing is a frequency dependent impedance response which can be used to describe the magnitudes and time constants associated with various physical and electrochemical processes occurring at the electrodes. In theory, individual processes can be modeled using so-called "equivalent" electrical circuit elements, namely resistors, capacitors and inductors. The impedance for a resistor-like element (Z_R) is frequency independent, and described by Ohm's law

$$Z_R = R = \frac{E}{I} \qquad \textbf{Eqn. 37}$$

where E is the open circuit potential, I is the observed current, and R is the equivalent resistance. The impedance of capacitors and inductors are both frequency dependent, and described for capacitor-like elements as

$$Z_C = \frac{1}{j\omega C} \qquad \textbf{Eqn. 38}$$

where *i* is the imaginary number ($j = \sqrt{-1}$), ω is the frequency and C is the capacitance. Likewise, for inductors the impedance is described as

$$Z_L = j\omega L \qquad \textbf{Eqn. 39}$$

where L is the equivalent circuit inductance. While resistors and capacitors are commonly utilized to describe electrochemical processes, inductors are only rarely introduced. Because electrochemical circuits do not behave as perfect analogues of electrical circuit elements, special elements are also used. One of particular importance is the constant phase element (CPE) which is used to replace capacitor elements in systems with inhomogeneous surface features. The impedance of a CPE is described as

$$Z_{CPE} = \frac{1}{(j\omega)^{\alpha} Y_0} \qquad \textbf{Eqn. 40}$$

where Y_0 is a parameter equivalent to the capacitance (C) in equation 38 and α is a parameter describing the deviation from the behavior of an ideal capacitor, which is always between 0 and 1. When α=1 Z_{CPE} is identical to Z_C.

Equivalent circuit models consisting of combinations of electrical circuit elements are used to describe electrochemical systems, and allow for quantification of individual elements. The Randles circuit is one such combination, and is often used as a starting

point when building equivalent circuits which describe more complicated electrochemical processes. As shown in Figure 3.8, the Randles circuit consists of a resistor (R_s) in series with a second resistor (R_{CT}) and capacitor (C_{dl}) which are in parallel. In the theoretical Randles circuit, R_S, R_{CT} and C_{DL} are associated with solution resistance, charge transfer resistance, and the double layer capacitance, respectively. More complicated circuits often build on the Randles circuit with repetitions of the parallel R/C circuit associated with different time constants.

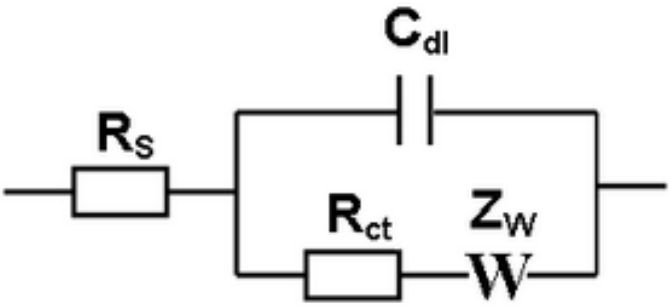

Figure 3.8 Randlles circuit used to quantify equivalent circuit elements observed during electrochemical impedance spectroscopy.

A new element included in Figure 3.8, known as the Warburg element (Z_W), concludes the equivalent circuit and describes ionic transport through a solid electrode. For diffusion through a layer with a finite thickness, the Warburg impedance is defined as

$$Z_W = \sigma\omega^{-\frac{1}{2}}(1-j)\tanh\left(\delta\left(\frac{j\omega}{D}\right)^{\frac{1}{2}}\right) \quad \textbf{Eqn. 41}$$

where σ is the Warburg coefficient with units of ohm-seconds$^{-1/2}$, δ is the thickness of the diffusion layer, and D is the apparent diffusivity of the diffusing species.

4 DEVELOPMENT OF LIMN2O4 COATED CARBON FIBER ELECTRODES

In this chapter, the development of $LiMn_2O_4$ coated carbon-fiber electrodes by hydrothermal precipitation is described. This approach removes the need for tape casting and the associated binders, solvents and metal foil current collectors and greatly simplifies electrode assembly. A schematic illustration of the composite electrodes constructed in this way is shown in Figure 4.1. Ideally, the carbon fibers would produce an uninterrupted electronic pathway to the surface coating of electrochemically active oxide, while the interconnecting voids between the fibers allow for electrolyte penetration into the electrode. Figure 4.1 suggests a possible cell design in which both the positive and negative electrode could be constructed in this manner, however this chapter will only focus on development of an $LiMn_2O_4$ based positive electrode.

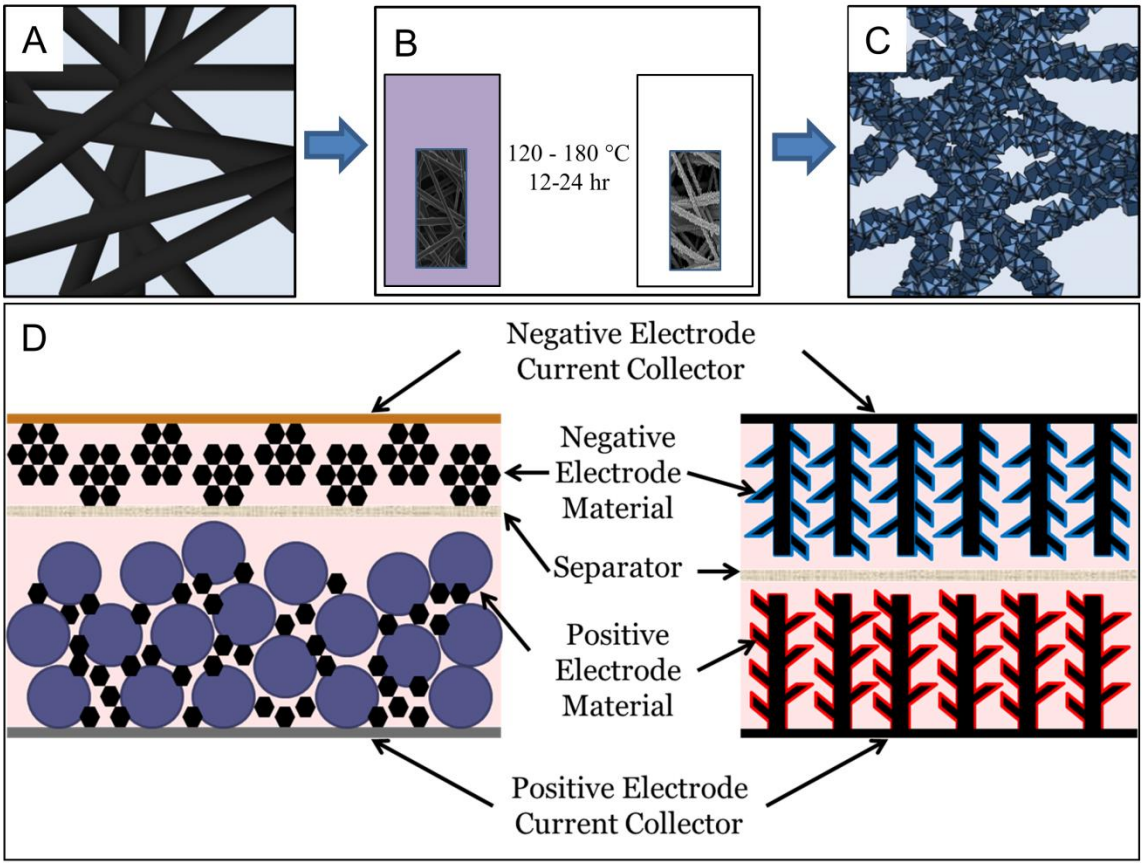

Figure 4.1 Schematic depiction of bare carbon fibers (A), hydrothermal process (B) and resultant coating of oxide (C). Oxide coated carbon fibers are used as a composite electrode, shown with an idealized microstructure and compared to a conventional tape cast electrode in (D) where carbon fibers form a continuous electronic pathway.

Careful control of the substrate preparation and oxide growth conditions were required to obtain a phase-pure and electrochemically reversible electrode. Several other phases of manganese oxides were produced in the process of refining the hydrothermal technique, and these are introduced along with possible opportunities for future research. The experimental conditions and testing results for the $LiMn_2O_4$ phase serve as a benchmark for the work presented in subsequent chapters.

4.1 Background of the Hydrothermal Method

Today, state-of-the-art positive electrodes are mixed cation layered oxides isostructural with $LiCoO_2$ (e.g. $LiNi_{1-y-z}Co_yAl_zO_2$). These materials allow close to 1 lithium extraction per formula unit, greatly enhancing energy densities, and are produced by solid-state synthesis[84-86]. Still, these compounds have some of the same drawbacks of high cost, toxicity of precursors, and poor safety intrinsic to $LiCoO_2$. While commercial application of $LiMn_2O_4$ has been limited due to issues with rapid capacity fading, research into nanostructured $LiMn_2O_4$ has shown that certain morphologies produce exceptional rate capabilities, enhanced capacity retention (even with a fluorine-containing electrolyte), and the ability to cycle below the 3 V vs. Li/Li^+ potential region in which a Jahn-Teller distortion normally causes additional capacity loss [35, 87, 88]. These considerations provide impetus towards re-evaluating $LiMn_2O_4$ as a commercial viability and provide the incentive for focusing on $LiMn_2O_4$ in the present work.

One branch of research into nanostructured $LiMn_2O_4$ has introduced an interesting dynamic to this re-evaluation. Namely, crystalline $LiMn_2O_4$ can be produced at very low temperatures via hydrothermal synthesis compared to solid-state calcination routes usually occurring above 500 °C. One approach uses pre-formed Mn-oxide (e.g. MnO_2) starting material as a template and reacts this with a solution of lithium salts in a hydrothermal autoclave to produce $LiMn_2O_4$ [89, 90]. These reactions have relatively high hydrothermal temperatures (≥ 200 °C) and long dwell times, requiring up to several days for a complete conversion. Another approach uses potassium permanganate ($KMnO_4$) in which manganese exists in the water soluble +7 oxidation state and can be readily reduced to form insoluble Mn-oxides. An aqueous solution of $KMnO_4$, $LiOH•H_2O$, and a

reducing agent can be used to obtain nano-crystalline $LiMn_2O_4$ at temperatures below 200 °C in a matter of hours [91]. An interesting variation of this approach incorporates carbon into the hydrothermal solution. Composites formed in this way show enhanced rate capabilities, especially when using carbon nanotubes [66, 67, 92].

Regardless of the fabrication methods, powders used as active materials in lithium-ion batteries are typically formed into electrodes using a ubiquitous tape casting process, which introduces certain limitations to electrode design. The cast tape consists of slurry of active material and binder in a solvent. A common solvent used for this process is N-methyl-2-pyrrolidone (NMP), which is toxic and expensive[12]. For positive electrodes a conductive dilutant, usually carbon, is added to raise the electrical conductivity of the composite electrode and greater amounts of carbon must be added to the slurry for high-power operation [56]. Tradeoffs between electrode energy density and rate capability, which are influenced by electrode thickness, weight percentage of inactive materials, and porosity, are necessarily inversely related [93]. A flow chart depicting the assembly of electrode by the tape-casting method in shown in Figure 4.2 [94].

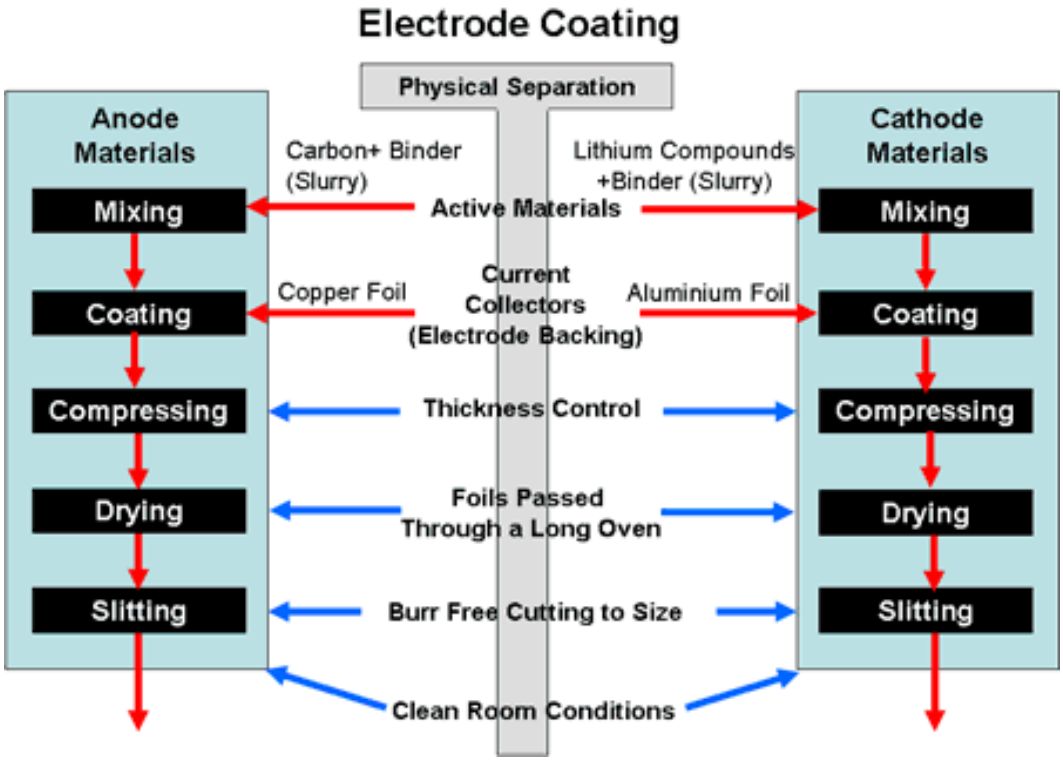

Figure 4.2 Flowchart for construction of a conventional Lithium-ion electrode by tape-casting.

Porous current collectors have also been applied to solve some of the issues inherent to tape-cast electrodes. Such structures can be made much thicker than tape-cast electrodes while maintaining ionic and electronic conduction pathways. Foams of metal and carbon have been demonstrated extensively for their application as porous current collectors in electrochemical devices [13, 95-97] . Whitehead and Schreiber reported that carbon current collectors have good electrochemical stability but are limited by their electrical conductivity [17]. However, the work of Dudney et al. has demonstrated that networks of carbon fibers infiltrated with a slurry containing pre-formed $LiFePO_4$ powder are capable of high cycling efficiency and high power outputs [21, 24]. Work in the Liu lab at Georgia Tech and others have focused on producing porous electrodes for electrochemical devices by growing oxide active materials directly onto carbon fiber paper (CFP) using hydrothermal synthesis [22, 98, 99]. While several example of high-

performance $LiMn_2O_4$ produced by hydrothermal synthesis have been introduced here, all of these examples required additional processing (e.g. tape casting) to produce an electrode. By using a pre-formed carbon fiber "backbone" the electrodes can be produced directly from the hydrothermal procedure. This greatly simplifies the electrode fabrication process described in Figure 4.2, removes the need for toxic organic solvents like NMP, and offers the potential for high power operation through an optimized current collector design.

4.2 Experimental Methods

4.2.1 Hydrothermal Coating of Mn-oxides on CFP

Several factors are important to control when producing samples by hydrothermal precipitation. Temperature, reaction time, reagent types and concentrations must be considered in any chemical reaction, however hydrothermal specific conditions such as the reaction vessel material, fill ratio (which influences the head-space pressure) and substrate type should also be considered. For all of the hydrothermal experiments presented in this dissertation, a carbon fiber substrate was utilized and oriented upright (i.e. perpendicular to the pressure vessel base) inside of a steel autoclave with a Teflon liner. The solvent used for every experiment was distilled water and the fill factor of the Teflon liner was 80% of the total volume. An electric oven was used to heat the hydrothermal pressure vessel, with heating and cooling ramp rates fixed at 60 °C/ hour. Reagent types, reaction temperatures, reaction times were varied in an effort to produce phase-pure $LiMn_2O_4$

The carbon fiber paper (CFP) used in this study was provided by Engineered Fibers Technology, LLC and has a network of interconnecting fibers with diameters averaging 8-10 μm with a total thickness of about 200 μm. Pieces of carbon fiber paper

with typical dimensions of 2.5 cm x 5 cm were first activated using a heat treatment at 350 °C for 5 h. The heat-treated CFP was placed into a 200 mL Teflon-lined stainless steel autoclave and oriented upright using a notched Teflon support. Various hydrothermal solutions were utilized to evaluate hydrothermal growth conditions, with the principle reagents being potassium permanganate ($KMnO_4$) as a manganese-oxide precursor, lithium hydroxide ($LiOH•H_2O$) as a lithium source, and ammonium chloride (NH_4Cl) as a mild reducing agent. Solutions containing the desired concentrations of $KMnO_4$, NH_4Cl and $LiOH•H_2O$ in distilled water were prepared by magnetic stirring at room temperature for 20 min until all the reagents were dissolved. To obtain phase-pure $LiMn_2O_4$, a hydrothermal solution containing 20 mM NH_4Cl, 20 mM $KMnO_4$ and 50 mM $LiOH•H_2O$ was used. The solution was added into the autoclave covering the CFP then sealed and allowed to sit at room temperature for a period of 3 h for the solution to soak into the CFP. After the soaking period, the autoclave was placed in a furnace and underwent a heating procedure to initiate the hydrothermal process. After the hydrothermal procedure the CFP became coated with a product phase and was rinsed several times with distilled water to remove residual salts from the hydrothermal procedure.

4.2.2 Tape cast electrodes

For comparison purposes, electrodes were prepared via tape casting by first mixing a slurry containing 80% by weight store bought $LiMn_2O_4$ powder (MTI) along with 10% by weight acetylene black conductive carbon and polyvinylidene fluoride (PVDF) binder into NMP. The slurry was mixed in a mortar and pestle until homogeneous and spread onto a sheet of aluminum foil but a doctor blade with a height set to 20 microns. After tape casting, the wet slurry film was dried in an oven set to 95 °C for 12 hours to

evaporate residual NMP. The dried electrode sheet was punched into circular discs which were calendared under a force of 1 ton in a uniaxial press. Typical mass loading of $LiMn_2O_4$ onto the electrodes was 2-3 mg/cm^2. According to the vendor, the active material used had a specific capacity at 105 mAh/g at a non-specified current density or mass loading.

4.2.3 Physical Characterization

Pieces of the larger LMO@CFP sample were cut out and prepared for X-ray Diffraction (XRD) and Scanning Electron Microscope (SEM) analysis. A PANalytical X'Pert PRO Alpha-1 with Cu K-α1 source was used for the X-ray diffraction experiments. All XRD data is presented as relative intensity, wherein the intensity scale was normalized for the particular sample. For strongly crystalline peaks, the intensity range was normalized relative to the most intense peak. For weakly crystalline or amorphous samples, the intensity was normalized relative to the background intensity. The SEM used was a LEO 1530 thermally-assisted field emission scanning electron microscope. No additional conductive coating was needed for the SEM analysis. To determine the mass loading of the hydrothermal treated CFP, pieces of bare CFP heat treated as per the pre-hydrothermal routine were weighed with a lab balance after vacuum drying inside an argon filled glovebox, with pieces of hydrothermal treated CFP weighed in a similar manner. Thermogravimetric analysis was performed to characterize the thermal properties of the CFP substrate using a TA Instruments Q600 SDT with air (Airgas, Ultra Zero purity) as the purge gas. After taring the alumina pans, samples of 10 mg or less were loaded and allowed to rest at room temperature for at least 1 h under 100 mL min^{-1} of purge gas until the mass loss due to suspected water evaporation stabilized.

Once the sample mass stabilized, the sample was heated at 10 °C min to 900 °C to oxidize the CFP.

4.2.4 Electrochemical Measurements

Using a circular punch, electrodes with a superficial area of approximately 1 cm^2 were cut from the larger hydrothermal treated CFP piece. These electrodes were placed in a vacuum drying oven at 100 °C overnight and then immediately transferred into an argon filled glovebox. The electrodes were assembled into half-cells using glass fiber separators (Whatman GF/D) soaked with 1 M $LiPF_6$ in 1:1 ethylene carbonate/dimethyl carbonate electrolyte (Novolyte). A piece of Li metal with an area of 1.26 cm^2 was used as both the counter and pseudo-reference electrode. All electrochemical measurements were made using an Arbin BT-2000 battery tester. For cycling measurements, current was fixed to a desired C rate (1C = 148 mA/g) using the mass of the active material and the cell was charged or discharged until the cell potential reached the desired cutoff. The charging cutoff potential was set at 4.4 V vs. Li/Li^+ and the discharge value was set at 3.1 V vs. Li/Li^+.

4.3 Structure and Morphology of Hydrothermal Phases

4.3.1 Carbon Fiber Paper Substrate

The CFP utilized in this study is available in large quantities with a variety of properties. All of the commercially available CFP's contain pyrolized polyacrylonitrile (PAN) fibers which are either woven or resin-bonded to form a two-dimensional sheet. Woven CFP's are commonly referred to as carbon cloth, are generally more flexible than resin-bonded CFP, and are significantly more compressible. One drawback is that carbon

felts typically have great pore volume, and thus lead to lower volumetric energy density in electrochemical devices. The typical application for both carbon cloth and CFP are electrodes in electrochemical devices such polymer-electrolyte membrane fuel cells, flow batteries, and electrolyzers. Macroscopically, CFP resembles a stiff textile and can be easily cut or punched into shapes. An SEM image of the as-received carbon fiber paper is shown in Figure 4.3. An area of resin bonding between two fibers is visible in the top left of Figure 4.3, which appears as a webbed region between two carbon fiber struts.

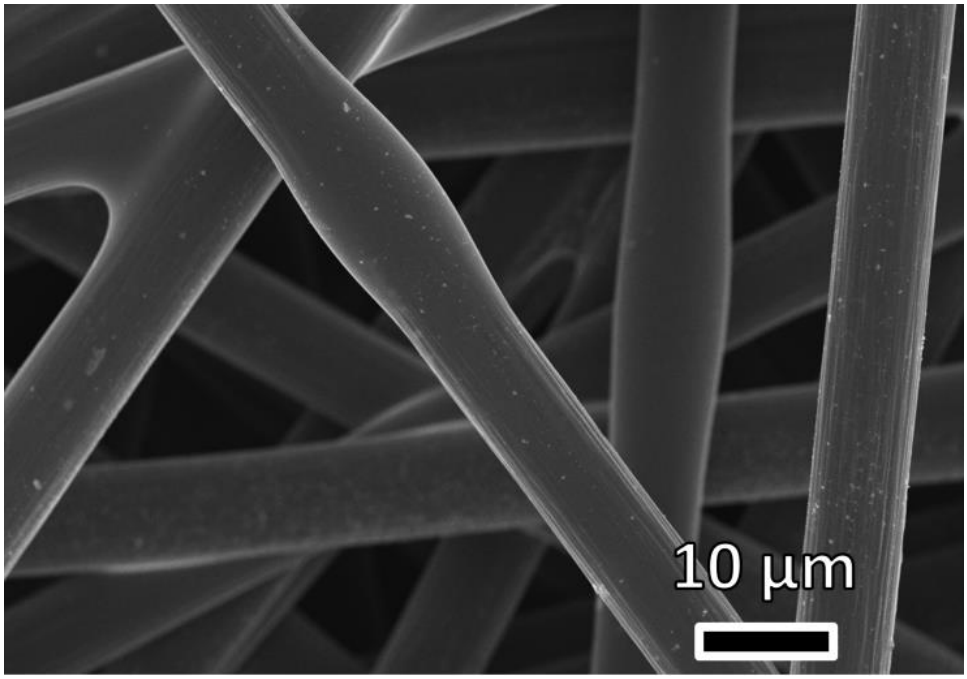

Figure 4.3 SEM image of as-received carbon fiber paper.

The heat treatment temperature used for the CFP substrates was selected by identifying the onset of thermal oxidation via TGA/DSC Shown in Figure 4.3, a large exothermic peak occurs at approximately 495 °C, while a slow onset of mass loss is observed around 300 – 500 °C. Temperatures within this range were used to pre-treat the CFP in order to increase the hydrophilicity of the samples, which improved the wettability of the carbon fiber substrate towards the hydrothermal solution.

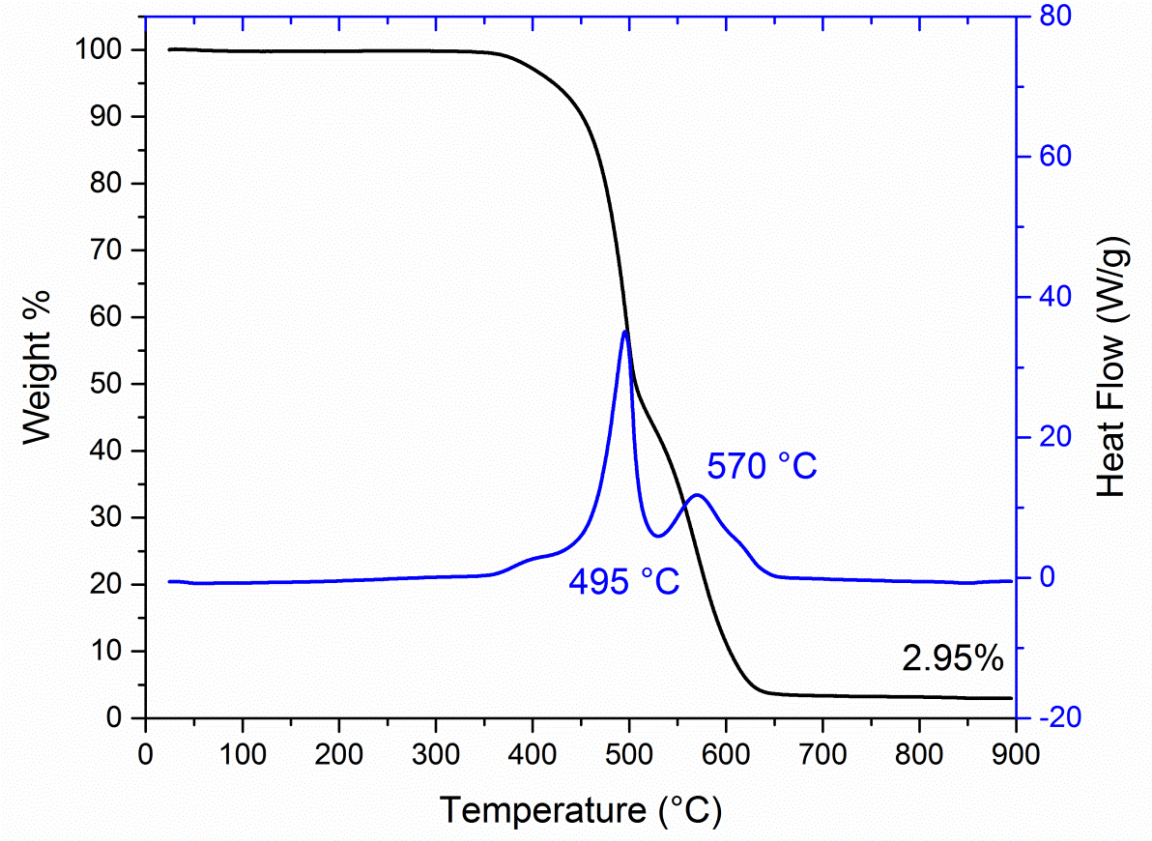

Figure 4.4 TGA/DSC for bare CFP in air.

For heat treatments at or above 400 °C, the CFP substrates became physically degraded observed as a loss of interconnectivity between the fibers which could be mechanically separated from each other. This is possibly due to thermal decomposition of the resin bonding, which might be attributed to the small exothermic hump beginning near 400 °C. At a temperature of 350 °C the CFP remains macroscopically unchanged, however a dramatic increase in wettability is observed. Surface-area and porosimetry measurements conducted on the 350 °C samples show an increase in surface area from < 5 m^2/g to 320 m^2/g after heat treatment. By 700 °C the residual CFP mass has decayed to a static value of about 3% of the original mass, which is attributed to inorganic "ash" content in the CFP which cannot be combusted or volatilized under the conditions used.

X-ray diffraction measurements of the uncoated CFP shown in Figure 4.5 feature only a broad amorphous region in the range of 25° 2θ. This implies that the carbon fibers contained within the CFP have not been pyrolized at a temperature high enough to induce significant graphitization, or that any existing graphitic domains are very small.

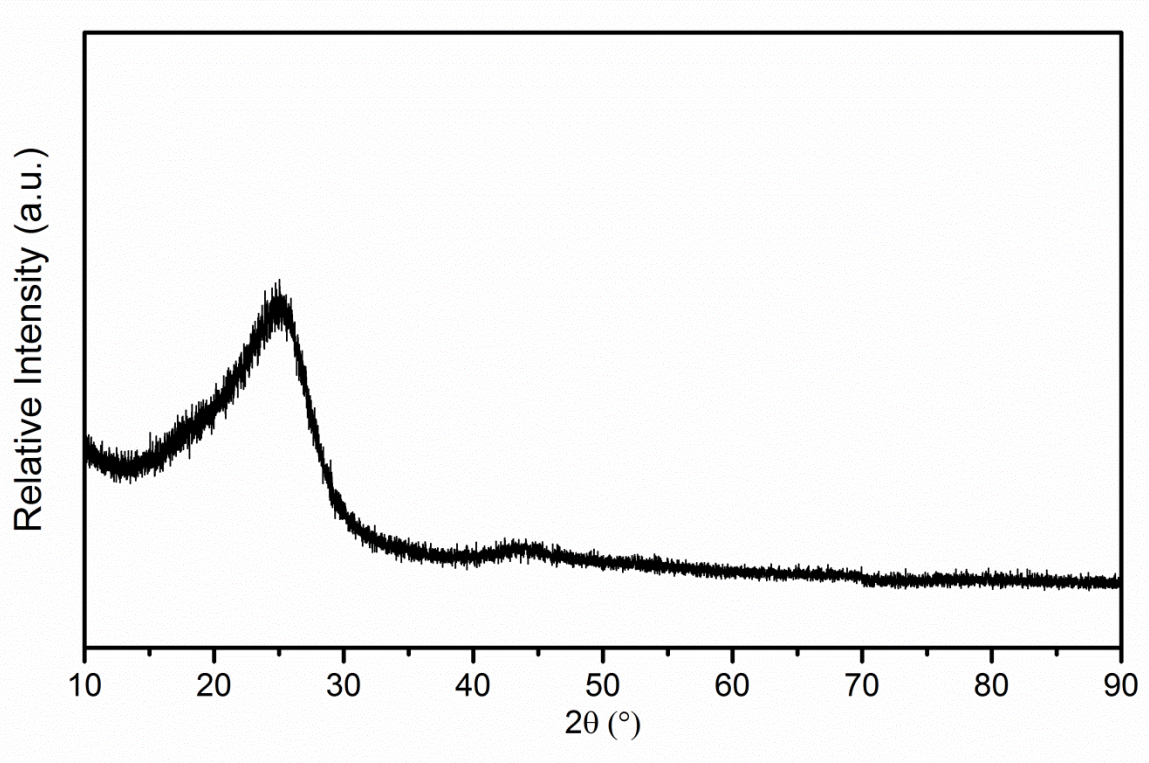

Figure 4.5 X-ray diffraction of CFP without coating.

Several physical properties provided by the vendor are listed in Table 4.1 and compared values collected in the lab for the as-received samples, and for samples of CFP after heat treatment at 350 °C.

Table 4.1 Physical properties of carbon-fiber paper supplied by vendor and after heat treatment at 350 °C in air for 5 hours.

	Density (g/cm^3)	Thickness (μm)	BET Surface Area (m^2/g)
Vendor Values	0.5	203	N/A
As received	0.58	180-190	5
After Heat-treatment	0.58	180-190	320

When cycled electrochemically, bare carbon fiber paper shows no redox activity in the region of 3-4.5 V vs. Li/Li+. CV measurements conducted at a rate of 50 uV/s (Figure 4.6) reveal a very low specific current density without faradaic peaks. A small excess oxidation current is observed during the first CV cycle which dissipates during subsequent cycles. This is perhaps attributed to an initial oxidation of the electrolyte for form an SEI type layer, or to oxidation of impurities in the electrolyte such as H_2O.

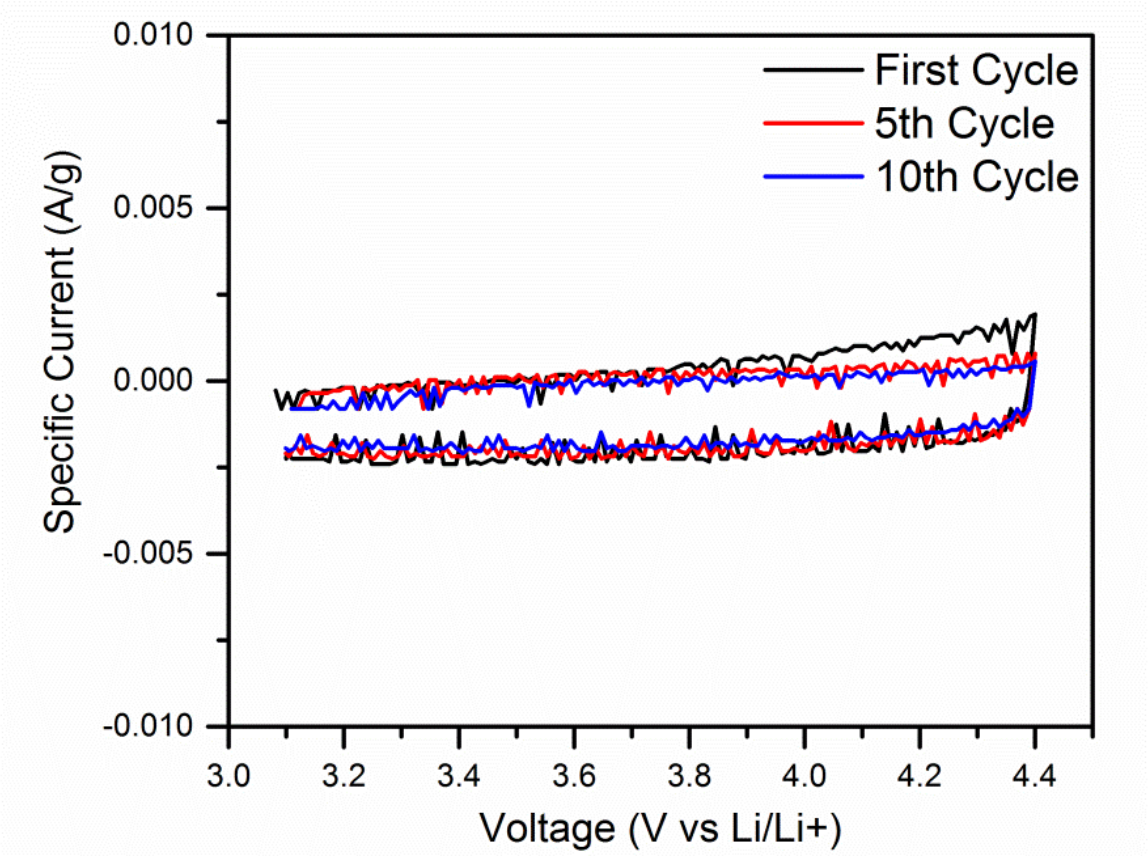

Figure 4.6 CV of LIB half-cell with Li metal counter electrode, CFP working electrode and 1 M $LiPF_6$ 1:1 EC:DMC LIB electrolyte conducted at 50 uV/s.

Even when normalized by the mass of the CFP working electrode the observed current density is very low, and for the majority of the voltage range is actually negative, which is likely due to measurement error in the Arbin BT2000 measurement system for total currents on the order of a few microamps. For all of the electrodes coated with hydrothermal precipitation, the total current density is significantly larger which minimizes this error.

4.3.2 Hydrothermal Reaction of Potassium Permanganate

Potassium permanganate ($KMnO_4$) was selected as the manganese precursor in the present work. As described in the introduction to this chapter, many previous

academic works have used $KMnO_4$ as a reactant for hydrothermal synthesis of manganese-oxides, including $LiMn_2O_4$. At room temperature $KMnO_4$ produces a stable aqueous solution with distilled water. Reduction of $KMnO_4$ is easily identified by a change in color from the brilliant pink or purple (depending on concentration) associated with Mn^{7+} ions, which helps in identifying appropriate reagent combinations. Several literature examples in which $LiMn_2O_4$ was produced using $KMnO_4$ utilized organic solvents as reducing agents, including ethanol and acetone [66, 91, 92]. Even at room temperature introducing these reducing agents to a solution of $KMnO_4$ leads to rapid precipitation of an amorphous manganese oxide phase, which prevents significant nucleation of any oxide directly onto the carbon fiber paper. Carbon itself has been reported as a reducing agent for $KMnO_4$ to form MnO_2 nanostructured composites, so an initial series of tests was conducted to determine the reactivity of CFP towards the aqueous $KMnO_4$ solution [100, 101].

A series of experiments using a fixed concentration of 20 mM $KMnO_4$ in distilled water heated to temperatures of 120 °C, 140 °C and 160 °C for a period of 12 hours were used to evaluate the reactivity of CFP towards the manganese precursor. At 120 °C a heavy but non-uniform coating observed by SEM consisting of clumps of elongated structures, as shown in Figure 4.7. At low magnifications it is apparent that the outermost fibers have a thicker coating of material while the internal fibers further from the CFP surface have less coating. Additionally, the internal fibers are by comparison smoother than the outer fibers and some cracks are observed in the coating.

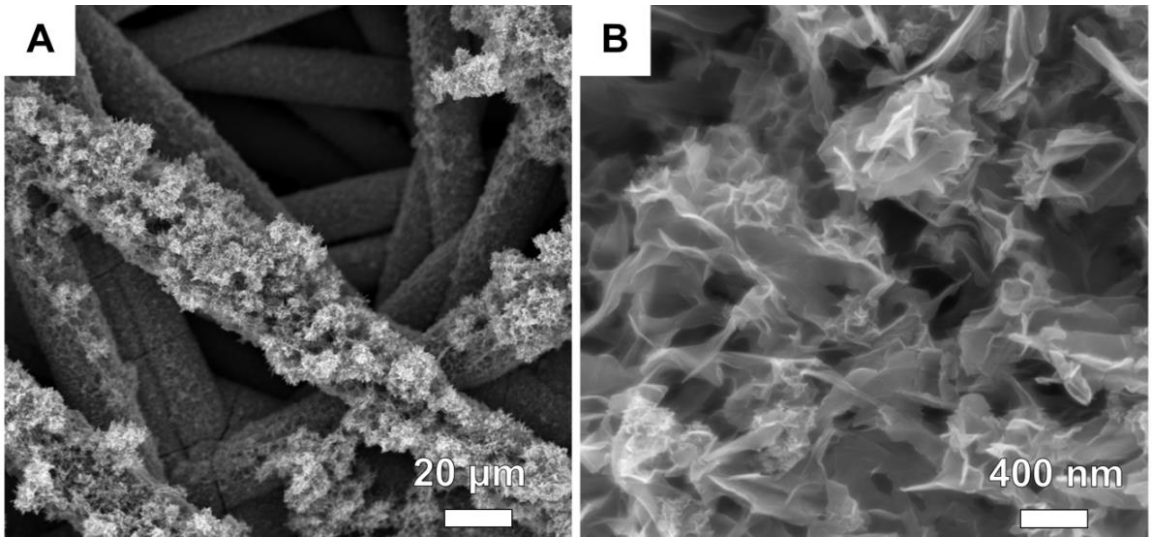

Figure 4.7 SEM image of coating formed from 20 mM $KMnO_4$ onto CFP at 120 °C for 12 hours taken at low magnification (A) and high magnification (B).

Increasing the hydrothermal temperature to 140 °C, while leaving other parameters identical (20 mM $KMnO_4$, 12 hour dwell time), has a noticeable effect on the coating morphology. Figure 4.8 shows that the coating produced at 140 °C also has a fairly inhomogeneous distribution between the outer and inner carbon fibers, while the high magnification reveals newly formed nanorods amongst the featured features observed at 120 °C.

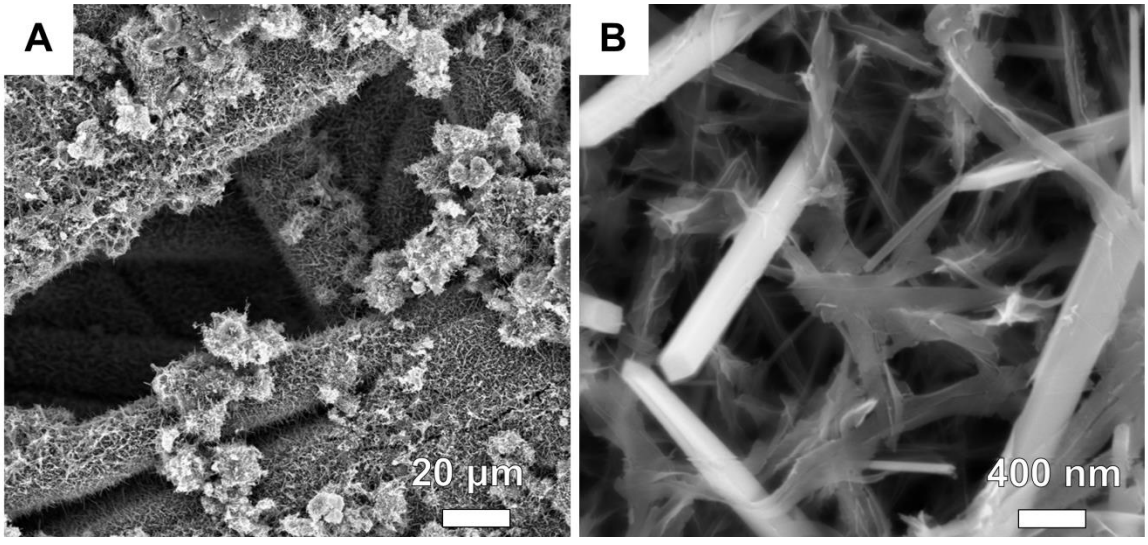

Figure 4.8 SEM image of coating formed from 20 mM $KMnO_4$ onto CFP at 140 °C for 12 hours taken at low magnification (A) and high magnification (B).

The trends observed of increased coating homogeneity as well as the appearance of nanorods when increasing the hydrothermal temperature from 120 °C to 140 °C is continued for the hydrothermal experiment performed at 160 °C. Figure 4.9 shows that the coating is now incredibly uniform into the depth of the CFP mat and free of thickness deviations along the length of the fiber. Similar to the 140 °C sample, both nanorods and feathered featured are observed at high magnification for the sample produced at 160 °C.

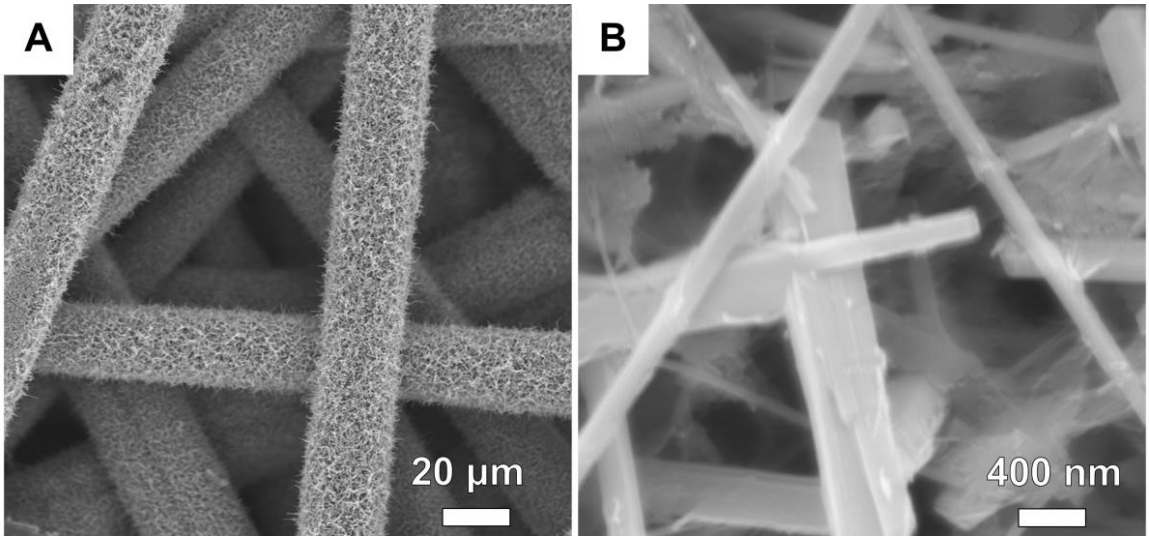

Figure 4.9 SEM image of coating formed from 20 mM $KMnO_4$ onto CFP at 160 °C for 12 hours taken at low magnification (A) and high magnification (B).

EDS analysis shown in Figure 4.10 for the samples produced by a hydrothermal reaction of $KMnO_4$ with CFP show that the coatings all contain Mn, O, and K in addition to a small C signal detected from the underlying carbon fiber. While the elemental content is consistent between the samples produced at different hydrothermal temperatures, the Mn:K ratio (defined simply as the ratio of the maximum peak intensity for the Mn Kα peak at 5.894 eV to the K Kα peak at 3.312 eV) increases from 1:1 for the 120 °C to 1.9:1 for the 140 °C, and up 2.9:1 for the 160 °C sample, indicating a decrease

in relative K content with increasing temperature. Meanwhile, the O:Mn ratio (defined as the ratio of the intensity of the Mn Kα peak at 5.894 eV and the O Kα peak at 0.525 eV) remains relatively constant at 10:1 O:Mn for the 120 °C and 140 °C samples and 11:1 for the 160 °C sample.

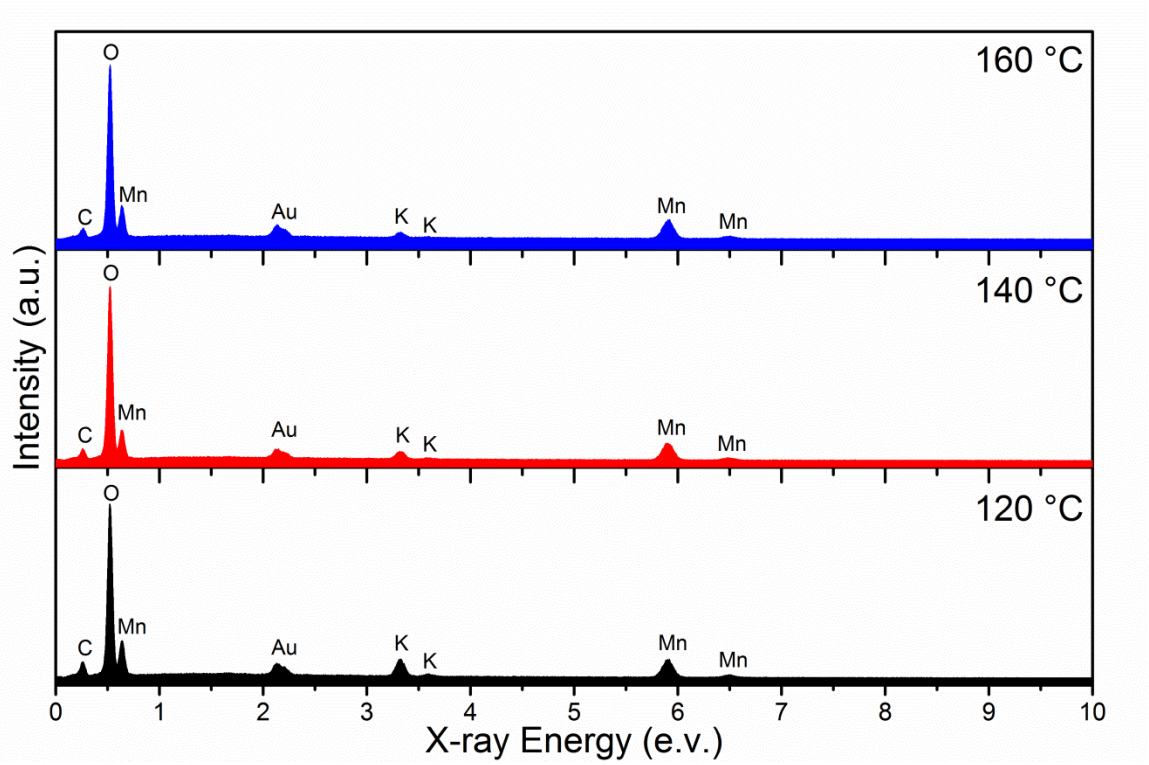

Figure 4.10 EDS of sample produced by decomposition of $KMnO_4$ at temperature from 120 °C, 140 °C and 160 °C onto CFP. Sample was sputtered with Au prior to analysis, and the intensity scale for each spectrum was normalized relative to the O Kα peak at 0.525 eV.

XRD (Figure 4.11) reveals that the coatings produced from the $KMnO_4$ only solution are only weakly crystalline. At 120 ° four broad peaks are observed at approximately 12.3°, 36.9° and 66° 2θ. Along with the observation of K in the same from EDS, it is likely that this phase is a K-birnessite with the general chemical formula $K_xMnO_2 \cdot yH_2O$ [102]. Birnessite has also been reported as a useful material for electrochemical capacitors and can be produced by hydrothermal reaction of $KMnO_4$

solutions [66, 103]. For the sample produced at 140 °C, the most intense peak attributable to K-birnessite at 12.3° 2θ is gone, while two new sharper peaks at 26° and 37° 2θ emerge. Accompanied with the appearance of the nanorod features and the decrease in relative K content, it seems that a new phase is present in the 140 °C sample. One possibility is a layered MnOx compound having similar inter-planar lattice spacing to and intermixed with a decreased amount of K-birnessite. After increasing the reaction temperature to 160 °C, the peaks which emerged at 140 °C are more prominent and joined by multiple less intense peaks. All of the peaks observed in the coating produced at 160°C can be attributed to γ-MnO(OH) (manganite) which has a similar layered structure to K-birnessite and some phases of MnO_2. The γ-MnO(OH) phase has been studied as an anode material for lithium-ion batteries, oxygen-reduction catalyst for lithium-air batteries, and electrochemical capacitors [104-107]. While the broad crystalline peaks observed in the 120 °C samples are not apparent in the 140 °C and 160 °C coatings, the morphology and elemental analysis conducted by SEM and EDS suggests that K-birnessite is likely still present in these coatings as an amorphous phase.

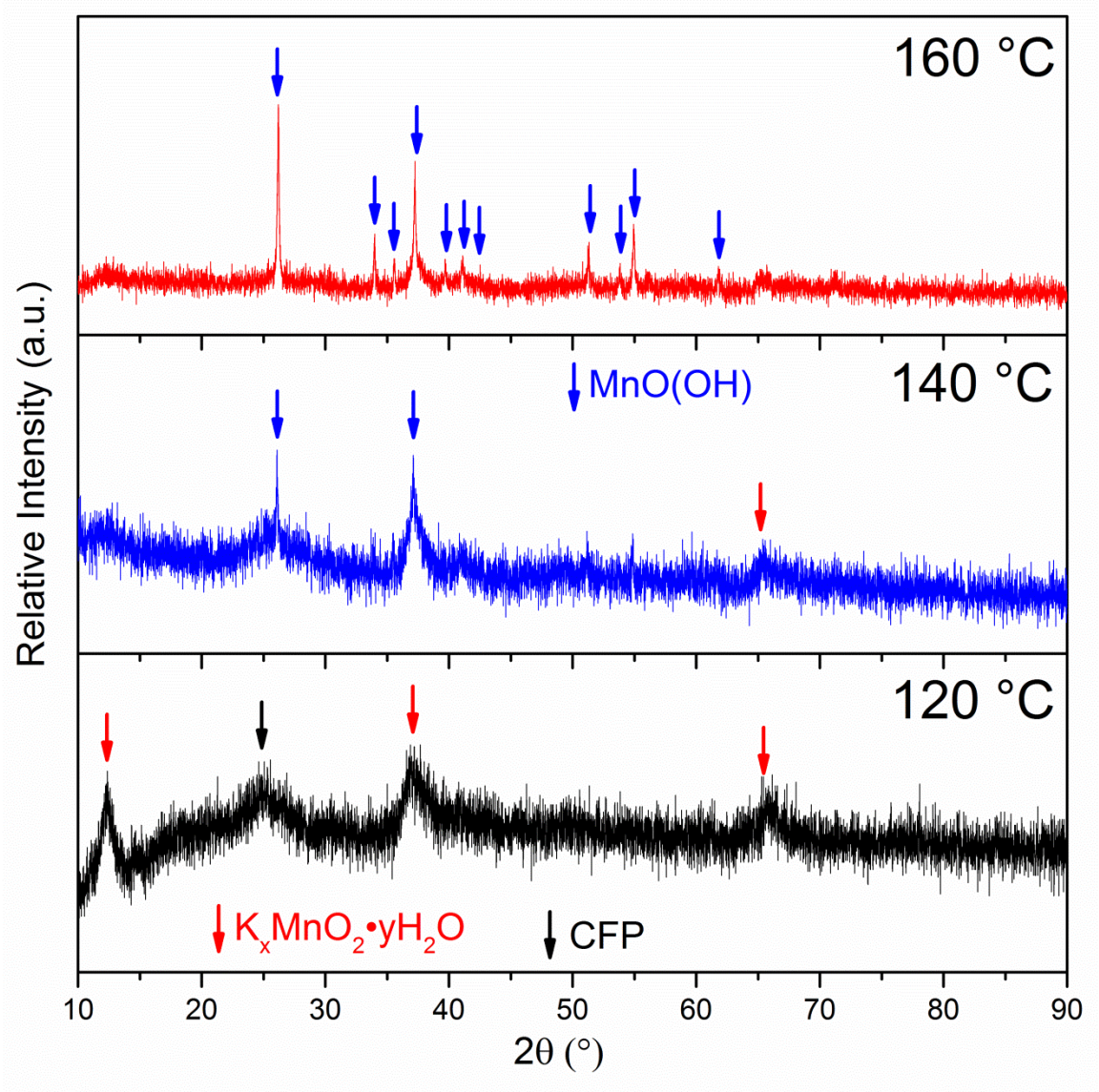

Figure 4.11 XRD of samples produced by hydrothermal precipitation of 20 mM $KMnO_4$ solution at 120 °C, 140 °C and 160 °C.

4.3.3 Influence of Lithium Hydroxide on Hydrothermal Phases

Lithium was added into the hydrothermal solution in the form of $LiOH•H_2O$, which was selected for its good solubility in water, compatibility with $KMnO_4$ at room temperature (i.e. no immediate precipitation occurs), and use in previously reported hydrothermal approaches to produce $LiMn_2O_4$ [66, 67, 89, 91, 108]. A solution containing 10 mM $LiOH•H_2O$ and 20 mM $KMnO_4$ (the stoichiometric ratio of Li:Mn found in $LiMn_2O_4$) was used for hydrothermal precipitation in an identical fashion to the pure

$KMnO_4$ experiments. At a hydrothermal temperature of 140 °C, a similar morphology to the 120 °C pure $KMnO_4$ sample is observed.

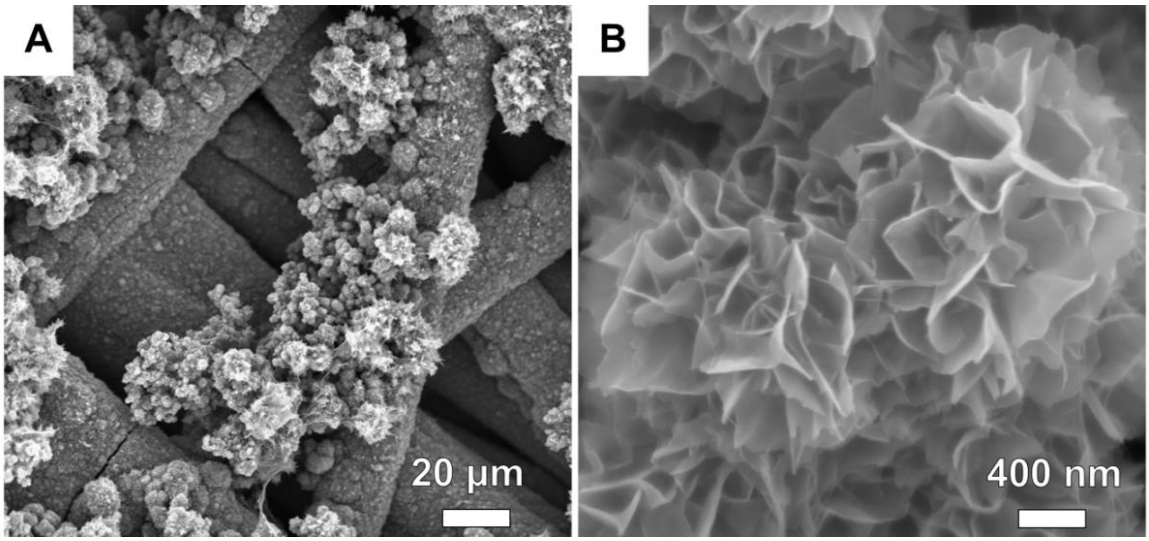

Figure 4.12 SEM image of coating formed from 20 mM $KMnO_4$, 10 mM $LiOH•H_2O$ onto CFP at 140 °C for 12 hours taken at low magnification (A) and high magnification (B).

Increasing the lithium salt content by five times (5:2 ratio of Li:Mn) results in a similar overall morphology compare to the 1:2 Li:Mn sample at low magnification, while at higher magnification small crystallites with clearly visible crystalline facets have appeared. Macroscopically, the coating produced at these conditions was found to have unusually poor adhesion compared to other samples. As a result, large sections of the CFP were found to be completely uncoated in SEM.

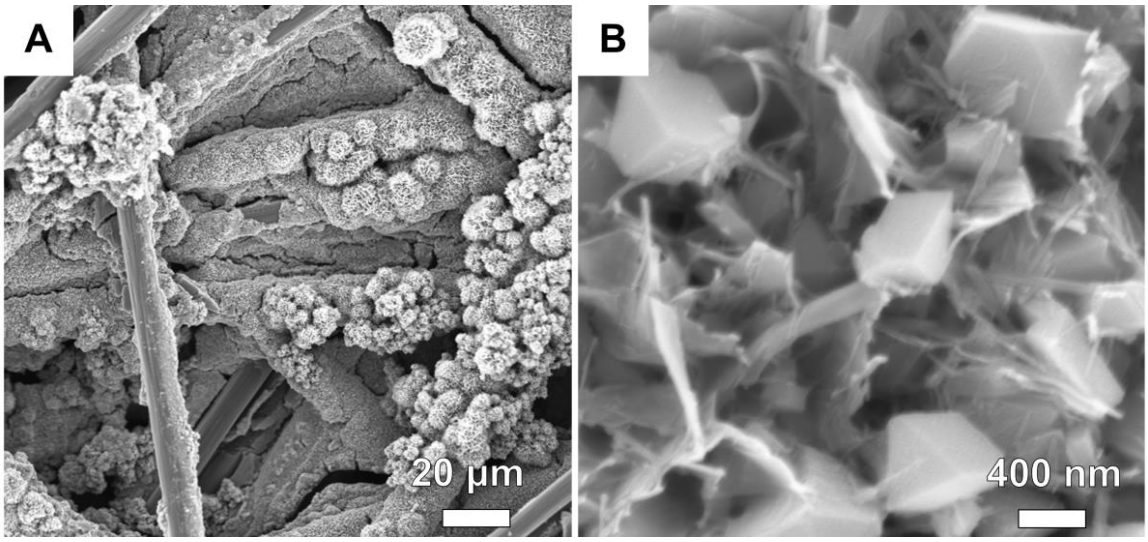

Figure 4.13 SEM image of coating formed from 20 mM $KMnO_4$, 50 mM $LiOH•H_2O$ onto CFP at 140 °C for 12 hours taken at low magnification (A) and high magnification (B).

Elemental analysis of the Li containing samples is somewhat less useful than for the sample produced from a $KMnO_4$ only solution as Li cannot be detected by EDS. However, it is apparent that for the sample produced from the hydrothermal solution which contains an excess of lithium compared to the stoichiometric ratio in $LiMn_2O_4$, the presence of K is decreased (Figure 4.14). This could indicate that the structure formed simply contains less K, or perhaps that Li has replaced K within the structure.

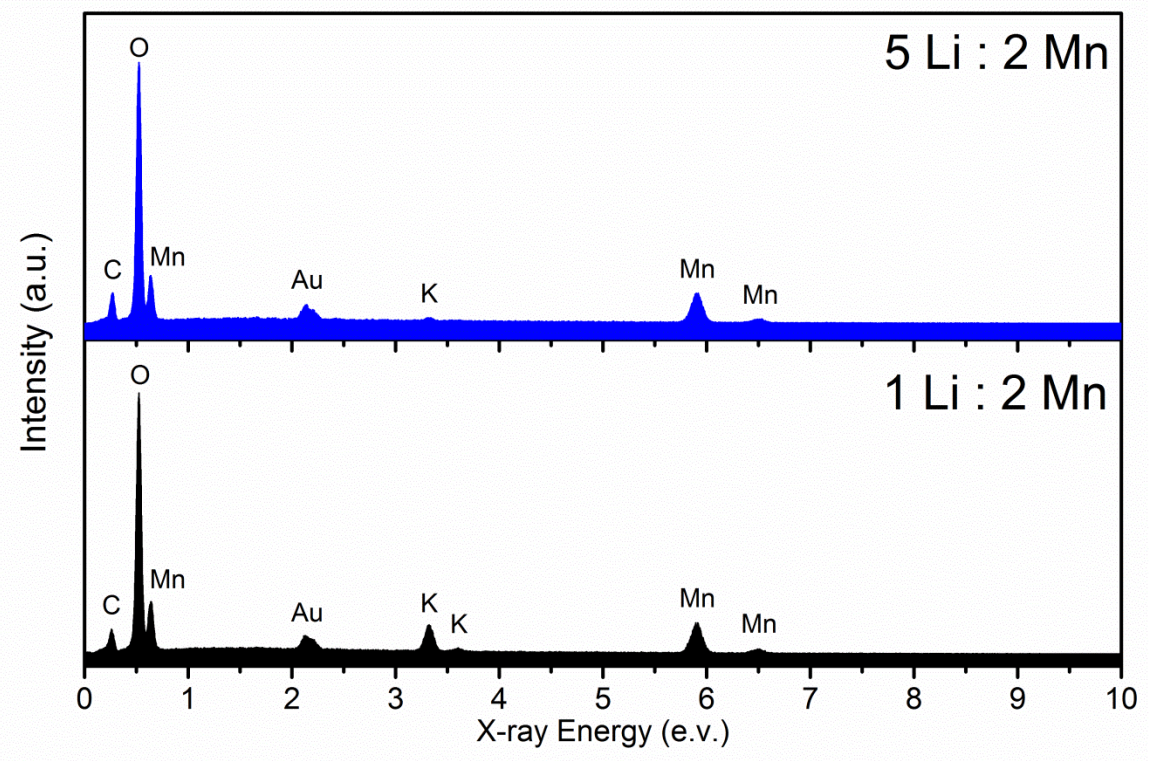

Figure 4.14 EDS of samples produced by decomposition of $KMnO_4$ with $LiOH{\bullet}H_2O$ at 140 °C in a molar ratio of 5:2 and 1:2. Samples were sputtered with Au prior to analysis, and the intensity scale for each spectrum was normalized relative to the O Kα peak at 0.525 eV.

Once analyzed with XRD (Figure 4.15), it is clear that the coating produced with excess lithium in the hydrothermal solution leads to the formation of the desired phase $LiMn_2O_4$, however a small impurity phase was also observed. Based on the location of the impurity peak in XRD the phase is suspected to be a mixed Li/K-birnessite previously discussed. Meanwhile, the coating produced with a stoichiometric ratio of Li:Mn to form $LiMn_2O_4$ has produced a phase with similar diffraction appearance to the $KMnO_4$ only solution at 120 °C, but with a slightly increased 2θ value of the most intense peak (12.42° 2θ vs. 12.31° 2θ), which corresponds to a slightly decreased lattice constant as determined by Equation 31. For the K/Li birnessite impurity phase observed in the hydrothermal produced with a 5:2 ratio of Li:Mn this peak has shifted further to 12.56° 2θ, which supports the assumption that Li is replacing K in the birnessite phase.

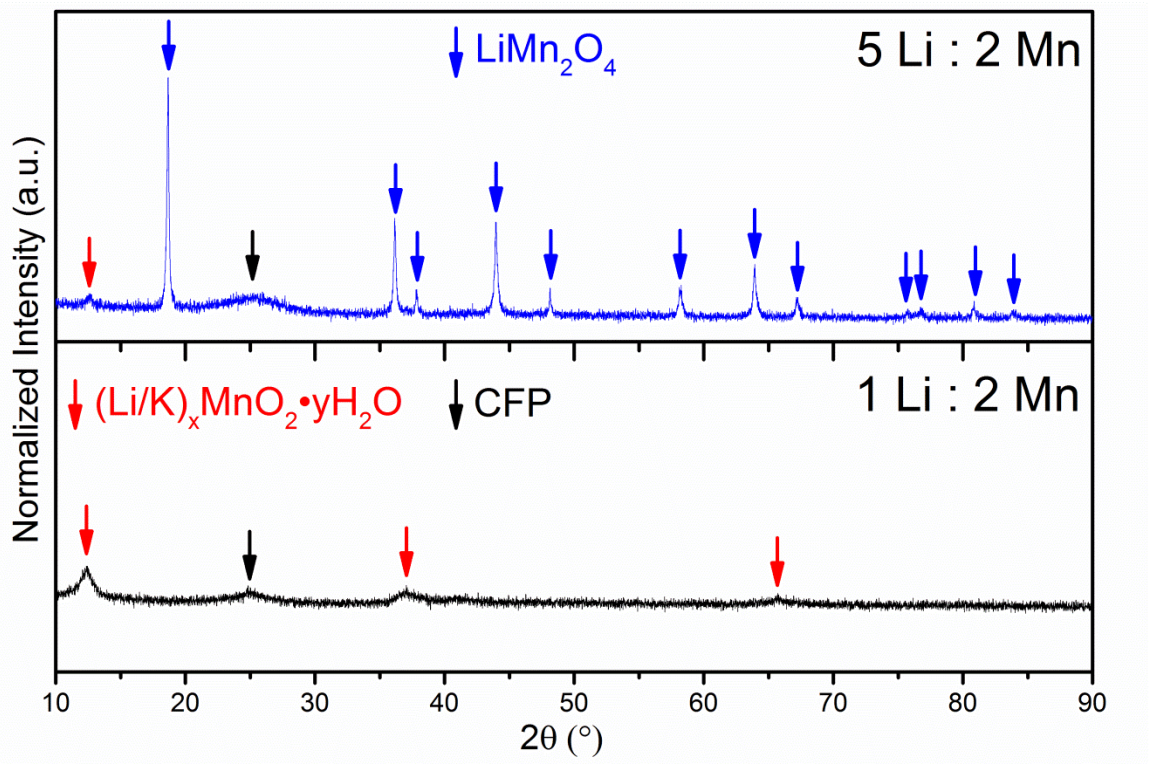

Figure 4.15 XRD patterns for hydrothermal samples produced with LiOH•H_2O added to the solution. Sample produced with 5:2 ratio of Li:Mn shows crystalline peaks assignable to LiMn2O4 with an impurity peak assignable to birnessite. All observed peaks for the 1:2 ratio of Li:Mn can be assigned to a birnessite phase containing Li an K.

4.3.4 Hydrothermal Phase Selection Using Ammonium Chloride

In previously reported hydrothermal experiments, NH_4Cl has been shows to act as a mild reducing agent and can influence phase morphology [109-111]. As will be shown in the next section, adding an equivalent molarity of NH_4Cl to $KMnO_4$ into the hydrothermal solution was found to be effective at suppressing the formation of birnessite, and was added to the hydrothermal solution to produce phase pure $LiMn_2O_4$. For hydrothermal solutions containing only $KMnO_4$ and NH_4Cl treated at 140 °C, a morphology reminiscent of the pure $KMnO_4$ solution at 140 °C is observed. Figure 4.16 shows that at low magnification, nanorods cover the surface of the carbon fibers. At higher magnification it is apparent that these nanorods are significantly thicker than the ones observed for the $KMnO_4$ only hydrothermal solution, while the coating retains some of the featured structures attributed to birnessite.

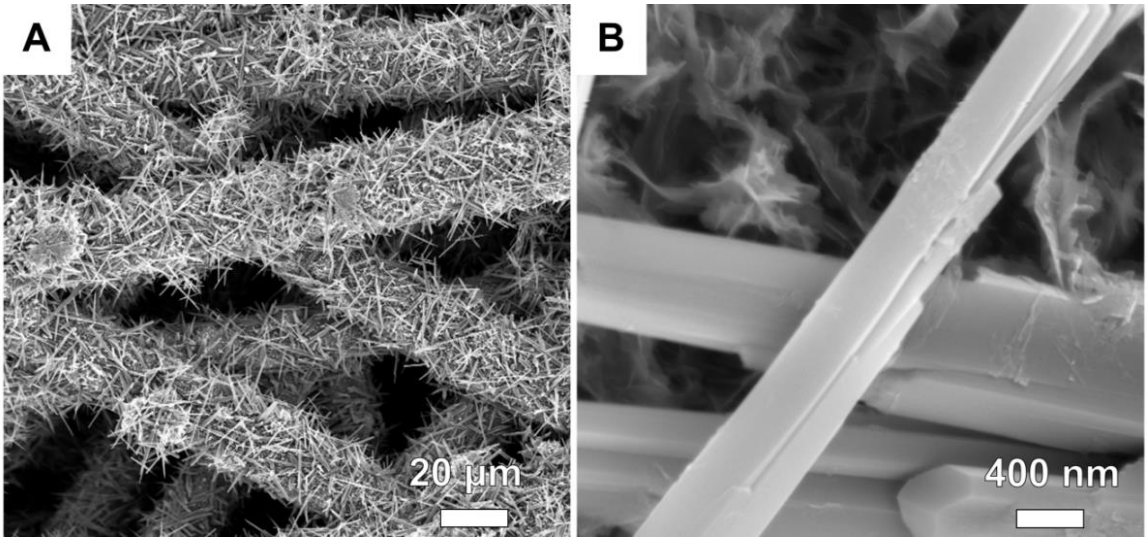

Figure 4.16 SEM image of coating formed from 20 mM $KMnO_4$, 20 mM NH_4Cl onto CFP at 140 °C for 12 hours taken at low magnification (A) and high magnification (B).

Adding $LiOH•H_2O$ at the stoichiometric ratio for $LiMn_2O_4$ (1:2 Li:Mn) to the hydrothermal solution containing NH_4Cl (Figure 4.17) seems to counteract its' influence, and a great proportion of feather-like birnessite is observed, while the nanorods become finer. In both cases containing NH_4Cl the overall uniformity of the coating is improved. EDS analysis of the samples produced with NH_4Cl added to the hydrothermal solution (Figure 4.18) show K is present in the coating, which is consistent with the observation of a residual birnessite-appearing phase by SEM. For the sample produced from the lithium-free hydrothermal solution, the relative K content is slightly decreased.

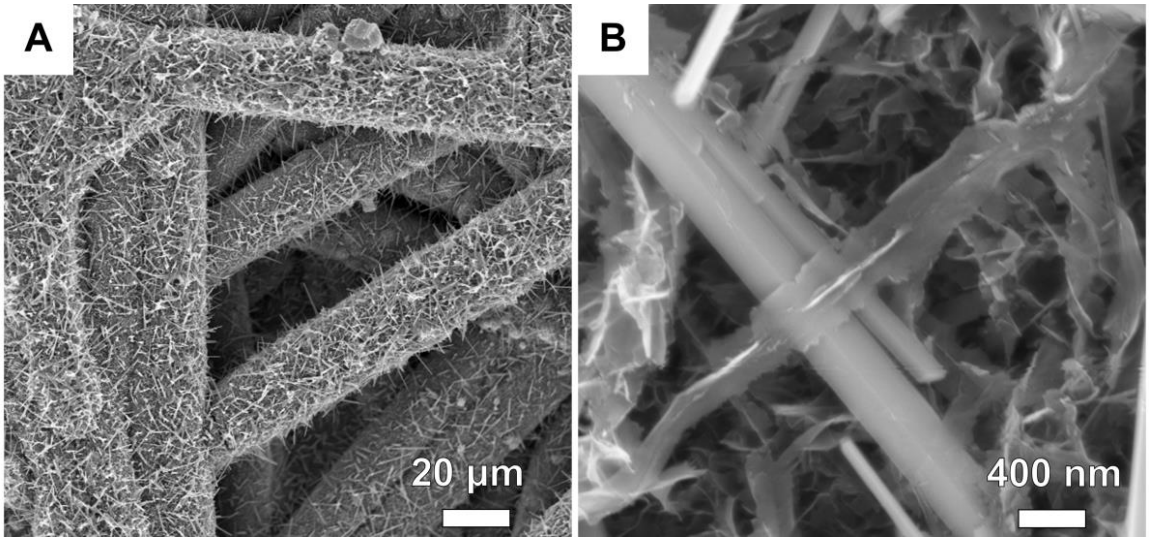

Figure 4.17 SEM image of coating formed from 20 mM $KMnO_4$, 20 mM NH_4Cl and 10 mM $LiOH•H_2O$ onto CFP at 140 °C for 12 hours taken at low magnification (A) and high magnification (B).

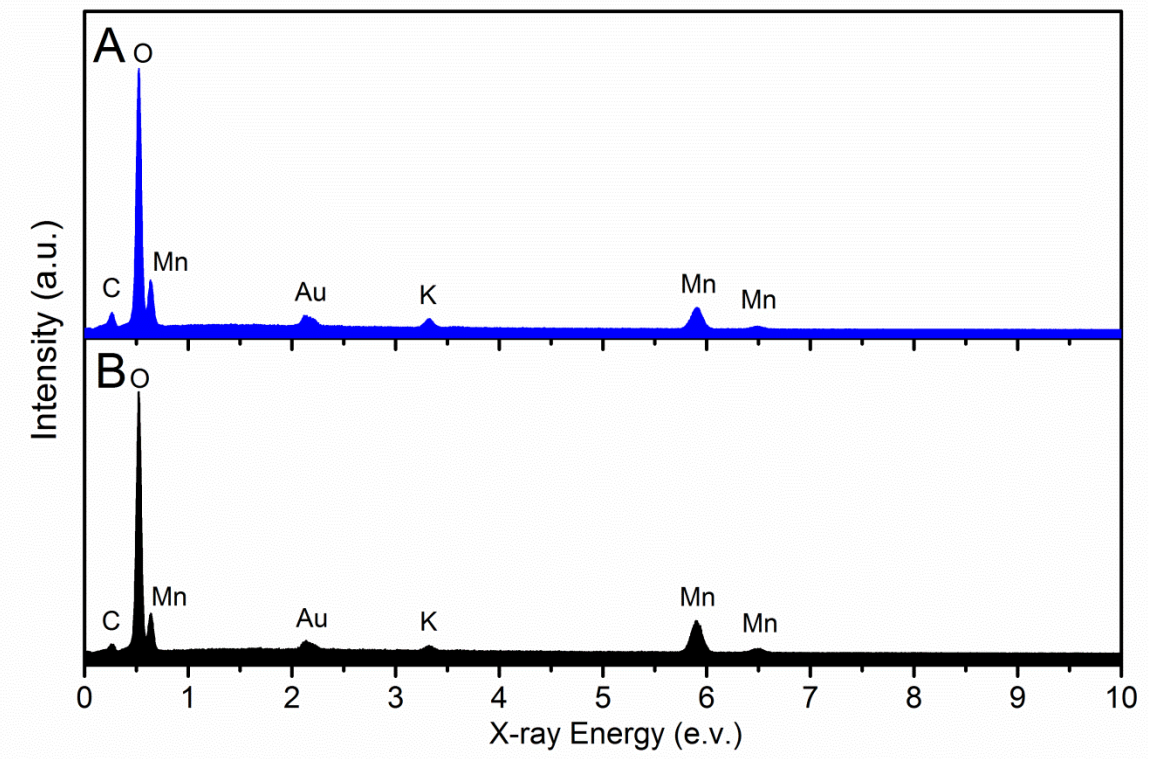

Figure 4.18 EDS for hydrothermal samples produced with NH_4Cl added to the solution. Sample shown in A was produced with 20 mM NH_4Cl, 20 mM $KMnO_4$ and 10 mM $LiOH•H_2O$. Sample shown in B produced with 20 mM NH_4Cl and 20 mM $KMnO_4$.

For the coatings produced with NH_4Cl in the hydrothermal solution, a major change is observed with XRD (Figure 4.19). For both samples, all of the observed peaks can be assigned to a single phase, γ-MnO(OH), which was also observed in the $KMnO_4$ only samples. However, while the samples produced without NH_4Cl at 140 °C had very weak crystalline peaks attributable to MnO(OH) (Figure 4.11), the sample with NH_4Cl shows strong diffraction peaks with no peaks attributed to birnessite. For the coating produced with Li in the hydrothermal solution, the relative intensity and signal to noise ratio of the crystalline peaks is significantly worse than for the coating produced without Li included in the hydrothermal solution. The peaks are broader, the background intensity is noisier, and some of the lower intensity peaks observed in the coating produced without Li in the hydrothermal solution are lost in the background noise for the Li containing sample.

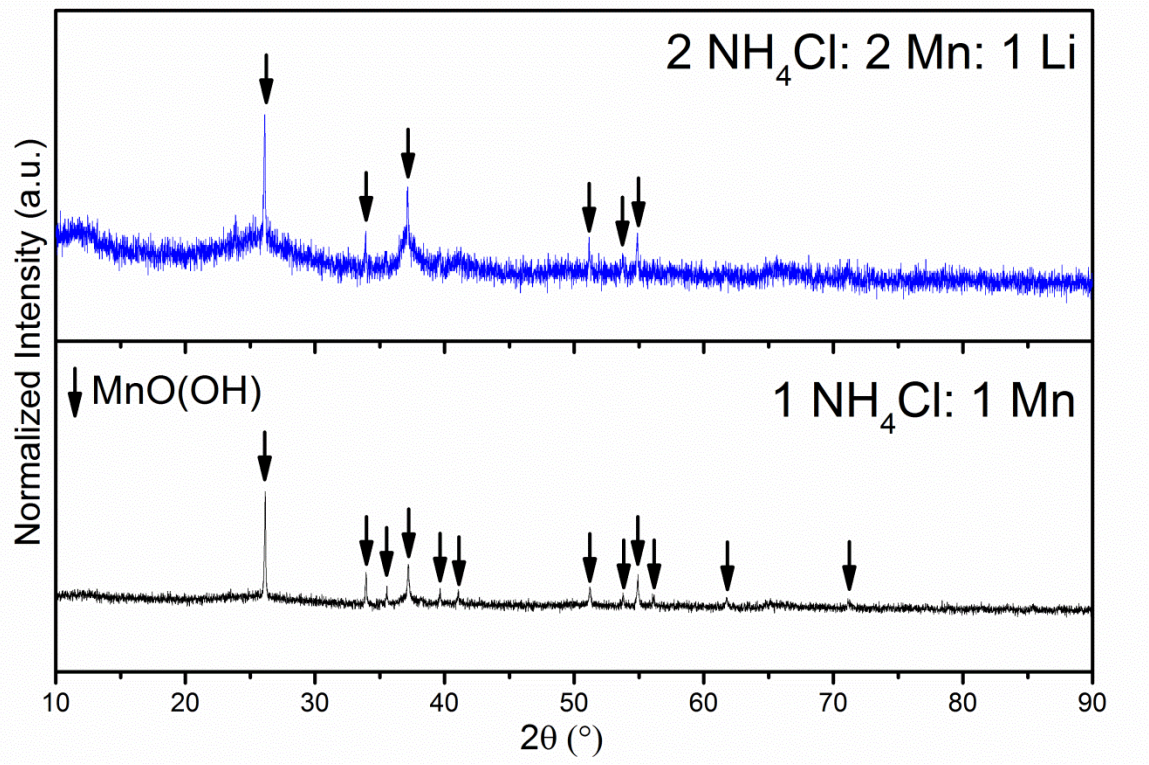

Figure 4.19 XRD patterns for hydrothermal samples produced with NH_4Cl added to the solution. Both samples show the formation of MnO(OH) regardless of Li content.

Once lithium is added in excess in the hydrothermal solution, for a reagent concentration of 50 mM $LiOH•H_2O$, 20 mM $KMnO_4$ and 20 mM NH_4Cl, new morphologies are produced. At a temperature of 120 °C (Figure 4.20), a morphology similar to the stoichiometric Li:Mn hydrothermal solution at 140 °C (Figure 4.12) is observed. A coating with a flower-like morphology covers the carbon fibers and protrudes in nodules along the surface of the fibers.

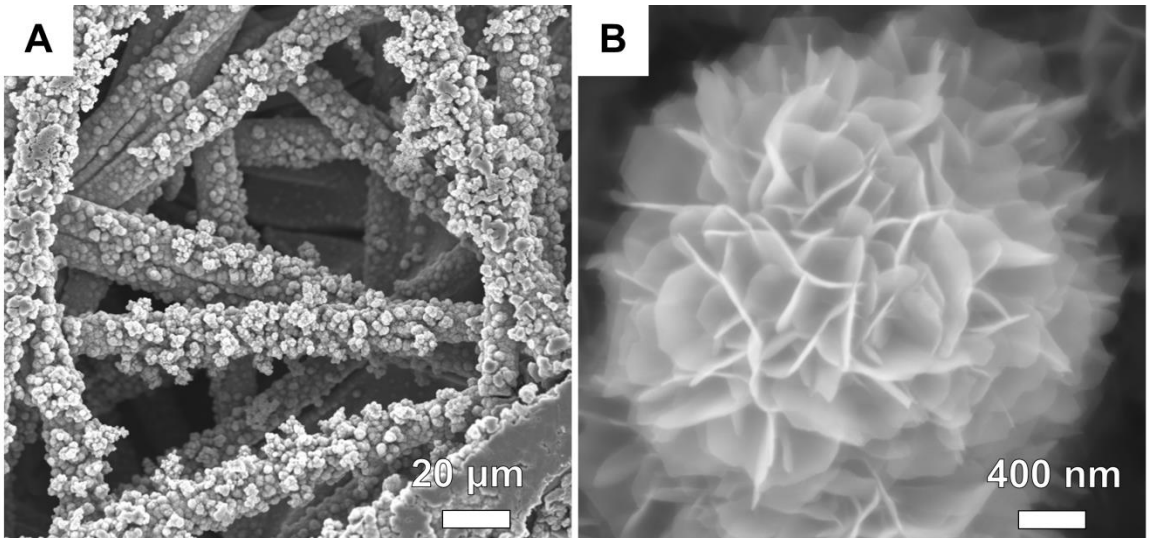

Figure 4.20 SEM image of coating formed from 20 mM KMnO4, 20 mM NH4Cl and 50 mM $LiOH•H_2O$ onto CFP at 120 °C for 12 hours taken at low magnification (A) and high magnification (B).

Increasing the hydrothermal temperature using the identical hydrothermal solution leads to dramatic change in overall morphology compared to the 120 °C coating shown in Figure 4.20. Figure 4.21 depicts a coating produced at 140 °C and shows a relatively uniform coating of containing octahedral crystallites similar to those observed for the excess lithium sample without NH_4Cl (Figure 4.13).

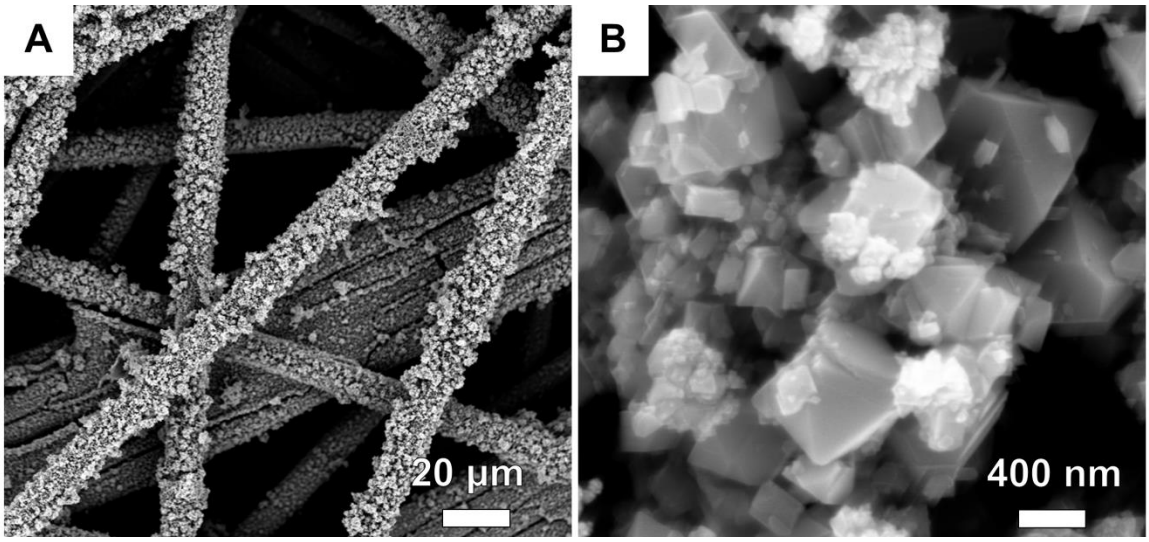

Figure 4.21 SEM image of coating formed from 20 mM KMnO4, 20 mM NH4Cl and 50 mM $LiOH•H_2O$ onto CFP at 140 °C for 12 hours taken at low magnification (A) and high magnification (B).

Increasing the hydrothermal temperature further to 160 °C (Figure 4.22) and 180 °C (Figure 4.23) seems to reduce the prevalence of the nodules observed at 120 °C and 140 °C, and as a result the coatings appear smoother at low magnifications. At high magnifications a mixture of polyhedron typed particulates is observed however the largest particulates, which have a predominately octahedral shape, are observed in the 140 °C coating. For the 160 °C and 180 °C similar crystallite morphologies, including octahedrons, are observed while the range in particulate sizes is smaller. For the 140 °C sample a few particulates are larger than the 400 nm scale bar and range between tens to hundreds of nanometers. With increasing hydrothermal temperature the maximum particulate size observed decreases and the resulting particulate size range decreases as result, which seems to be consistent with the expectation that Ostwald ripening due to mass transport between particulates will occur more rapidly at elevated temperatures. From the SEM analysis, it appears that the coating produced at 180 °C has the smallest overall particulate size, which is inconsistent with an assignment of Ostwald ripening, which predicts a larger final particulate size is. While a similar overall morphology is

observed, the mass loading of the predominately $LiMn_2O_4$ samples decreases significantly with increasing temperature, which suggests increased solubility of $LiMn_2O_4$ into the hydrothermal solution. For the sample produced at 180 °C the apparent coating mass is only 17 wt% of the composite electrode, compared to 27 wt% for the coating produced at 140 °C. Furthermore, all samples which contain $LiMn_2O_4$ have lower mass loadings than the samples which do not, which implies that the birnessite and MnO(OH) coatings are thicker and/or denser (Table 4.3). Thus, the changes in average crystallite size and particulate size distribution for the predominantly $LiMn_2O_4$ containing coatings are likely due to a coalescence of factors including greater oxide solubility and more rapid particle nucleation, which would produce a smaller final crystallite size, than Ostwald ripening.

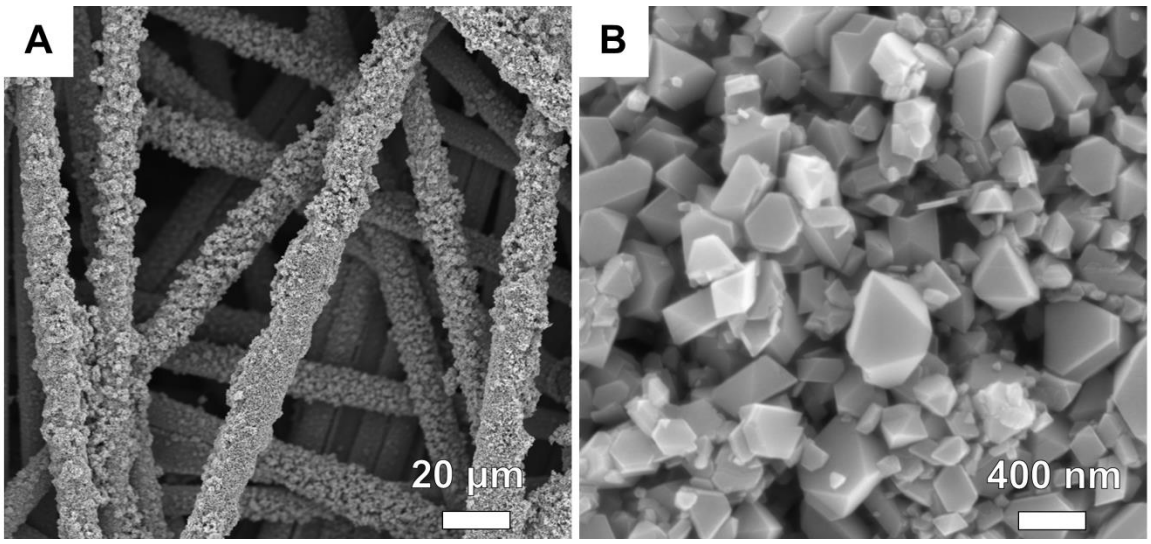

Figure 4.22 SEM image of coating formed from 20 mM $KMnO_4$, 20 mM NH_4Cl and 50 mM $LiOH•H_2O$ onto CFP at 160 °C for 12 hours taken at low magnification (A) and high magnification (B).

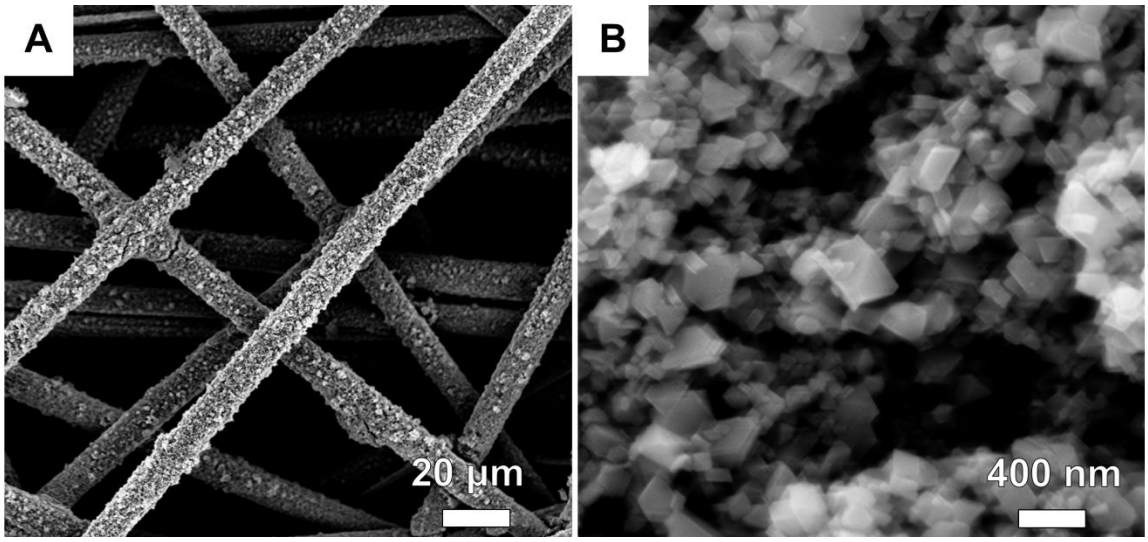

Figure 4.23 SEM image of coating formed from 20 mM $KMnO_4$, 20 mM NH_4Cl and 50 mM $LiOH•H_2O$ onto CFP at 180 °C for 12 hours taken at low magnification (A) and high magnification (B).

Along with the change in morphology from flower-like nanosheets at 120 °C to discrete crystallites formed at 140 °C, 160 °C and 180 °C, no K is observed via EDS for the higher temperature samples suggesting that the low temperature phase is likely K containing birnessite.

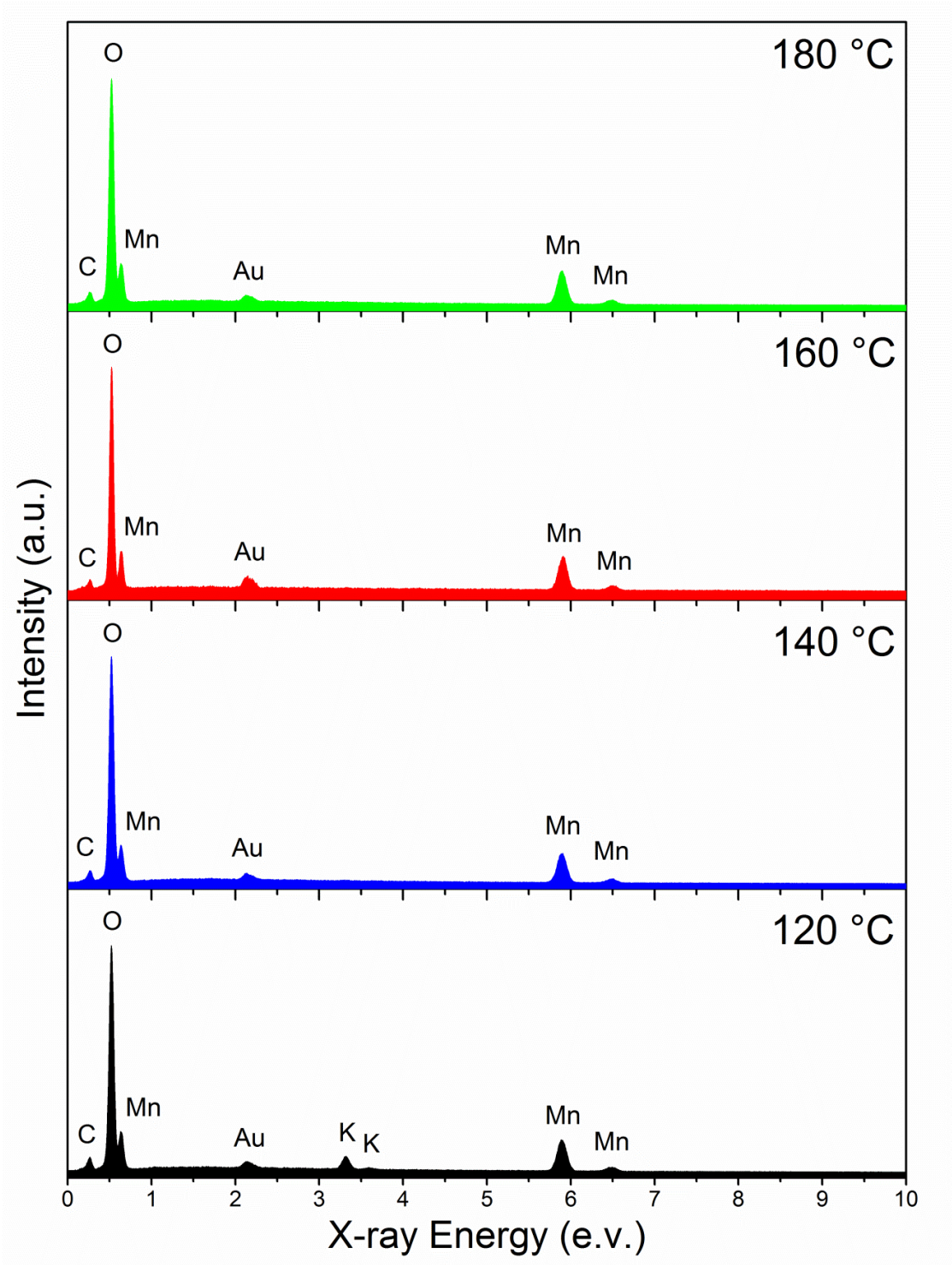

Figure 4.24 EDS of samples produced by decomposition of $LiOH•H_2O$ with $KMnO_4$and NH_4Cl in a ratio of 5:2:2 at various temperatures for 12 hours. Samples were sputtered with Au prior to analysis, and the intensity scale for each spectrum was normalized relative to the O Kα peak at 0.525 eV.

Consistent with the changes in morphology and elemental content, XRD confirms that above 140 °C, a phase change corresponding to the emergence of $LiMn_2O_4$. Unlike the coating produced with excess lithium but without NH_4Cl (Figure 4.13), no birnessite phase is observed at 140 °C or for any of the higher temperature samples. At 180 °C a pair of small impurity peaks attributable to Mn_3O_4 are observed, however there is no obvious new phase visible by SEM. Like $LiMn_2O_4$, Mn_3O_4 has a spinel structure and thus may form similar crystalline morphologies. For the coating produced at 120 °C, the strongest diffraction peak occurs at 12.57 °which as discussed in section 4.3.3 indicates some replacement of K by Li in the birnessite structure.

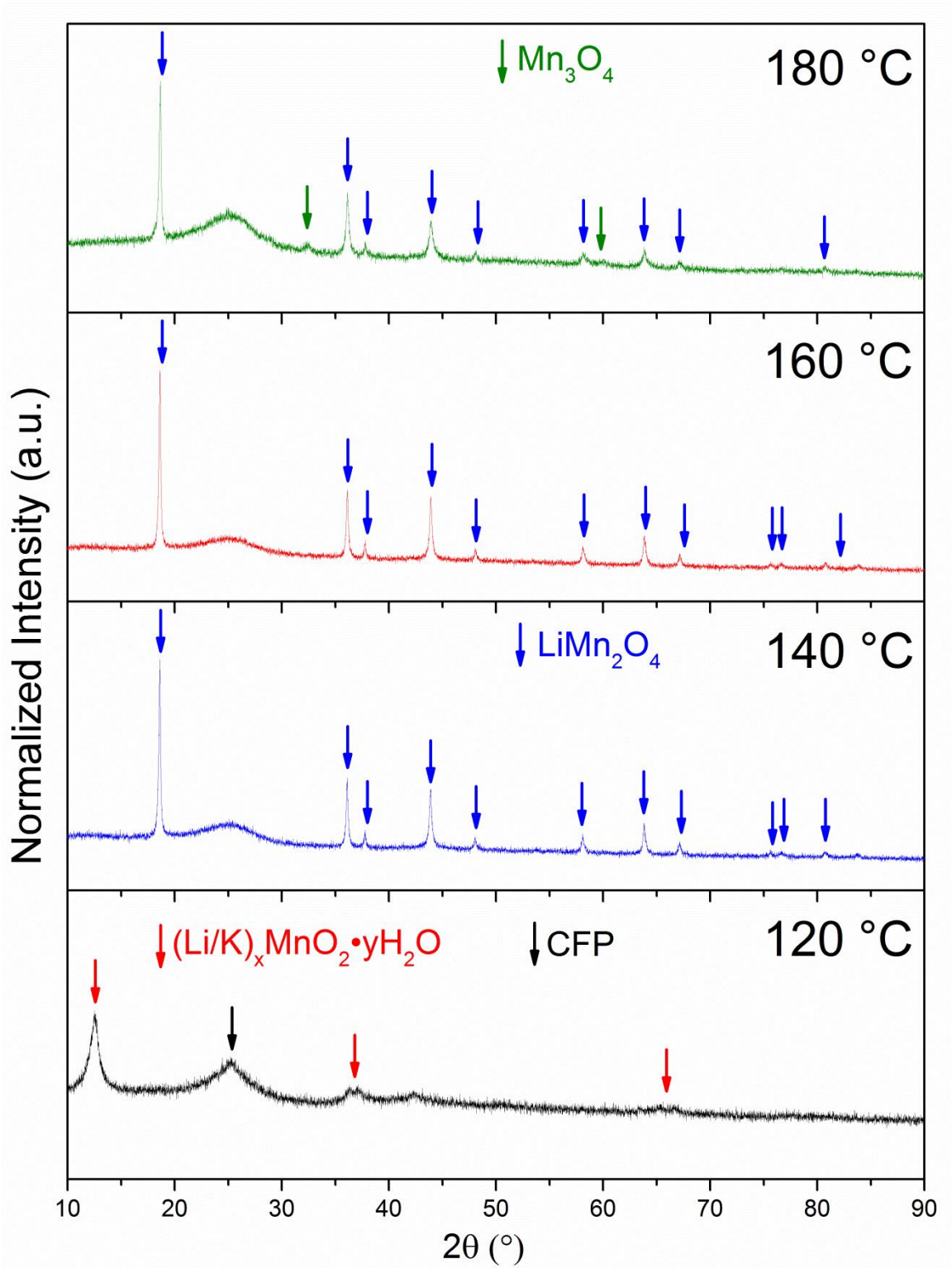

Figure 4.25 XRD patterns for hydrothermal samples produced with 50 mM $LiOH•H_2O$, 20 mM $KMnO_4$ and 20 mM NH_4Cl at various hydrothermal temperatures for a total reaction time of 12 hours.

The hydrothermal solution was further optimized to increase mass loading while maintaining a maximum temperature of 140 °C to avoid the formation of Mn_3O_4. The optimized approach involved two temperature regions, one at 100 °C for 12 hours to form a dense birnessite phase and a second step at 140 °C for 24 hours. Mass loadings for this approach had an average value of 32 wt%, and consist of phase-pure $LiMn_2O_4$. SEM images of the coatings produced by the preliminary 100 °C step and after the complete two step reaction are shown in Figure 4.26. In subsequent chapters, the two temperature approach was used to produce hydrothermal coatings of $LiMn_2O_4$ on carbon fibers.

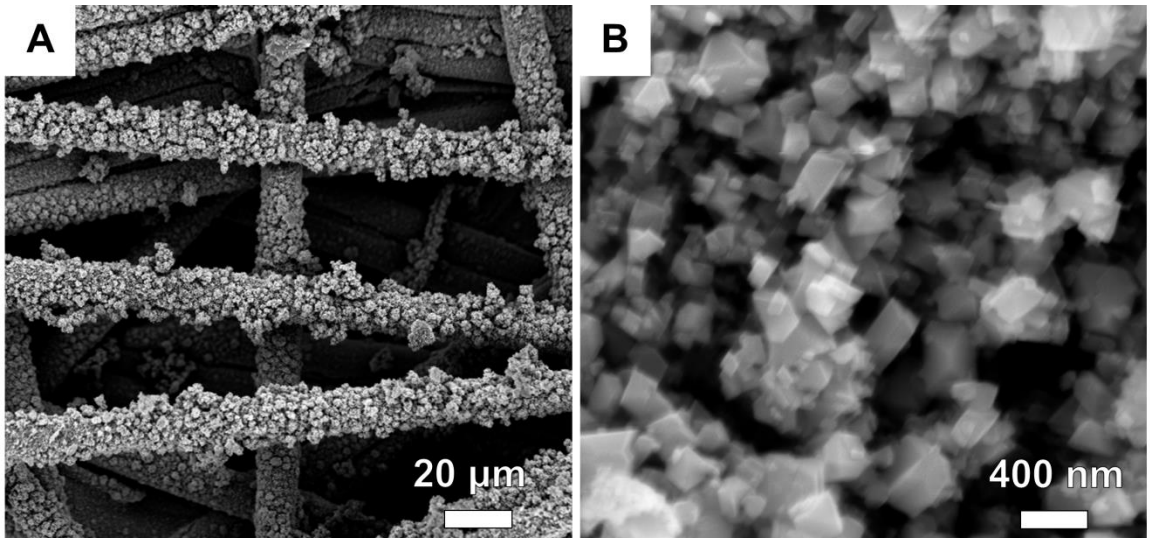

Figure 4.26 SEM images of carbon fiber papers coated using hydrothermal synthesis at 100 °C for 12 hours followed by 140 °C for 24 taken at low magnification (A) and high magnification (B).

Increasing hydrothermal temperature also leads to a decrease in average crystallite size, which was estimated using the Scherrer equation (Equation 33). The average crystallite size derived from the FWHM values for the three most intense diffraction peaks which are the (111) peak at 18.6° 2θ, the (113) peak at 36.1° 2θ, and the (004) peak at 43.9° 2θ, and is summarized in Table 4.2. While the coating produced at 180 °C has the smallest average crystallite size, the two-step hydrothermal coating with a longer dwell time at 140 °C has a slightly reduced crystallite size compare to the single step 12 hour dwell time.

Table 4.2 Calculated crystallite size for $LiMn_2O_4$ samples produced from hydrothermal solution containing $LiOH•H_2O$, $KMnO_4$ and NH_4Cl in a 5:2:2 ratio at various temperatures.

Hydrothermal Temperature / time	Average crystallite size (nm)	Standard deviation (nm)
140°C / 12 Hr	42.2	2.5
160°C / 12 Hr	39.7	0.7
180°C / 12 Hr	31.6	2.3
100°C / 12 Hr → 140°C / 24 Hr	38.8	2.3

4.3.5 Summary of Hydrothermal Phases

For the conditions studied, the three predominant phases appear to be birnessite ($M_xMnO_2•yH_2O$) where M can be either Li or K, manganite (γ-MnO(OH)), and spinel lithium-manganese oxide ($LiMn_2O_4$). A minority crystalline phase of Mn_3O_4 was also observed, however it is plausible based on relative mass loadings and elemental composition of the various coatings that other amorphous phases, in particular manganese oxides, are also included. Only phases in which $LiMn_2O_4$ was the majority crystalline phase did not include K, where K is a strong indication that birnessite is included in the coating. For coatings identified as birnessite produced by Li containing hydrothermal solutions, a shift in the strongest diffraction peak was associated with a partial replacement of K by Li in the birnessite structure. This conclusion is also supported by an observed increase in the relative concentration of Mn to K in these coatings. Manipulation of the hydrothermal solution and reaction temperature were sufficient to control the crystallographic phase and elemental content of the coatings produced, however mass loading (expressed as weight percent oxide in the composite electrode) was minimized under the conditions found to produce a phase pure coating of $LiMn_2O_4$.

For this reason a two temperature hydrothermal approach was used with a moderately beneficial effect.

Table 4.3 Summary of phases, mass loadings and elemental content for hydrothermal coatings on CFP. All coatings produced with 12 hour dwell time unless otherwise indicated.

Solution	Temperature	Mn:O	Mn:K	Phase	Mass Loading
20 mM $KMnO_4$	120 °C	0.11	1.0	K-Birnessite	59 wt%
20 mM $KMnO_4$	140 °C	0.10	1.9	K-Birnessite + MnO(OH)	55 wt%
20 mM $KMnO_4$	160 °C	0.11	2.9	MnO(OH) + K-Birnessite	58 wt%
20 mM $KMnO_4$, 10 mM $LiOH•H_2O$	140 °C	0.12	1.1	K/Li-Birnessite	53 wt%
20 mM $KMnO_4$, 50 mM $LiOH•H_2O$	140 °C	0.12	5.4	$LiMn_2O_4$ + Li-Birnessite	40 wt%
20 mM $KMnO_4$, 20 mM NH_4Cl	140 °C	0.12	4.1	MnO(OH) + K-Birnessite	51 wt%
20 mM $KMnO_4$, 20 mM NH_4Cl, 10 mM $LiOH•H_2O$	140 °C	0.09	2.1	MnO(OH) + K/Li-Birnessite	47 wt%
20 mM $KMnO_4$, 20 mM NH_4Cl, 50 mM $LiOH•H_2O$	120 °C	0.14	2.05	K/Li-Birnessite	36 wt%
20 mM $KMnO_4$, 20 mM NH_4Cl, 50 mM $LiOH•H_2O$	140 °C	0.13	N/A	$LiMn_2O_4$	27 wt%
20 mM $KMnO_4$, 20 mM NH_4Cl, 50 mM $LiOH•H_2O$	160 °C	0.16	N/A	$LiMn_2O_4$	26 wt%
20 mM $KMnO_4$, 20 mM NH_4Cl, 50 mM $LiOH•H_2O$	180 °C	0.15	N/A	$LiMn_2O_4$ + Mn_3O_4	17 wt%
20 mM $KMnO_4$, 20 mM NH_4Cl, 50 mM $LiOH•H_2O$	100°C / 12 Hr -> 140°C / 24 Hr	0.13	N/A	$LiMn_2O_4$	28-36 wt%

4.4 Electrochemical Testing of Hydrothermal Phases

To evaluate the charge storage capability of the oxide-coated CFP produced by the hydrothermal method, electrochemical testing was conducted on all of the identified phases. Electrodes were tested by CV at a rate of 50 μV/s to identify any redox peaks within the potential range of 3.1 V to 4.4 V vs. Li/Li^+, which is a typical potential region for lithium-ion cathode materials. Galvanostatic testing was also conducted with a current density normalized to the mass of the coating. A rate of C/10 as defined in section 3.3.3 was used as defined by the theoretical capacity of $LiMn_2O_4$ (148 mAh/g) regardless of whether this phase was present in the sample being tested. The results from galvanostatic testing were used to calculate the specific capacity of the various phases in the potential region tested. All samples were dried in a vacuum oven prior to use as testing as half-cells using Swagelok type cell hardware. All testing was conducted using a 1 M $LiPF_6$ in 1:1 EC:DMC electrolyte (Novolote) soaked into glass fiber separators (Whatman).

4.4.1 Electrochemical Testing of Li-free Phases

For the CFP coatings produced from a hydrothermal solution containing only $KMnO_4$ and NH_4Cl, a similar electrochemical response is observed during cyclic voltammetry. All of these samples contain some content of K-birnessite, whereas a new phase, γ-MnO(OH), emerged with increasing temperature or with the addition of NH_4Cl. Figure 4.27 shows the first, fifth and tenth cycle at a voltage sweep rate of 50 uV/s for the coatings produced by hydrothermal reaction of CFP with a 20 mM solution of $KMnO_4$ for 12 hours.

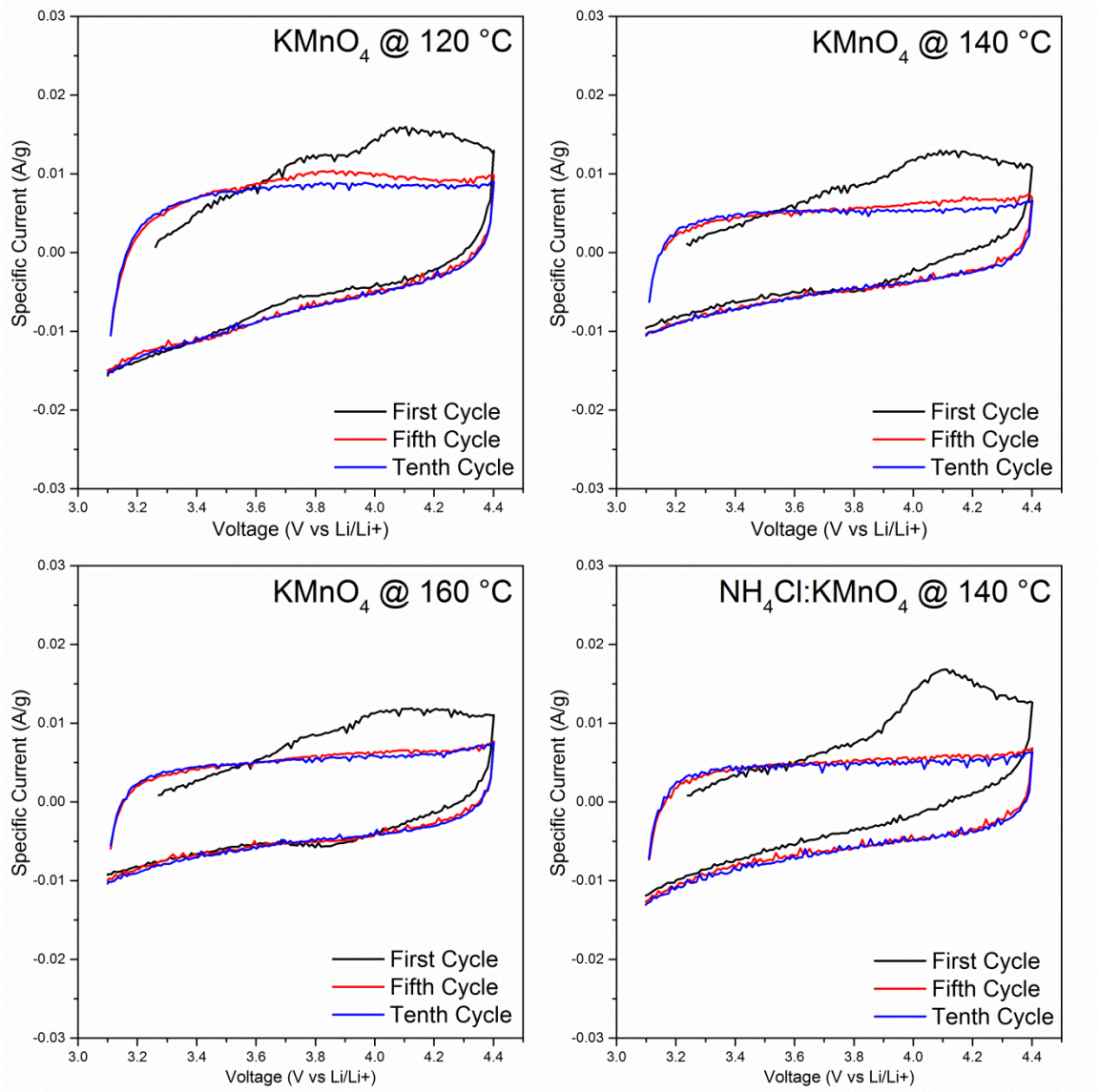

Figure 4.27 Cyclic voltammograms for coatings produced by hydrothermal reaction of hydrothermal solutions containing no Li ($KMnO_4$ and NH_4Cl only) with CFP at various temperatures at a scan rate of 50 µV/s.

All of the Li-free coatings show a similar reactivity towards Li^+ in the potential region tested. On the first cycle, a slightly increased current is observed during the first anodic sweep, which is found to be irreversible on the first cathodic sweep. This feature was also observed for the bare CFP, although at a much lower total current, so it could possibly be attributed to electrolyte oxidation. For the fifth and tenth cycle the CVs are

coincident, suggesting the irreversible reactions observed on the first cycle have dissipated. While the coating produced at 120 °C had the highest total mass loading (59 wt%), this sample also had the highest normalized current density. None of these coatings shown in Figure 4.27 have redox peaks, and instead portray a relatively constant current density across the potential region tested. Still, the overall normalized current density is higher than that observed for the bare CFP substrate (approximately 50 mA/g for the electrodes in Figure 4.27 compared to 2.5 mA/g for bare CFP in Figure 4.6), which can only store charge through double-layer capacitance. Thus we can conclude that the coatings produced from the $KMnO_4$ only hydrothermal solution introduce some pseudocapactive charge storage into the electrode.

For the coating produced by a reaction of NH_4Cl and $KMnO_4$ at 140 °C which contained a highly crystalline γ-MnO(OH) phase (Figure 4.16), shows a very similar CV response for the samples produced from a $KMnO_4$ only solution. During the first cycle, what appears to be an oxidation peak is observed and is more pronounced than for the voltammograms for coatings produced from only $KMnO_4$, however just like the previous samples ($KMnO_4$ only solution) this reaction is irreversible. By the fifth cycle only pseudocapactive behavior is observed.

Figure 4.28 compares the specific charge and discharge capacity for the four lithium-free coatings discussed in this section. Consistent with the CV analysis in Figure 4.27, the charge and discharge behavior is linear as a function of potential, suggesting that no bulk faradic activity is occurring in these samples.

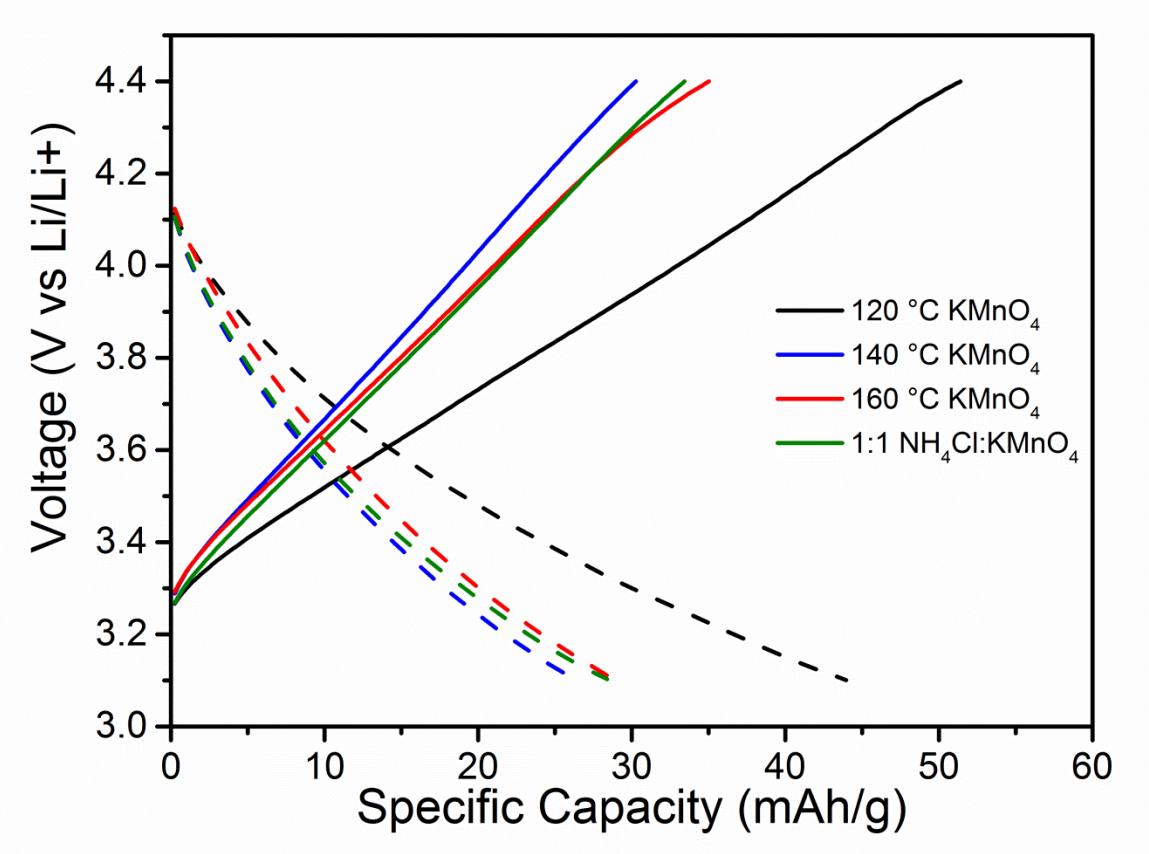

Figure 4.28 Charge (solid lines) and discharge (dashed lines) Voltage vs. Specific Capacity plots for hydrothermal coatings on CFP produced without Li. All samples were tested at a current density of 14.8 mA/g (C/10 for theoretical capacity of $LiMn_2O_4$), normalized relative to the mass content of oxide in the electrode

All of the samples produced without lithium, regardless of phase, crystallinity or morphology, showed specific capacities less than 50 mAh/g in the voltage region of 3.1 to 4.4 V vs. Li/Li^+, making them unsuitable for application as lithium-ion battery cathodes.

4.4.2 Electrochemical Testing of Li-containing Phases

For the coatings produced while including $LiOH•H_2O$ in the hydrothermal solution similar trends in phases produced and overall morphology were observed when compared to the coatings without any Li source. Due to the similar appearance and crystalline structure, as well as the inability to detect Li using EDS, Li inclusion was inferred from

relative changes in Mn:K ratio by EDS and lattice constant by XRD. Birnessite has been produced to include Li, Na, K in the spacing between the layers of octahedrally coordinated Mn, while manganite is not expected to incorporate Li to any degree [112]. This section will focus on the electrochemical response for phases produced which likely contain some lithium, but not the performance of coatings which were determined to include only $LiMn_2O_4$ as the lithium-containing phase. The testing of these coatings will be treated in the next section.

Figure 4.29 shows the CV results for several coatings produced at various temperatures with various Li contents in the hydrothermal solution. All of these coatings contain some fraction of birnessite, which based on the position of the diffraction peak and relative Mn:K content observed by EDS is assumed to contain some Li. For the coating produced at 140 °C with NH_4Cl and the coating produced with a 2:5 ratio of Mn:Li, MnO(OH) and $LiMn_2O_4$ were also observed by XRD, respectively, along with birnessite. One hypothesis being evaluated in Figure 4.29 is that for coatings containing lithium in the structure, a greater reactivity to Li in the studied potential region could be expected. In fact, with the exception of the coating containing some content of $LiMn_2O_4$ the CV response is nearly identical to the Li free coatings shown in Figures 4.27. In the case of the sample containing $LiMn_2O_4$, the observed gravimetric current density is an order of magnitude higher than all of the previously analyzed samples. As with the Li free coatings, of the samples in Figure 4.29 show some irreversibility during the first CV cycle.

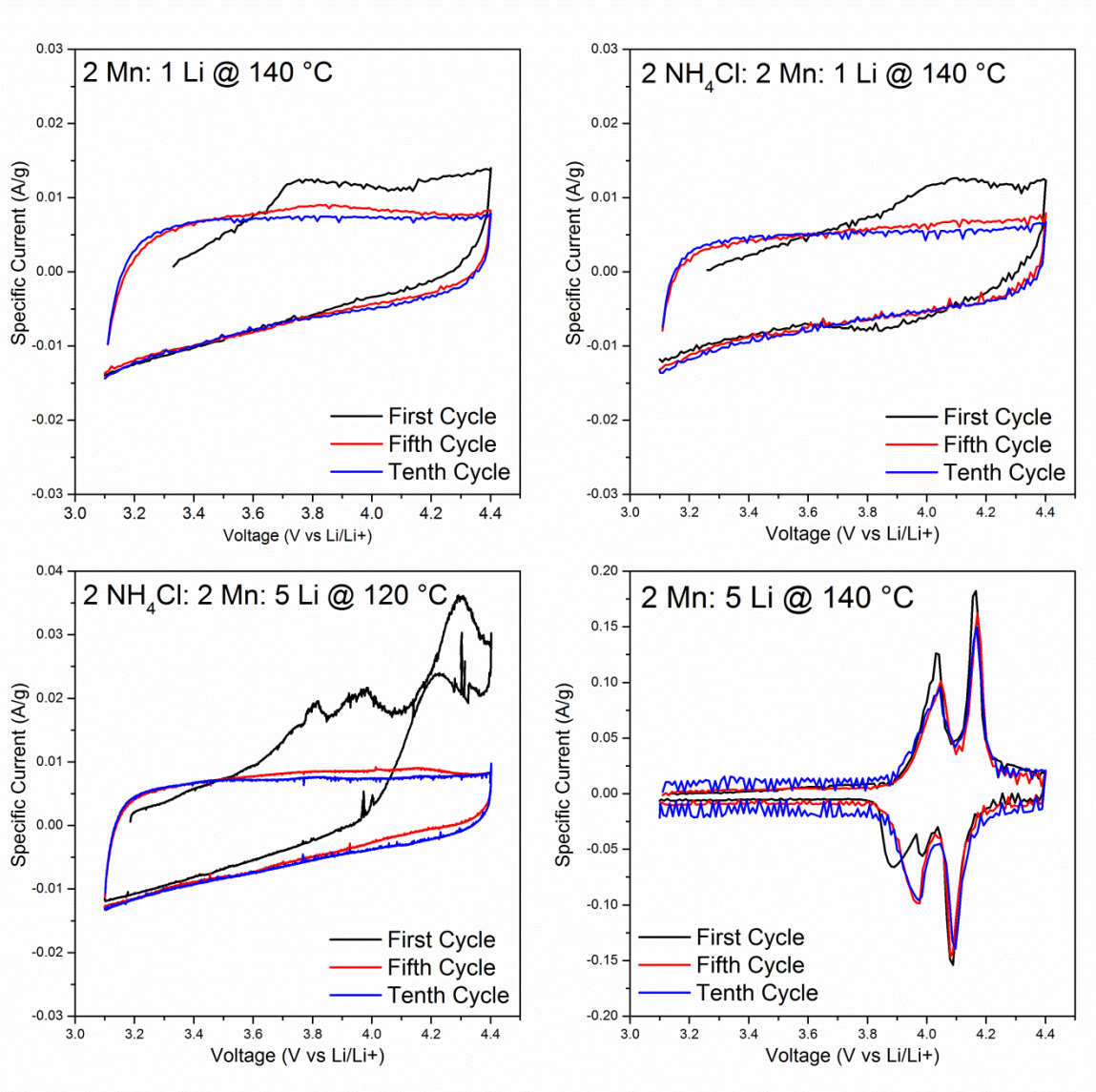

Figure 4.29 Cyclic voltammograms for coatings from hydrothermal solutions containing $KMnO_4$, Li in the form of $LiOH•H_2O$ and NH_4Cl with CFP at various temperatures for a period of 12 hours. Cycles were conducted at a scan rate of 50 μV/s and current density is normalized by the mass of $LiMn_2O_4$ in the electrode.

When analyzed by galvanostatic testing the sample containing $LiMn_2O_4$ demonstrates a reversible specific capacity over three times that of the other Li containing phases produced. This observation is invariant of phase, crystalline quality or relative K content which leads to the conclusion that among all of the phase produced only $LiMn_2O_4$ is active towards Li through a faradaic reaction. Meanwhile,

pseudocapactive reactions involving the formation of a Li containing double layer are possible but difficult to extrapolate.

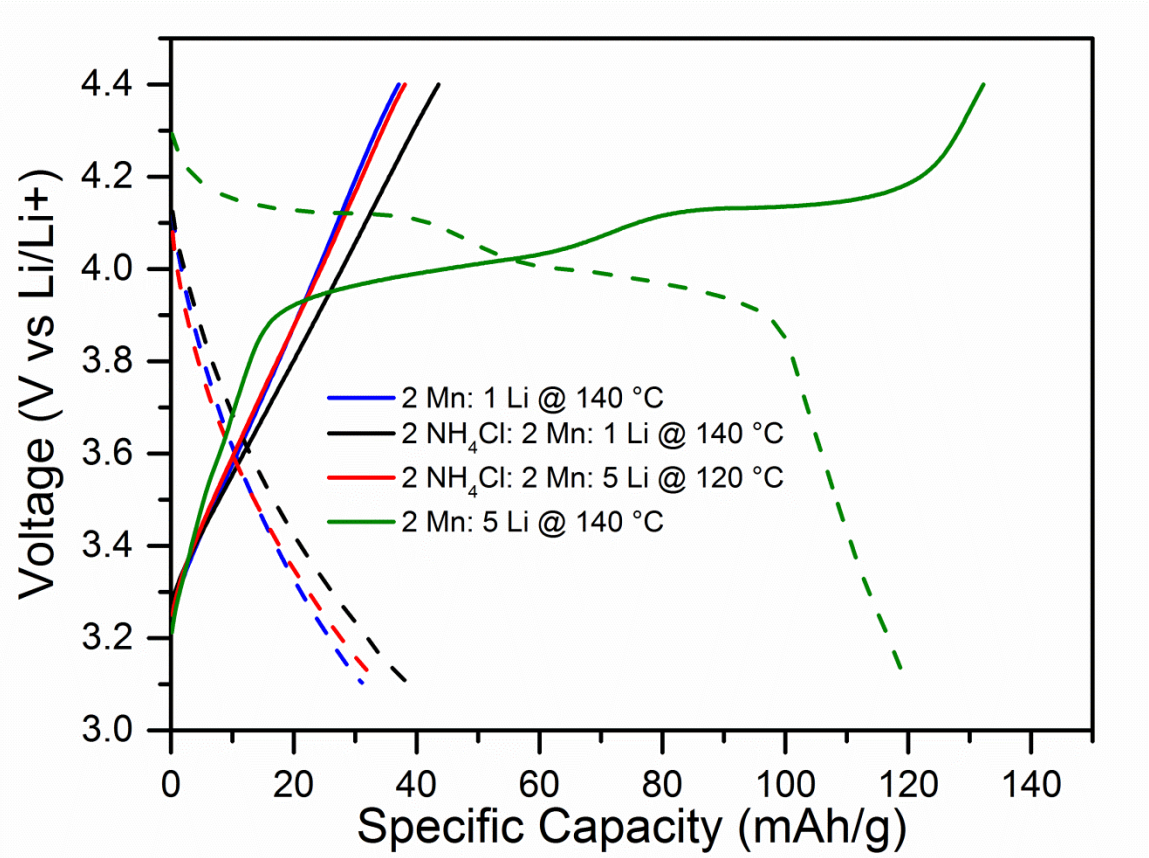

Figure 4.30 Charge (solid lines) and discharge (dashed lines) Voltage vs. Specific Capacity plots for hydrothermal coatings on CFP produced with Li in the hydrothermal solution. All samples were tested at a current density of 14.8 mA/g (C/10 for theoretical capacity of $LiMn_2O_4$), normalized relative to mass content of oxide in the electrode.

4.4.3 Electrochemical Testing of $LiMn_2O_4$ on CFP

At temperatures of 140 °C to 180°C, mostly phase pure $LiMn_2O_4$ coatings could be produced with a solution of 20 mM $KMnO_4$, 20 mM NH_4Cl and 50 mM $LiOH•H_2O$. At 180 °C a small impurity phase identified by XRD as Mn_3O_4 appears while the general morphology and chemical composition for samples prepared in this range were similar (Figures 4.21 – 4.24). An optimized mass loading was achieved with a two-step hydrothermal process involving an initial formation of birnessite at 100 °C which was then converted to $LiMn_2O_4$ by a 24 hour period at 140 °C.

Cyclic voltammograms of electrodes containing primarily $LiMn_2O_4$ show similar positions of current peaks and overall magnitude when normalized by the oxide content in the composite. All sample shows two oxidation (O_1 and O_2) peaks in the region of 4.04 V vs. Li/Li+ and 4.17 V vs. Li/Li+, and two reduction peaks (R_1 and R_2) in the region of 3.96 V vs. Li/Li+ and 4.09 V vs. Li/Li+, with maximum current densities between 0.10 and 0.15 A/g. These values are close to what has been reported for $LiMn_2O_4$ produced using high temperature calcinations to ensure excellent crystallinity [33, 113]. Reversibility of the electrochemically active material can be evaluated from the CV by comparing the position of the forward and reverse current peaks, as well as the magnitude of forward and reverse current. As described in section 3.3.2, a completely reversible faradaic reaction should have a ratio of oxidation and reduction peak currents of 1.0, and at separation of peak voltages ($\Delta V=V_{ox}-V_{red}$) of 59.2/n mV, where n is the number of electron transfers. While $LiMn_2O_4$ is expected to undergo a single electron transfer during the reaction between $LiMn_2O_4$ in the discharged state and λ-MnO_2 in the charged state, the removal of half of the tetrahedrally coordinated lithium atoms occurs at a lower potential than the remaining half, making "expected" peak separation somewhat unclear.

Values derived from the CV analysis of $LiMn_2O_4$ coated carbon fibers are shown in Table 4.4. All of the samples showed peak current ratios above 90%, however a few examples of a current ratio exceeding 100% imply either inaccurate current measurement or side reactions occurring simultaneously with lithium intercalation. Peak separations for all samples are on the order of 70-80 mV, and appear to be smallest among all of the hydrothermal temperatures presented in the 140 °C coating. Along with the apparently stable CV response between the 1st through 10th cycle, this could imply that the coatings produced at 140 °C for 12 hours have super electrochemical reversibility.

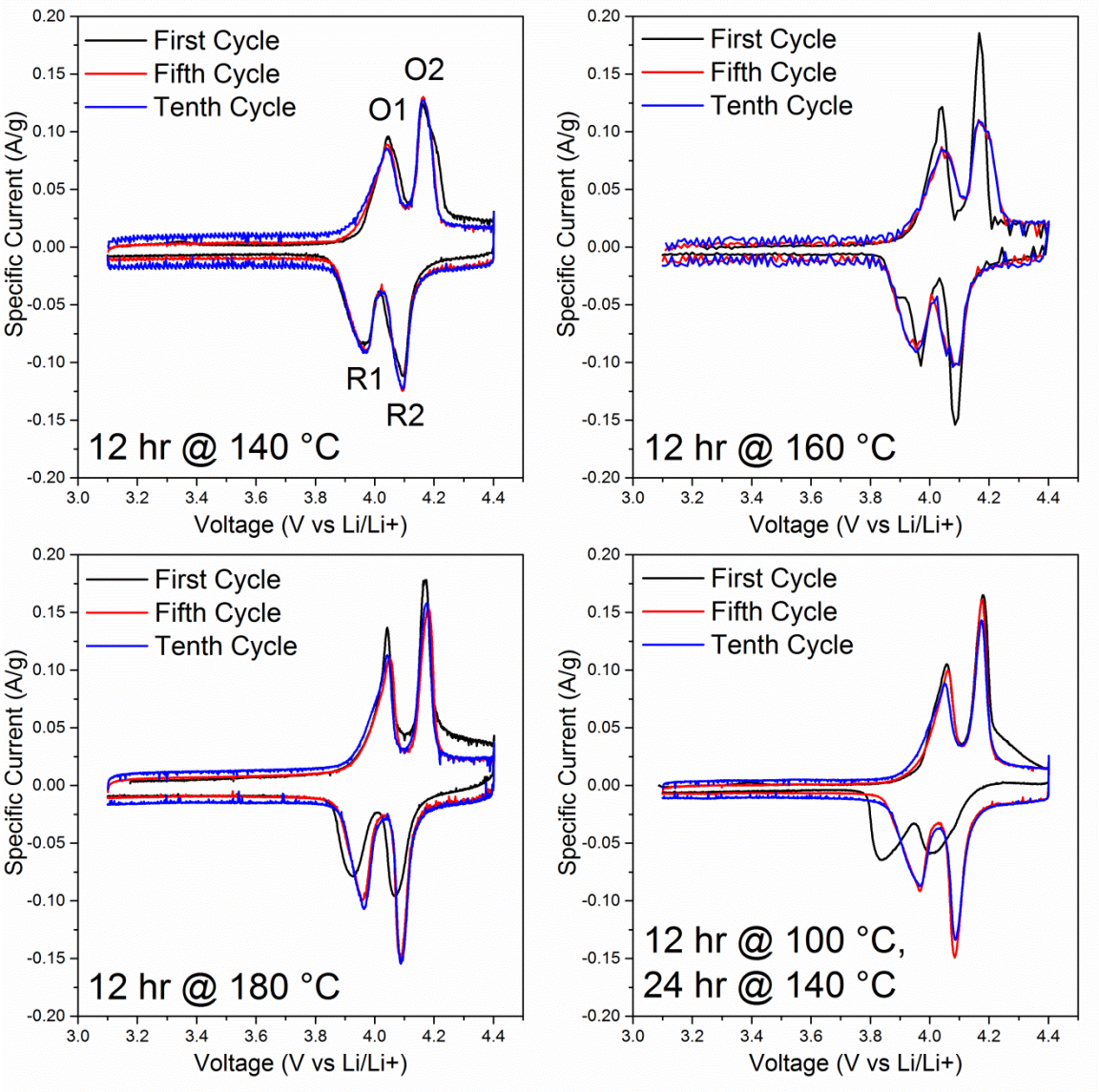

Figure 4.31 Cyclic voltammograms for coatings produced from hydrothermal solutions containing 20 mM $KMnO_4$, 20 mM NH_4Cl and 50 mM $LiOH•H_2O$ CFP at various temperatures and times. Cycles were conducted at a scan rate of 50 µV/s and current density is normalized by the mass of $LiMn_2O_4$ in the electrode.

Table 4.4 Summary of peak parameters for CVs of $LiMn_2O_4$ coated CFP conducted at 50 µV/s

Hydrothermal Temperature / time	I_{R1}/I_{O1}	I_{R2}/I_{O2}	$\Delta V_{(O1-R1)}$ (mV)	$\Delta V_{(O2-R2)}$ (mV)
140°C / 12 Hr	1.06	0.96	73.0	67.8
160°C / 12 Hr	1.07	0.94	87.8	88.4
180°C / 12 Hr	0.95	0.97	76.7	85.3
100°C / 12 Hr -> 140°C / 24 Hr	0.99	0.93	81.0	86.9

Galvanostatic testing of the $LiMn_2O_4$ containing coatings shows that the two-temperature hydrothermal process has the highest specific capacity in the voltage region tested. Furthermore, capacity is observed to increase with increasing hydrothermal temperature for the single temperature coatings. As with the CV measurements, the coatings containing $LiMn_2O_4$ show similar voltage plateaus and some degree of irreversibility, which is observed as a greater charge capacity than discharge capacity.

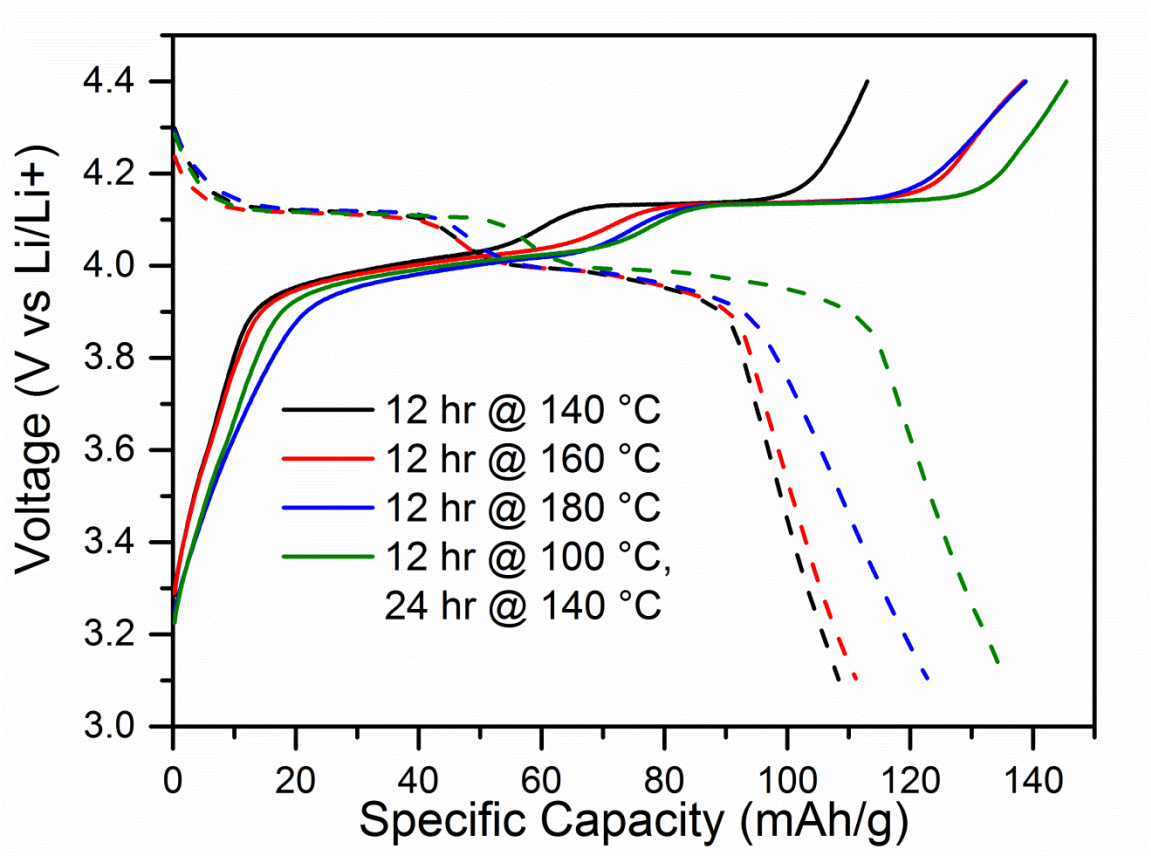

Figure 4.32 Charge (solid lines) and discharge (dashed lines) Voltage vs. Specific Capacity plots for hydrothermal coating containing primarily $LiMn_2O_4$. All samples were tested at a current density of 14.8 mA/g (C/10 for theoretical capacity of $LiMn_2O_4$), normalized relative to mass content of oxide in the electrode.

4.4.4 Rate capability and lifetime of $LiMn_2O_4$ on CFP

$LiMn_2O_4$ coatings produced using the two-step hydrothermal procedure were further evaluated by increasing the current density used during galvanostatic testing as well as repeated charge and discharge cycles. In this way the overpotential and capacity could be studied under more realistic use conditions, which typically need to operate at a variety of current densities for hundreds or thousands of charge and discharge cycles. As a comparison, a tape cast electrode was prepared using store bought $LiMn_2O_4$.

Figure 4.33 shows that the $LiMn_2O_4$ coated CFP electrodes have higher specific capacity than the tape cast counterparts at all current densities tested except for the 5C

(740 mA/g) rate, in which the CFP based electrode shows a large increase in overpotential leading to a decreased discharge voltage plateau. Another important distinction between the two electrode types occurs at the end of discharge polarization region, typically associated with concentration polarization. In this region the tape cast electrodes show a rapid drop in cell potential while the CFP based electrodes display a gentle slope. This could be a contribution from a pseudocapactive charge storage mechanism, which as observed for the non-$LiMn_2O_4$ hydrothermal samples would have a linear voltage throughout the entire discharge potential window. Alternatively, the sloping discharge potential may be a consequence of the range of particle sizes observed for the hydrothermal coatings compared to the monodisperse nature of the commercial powder, which according to the vendor has an average particle size between 10-20 microns. In this case smaller particles with shorter ionic pathways would become lithiated faster than larger particles leading to a gradient of concentrations and thus potentials.

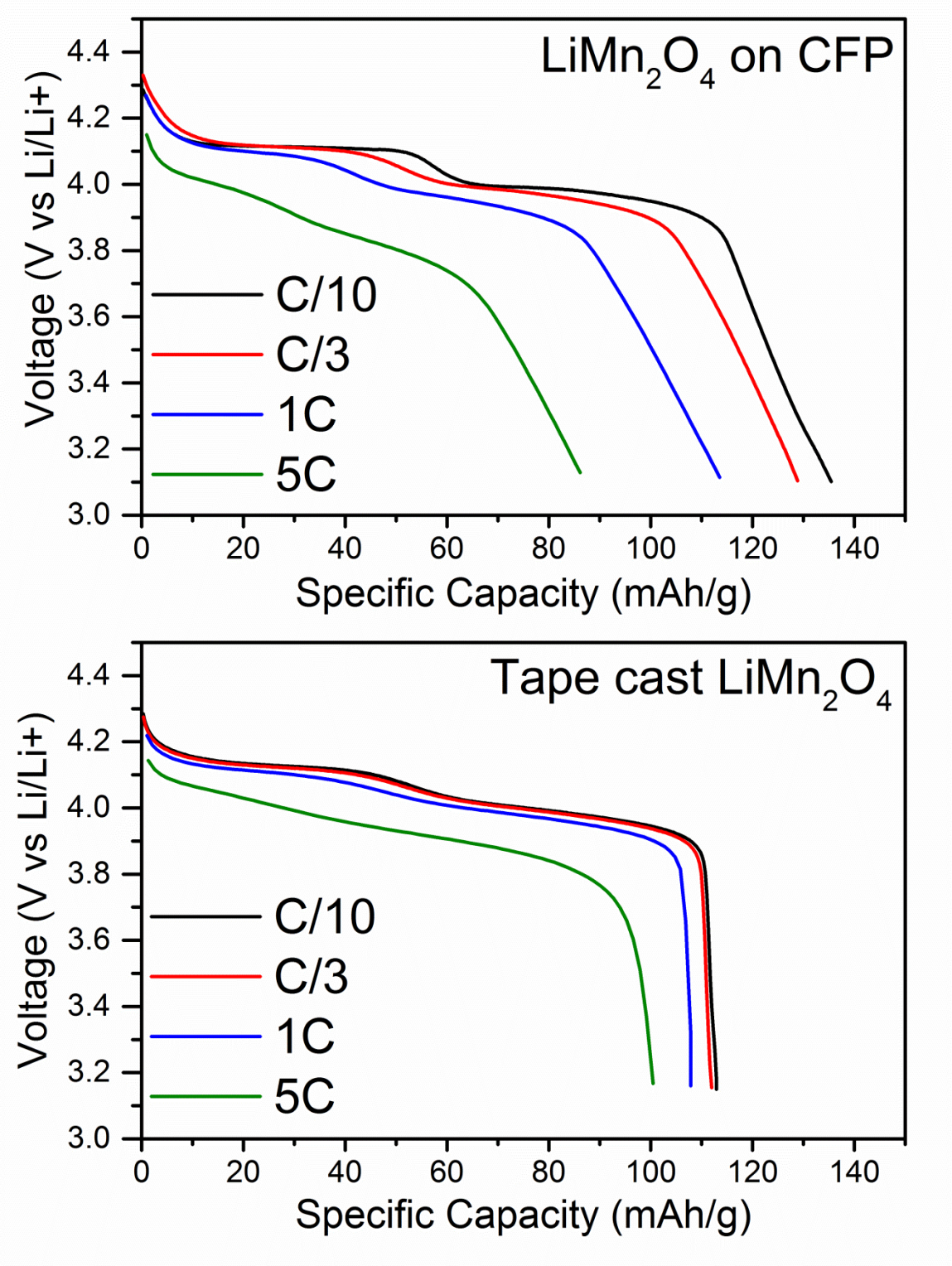

Figure 4.33 Galvanostatic discharge of $LiMn_2O_4$ electrodes prepared by hydrothermal coatings on CFP and tape casting of store bought powders. Current densities were normalized relative to mass content of oxide in the electrode.

When the $LiMn_2O_4$ cells are cycled at a rate of 1C at room temperature, the comparatively rapid capacity fade of the $LiMn_2O_4$ on CFP electrode is apparent. While the CFP electrode starts with a higher specific capacity this is negated around cycle 100. Over 100 cycles the CFP based electrode loses approximately 14% of the first cycle capacity compared to only 3% for the tape cast electrode. While both samples are expected to undergo capacity loss through a similar mechanism, the higher surface area in the nanostructured $LiMn_2O_4$ coating on the CFP electrodes may increase the rate relative to the micron-sized particles in the tape cast electrode.

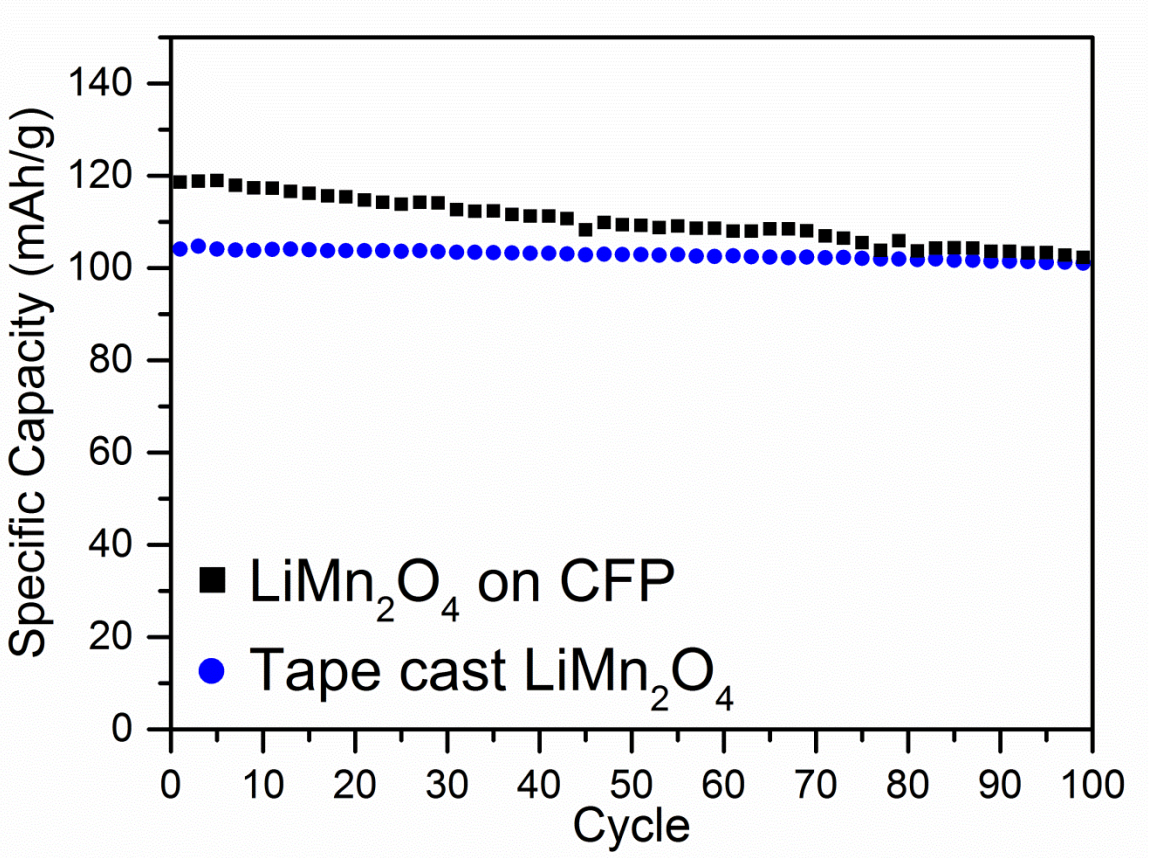

Figure 4.34 Cycling at a 1C rate and room temperature for $LiMn_2O_4$ electrodes produced by hydrothermal coatings on CFP and tape casting commercial powders.

4.5 Conclusions

In this chapter, a hydrothermal process was used to coat various oxides of Mn onto a commercial carbon fiber paper substrate. While a number of crystalline phases and compositions were identified using SEM, EDS and XRD, electrochemical testing revealed that only $LiMn_2O_4$ has significant charge storage capability when paired with a lithium metal counter electrode and lithium-containing electrolyte. Mass loading of $LiMn_2O_4$, which is the critical factor for improving the energy density of electrodes containing active and inactive components, was increased by using a two-temperature hydrothermal approach. Still, the highest mass loading obtained was approximately 30 wt%, corresponding to an active material loading of 6-7 mg/cm^2. Comparatively, the tape cast electrode used in this chapter had an 80 wt% $LiMn_2O_4$ electrode (excluding the weight of the Al foil current collector), corresponding to an active material loading of 2-3 mg/cm^2. It is important to recognize, however, that tape cast electrodes used in devices can exceed 20-30 mg/cm^2 of active material. For these heavily loaded commercial electrodes the effective active mass percentage is about 75 wt%. Assuming a capacity of 110 mA/g for both electrode types at a 1C rate, the effective capacity based on the entire electrode mass becomes 82 $mAh/g_{electrode}$ for the commercially used tape cast electrodes and only 33 $mAh/g_{electrode}$ for the electrodes produced by hydrothermal coatings on CFP.

Additionally, the hydrothermal produced electrodes showed a significantly faster capacity loss than the tape cast electrodes with commercial powders. This was observed by comparing the capacity loss at a fixed current density for the two electrode types. Increasing the temperature or current density would typically lead to even faster rates of

capacity loss. Subsequent chapters will focus on methods to improve both the overall energy density and capacity loss of carbon fiber based electrodes.

5 IMPROVING LIFETIME OF LIMN2O4 ON CARBON FIBER ELECTRODES WITH ALD COATINGS

In the previous chapter, the hydrothermal method was used to produce a variety of manganese-oxide phases on carbon fiber paper. Of the phases produced, only $LiMn_2O_4$ displays high reactivity towards lithium-ions in the potential region of 3 – 4.5 V vs Li/Li+. The $LiMn_2O_4$ on CFP electrodes showed well-defined redox peaks and near theoretical capacity at low rates, which are excellent signs that producing electrodes by hydrothermal precipitation of oxides onto carbon fibers may be a viable approach. However, rapid capacity fading was observed for the as-prepared electrodes and this presents a significant challenge which must be overcome. In this chapter, a surface modification technique is introduced – atomic layer deposition – which is capable of depositing ultra-thin and highly conformal layers of oxides onto the surface of the $LiMn_2O_4$ electrodes. These surface coatings can dramatically enhance the capacity retention of $LiMn_2O_4$ during electrochemical cycling. Aluminum-oxide was selected for this study as its growth rates are well understood, and it can be deposited well below the observed onset of $LiMn_2O_4$ catalyzed carbon oxidation at around 400 °C.

5.1 Methods to Improve $LiMn_2O_4$ Capacity Retention

There have been over two decades of research studies devoted to improving the capacity retention of $LiMn_2O_4$ cathodes, likely driven by the promise of low cost and high safety batteries. As described in the introductory chapters, $LiMn_2O_4$ capacity loss is believed to be primarily due to Mn disproportionation and dissolution through the Hunter reaction, typically expressed as

$$2LiMn_2O_4(s) \rightarrow Li_2O + 3MnO_2(s) + MnO(aq) \quad \textbf{Reaction 1}$$

which was observed by exposure of $LiMn_2O_4$ to HCl[41]. While $LiMn_2O_4$ contains Mn in both Mn^{3+} and Mn^{4+} oxidation states, Mn^{3+} cations are more susceptible to disproportionation and result in a soluble Mn^{2+} species and an insoluble Mn^{4+} species.

In an operational LIB, acidic species are attributed to spontaneously formed HF due to a reaction of $LiPF_6$ with water impurities in the organic liquid electrolyte. This reaction shown below,

$$LiPF_6 + H_2O \rightarrow POF_3 + LiF + 2HF \qquad \textbf{Reaction 2}$$

is often invoked in academic literature to explain capacity fading in $LiMn_2O_4$ and can be avoided by simply changing the electrolyte salt or including additives, however $LiPF_6$ is still the industry preferred salt[8, 49, 50].

An acid-enabled variation of the Hunter reaction described by Benedek and Thackeray (Reaction 3)

$$2LiMn_2O_4(s) + 4H^+(aq) \rightarrow 3MnO_2(s) + Mn^{2+}(aq) + 2Li^+(aq) + 2H_2O\ (aq)$$

Reaction 3

and shows that as a result of Mn dissolution more water is generated, which can in turn lead to more decomposition of $LiPF_6$ [43].

Cation substitution with 1+ and 2+ cations in the octahedral sites (i.e. $Li(Mn_{2-x}M_x)_2O_4$) of the spinel structure was an early identified route to raise the average oxidation state of Mn and reduce Mn dissolution rates. The substitute species, "M", typically include first row transition metal elements (e.g. Cr, Co, Ni) as well as Al and

"extra" Li (beyond 1 atom per formula unit) residing in the tetrahedral sites[114-116]. Combinations of cations have also been reported with much the same effect[117-119]. A consequence of cation substitution is usually a lower initial reversible capacity; however, this shortcoming is negated at some point during cycling, as the capacity of the standard stoichiometry cathode decays at a faster rate and the doped cathode maintains a higher capacity thereafter.

Surface coatings have also been widely employed to reduce capacity fade in $LiMn_2O_4$. In some cases, lithium-conducting phases, such as other cathode materials and lithium-conducting glasses (e.g. $LiCoO_2$ and lithium-boron oxide) with favorable surface properties, can be employed to act as a physical barrier between $LiMn_2O_4$ and the electrolyte[53, 120]. Interestingly, $LiMn_2O_4$ itself has been reported as a coating material to improve the thermal stability of $LiCoO_2$[121, 122]. Other protective coatings for $LiMn_2O_4$ utilize oxides of Al, Zn, Mg, Si and Zr to reportedly sequester acidic species in the electrolyte and thus inhibit Mn dissolution[123-125]. Like with the cation substituted electrodes, capacity retention is improved and can be correlated with a decreased Mn content in the electrolyte after cycling. One work using this approach suggested that surface coatings play a role in structurally reinforcing the underlying spinel to prevent microstrain during cycling at elevated temperatures (elevated temperatures are used to accelerate the Mn dissolution process)[126]. The influence of the protective coating morphology has also been investigated. Several groups have reported that high surface area coatings consisting of agglomerated nanoparticles provide superior protection compared to dense coatings[40, 55, 123].

Very recently a new technique has been used to pursue the goal of long-lived cathode materials. In 2010, Jung, et al. (U.C. Boulder and the National Renewable Energy Laboratory) reported that coatings of Al_2O_3 of less than one nanometer in thickness provided a significant improvement in capacity retention for a $LiCoO_2$ cathode [127]. The work of the X. Sun and Y. Wang groups have been actively exploring this area and demonstrated similar results with ALD using a variety of coating and cathode materials [128-131]. Unlike previous sol-gel based, colloidal solution based, or conventional solid-state reaction processes, which produce porous electrode coatings consisting of nanoparticles, these ALD coatings of Al_2O_3 were assumed to be fully dense and to behave as both electronic and ionic insulators [132]. Thin oxide coatings produced by ALD have also been investigated for anode coatings and solid-state electrolyte materials [133].

In this chapter the electrodes produced by coating $LiMn_2O_4$ onto carbon fibers in the previous chapter are utilized as a platform for further study by modifying the surface of these electrodes with oxide coatings. This is in contrast to previous approaches in which either discrete powders or tape-cast electrodes were coated by ALD, wherein maintaining an uninterrupted interface was found to be critical to good electrode performance [131, 134]. Using conventional electrochemical testing techniques along with *ex situ* structural and surface chemistry characterization, the influence of ALD coatings on morphology, rate capability and capacity retention was investigated.

5.2 Experimental Methods

$LiMn_2O_4$ on carbon fiber electrodes were produced according to the two-step hydrothermal process described in Chapter 4. Aluminum-oxide coatings were applied by a Savannah 100 (Ultratech, MA, USA) atomic layer deposition system. Each ALD cycle

was deposited at 175 °C with a pulse time of 0.1 s for the trimethylaluminum (TMA) precursor and 0.015 s for the water vapor. Pulsing of each solution was followed by 15 s of pause under vacuum to completely remove any remainder precursor. To ensure thermal equilibrium, the chamber was held under vacuum for a minimum of 10 minutes before deposition. During deposition, the N_2 (Ultra High Purity, AirGas, PA, USA) carrier gas was set to flow at 20 SCCM.

Half-cells of the ALD coated and uncoated LMO@CFP electrodes were assembled in an Ar filled glove box using Swagelok-type cell hardware after drying electrode discs in a vacuum oven overnight. The counter and pseudo-reference electrode was Li metal and the electrolyte was 1 M $LiPF_6$ in 1:1 EC:DMC (Novolyte) soaked into a glass-fiber separator (Whatman GF/D). After assembly, cells were cycled using an Arbin BT2000 battery cycler at room temperature with rates of C/10 to 10C (1C = 148 mA/g $LiMn_2O_4$). Electrochemical Impedance Spectroscopy (EIS) was also measured after various numbers of total cycles using a Solartron SI 1287 Electrochemical Interface and Solartron SI 1255 Frequency Response Analyzer. For the equivalent circuit modeling, Scriber Associates "ZView" software was used. Circuit elements were added sequentially and optimized with constraints before the entire equivalent circuit was left free to vary to ensure a reasonable fit.

Thermogravimetric analysis was performed to confirm the measurements made with the lab balance using a TA Instruments Q600 SDT with air (Airgas, Ultra Zero purity) as the purge gas. After taring the alumina pans, samples of 10 mg or less were loaded and allowed to rest at room temperature for at least 1 h under 100 mL/min of purge gas until the mass loss due to suspected water evaporation stabilized. Once the

sample mass stabilized, the sample was heated at 10 °C/min to 900 °C to oxidize the CFP. The remaining mass is then presumed to be the oxide coating.

Like with the previous chapter, the observed charge and discharge capacities in mAh were normalized using the assumed mass loading of $LiMn_2O_4$. This value was obtained by multiplying the measured electrode mass by the weight percent increase calculated from the hydrothermal experiment-typically about 30 wt%. However, while the uncoated and 10 ALD layer coated electrodes had very similar calculated oxide mass loadings (6.58 mg_{oxide}/cm^2 and 6.56 mg_{oxide}/cm^2) respectively, the 50 ALD layer coated electrode was measured at 6.89 mg_{oxide}/cm^2, representing an increased mass for the 50 ALD layer electrode relative to the uncoated and 10 ALD layer electrodes of about 5% (Figure 5.1). Including the mass of the ALD layer would artificially decrease the calculated specific capacity for the 50 ALD layer coated electrode. To compensate for this the "extra" mass added by the ALD process for the 50 ALD layer coated electrodes (0.33 mg/cm^2) was removed when calculating the specific capacity. As expected, 20 layers of ALD coating (not tested further) produced an intermediate mass relative to the 10 and 50 ALD layer coatings.

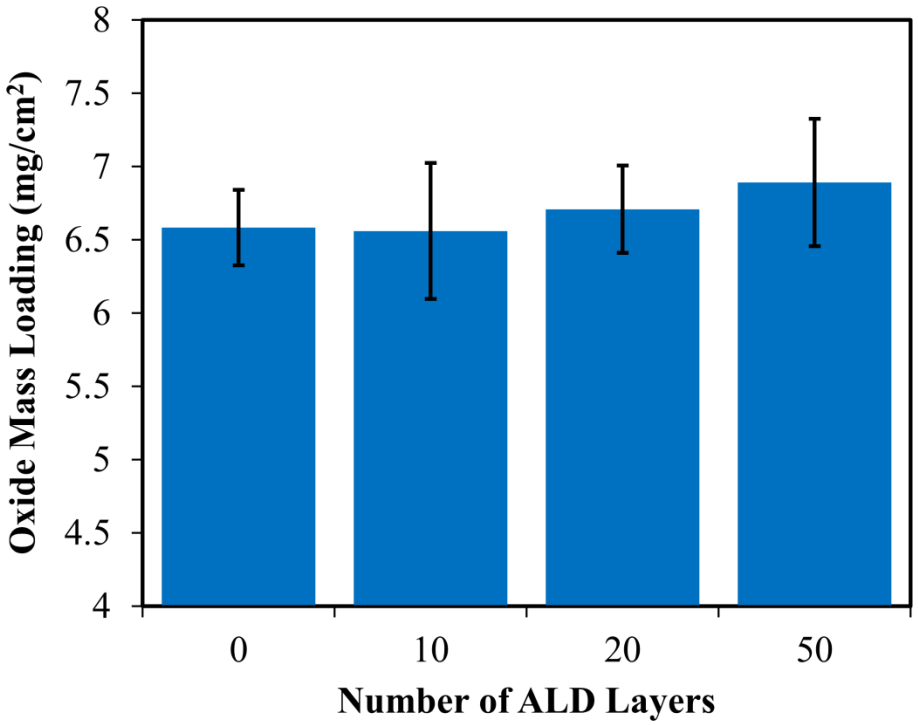

Figure 5.1 Mass variations for ALD coated electrodes. Each electrode area was ~1 cm^2. Error bars indicate the standard deviation as obtained from at least 5 electrodes.

Electrodes were further characterized *ex situ* before and after cycling via powder x-ray diffraction (XRD), scanning electron microscopy (SEM, LEO 1530 thermally-assisted field emission SEM), energy dispersive x-ray spectroscopy (EDS, Oxford Instruments thin window silicon drift detector), and x-ray photoelectron spectroscopy (XPS, Thermo Scientific K-alpha), and transmission electron microscopy (TEM, FEI Technai F30). Powder x-ray diffraction was conducted using Beamline X7B at the National Synchrotron Light Source at Brookhaven National Lab with an x-ray wavelength of 0.3196 Å. XPS analysis utilized a low-energy electron flood gun to reduce charging effects, and binding energies were corrected using the C 1s peak position at 284.8 eV. XPS peaks were fitted using the software XPSPEAK 4.1. Backgrounds were fitted using a Shirley type background function and a mixed Gaussian-Lorentzian peak

shape was used. For the Al 2p photoemission in uncycled samples, no limitations were placed on the % Gaussian, full width at half maximum (FWHM), or peak position. For Al 2p after cycling, a second peak was added with the constraints that it had the same FWHM and % Gaussian as the first peak. Peak fitting for the Mn 2p photoelectron relied on the use of a reference sample of store bought $LiMn_2O_4$ (Sigma Aldrich, 99.9% pure). $LiMn_2O_4$ powder was cold pressed into a pellet approximately 1 mm in thickness and held in place with a copper clip. For the reference sample, the relative intensities and %Gaussian of the two Mn $2p_{3/2}$ sub-peaks were fixed to each other while the FWHM was allowed to vary within the range of 2.4-2.6 eV. The asymmetry parameters in the XPS peak software were manipulated manually until a good fit was obtained. As a "check" of the Mn $2p_{3/2}$ fit for the reference sample, Mn $2p_{1/2}$ sub peaks were added with a separate background region and identical FWHM, % Gaussian, and asymmetry parameters but with peak areas fixed at 50% of their corresponding Mn $2p_{3/2}$ peaks. All of the line shape values obtained from the reference were fixed for the experimental samples in this study, while peak position and relative area were free to vary.

5.3 Influence of ALD coatings on $LiMn_2O_4$ Electrodes

5.3.1 Morphology of ALD coated electrodes

The morphologies of as-prepared LMO@CFP and ALD coated LMO@CFP were quite similar as shown in Figure 5.2. All samples consisted of discrete crystallites in the size range of 100-500 nm and no changes in surface features were apparent (at the indicated scale in Figure 5.2) as a function of the Al_2O_3 coating thickness. When analyzed using EDS during SEM analysis, as-prepared Al_2O_3 coated electrodes exhibited

an increase in Al and O content with an increase in the number of ALD cycles. Likewise, the average areal mass loading of the electrodes (mg_{oxide}/cm^2) increased slightly with increasing ALD cycles, shown in Figure 5.1.

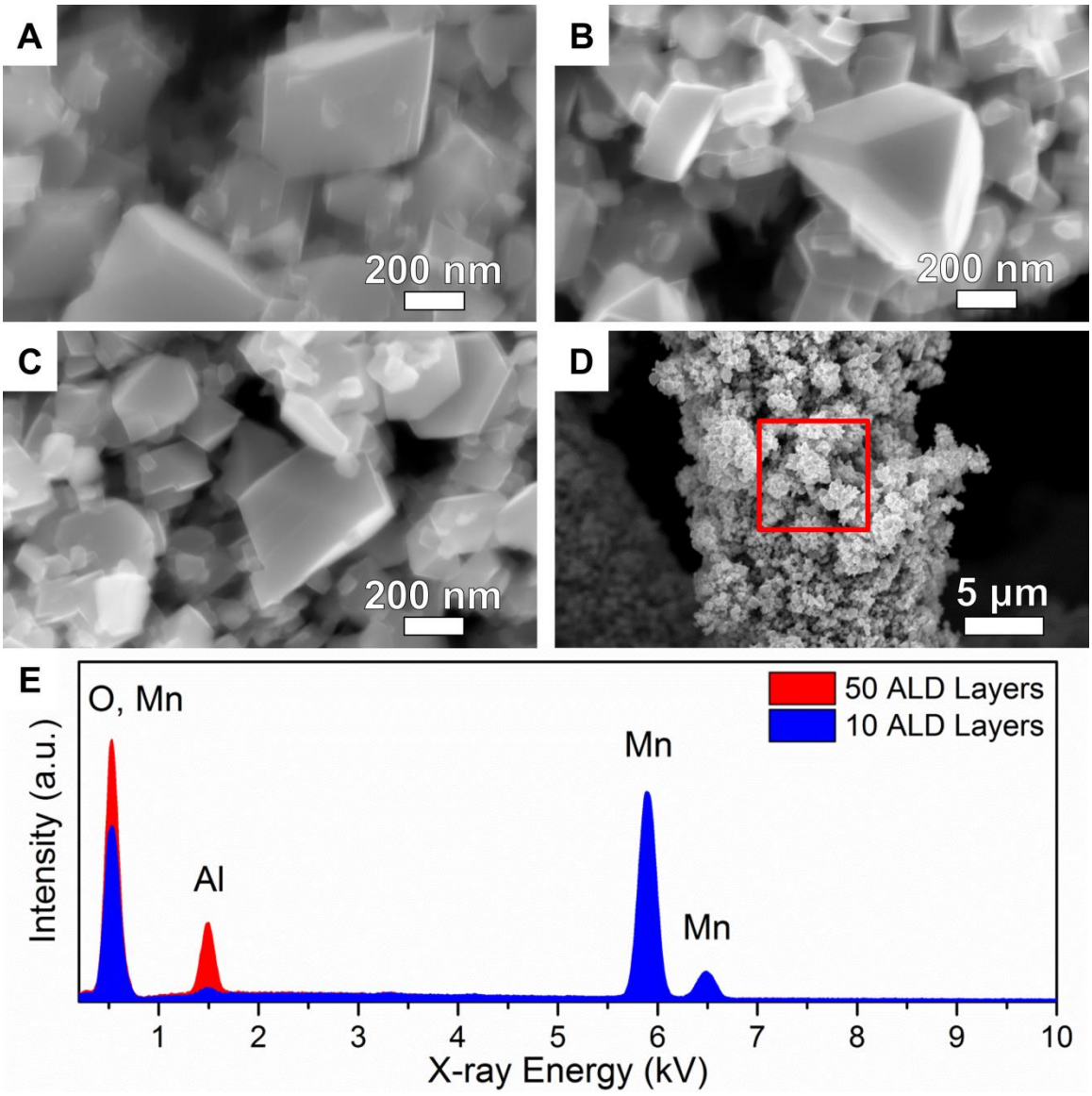

Figure 5.2 SEM images of $LiMn_2O_4$ as grown on CFP (A) and Al_2O_3-coated $LiMn_2O_4$ derived from 10 (B) and 50 (C) ALD cycles. A representative area of collection for EDS is shown in (D). EDS spectrum (E) collected at 20 kV accelerating voltage shows higher Al and O content with increasing ALD coating thickness.

TGA/DSC was used to verify the mass increase due to the ALD coating shown in Figure 5.1, and to determine if the ALD coating had any influence on the thermal decomposition of the $LiMn_2O_4$ on CFP composite. Figure 5.3 shows that the relative mass loadings for the ALD coated electrodes are consistent with the measurements made on complete electrodes, reporting an approximately 5 wt% increase for the thickest (50 layer) ALD coating. Similar to the bare CFP TGA/DSC results presented in Figure 4.4, two exothermic peaks are observed coincident with sample mass loss. For all of the samples containing $LiMn_2O_4$, the first exothermic peak occurs at a significantly lower temperature than for the bare CFP (402 °C with $LiMn_2O_4$ vs 495 °C without). $LiMn_2O_4$ has been previously reported to catalyze the decomposition of carbon when heated in an oxidizing atmosphere[135]. Meanwhile, the second exothermic peak is broadened and the apparent maximum heat flow shifts to higher temperatures with increasing coating thickness, suggesting that the alumina coating possibly impedes this reaction.

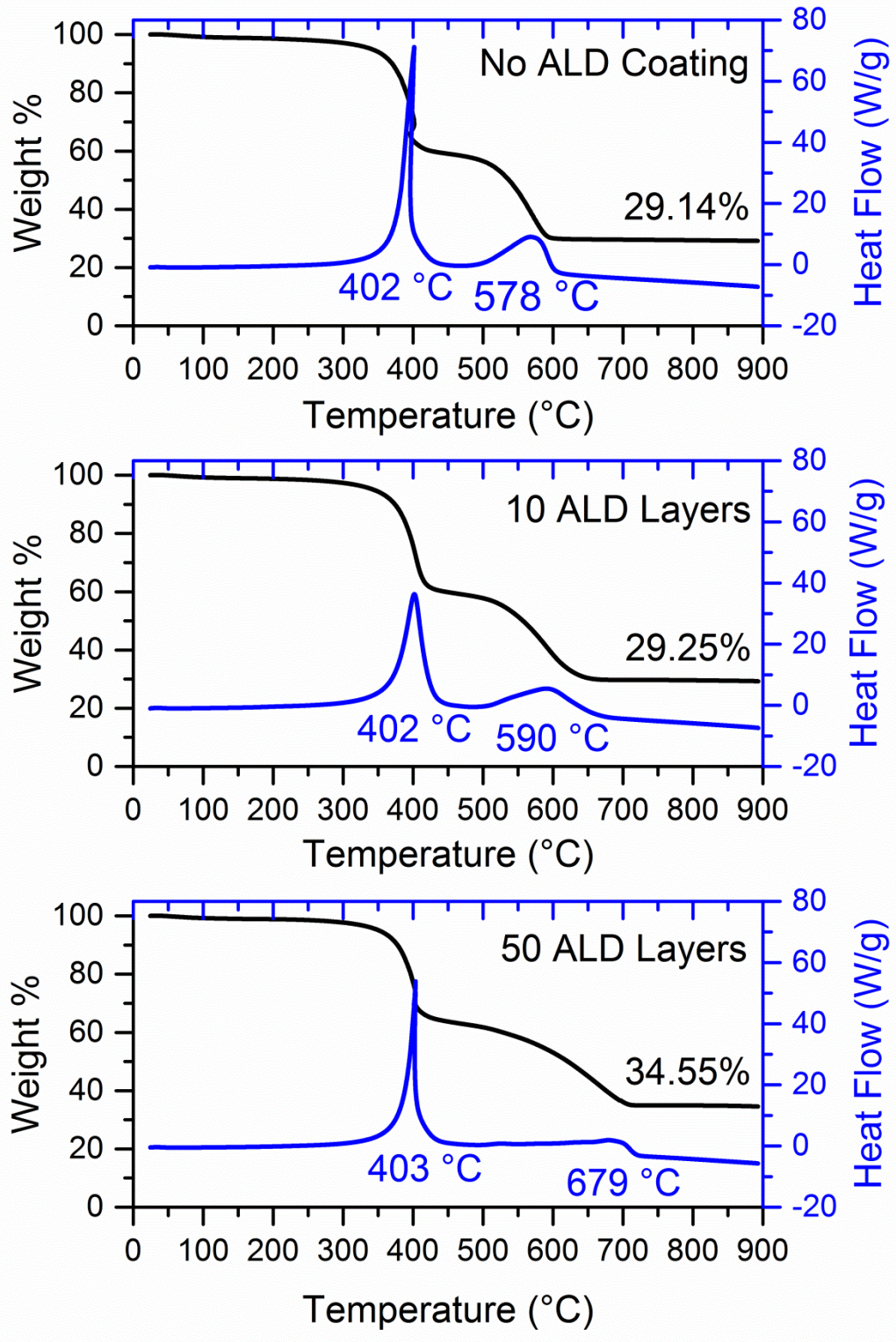

Figure 5.3 TGA/DSC for ALD coated $LiMn_2O_4$ on CFP electrodes.

Analysis by TEM revealed a clear delineation between the crystalline $LiMn_2O_4$ particle and the amorphous ALD coating. A 50 ALD layer coating of approximately 5.1 nm thickness (Figure 5.4) was consistent with an assumed ALD growth rate of 0.9-1.1 Å per layer for Al_2O_3 on Si using a TMA precursor. An EDS line-scan conducted during TEM analysis shows that the signal intensity for Al began to increase slightly before the Mn signal, and then remained relatively constant. The Mn signal continued to increase along the distance of the line scan as the $LiMn_2O_4$ particle became thicker. A TEM image of the 10 ALD layer coated sample is also shown in Figure 5.4, however the 10 ALD layer Al_2O_3 coating was too thin for chemical analyses by EDS.

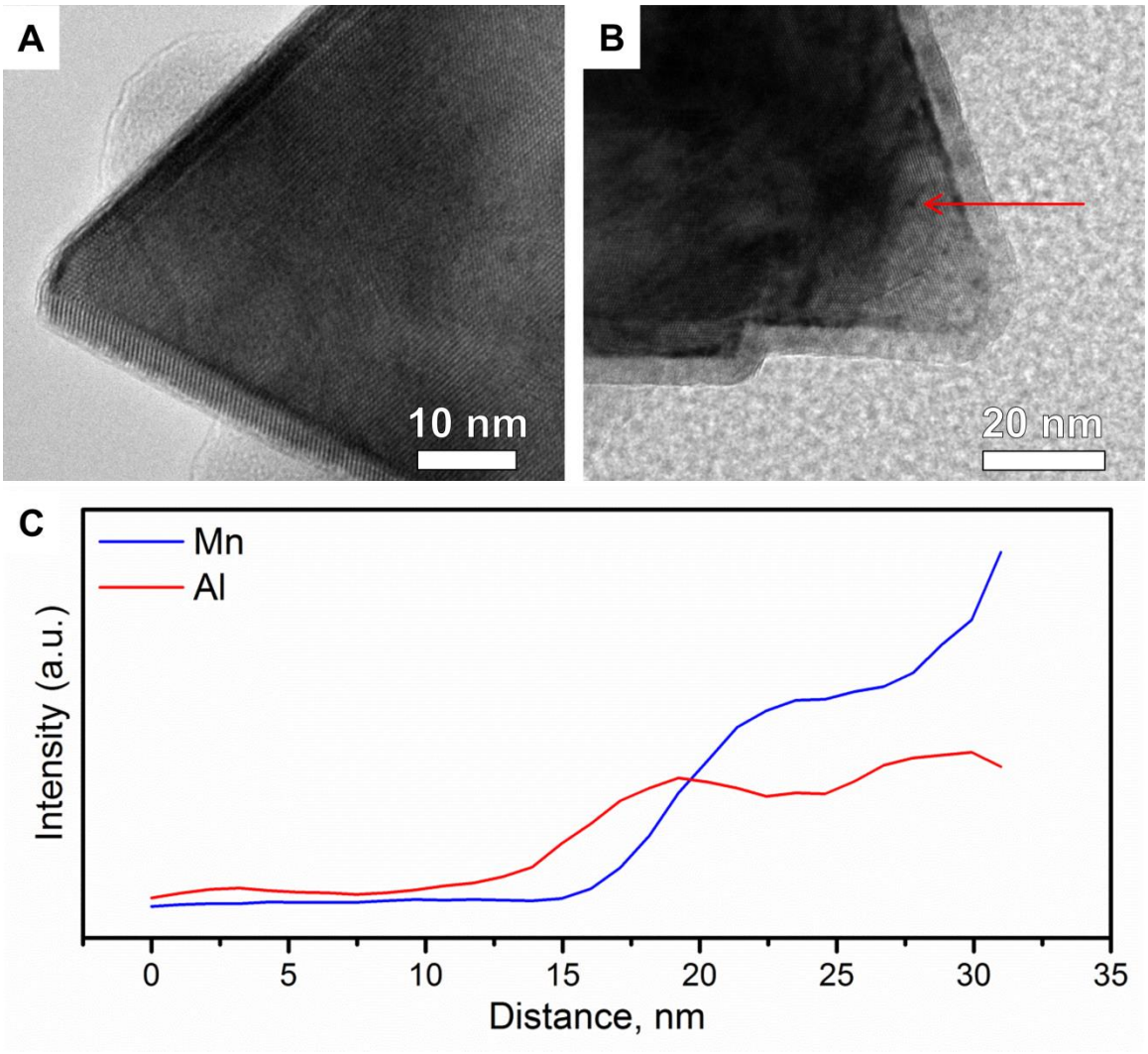

Figure 5.4 High-resolution TEM image of a 10 ALD cycle coated (A) and 50 ALD cycle coated $LiMn_2O_4$ particle (B). Arrow in (B) indicates the direction of the EDS line-scan shown in (C) conducted for the 50 ALD cycle coated electrode. The EDS signal collected for the first ~ 10 nm is expected to come exclusively from the underlying carbon in the TEM grid.

5.3.2 Electrochemical cycling of ALD coated electrodes

The observed capacities of the LMO@CFP electrodes were normalized by the mass of the $LiMn_2O_4$ content in each electrode, which was about 30 wt% of the total electrode mass as shown in the previous chapter. For the 50 ALD layer coated electrodes, the mass contribution from the ALD coatings (Figure 5.1) was removed when calculating

the normalized capacity, while the mass difference for the 10 ALD layer electrodes was negligible compared to the uncoated electrode. Despite these corrections, it is apparent in Figure 5.5 that the discharge capacity of the 50 ALD layer coated electrodes was significantly lower than for the 10 ALD layer coated and uncoated electrodes, even when cycled at a rate of C/10. At the lowest rate tested the uncoated and 10 ALD layer coated electrodes exhibited similar capacities, whereas for rates up to 1C, the 10 ALD layer coated electrode exhibited higher capacity compared to the uncoated electrode. This was similar to the observation reported by Walz *et al*. who found that an $LiMn_2O_4$ electrode coated with TiO_2 nanoparticles had a higher rate capability than an uncoated electrode, which was attributed to the coating resulting in a more uniform current density[40].

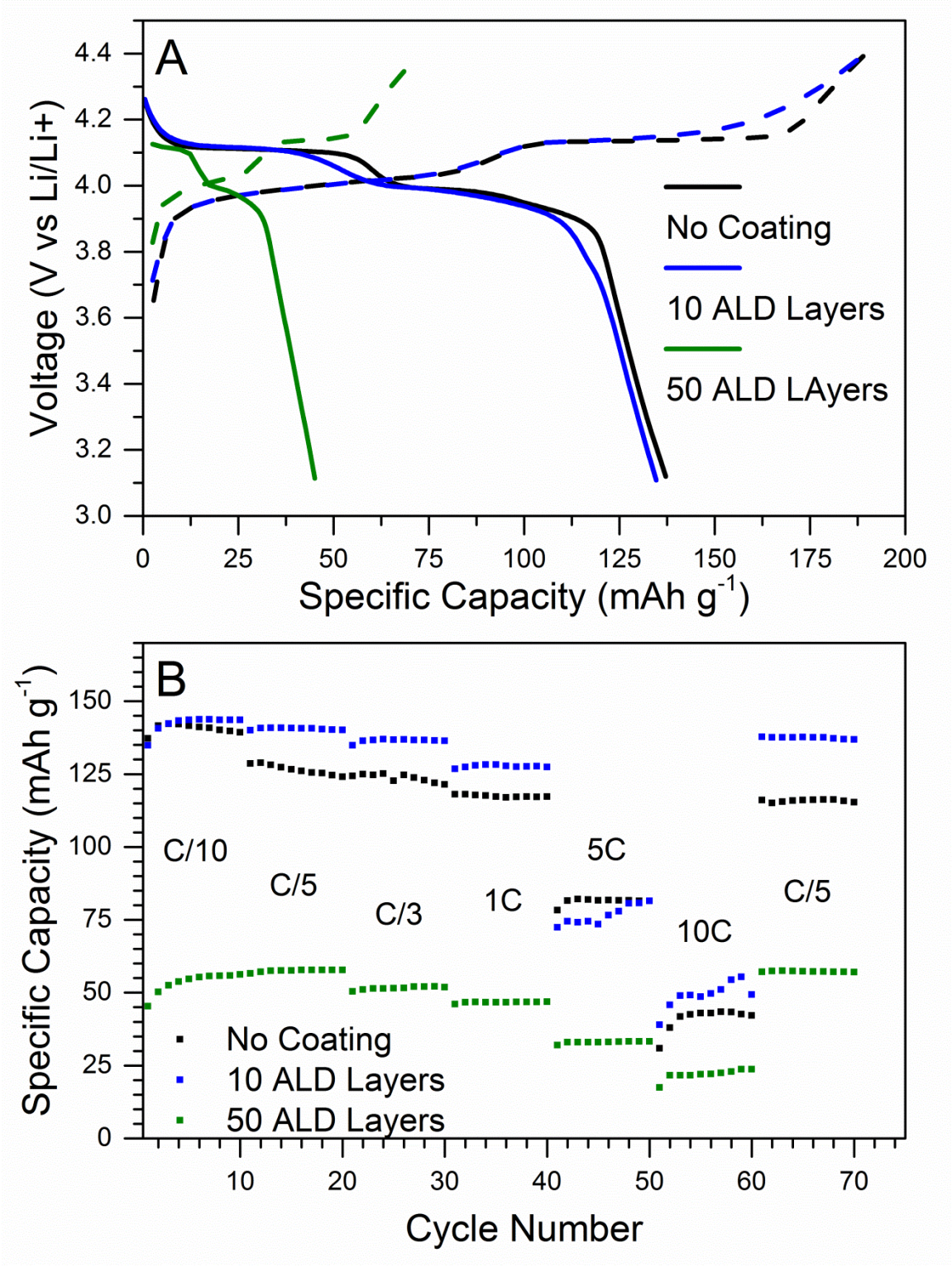

Figure 5.5 First cycle charge (dashed lines) and discharge (solid lines) profile at a C/10 rate (A) and rate capability testing (B) for $LiMn_2O_4$ coated CFP with and without ALD coatings. 1C is defined as 148 mA/g base on the mass of $LiMn_2O_4$ in the electrode.

While the total capacity of the 50 ALD layer coated electrode was severely reduced, the relative rate capability (i.e., the percentage of original capacity maintained at increasing current density) was not similarly influenced. The capacity of the 50 ALD layer electrode actually increased very slightly between the C/10 and C/5 rate regions and exhibited the smallest drop between the 1C and 5C regions, which was consistent with the ALD coating improving the homogeneity of near-surface current density on the coated electrodes. At rates of 5C and 10C the uncoated and 10 ALD layer coated electrodes show roughly comparable capacities. The effect of the coating on improving capacity retention was apparent even during rate capability testing. After returning to a C/5 rate, the 10 and 50 ALD layer electrodes recovered 98.5% and 99.1% of their original C/5 discharge capacity, respectively, compared to 93.5% for the uncoated electrode.

Differential capacity plots for the first and tenth cycles at a C/10 rate (Figure 5.6) show the typical pair of redox peaks expected for $LiMn_2O_4$ during charging and discharging. For the ALD coated electrodes, an increased differential capacity was observed above about 4.2 V vs. Li/Li^+ on the first cycle, which was greatly reduced by the 10^{th} cycle. While all of the electrodes exhibited a larger charge capacity than discharge capacity during the first cycle, it was not clear why only the ALD coated electrodes showed a slight increase of differential capacity in the 4.2-4.4 V vs. Li/Li^+ region during the first charge. One explanation could be that ALD coatings increased the over potential for the initial delithiation of the underlying $LiMn_2O_4$, which would be consistent with the slightly higher oxidation potentials and slightly lower reduction potentials for the ALD coated electrodes on the first cycle compared to the uncoated

electrode. By the 10th cycle, all of the electrodes exhibited redox peaks at 4.01 V and 4.13 V during charging and 4.11 V and 3.99 V during discharging.

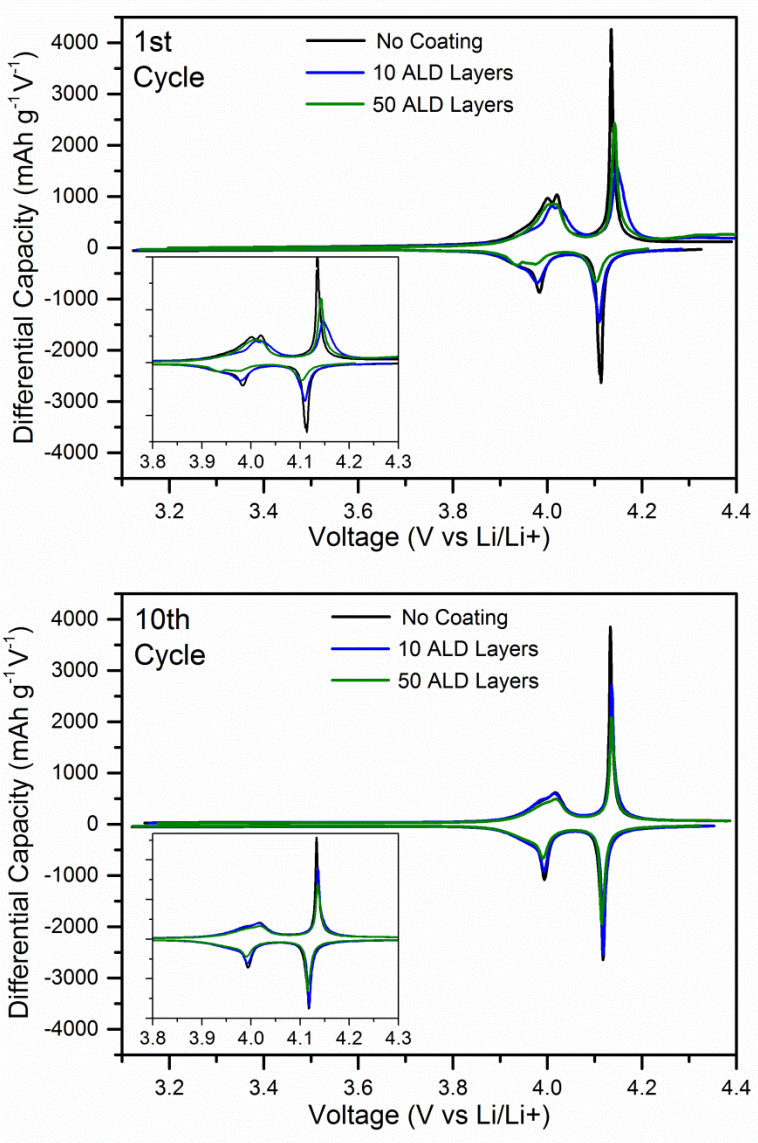

Figure 5.6 Differential capacity plots for the first and tenth cycle at a C/10 rate are shown for both ALD coated and uncoated electrodes. Insets show close up of redox peak region for each associated graph.

The consistency in redox potential observed for the differential capacity plots, in comparison to the inconsistency in observed specific capacity, highlights an unusual

aspect of the ALD coated electrodes. While an increasing thickness of a dense aluminum oxide could be expected to behave as a barrier to ionic conductivity, thus increasing the effective concentration overpotential, a corresponding change in cell voltage is not observed. To study this discrepancy further, cyclic voltammograms were conducted at multiple voltage scan rates on uncoated and ALD coated electrodes. According to the Randles-Sevchick equation (Equation 35), the observed peak current should be related to the square-root of the voltage scan rate for a diffusion controlled reaction. Furthermore, using the peak parameters introduced in the previous chapter some measure of relative electrochemical reversibility can be obtained by studying the redox peak separation and ratio of oxidation and reduction currents.

Figure 5.7 shows that as expected from galvanostatic testing, the specific current observed in cyclic voltammetry testing decreases with increasing thickness of the ALD layer. However, it is also apparent the that greatest specific current observed occurs in the 10 ALD layer coated sample, and further that the change in CV shape with increasing scan rate is most significant for the electrode with no ALD coating at all. Put another way, while the 50 ALD layer has the smallest capacity it seems to have the greatest electrochemical reversibility. Table 5.1 summarizes the values obtained from the CV measurements in Figure 5.7, revealing that ALD coatings dramatically reduce the peak separation between reduction and oxidation peaks and increase the ratio of maximum reducing and oxidizing current. Both of these changes confirm an increase in overall electrochemical reversibility.

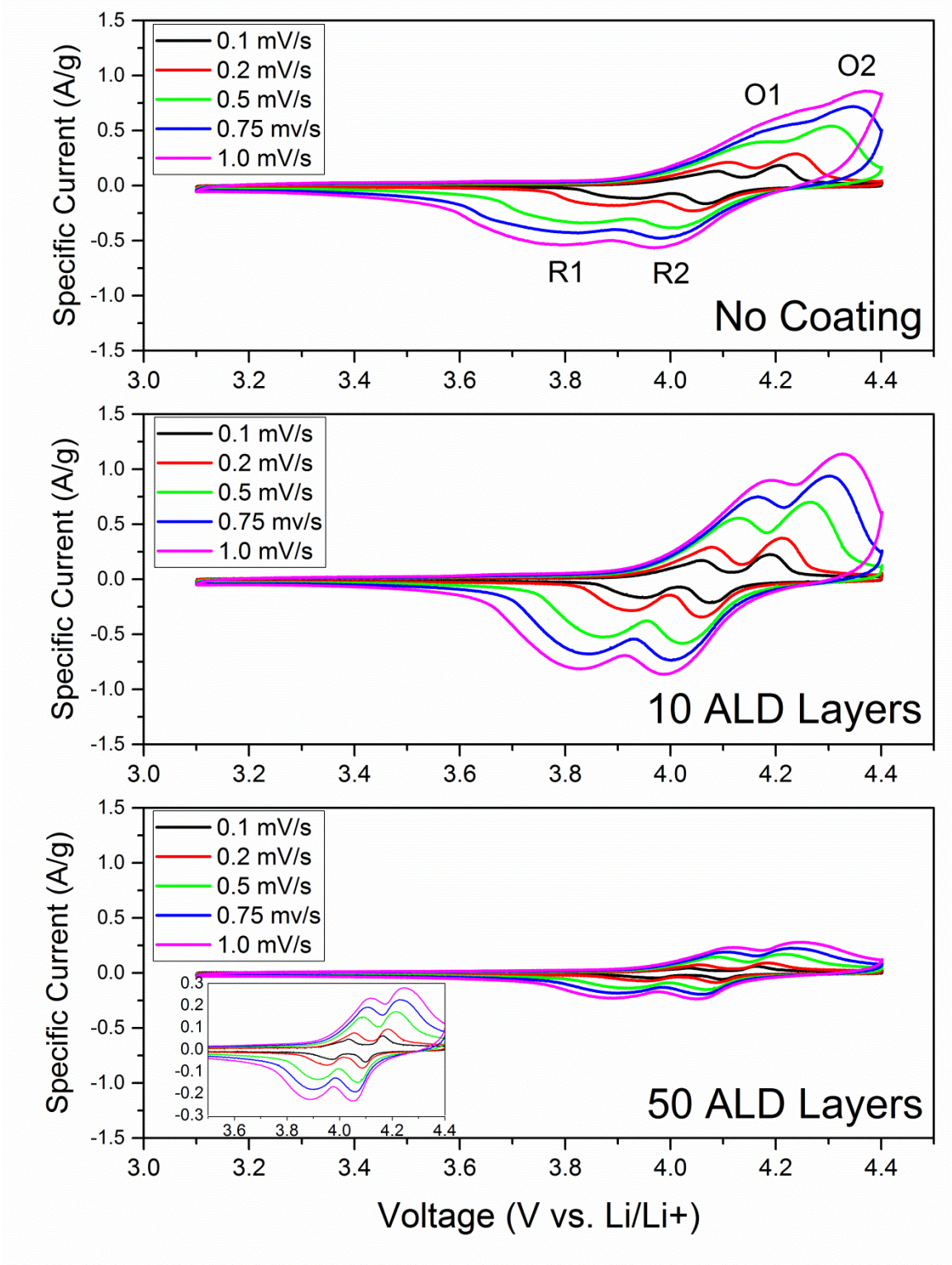

Figure 5.7 Cyclic voltammograms for $LiMn_2O_4$ on carbon fiber electrodes with and without ALD coatings. Current densities are normalized relative to the $LiMn_2O_4$ content in the electrode, which for this case is assumed to be identical regardless of ALD coating.

Table 5.1 Summary of values derived from CV measurements for $LiMn_2O_4$ coated CFP with and without ALD coatings. Note that for scan rates of 0.75 and 1.0 mV/s, O_1 could not be identified for the electrode without ALD coating.

Scan rate (mV/s)	I_{R1}/I_{O1}	I_{R2}/I_{O2}	$\Delta V_{(O1-R1)}$ (mV)	$\Delta V_{(O2-R2)}$ (mV)
No Coating				
0.1	0.89	0.87	149	136
0.2	0.90	0.80	208	185
0.5	0.90	0.72	329	288
0.75	N/A	0.67	N/A	352
1.0	N/A	0.67	N/A	392
10 ALD Layers				
0.1	0.97	0.96	104	106
0.2	0.93	0.90	154	150
0.5	0.91	0.82	256	244
0.75	0.88	0.77	320	300
1.0	0.87	0.76	371	341
50 ALD layers				
0.1	1.05	1.00	68	70
0.2	0.99	0.95	101	98
0.5	0.96	0.86	188	165
0.75	0.97	0.82	201	199
1.0	0.98	0.79	216	233

Peak current values for all of the $LiMn_2O_4$ on CFP electrodes show a linear relationship with the square root of the scan rate (Figure 5.8), and thus are diffusion controlled[136-138] . It is also clear that the peak current observed for the 10 ALD layer electrode is highest among all of the electrodes tested, while the 50 ALD layer electrode is the lowest. Calculation of the average lithium diffusivity (D_{Li}) using the Randles-Sevchik equation yields values in the range of 10^{-11} to 10^{-10} cm^2/s for the $LiMn_2O_4$ coated CFP electrodes, and is summarized in Table 5.2 for the second oxidation and reduction peaks. For these calculations the concentration of lithium in $LiMn_2O_4$ was assumed as a constant 0.238 mol/cm^3, which is derived from the theoretical density of $LiMn_2O_4$ (4.3

g/cm^3). As expected, the 10 ALD layer coated electrodes show the highest average lithium diffusivity at approximately double that observed for the uncoated electrodes, while the 50 ALD layer coated electrodes are an order of magnitude lower. The diffusivity values shown in Table 5.2 do not reflect changes in the stoichiometry in $LiMn_2O_4$ which has been reported to influence diffusivity. However, the values found in this study are consistent with previous reports of lithium diffusivity in $LiMn_2O_4$ as measured by CV and other techniques[136-139].

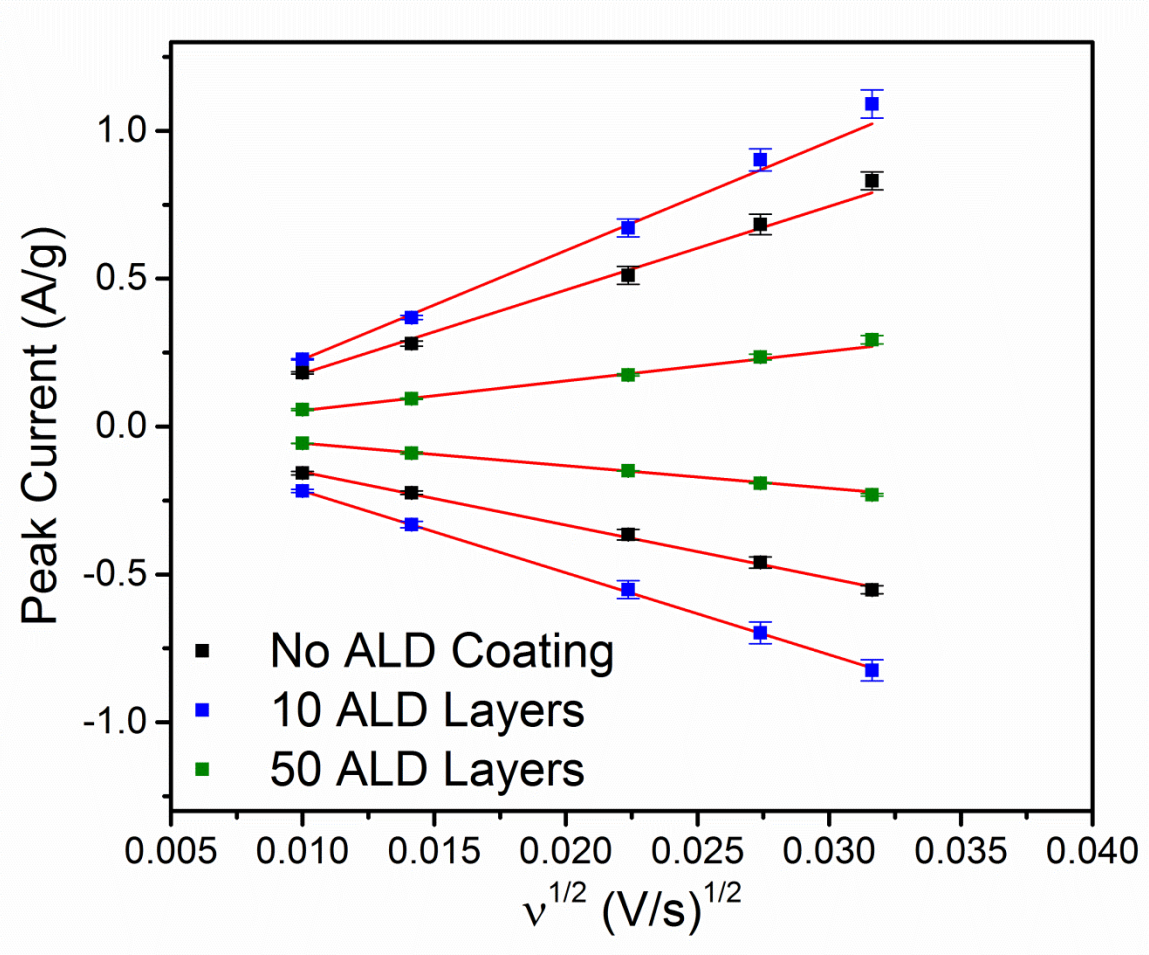

Figure 5.8 Peak current vs. square root of scan rate for $LiMn_2O_4$ on CFP electrodes with and without ALD coatings.

Table 5.2 Calculated values of lithium diffusivity for $LiMn_2O_4$ on CFP electrodes derived from the second oxidation and reduction peaks observed by CV.

Sample	D_{Li}, O_2 (cm^2/s)	D_{Li}, R_2 (cm^2/s)
No ALD coating	$2.09\text{-}4.36 \times 10^{-10}$	$1.57\text{-}1.93 \times 10^{-10}$
10 ALD Layers	$3.28\text{-}7.52 \times 10^{-10}$	$2.99\text{-}4.30 \times 10^{-10}$
50 ALD Layers	$2.06\text{-}5.44 \times 10^{-11}$	$2.02\text{-}3.37 \times 10^{-11}$

Extended cycling at room temperature for the uncoated and 10 ALD layer electrodes revealed that, after 500 cycles (Figure 5.9) at a 1C rate, the 10 ALD layer coated electrode retained over 2.5 times the roughly identical starting capacity compared to the uncoated electrode. For the 50 ALD layer coated electrodes, only 300 cycles were conducted at a rate of 1C, whereupon a capacity retention comparable to that of the 10 ALD layer coated electrodes was observed. A small discrepancy was apparent when comparing the 1C rate capacity for the uncoated electrodes in Figures 5.5B and 5.9. For the extended cycling tests, electrodes were cycled first for one C/10 formation cycle followed by extended cycling at 1C. During this testing, both the 10 ALD layer coated and uncoated electrodes had starting 1C capacities above 130 mAh/g. Meanwhile, the 1C capacity for both electrodes during the rate capability tests was about 128 mAh/g for the 10 ALD layer coated electrode and only 117 mAh/g for the uncoated electrode. However, when considering the 30^{th} cycle capacity for the extended cycling test, which should be equivalent to the first 1C cycle observed for the multi rate tests, the capacities of the uncoated and 10 ALD layer coated electrodes were 121 mAh/g and 127 mAh/g, respectively, which were consistent with the observed 1C capacities in Figure 5.5B.

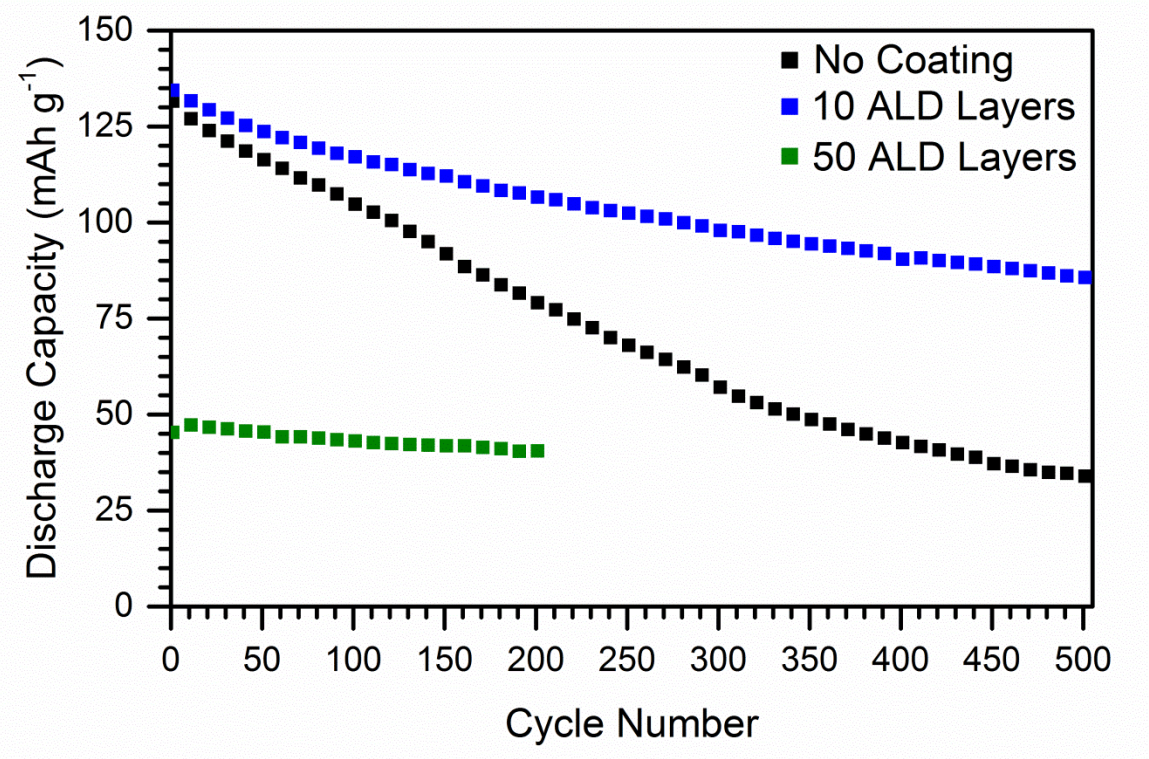

Figure 5.9 Extended cycling conducted at room temperature and a rate of 1C for ALD coated and uncoated samples.

5.3.3 Evolution of structure, impedance and surface chemistry

To better understand the mechanism by which the ALD Al_2O_3 coating improved the capacity retention and apparent lithium diffusivity of $LiMn_2O_4$ electrodes, synchrotron X-ray diffraction analysis was used to characterize the structure of coated and uncoated electrodes before and after cycling. Rietveld refinements of the XRD patterns (Figure 5.10) yielded a virtually identical lattice constant for uncycled electrodes with and without ALD coating. For the uncycled electrodes, the lattice constant was slightly less than the 8.247 Å value reported for stoichiometric, bulk $LiMn_2O_4$ (JCPDS No. 35-0782), which was consistent with a Li-rich composition reported for other hydrothermally produced lithium-manganese spinel oxides[91].

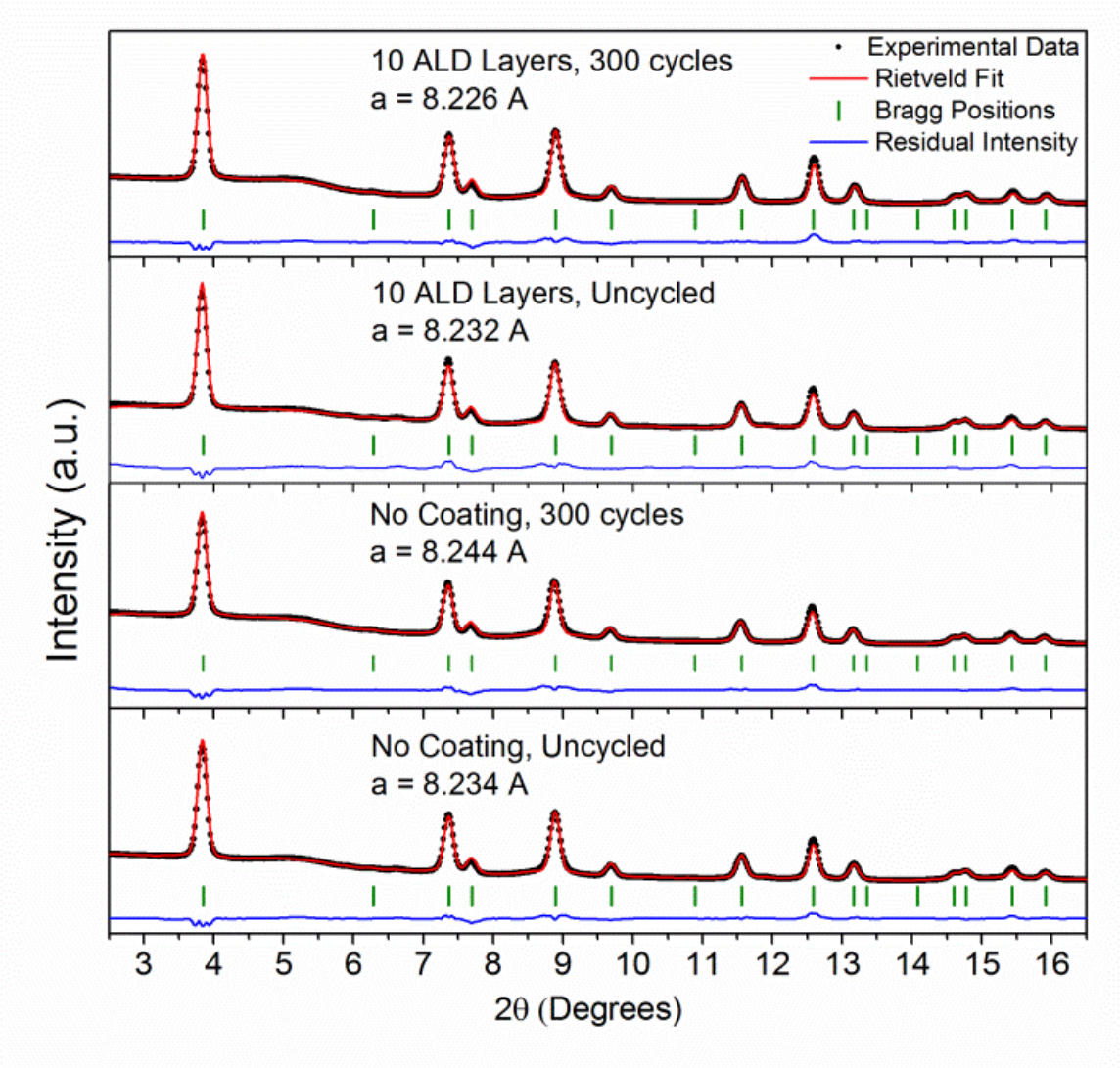

Figure 5.10 Synchrotron XRD patterns collected using 0.3196 Å X-rays with Rietveld refinement results. All peaks identified by green vertical lines are assigned to $LiMn_2O_4$ with a lattice spacing of 8.247 Å.

Three small impurity peaks (Figure 5.11) were also apparent in the pre-cycled electrodes, which appear at the same 2θ locations for both the ALD coated and uncoated electrodes, suggesting that these peaks were not related to the ALD process or the Al_2O_3 coating. These peaks were not resolvable using the laboratory scale powder XRD utilized in Chapter 4, though are likely still present in several samples. After cycling, these impurity peaks disappeared while the peaks associated with the spinel phase remained

essentially unchanged in both position and relative peak intensity. The phase associated with the impurity peaks could possibly be another manganese oxide which was either chemically or electrochemically consumed during cycling, which is consistent with the observation of an increased charge capacity and slightly shifted potentials for the first charge and discharge cycle shown in Figure 5.5. Only a small change in lattice parameter in the main spinel phase was observed after cycling. For the uncoated electrode, a slight dilation towards the standard lattice parameter was observed, while for the 10 ALD cycle coated electrode the lattice parameter is constricted by a similar amount. In both cases, the change in lattice parameter was less than 0.5% of the starting value, which could perhaps be explained by a slight variation in sample positioning relative to the x-ray detector. An amorphous (broad hump) region between 4-6° 2θ observed for all electrodes was attributed to the carbon fiber current collector.

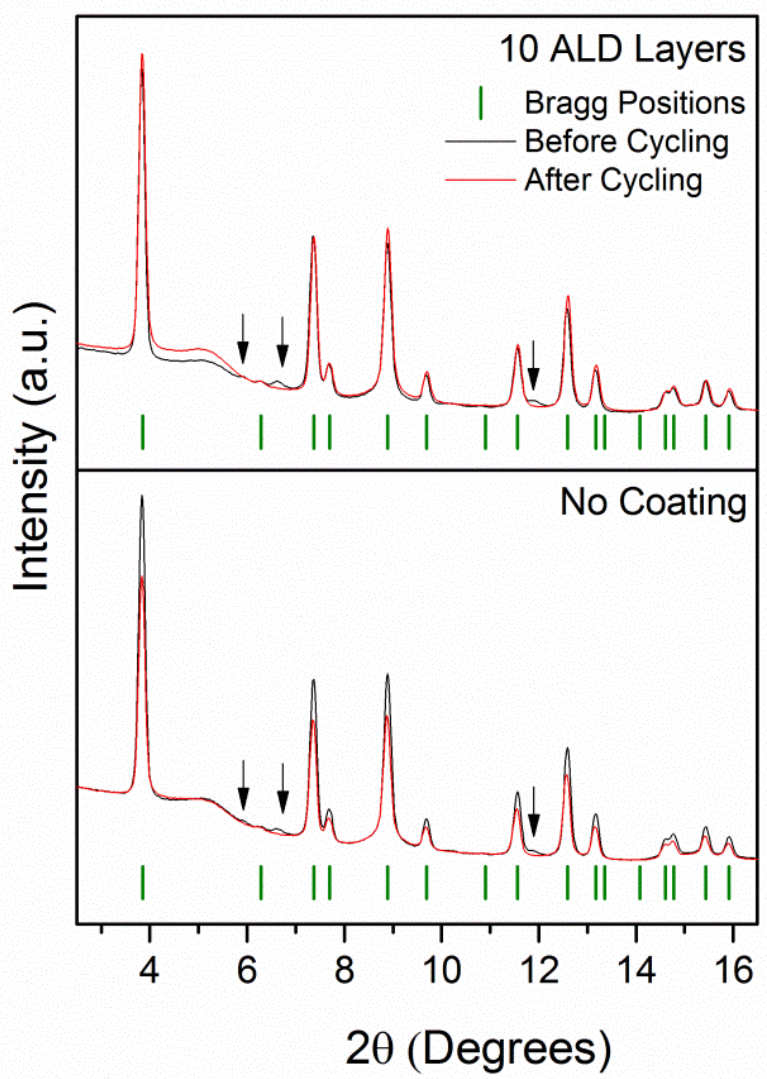

Figure 5.11 Overlay of synchrotron XRD patterns for 10 ALD layer coated and uncoated samples before and after electrochemical cycling. Observed impurity peaks are identified with black arrows, and appear in both coated and uncoated samples.

SEM images of the $LiMn_2O_4$ particles in ALD coated and uncoated electrodes after electrochemical cycling are shown in Figure 5.12, and appear to have a slightly rougher morphology and decreased image quality than the uncycled electrodes. Both of these observations could be attributed to the formation of organic phases from electrolyte decomposition. Meanwhile, no obvious pitting, cracking or particulate pulverization is observed.

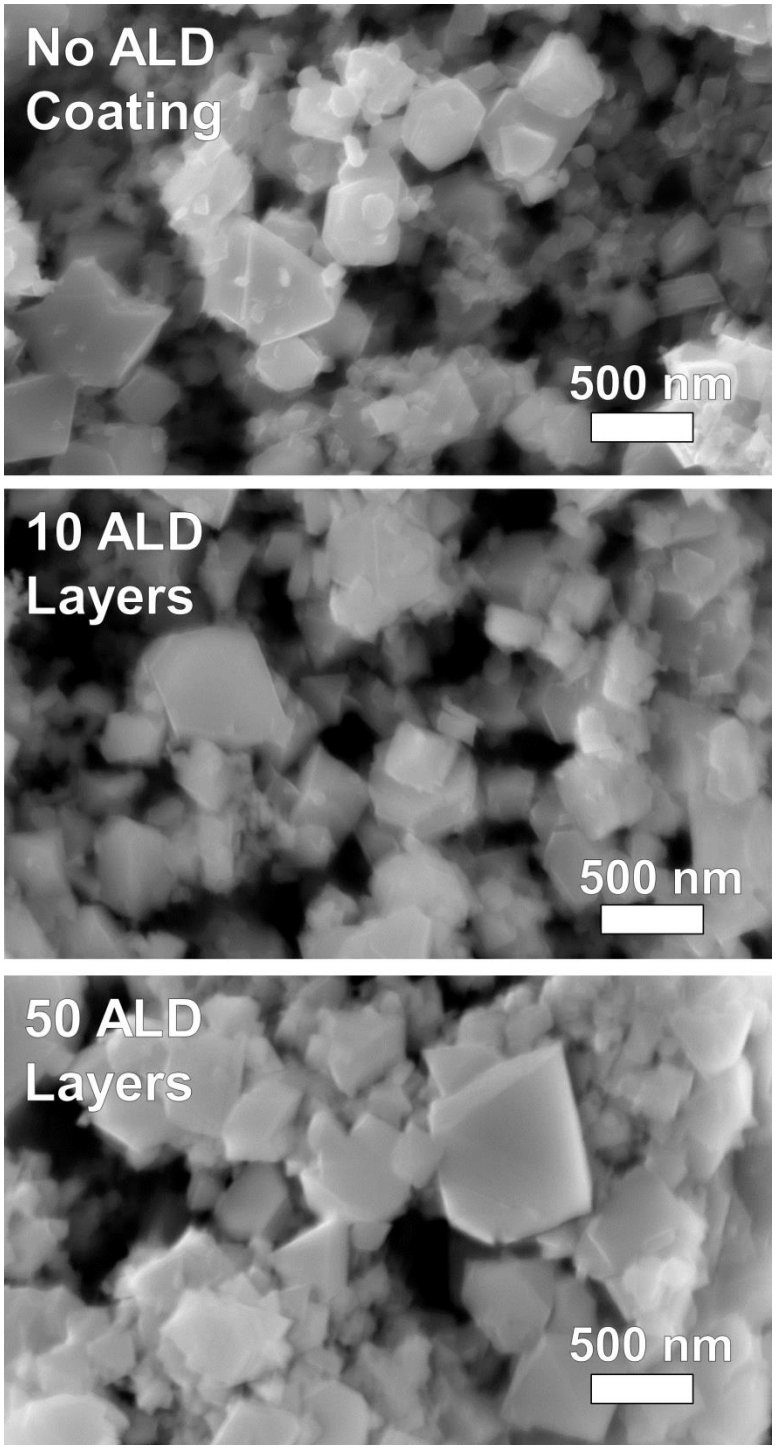

Figure 5.12 SEM images of unmodified and ALD coated $LiMn_2O_4$ on CFP electrodes after 300 charge and discharge cycles at a 1C rate. Samples were rinsed with dimethyl carbonate and allowed to dry in an Ar filled glovebox prior to inspection by electron microscopy.

EIS analysis was conducted for cells in the discharged state (3.1 V vs. Li/Li+) after various numbers of cycles. Cycling was conducted at a rate of 1C. However, before each impedance spectrum was collected, a single cycle at a C/10 rate was conducted to create a uniform reaction rate and open-cell potential. The equivalent circuit model used for the fitting procedure, as well as Nyquist plots for the observed and fitted impedance spectrum, are shown in Figure 5.13.

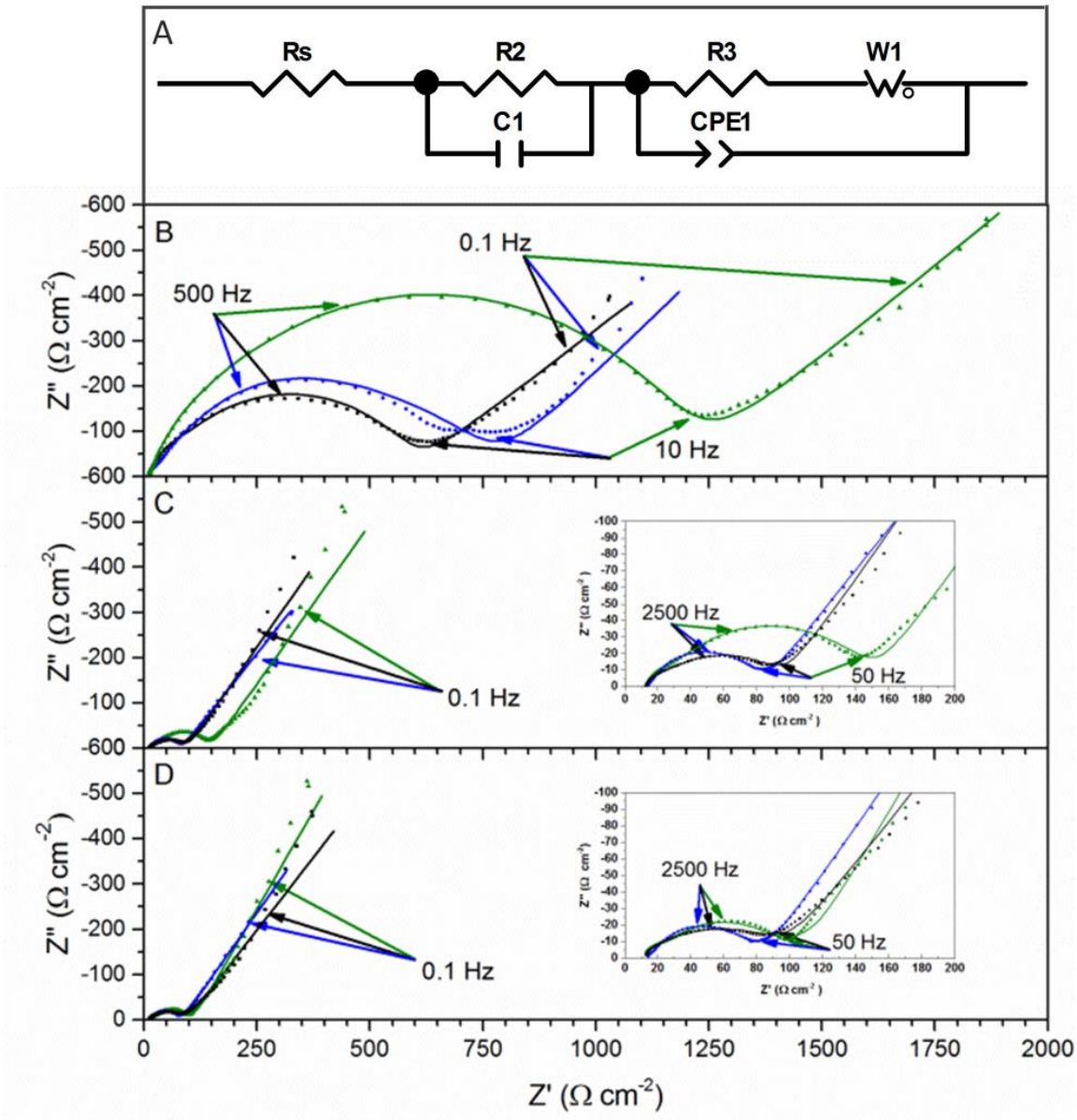

Figure 5.13 Equivalent circuit model (A) and fitting results for representative EIS spectra of uncoated (black squares), 10 ALD layer coated (blue circles), and 50 ALD cycle coated electrodes (green triangles) after the 1st (B), 50th (C) and 100th (D) cycles. All spectra shown were collected for half cells discharged to 3.1 V vs. Li/Li+. Color coded arrows (black for uncoated electrode, blue for 10 ALD cycle coated and green for 50 ALD cycle coated) are used to identify points corresponding to individual frequencies and to facilitate comparison between the electrodes.

The fitting results are summarized in Table 5.3 with values presented as an average of three identical electrodes of each type. Two semi-circles offset from the origin along the X-axis and a sloped linear region was observed for each impedance spectrum.

The highest frequency semi-circle was fitted using a circuit model consisting of a resistor and capacitor in parallel (R_2 and C_1), while the lower frequency semi-circle was depressed and fitted with a model of a resistor and constant-phase element in parallel (R_3 and CPE_1). The lowest frequency region is fitted with an open-circuit Warburg element (W1). As has often been previously reported, the x-axis offset was treated as the solution resistance (R_s), which contained contributions from both the electrolyte conductivity and the contact resistance between the electrode and current-collector. For the semi-circle regions, the higher-frequency R_2 and C_1 were attributed to the SEI or sometimes "surface film", the lower-frequency R_3 and CPE_1 were attributed to the charge-transfer resistance and double-layer capacitance, respectively, while the sloped linear region was associated with solid-state lithium diffusion[140-143]. Impedance analyses indicated that the two semi-circles have distinct time constants, which were identified by the positions of the marked frequencies in Figure 5.13. However, the half-cell measurements did not provide enough information to unambiguously confirm each of the proposed circuit elements suggested in the literature. Instead, further discussion will only consider the solution resistance (R_s) and polarization resistance (R_p) defined as the sum of the R_2 and R_3 values.

The general trend shows that the ALD coating had minimal influence on the solution resistance R_s for all samples and for all of the number of cycles. A large drop in R_p was observed between the first and 50^{th} cycles, which was perhaps due to the removal of the unidentified phase observed in the pre-cycled electrode by XRD analysis or due to the influence of a native passivation layer on the Li anode. Comparatively small changes in R_p were observed between the 50^{th} and 100^{th} cycles. After 50 cycles, the 10 ALD layer coated electrodes exhibited the smallest value in R_p, which was slightly below the value

observed for the uncoated electrode. The average R_p value for the 50 ALD layer coated electrodes was more than twice the average value for the 10 ALD layer coated electrodes, which was consistent with the lower capacity observed in Figure 5.5.

Table 5.3 Summary of EIS fitting results, where RΩ and Rp are presented as average (AVG) values of three identical cells along with standard deviations (STDEV).

Sample	R_s (Ω cm^{-2})		R_p (Ω cm^{-2})	
After 1st Cycle	**AVG**	**STDEV**	**AVG**	**STDEV**
No Coating	8.1	1.3	637.3	60.9
10 ALD Layers	10.5	2.2	520.5	180.4
50 ALD Layers	9.1	0.3	653.2	384.9
After 50th Cycle				
No Coating	10.8	1.2	86.8	30.1
10 ALD Layers	14.5	0.5	73.9	11.3
50 ALD Layers	12.5	0.7	295.0	235.3
After 100th Cycle				
No Coating	9.6	0.5	91.2	19.7
10 ALD Layers	14.0	0.7	68.4	4.4
50 ALD Layers	11.8	1.0	179.2	104.6

X-ray photoelectron spectroscopy was used to determine the binding energies of the Mn 2p photoelectron line on all electrodes and the Al 2p photoelectron line for ALD coated electrodes, both before cycling and after 300 charge and discharge cycles at a rate of 1C. Peak fitting was used to quantify the relative positions and areas of any sub-peaks within each photoelectron line. Binding energies for all Mn 2p peaks, as well as the doublet separations (ΔB.E.) and calculated Mn oxidation state (Mn Ox.), are summarized in Table 5.4.

The Mn 2p peak has been commonly used to characterize the near-surface oxidation state of $LiMn_2O_4$ and other manganese oxides[140, 141, 144-147]. Prior XPS studies of $LiMn_2O_4$ have yielded between 641.4 eV to 642.1 eV for the Mn $2p_{3/2}$ sub-peak assigned to Mn^{3+} and 642.4 eV to 643.6 eV for the Mn $2p_{3/2}$ sub-peak assigned to Mn^{4+}. Furthermore, the doublet separation between the Mn $2p_{3/2}$ and Mn $2p_{1/2}$ is listed in the NIST database as ranging from 11.6 eV to 11.8 eV for Mn oxides, with a value of 11.6 eV reported for $LiMn_2O_4$[147]. Interpretation of the Mn 2p can be particularly challenging because of the possibility for multiple oxidation states, which vary as a function of state of charge as well as cycling history, but also due to the intrinsically asymmetric Mn 2p peak shape. To minimize any cognitive bias introduced during the fitting procedure, a cold-pressed $LiMn_2O_4$ pellet was used as a reference sample. Values for an asymmetrical Voight-type peak shape were derived from the reference sample and fixed for all other electrodes. The full width at half maximum (FWHM) values was allowed to vary within a narrow range. Figure 5.14 shows the Mn 2p peak shape for the reference sample (cold pressed $LiMn_2O_4$ pellet used to derive the peak shape parameters.

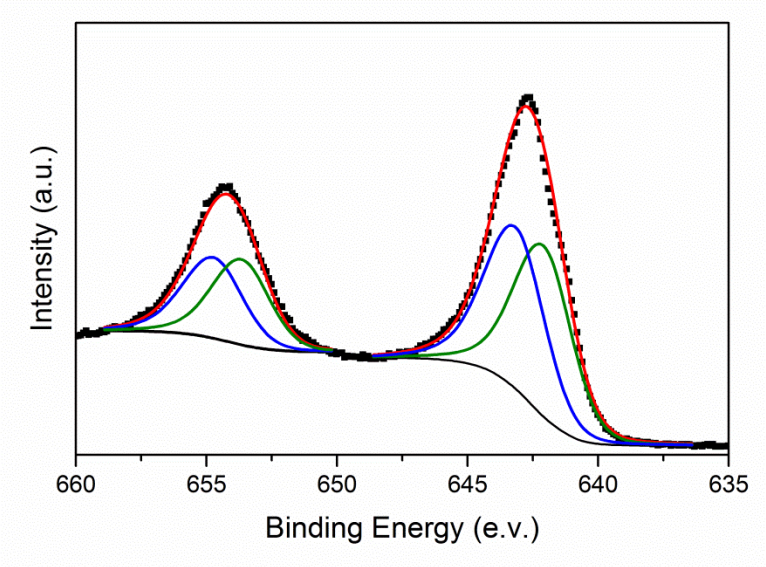

Figure 5.14 Fitted Mn 2p photoemission peak in a cold-pressed $LiMn_2O_4$ reference sample.

As shown in Figure 5.15, all electrodes before cycling exhibited Mn 2p binding energies slightly lower than previously reported literature values, but were internally consistent regardless of the presence of an ALD coating. However, an obvious decrease in the Mn 2p signal for the 50 ALD layer coated electrode was apparent before cycling. While this observation was reasonable given the increased thickness of the ALD layer compared to the 10 ALD layer coated electrode, it introduced some uncertainty into the analysis of the uncycled 50 ALD layer electrode. With the exception of the 50 ALD layer electrode, the Mn $2p_{3/2}$ and Mn $2p_{1/2}$ doublet separation for each set of sub-peaks was near 11.6 eV, suggesting that the peak fitting routine was reasonable. The near-surface Mn oxidation state was calculated using the relative area for peaks associated with Mn^{4+} and Mn^{3+} in the Mn $2p_{3/2}$ region. For the uncoated, uncycled electrode, an average oxidation state of $Mn^{3.5+}$ was obtained, which was expected for stoichiometric $LiMn_2O_4$.

Meanwhile, the relative peak area associated with Mn^{3+} increased with increasing ALD layer thickness, and as a result both of the 10 ALD layer and 50 ALD layer

electrodes show a decreased Mn oxidation state relative to the $LiMn_2O_4$ surface without any ALD coating. It is unclear whether this reduction was due to a reaction occurring during the ALD process or due to the decreasing signal-to-noise ratio for the Mn 2p peak. At the temperature used for the ALD process (175 °C), no reaction is expected between the carbon fiber substrate and $LiMn_2O_4$ coating (Figure 5.3). However, the Al precursor TMA is in fact a strong reducing agent which suggests the possibility that this decreased oxidation state is due to a reaction of the substrate with the ALD precursors [148]. The typical depiction of the ALD process using TMA and H_2O reactants is the two-step methyl transfer reaction described by George et. Al. with surface species indicated by asterisks,

$$AlOH^* + Al(CH_3)_3 \rightarrow AlOAl(CH_3)_2{}^* + CH_4 \qquad \textbf{Reaction 4}$$

$$AlCH_3{}^* + H_2O \rightarrow \ AlO - AlOH^* + CH_4 \qquad \textbf{Reaction 5}$$

assumes a reaction between incoming TMA molecules and omnipresent hydroxyl groups on the surface of an oxide substrate [149, 150]. However, these reactions do not explicitly involve reduction of the substrate, and in fact ALD coatings using TMA have been demonstrated for relatively inert surfaces including carbon and gold [150, 151]. Furthermore, according to the Hunter reaction (Reaction 1) a decreased oxidation state of Mn should lead to an accelerated capacity fade due to Mn dissolution, which is not observed for the ALD coated samples during electrochemical cycling. Thus, while TMA may be the reducing agent responsible for the observed Mn oxidation state change in the ALD alumina coated electrodes this effect does not override the benefits of the alumina coating.

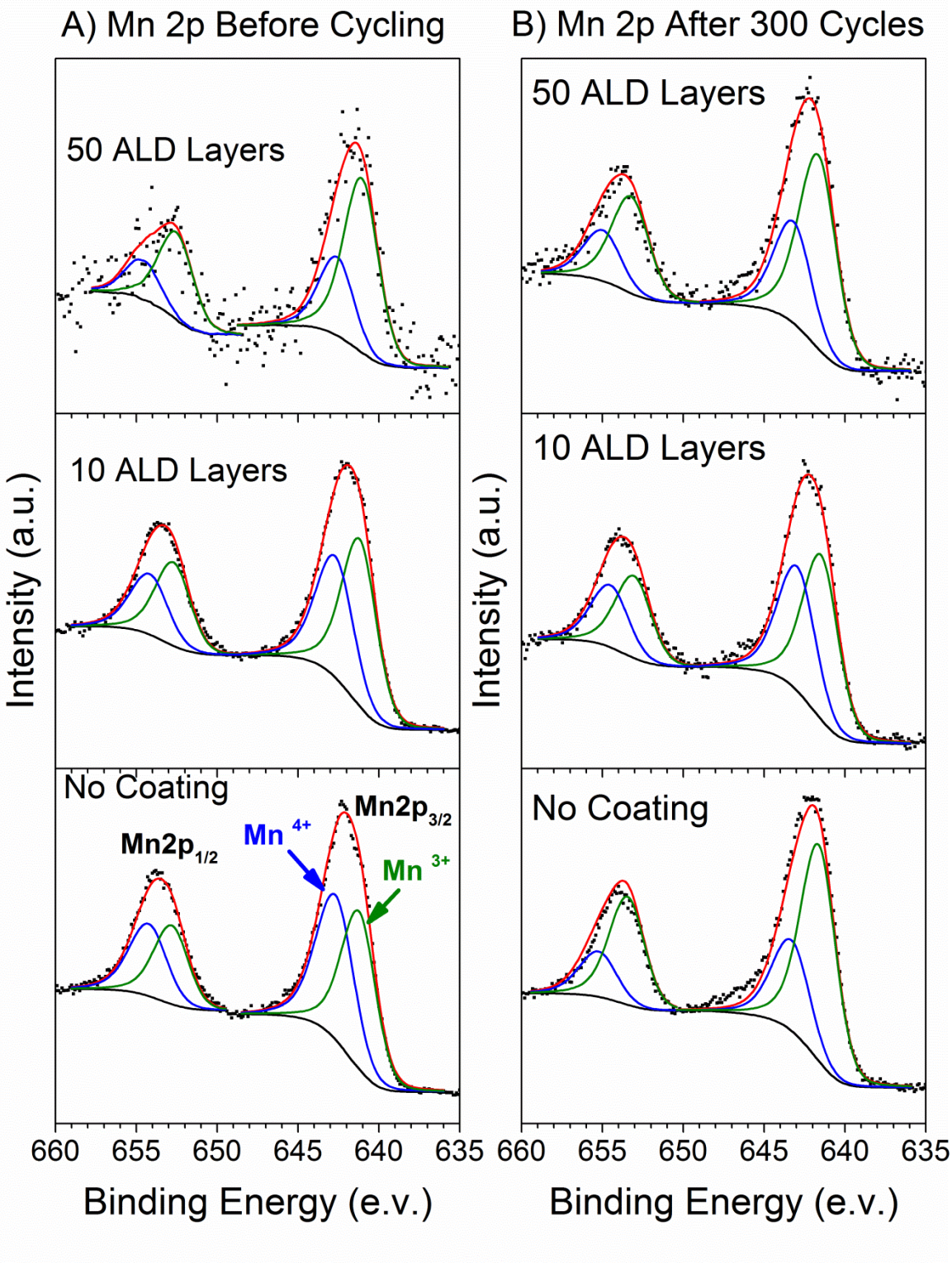

Figure 5.15 Mn 2p spectra before cycling (A) and after 300 cycles (B) at a 1C rate. Blue and green peaks identify contributions attributed to Mn 4+ and Mn 3+ ions, respectively.

After cycling, all of the Mn 2p peaks shifted to slightly higher binding energies, suggesting an increased oxidation state for Mn. However, only the uncoated electrode exhibited a change in relative $Mn^{3+/4+}$ peak areas and thus, a change in the average Mn oxidation state. Previous works have also reported reduction of manganese and other transition metals during electrochemical cycling of lithium-ion battery positive electrodes, and that this reduction can be inhibited with appropriate surface coatings [152] [129].

Two important changes were observed when comparing the Mn 2p peaks before and after cycling. First, the apparent Mn 2p signal-to-noise ratio for the cycled 50 ALD layer electrode improved dramatically compared with the uncycled electrode using identical XPS analysis conditions. This could imply that the ALD layer experienced a significant change in morphology or thickness, which resulted in an improved yield of Mn 2p photoelectrons. An alternative explanation is that Mn ions can migrate into the coating and nearer to the surface during the Mn dissolution process or form a new phase on the surface of the electrodes. A recent study of spinel $Li_xNi_{0.5}Mn_{1.5}O_{4-\delta}$ revealed the formation of Ni^{2+} and $Mn^{2+/3+}$ complexes with β-diketonate ligands produced by oxidation of the electrolyte during electrochemical cycling [153]. These phases or others like it may also be present at the surface of the ALD coated electrodes after electrochemical cycling, leading to an enhanced Mn 2p signal in XPS, though from the current analysis these complexes cannot be specifically identified. High-angle annular dark-field (HAADF) scanning transmission electron microscopy (STEM) images (Figure 5.16) comparing the 50 ALD layer coated electrode before and after cycling revealed a brighter edge on the cycled electrode. The increased contrast in the cycled sample could

be attributed to the presence of higher atomic number Mn, indicating diffusion of Mn from the $LiMn_2O_4$ particle into the Al_2O_3 coating. This was consistent with the both the EDS data collected in TEM (Figure 5.16C), which indicated an increase in Mn and Al signal at roughly the same lateral position, as well as the increased signal to noise ratio for the 50 ALD layer electrode shown in Figure 5.15A compared to Figure 5.15B .

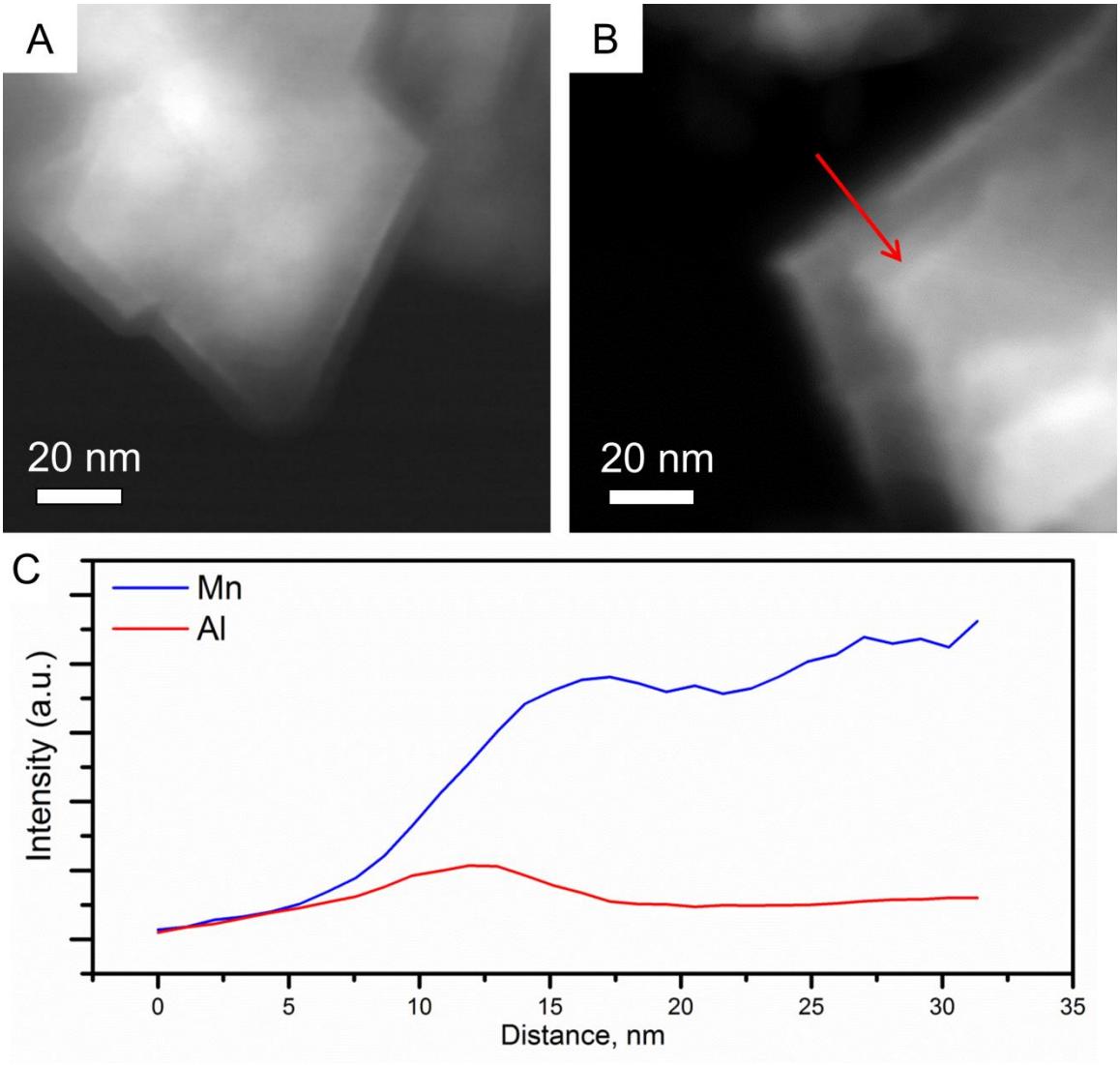

Figure 5.16 HAADF (high-angle annular dark-field) STEM (scanning transmission electron microscopy) images for a 50 ALD layer coated electrode before (A) and after (B) 300 cycles. An EDS line scan using the direction indicated by the red arrow in (B) is shown in (C).

The second observation is that while the cycled ALD coated electrodes showed qualitatively reasonable fits under the same conditions used for the uncycled electrodes, the uncoated electrode after cycling did not. This was observed as a slight under-estimation of the total peak intensity for the Mn $2p_{3/2}$ peak and a slight over-estimation for the Mn $2p_{1/2}$ peak when comparing the raw experimental data with the calculated fit. Furthermore, while the Mn 2p signal-to-noise ratio for the bare electrodes remained high, the doublet separation between the Mn $2p_{1/2}$ and Mn $2p_{3/2}$ peaks increased relative to the uncycled electrode. These observations likely resulted from the formation of a new phase on the surface of the uncoated electrode after cycling.

Table 5.4 Summary of XPS fitting results for Mn 2p. Binding energies (B.E.) are corrected relative to adventitious carbon on each sample.

	Mn 3+			Mn 4+			
Sample	**Mn 2p 3/2 B.E. (eV)**	**Mn2p1/2 B.E. (eV)**	**ΔB.E. (eV)**	**Mn 2p 3/2 B.E. (eV)**	**Mn2p1/2 B.E. (eV)**	**ΔB.E. (eV)**	**Mn Ox.**
Before Cycling							
No Coating	641.2	652.8	11.6	642.7	654.2	11.6	3.5
10 ALD Layers	641.2	652.7	11.5	642.7	654.2	11.5	3.4
50 ALD Layers	641.1	652.5	11.4	642.6	654.6	12.0	3.3
After Cycling							
No Coating	641.6	653.5	11.8	643.3	655.2	11.9	3.3
10 ALD Layers	641.5	653.1	11.6	643.0	654.5	11.6	3.4
50 ALD Layers	641.6	653.2	11.6	643.2	655.0	11.8	3.3

Compared to the Mn 2p spectra, analysis of the Al 2p photoelectron peaks shown in Figure 5.17 revealed a much more dramatic change as a result of electrochemical cycling. Regardless of ALD coating thickness, a single well defined peak is identified in the Al 2p region before electrochemical cycling.

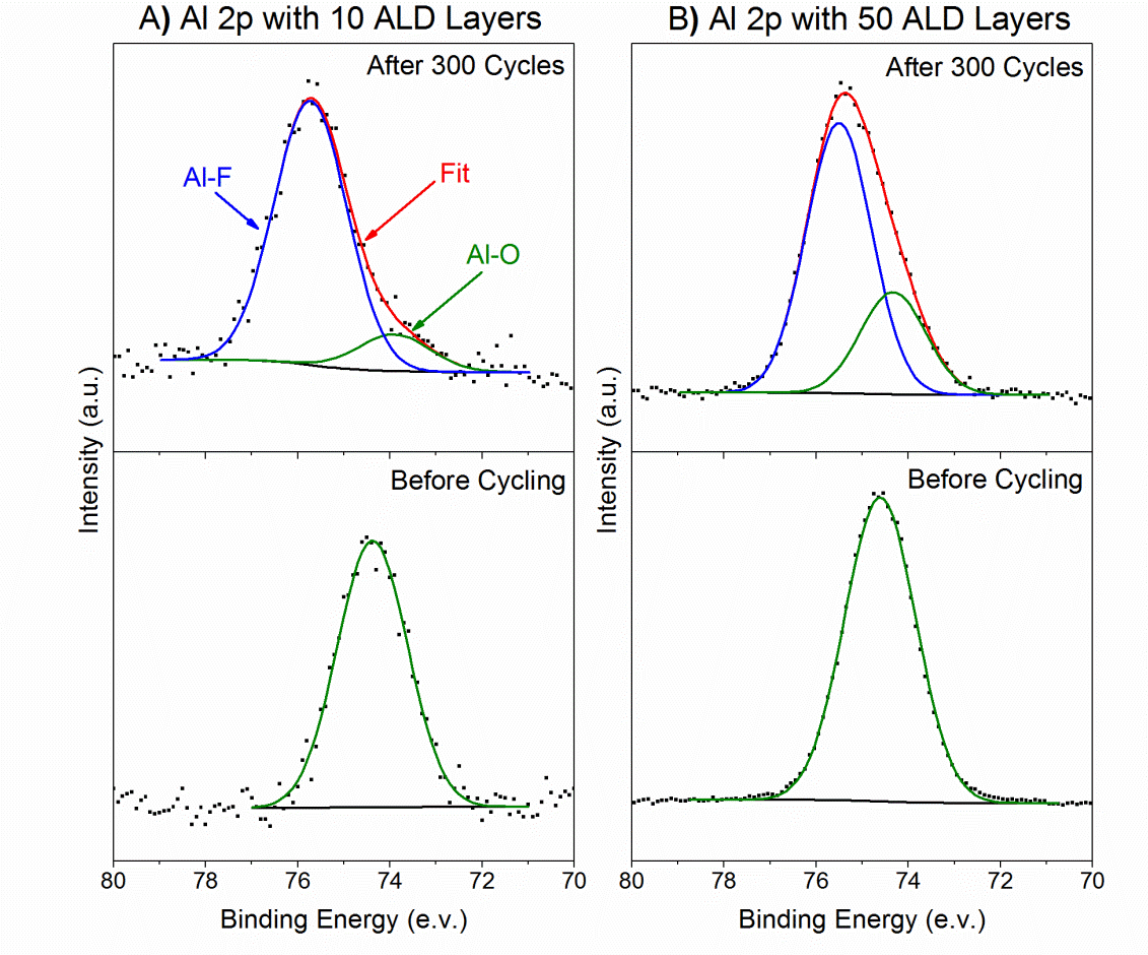

Figure 5.17 Al 2p XPS peak comparing 10 ALD layer coated (A) and 50 ALD layer coated (B) electrode before and after 300 cycles at a 1C rate.

Binding energies and FWHM values for the Al 2p photoelectron peaks shown in Figure 5.17 are summarized in Table 5.5.

Table 5.5 Summary of XPS fitting results for Al 2p peak.

Sample	Al-O B.E. (eV)	Al-F B.E. (eV)	Al 2p FWHM (eV)
Before Cycling			
10 ALD Layers	74.4	-	1.81
50 ALD Layers	74.6	-	1.81
After Cycling			
10 ALD Layers	73.8	75.7	1.88
50 ALD Layers	74.3	75.5	1.67

The binding energies of these peaks were approximately 74.5 eV, which was consistent with previous reports of aluminum oxide deposited onto $LiMn_2O_4$ by ALD[154]. After cycling, the peak maximum shifted to higher binding energies and developed a broader, slightly asymmetrical peak shape. Al was assumed to exist with a single oxidation state, Al^{3+} (unlike Manganese). Thus, the observed binding energy shift was likely due to a change in chemical bonding. An increased binding energy could be caused by increased electronegativity in the bonding character. Among the available and likely bond forming anions that are more electronegative than oxygen, only fluorine can be responsible for the large change in binding energy observed after cycling. The peak associated with residual aluminum oxide was also found to shift slightly to lower binding energies for both the 10 ALD layer and 50 ALD layer electrodes. Thus, the data suggested that, after electrochemical cycling the originally pure alumina coating consisted of a mixture of aluminum fluoride, aluminum oxy-fluoride, or fluorine-doped alumina and unreacted alumina. This conclusion was further supported by observing the relative intensity of the assumed Al-F and Al-O peaks. For the thinner 10 ALD layer electrode, only a small shoulder region could be attributed to residual unreacted

aluminum-oxide, while for the 50 ALD layer electrode, the residual peak was distinctly stronger.

Some authors have suggested that Al_2O_3 can sequester HF by the following reaction[155, 156]

$$Al_2O_3(s) + 6\,HF(l) \rightarrow 2\,AlF_3(s) + 3H_2O(l) \qquad \textbf{Reaction 6.}$$

Thermodynamic data for Reaction 6 yielded a value for the standard Gibbs free energy of Reaction 6 of -356.1 kJ/mol at 298K[157, 158]. Myung *et al.* reached a similar conclusion for higher temperature (400°C) solution-deposited Al_2O_3 coatings on $Li[Li_{0.05}Ni_{0.4}Co_{0.15}Mn_{0.4}]O_2$, and observed various aluminum-oxy-fluoride compounds including $Al_2O_2F_2$ and Al_2OF_4 using time-of-flight secondary ion mass spectroscopy (TOF-SIMS), accompanied by a decreased HF content in the electrolyte, with eventual formation of AlF_3[155]. However, the byproduct of water formed along with AlF_3 according to Reaction 6 would enable further HF production and thus increase the rate of Mn dissolution (Reaction 2), which seems counterintuitive based on the large amount of empirical evidence showing that aluminum-oxides and other compound do indeed improve capacity retention for $LiMn_2O_4$ and reduce HF content in the electrolyte. In light of this contradiction, Oh *et al.* utilized TOF-SIMS to observe Al_2O_3 coated $LiCoO_2$ cathodes after electrochemical cycling and suggested that Al_2O_3 coatings instead form a final compound of $AlF_3{\bullet}H_2O$ in the presence of HF[159]. The residual Al-O bonding shown in the XPS analysis may indicate that HF molecules are not completely disassociated by contact with Al_2O_3 and that a compound with both Al-O and Al-F bonding remains. This is shown schematically, and compared to the assumed case for Mn dissolution by the Hunter reaction, in Figure 5.18.

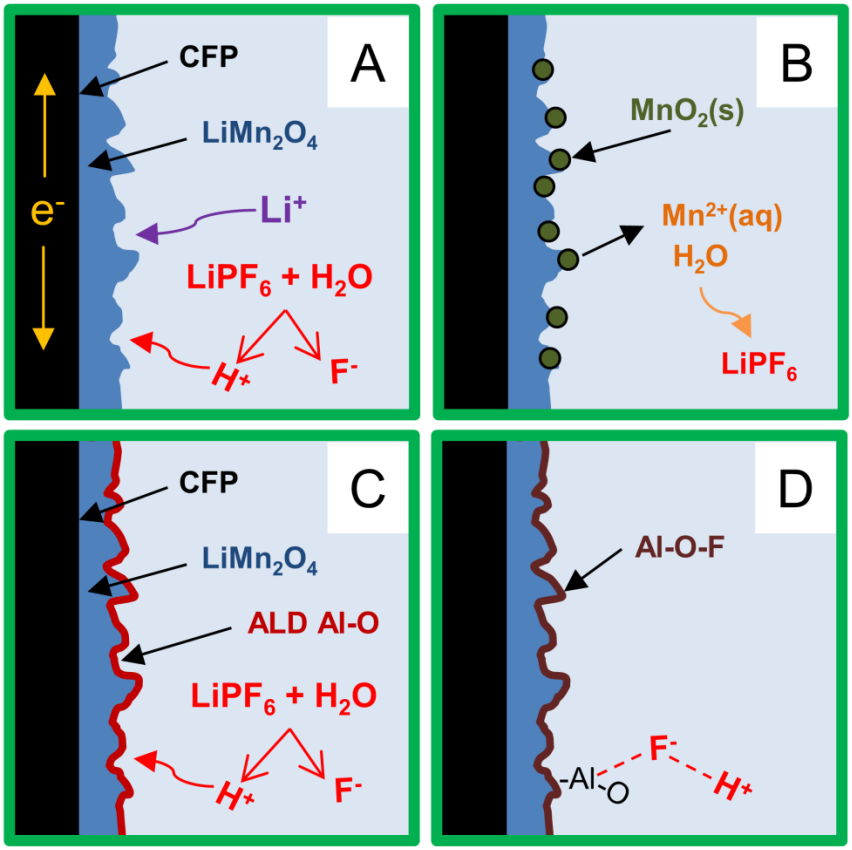

Figure 5.18 Schematic of proposed mechanism through which ALD protects $LiMn_2O_4$ surface. For the uncoated electrode, $LiPF_6$ decomposition proceeds in (A) leading to Mn^{2+} dissolution and formation of MnO_2 on the electrode surface (B). For the ALD coating, $LiPF_6$ still decomposes for form HF (C) which reacts instead with Al-O to form a new phase and prevent extensive Mn dissolution (D).

5.4 Conclusions

In this chapter ALD was used to deposit coatings of Al_2O_3 onto $LiMn_2O_4$ grown on carbon fiber electrodes via hydrothermal synthesis. Among the samples studied, the 10 ALD layer coated electrodes exhibited the best performance, with significantly enhanced capacity retention and improved rate capability. By studying the peak current of cyclic voltammograms the lithium diffusivity of the 10 ALD layer coated electrode was found to be slightly higher than the uncoated electrode, which could explain the increased rate

capability. Meanwhile, the structure of the electrodes remained virtually unchanged when examined using synchrotron X-ray diffraction and electron microscopy. No cracking or electrode pulverization was observed for either the coated or uncoated electrodes. These observations suggest that the capacity loss observed in the uncoated electrodes is due primarily to Mn dissolution.

XPS analysis of the Mn 2p photoelectron line showed that the oxidation state of Mn decreased slightly for the uncoated sample after electrochemical cycling, while for the ALD coated samples the Mn oxidation state was unchanged. While the static oxidation state for the ALD coated samples indicate that the Mn dissolution reaction has been subdued, the expected increase in Mn oxidation state for the uncoated sample (due to buildup of insoluble Mn^{4+}) is not observed. Meanwhile, XPS analysis of the Al 2p photoelectron line revealed a large shift in the binding energy and change in the Al 2p peak shape, implying that aluminum oxide is capable of scavenging HF from the electrolyte through the formation of an aluminum-oxy-fluoride compound. Finally, redistribution of Mn was observed both with TEM and XPS analysis in the 50 ALD layer coated electrode, suggesting that Mn migration due to the HF activated dissolution process is not completely arrested by the coatings. This important observation suggests that the ALD coatings do not simply act as a mechanical barrier between the electrolyte and cathode surface. Rather, the spontaneous formation of a new phase of good ionic conductivity on the electrode surface prevents the dramatic increase in polarization resistance or decrease in discharge capacity reported for other coating morphologies and techniques.

6 CARBON NANOFIBER BASED ELECTRODES PREPARED BY ELECTROSPINNING

In the previous chapters electrodes were produced by coating commercially available CFP with $LiMn_2O_4$ by the hydrothermal method. With CFP substrates average mass loading obtained was only 32 wt%, which significantly compromises the overall energy density of the electrodes. Because the active charge storing material is deposited only on the surface of the carbon fibers, the relatively low ratio of surface are to volume for the micron sized fibers leads to a low overall content of oxide. Similarly, the large void space between carbon fibers also contributes nothing to charge storage. By reducing the diameter of the carbon fibers, as well as the voids between them, the available area for oxide coating increases. Substrates which meet this requirement are not commercially available; however electrospinning is a commonly used technique to produce them in the lab. This chapter introduces the process of electrospinning and demonstrates how this technique can be utilized to create carbon fiber substrates with favorable properties which were then coated by $LiMn_2O_4$ and tested in electrochemical devices.

6.1 Background on electrospinning and application of carbon nanofibers for electrochemical devices

Electrospun fibers have been used in electrochemical devices in a number of ways. Because of the nanoscale dimensions obtainable, electrospinning has frequently been used as a templating approach for oxides used in lithium-ion batteries and pseudocapacitors. A typical experiment in which electrospinning is used to produce electrode materials utilizes a solution in which a stoichiometric mixture of the desired metal oxide compounds precursors (e.g. metal salts such as nitrates, acetates or

carbonates) are dissolved into a solution along with a polymer. The polymer serves only to increase the viscosity of the solution, and thereby enable the electrospinning process to occur. Following the electrospinning experiment the metal-salt loaded polymer fibers are calcined in air to convert the metal salts to metal oxides and burn away the polymer. The metal oxides formed by this process usually inherit the high aspect ratio of the pre-calcination fibers. This approach has been used to produce cathode materials for lithium-ion batteries including $LiMn_2O_4$[160, 161], $LiCoO_2$ [162] and $LiNi_{1/3}Mn_{1/3}Co_{1/3}O_2$[163]. For all of these reports however, the materials produced were tested electrochemically by mechanically powdering the calcined fibers and then tape-casting electrodes containing the resultant powders. This is presumably due to the poor electronic conductivity and mechanical integrity of the pure oxide fibers.

Another approach to create electrochemical devices by electrospinning utilizes polymers which can be converted into carbon during pyrolysis. Suitable polymers have high residual carbon content when thermally decomposed in an inert atmosphere, and preferably have the ability to produce graphitic domains which improves overall strength and electronic conductivity. The polymer polyacrylonitrile (PAN) is by far the most common carbon precursor utilized in electrospinning experiments[164]. As mentioned in Chapter 4 PAN is also the polymer used for producing the carbon fibers found in CFP and accounts for over 90% of commercial carbon fiber production, though these fibers are formed by methods other than electrospinning [165]. Carbon fibers produced by electrospinning solutions of PAN dissolved in DMF usually have dimensions ranging from 100-1000 nm and remain amorphous for pyrolysis temperatures up to 2000 °C [166-168]. Electrical conductivity is also strongly influenced by pyrolysis temperature, and has

been reported to increase by four orders of magnitude between 600 °C to 1000 °C [169]. Bare PAN derived carbon fibers have been demonstrated as binderless electrodes for both lithium-ion battery anodes, as well as carbon-carbon supercapacitors after chemical or physical activation [166, 170, 171].

While PAN is the most frequently used polymer for producing carbon nanofibers by electrospinning another polymer, the biomass product lignin, has been demonstrated in electrochemical devices very recently. Because of its' high natural abundance, low cost (~10% of PAN), and high-carbon content, lignin has been sought after as replacement for PAN in structural carbon fibers for a number of years but these fibers have yet to be proven competitive with PAN based fibers in terms of tensile strength and elastic modulus [172, 173]. Lignin exists as part of the cellular structure in vascular plants and is particularly prevalent in trees and other rigid, woody biomass. Lignin is most commonly produced as a byproduct of the pulp-and-paper industry, wherein it is separated from cellulose in the puling process. Different pulping processes produce varieties of lignin with varying properties, and the two most frequently encountered varieties are referred to as Kraft and Alcell lignin named for their respective pulping approach. Typically only Alcell lignin is used for structural applications due to its higher purity, while Kraft lignin is more readily available[174]. An important difference between Alcell and Kraft lignin is that only Kraft lignin is soluble in water due to the salts used in the Kraft pulping process. The downside of this is that Kraft lignin contains inorganic impurities which end up in the carbon fiber. A few demonstrations utilizing bare lignin derived carbon fibers have been demonstrated in academic literature by producing fibers from electrospinning as well as extrusion processes[175-178]. This chapter compares the experimental approach for

producing carbon nanofiber webs from PAN and Kraft lignin by electrospinning, as well as the performance of $LiMn_2O_4$ electrodes using these webs as substrates.

6.2 Experimental Methods

6.2.1 Electrospinning of PAN and Lignin solutions

PAN based electrospinning solutions were prepared by dissolving a given mass of the polymer (Mw=150 kDa) into N,N dimethylformamide (DMF) at 70 °C under constant magnetic stirring for a period of 12 hours to produce a homogenous mixture. While the Kraft lignin used for electrospinning in this work is water soluble, it cannot form a viscous solution due to the low molecular weight of the polymer. Thus, for the lignin based solutions the supporting polymer polyvinyl alcohol (Mw = 89-98 kDa) was used. Solutions were prepared by first dissolving PVA into distilled water at 70 °C with magnetic stirring until a clear solution was obtained. Lignin powder (Mw ~10 kDa) was then added to the PVA solution and stirred for 12 hours at 70 °C.

After mixing the solutions were allowed to cool to room temperature and then loaded into a plastic syringes with a luer-lock fitting. A 21 gauge needle tip (ID = 514 μm) was affixed to a the polymer solution containing syringe by flexible tube, while the syringe was placed into a programmable syringe pump (NE-1000 New Era Pump Systems) with the desired flow rate. An alligator clip was used to attach the high-voltage power supply (Gamma High Voltage ES30) lead to the needle tip. The capillary fed needle tip, while connected to the high voltage power supply, was translated along the length of the fiber mat collector by a programmable linear-motion track. The collector used was a custom built drum with a diameter of 4 inches which was connected to ground by a metal brush. Sheets of aluminum foil were first sprayed with PTFE mold release and taped to the drum to collect the electrospun fibers. The concentrations of PAN and lignin/PVA were selected based on literature reports with the goal of producing smooth,

unbroken fibers with as many identical parameters as possible. As described in section 3.1.2, many factor influence not only the fiber morphology but the ability to form fibers by electrospinning at all. Thus, emitter to collector distance and solution preparatory conditions were consistent between solution types while concentration, voltage, and flow rate varied as needed to optimize the electrospinning process. Lignin/PVA solutions have a relatively narrow range of parameters in which fibers will form, and as a result the values used are the result of optimization around a stable electrospinning process rather than a desired fiber morphology [176, 177]. Meanwhile, PAN has been produced with wide range of solution and spinning parameters. Parameters were chosen to produce small diameter and smooth fibers[168, 179]. Critical parameters used during the electrospinning experiment are summarized in Table 6.1.

Table 6.1 Parameters used for electrospinning of polymer solutions

Solution	Concentration	Emitter/Collector Distance	Voltage	Flow Rate	Sheet Thickness
Lignin + PVA in H_2O	15 wt% lignin + 7.8 wt% PVA	10 cm	25 kV	0.9 mL/hour	120-170 μm
PAN in DMF	10 wt%	10 cm	15 kV	3 mL/hour	140-160 μm

After the electrospinning process, the fiber mat was peeled away from the aluminum foil and pressed under a weight (textbook) for 12 hours. Total dimensions of the electrospun sheet are approximately 25 cm by 10 cm. Strips approximately 2.5 cm wide and 10 cm long were cut from the larger sheet and stored in a desiccator. The thickness across the width of the electrospun sheet varied somewhat, and strips were cut to maximize thickness homogeneity. A schematic showing the custom built electrospinning apparatus used for these experiments is shown in Figure 6.1.

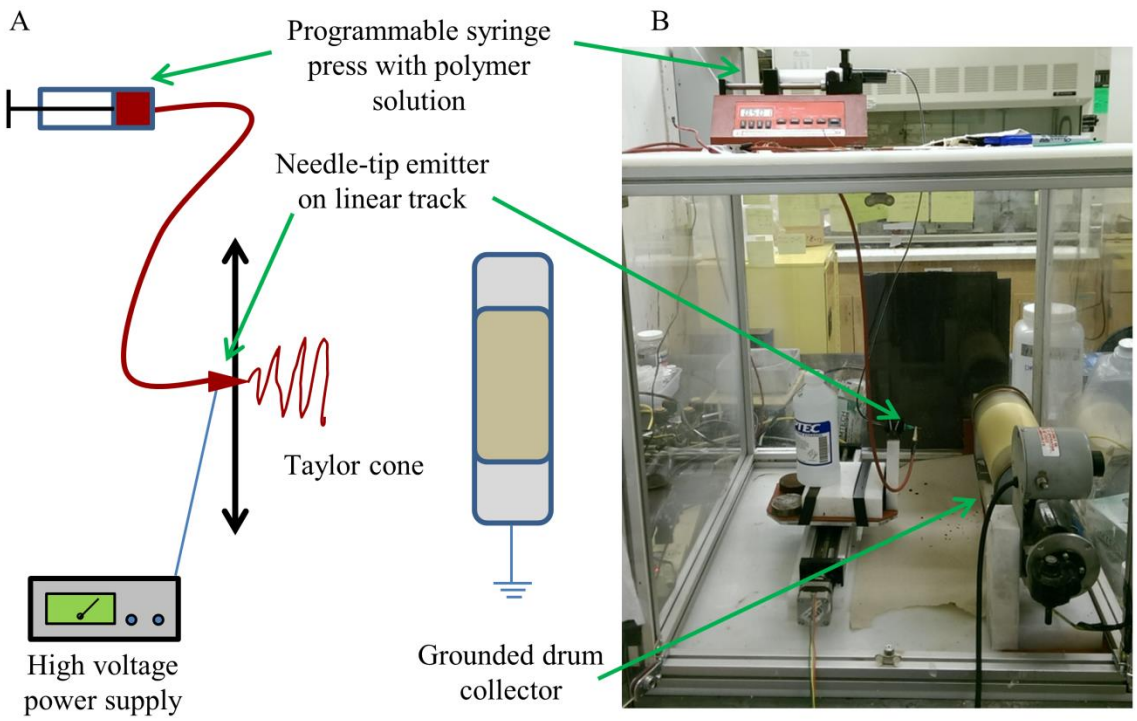

Figure 6.1 Schematic of electrospinning apparatus (A) with important features identified in digital photograph (B).

6.2.2 Pyrolysis of electrospun fiber mats

Strips of electrospun fiber mats were sandwiched between alumina plates and wrapped tightly with silver wire to apply tension to the mat and prevent warping or wrinkling of the polymer fiber sheet as it became carbon. The sandwiched fiber mats were then loaded into a quartz tube-furnace tube and sealed with rubber stoppers. The pyrolysis procedure is preceded by stabilizing the polymer fibers through thermal oxidation in air. This step is frequently used when producing high-strength fibers from PAN and commonly appears in academic literature covering electrospinning of both PAN and lignin, and for both polymers stabilization temperatures in the range of 200 °C to 300 °C are typical [166, 174-178, 180, 181]. In this dissertation, a single temperature of 280 °C for a period of 2 hours was used for thermal oxidation. After thermal stabilization in air the tube was flooded with N_2 at a flow rate of at least 100 sccm for a period of one hour at

the stabilization temperature, and then heated to a desired pyrolysis set-point. Temperatures of 600 °C and 900 °C were used, with the max temperature in the configuration used limited by the melting point of silver (Ag T_m = 962 °C). The furnace was kept at the pyrolysis temperature for 2 hours then cooled under flowing nitrogen to room temperature. All heating and cooling rates were set at 3 °C min^{-1}.

6.2.3 Hydrothermal coating of $LiMn_2O_4$, Electrochemical Testing and Physical Characterization

Samples of pyrolized PAN and lignin were coated with $LiMn_2O_4$ in an identical fashion to what was described in previous chapters. In short, coupons of pyrolized electrospun fibers were loaded into a hydrothermal autoclave with a solution of 20 mM $KMnO_4$, 20 mM NH_4Cl and 50 mM $LiOH{\bullet}H_2O$ and sealed. The autoclaves were then heated in an electric box furnace to a temperature of 100 °C for 12 hours followed by a temperature of 140 °C for 24 hours. After cooling to room temperature the samples were thoroughly rinsed in distilled water and then dried.

Conductivity and structure of the pyrolized fibers was determined by four-point probe conductivity testing, where the resistance was determined by Ohm's law (R=V/I) for a range of applied current values and repeated over multiple regions and samples of each type. Resistance was converted to bulk resistivity by the following equation

$$Bulk\ Resistivity = 2a\pi s * \rho * t \qquad \text{Equation 42}$$

where a is the thickness correction factor, s is the inter-probe spacing, ρ is the resistance value derived from Ohm's law, and t is the sample thickness. For samples in which the ratio of sample thickness to inter-probe spacing is sufficiently small ($t/s \leq 0.5$), the constant correction factor term ($2\ a\pi s$) can be simplified to 4.53. Because the inter-probe

spacing used was 1016 microns, and the thickest samples tested were less than 200 microns, all of the samples tested fit this criterion.

Ex situ Raman spectroscopy was used to characterize the relative content of graphitic and disordered (amorphous) carbon in the pyrolized fibers by studying the relative intensity and FWHM values for the D and G band, which are linked to electrical conductivity[167, 169] . For all of the Raman experiments in this chapter a laser wavelength of 633 nm, a 20x objective, and a 0.4 numerical aperture. Peak fitting of the Raman bands was conducted using a mixed Gaussian-Lorentizan peak shape, but without further restrictions. Electrochemical testing was conducted by cutting discs of hydrothermal coated carbon fiber mats and evaluating the rate capability, redox potentials, and cycling stability in lithium-ion half cells. Swagelok type cell hardware was used along with glass-fiber separators soaked with a 1 M $LiPF_6$ in 1:1 ethylene carbonate: dimethyl carbonate electrolyte. SEM, EDS and XRD were conducted as described in previous chapters on both the electrospun fibers before and after pyrolysis and after hydrothermal coating.

6.3 Results and Discussion

6.3.1 Morphology and composition of electrospun fibers

As shown in Figure 6.2 fibers produced from both PAN and lignin are smooth and cylindrical, with diameters for as prepared polymer fibers range from 400-600 nm for the PAN derived fibers and 100-200 nm for the lignin derived fibers. Both fibers show significant charging during SEM analysis even after sputtering with Au, and as a result produce relatively poor resolution images.

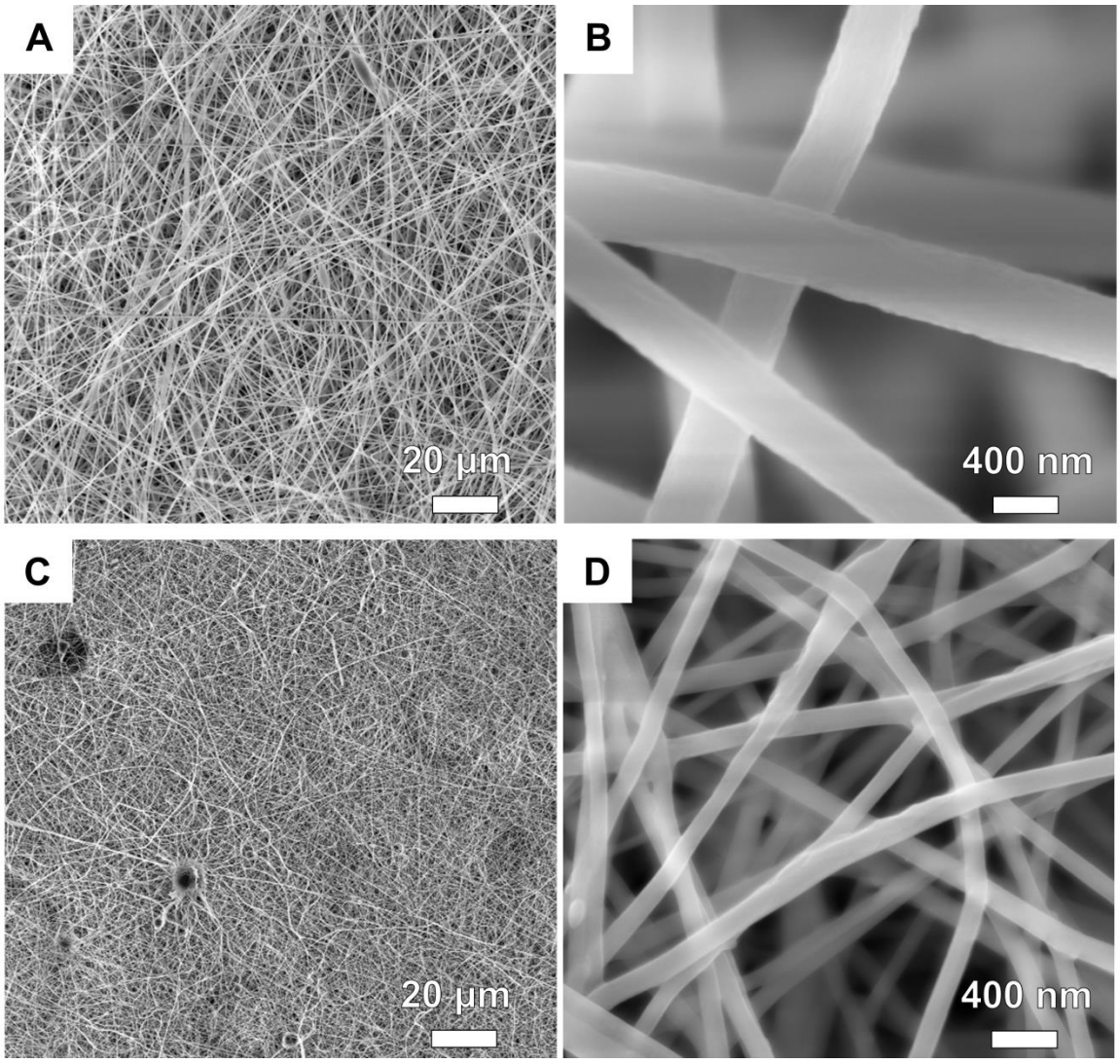

Figure 6.2 SEM images of electrospun polymer fibers prior to pyrolysis. Fibers from PAN in DMF solution are shown at low magnification (A) and high magnification (B), as well as fibers from a lignin, PVA and water solution are shown at low magnification (C) and high magnification (D).

EDS analysis was used to benchmark the initial composition of both polymer fiber types before pyrolysis. As expected, the PAN derived fibers with a monomer composition $(C_3H_3N)n$ show only C, N and trace amounts of O in the EDS spectra. Meanwhile for the lignin and PVA polymer fibers, which have monomer composition of $(C_{31}H_{34}O_{11})n$ and $(C_2H_4O)n$, respectively, include a significant content of Na and S in the

EDS spectra. This is attributed to the Kraft pulping process, which uses alkaline solutions containing sodium sulfide to separate lignin from cellulose.

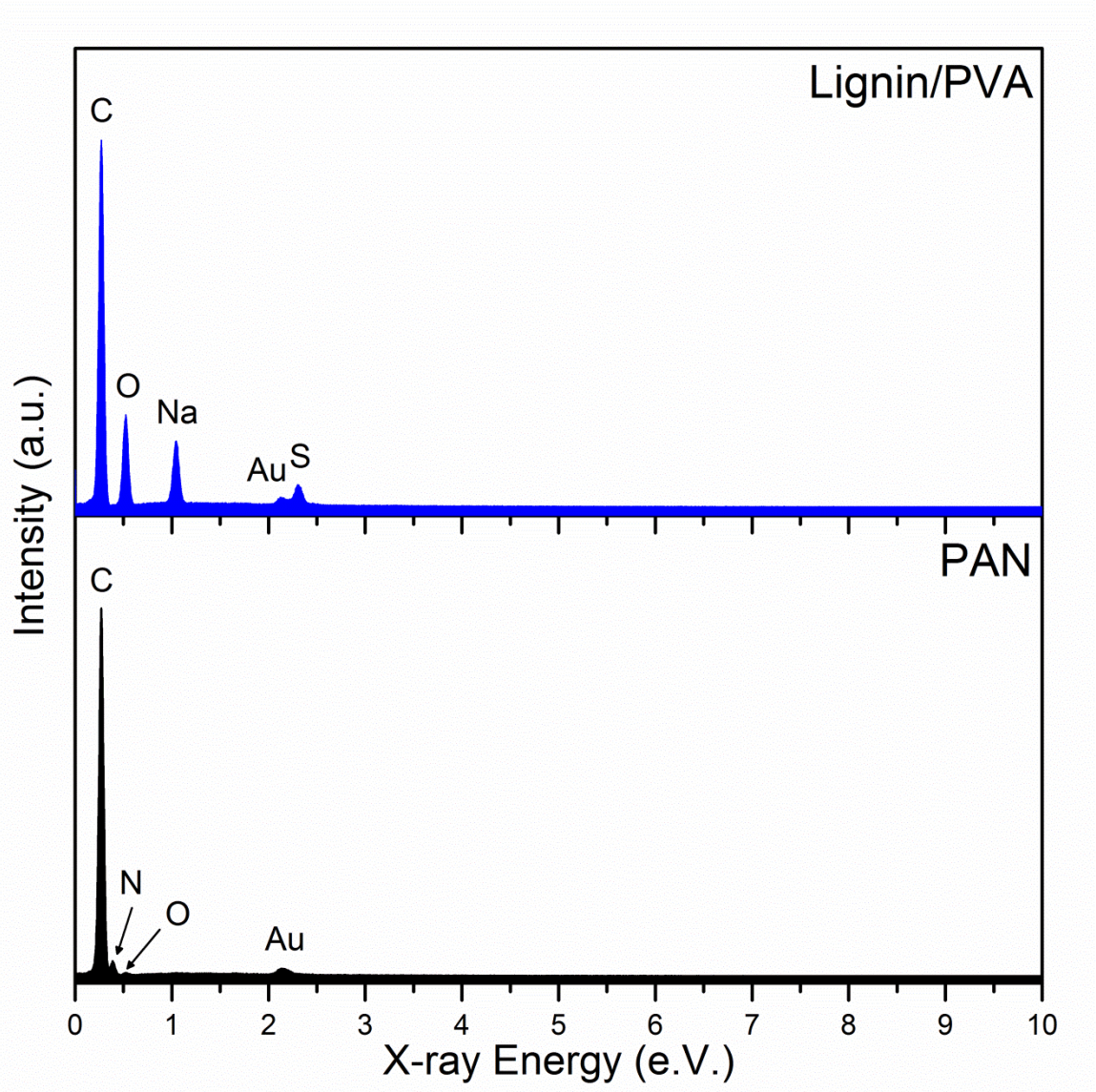

Figure 6.3 EDS of electrospun PAN and Lignin/PVA fibers. Samples were sputtered with Au prior to analysis to prevent charging. Intensity scales are normalized relative to the C Kα peak at 0.277 eV.

Pyrolysis was conducted at two temperatures, 600 °C and 900 °C, under flowing nitrogen following a thermal oxidation in air at 280 °C. Both pyrolysis temperatures led to blackening of the fiber mat as well as some shrinkage and mass loss. All fibers were

thoroughly rinsed in distilled water and dried after pyrolysis and prior to weighing. While this was not observed to have any influence on the PAN derived carbon fiber mass, a significant portion of "extra" water soluble mass was removed by this step for the lignin derived fibers. Because the pulping salts such as sodium sulfide are water soluble, but have appreciably high melting points (>1000 °C), this mas loss is attributed to dissolving some of the inorganic salts not contained within the fibers.

After pyrolysis the PAN derived fibers show a large decrease in fiber diameter, but in general maintain the same smooth and cylindrical morphology. For the 600 °C pyrolized PAN fibers the average diameter shrunk from 503 nm for the as-spun fibers to 378 nm, while after a 900 °C pyrolysis the fibers had an average diameter of 339 nm. Even without Au sputtering the pyrolized PAN fibers can be easily resolved by SEM indicating a large increase in electronic conductivity leading to a reduced charging effect.

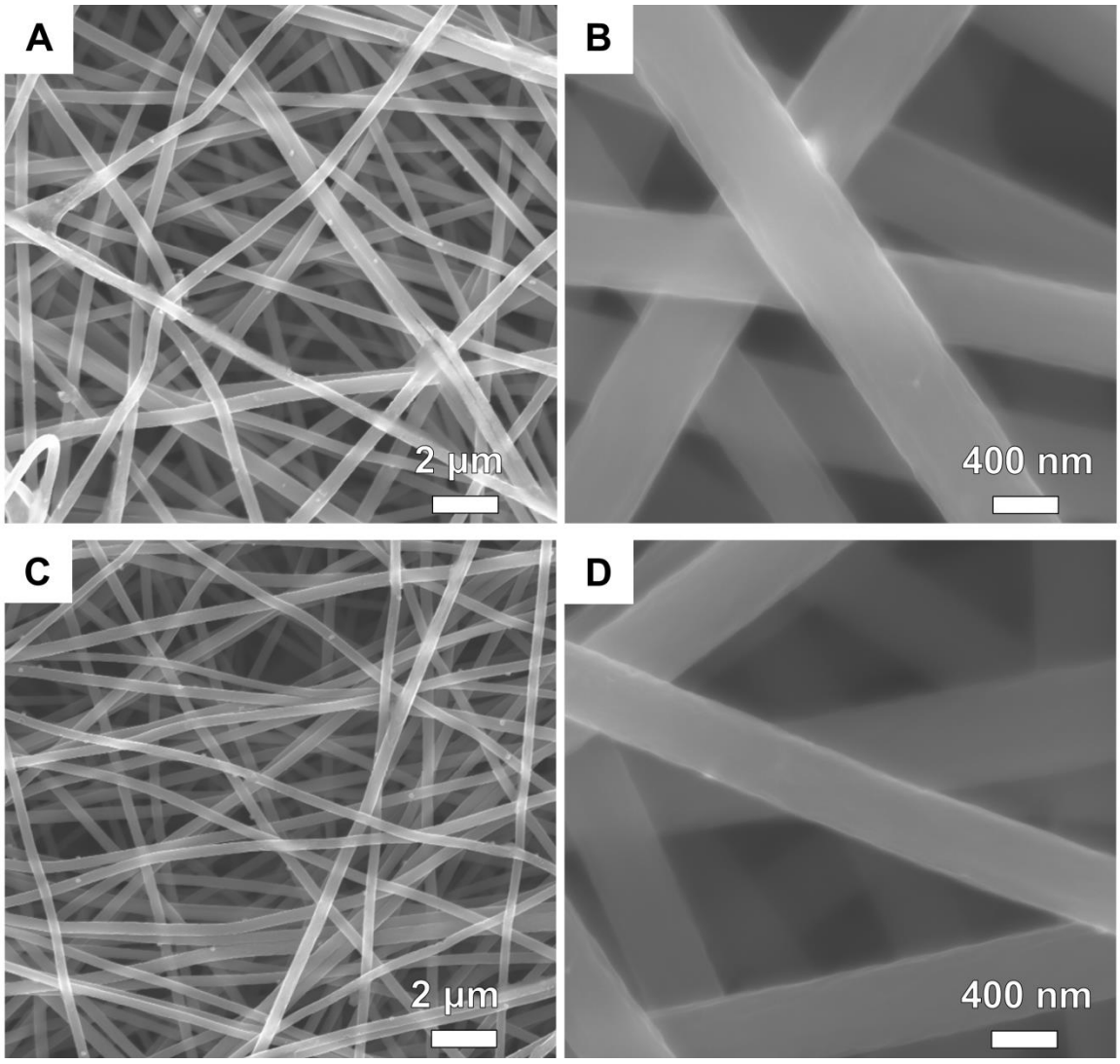

Figure 6.4 SEM images fibers electrospun from PAN solution pyrolized at 600 °C (A,B) and 900 °C (C,D) and low magnification (A,C) and high magnification (B,D).

Elemental analysis of the pyrolized PAN fibers shows that even up to 900 °C the fibers contain a small amount of N, which suggests that all of the C-N triple bonds in the PAN monomers are not completely destroyed, or that N exists within a graphitic framework as dopant atoms. The relative N content is noticeably larger in the 600 °C sample which supports the hypothesis that some of the carbon-nitrogen bonding in the as-spun PAN fibers remains intact.

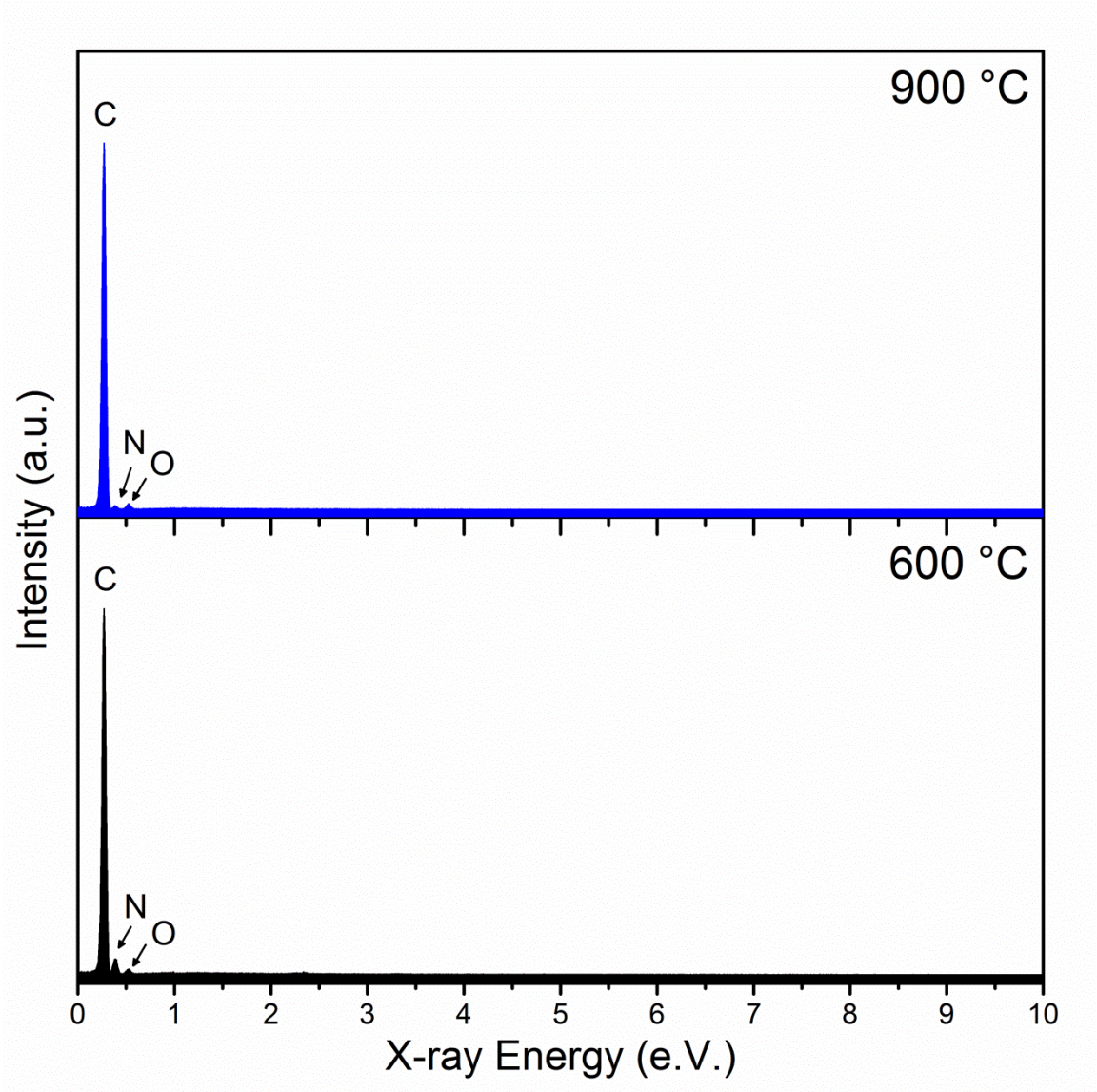

Figure 6.5 EDS of electrospun PAN fibers after pyrolysis at 600 °C and 900 °C in nitrogen. Intensity scales are normalized relative to the C Kα peak at 0.277 eV.

Compared to the PAN derived fibers, lignin/PVA fibers show virtually no decrease in fiber diameter which is maintained around 150 nm for all of the conditions tested, while similar to PAN the apparent electronic conductivity is greatly improved. Anecdotally, the lignin derived fibers exhibited a greater degree of macroscopic shrinkage during pyrolysis which may explain the apparent lack of diameter change.

Even after pyrolysis the lignin/PVA fibers show a high degree of interconnectivity compared to the PAN derived fibers. Many forked branches are apparent in Figure 6.6 for the lignin/PVA fibers after pyrolysis while the PAN derived fibers show very few examples of similar fiber architecture.

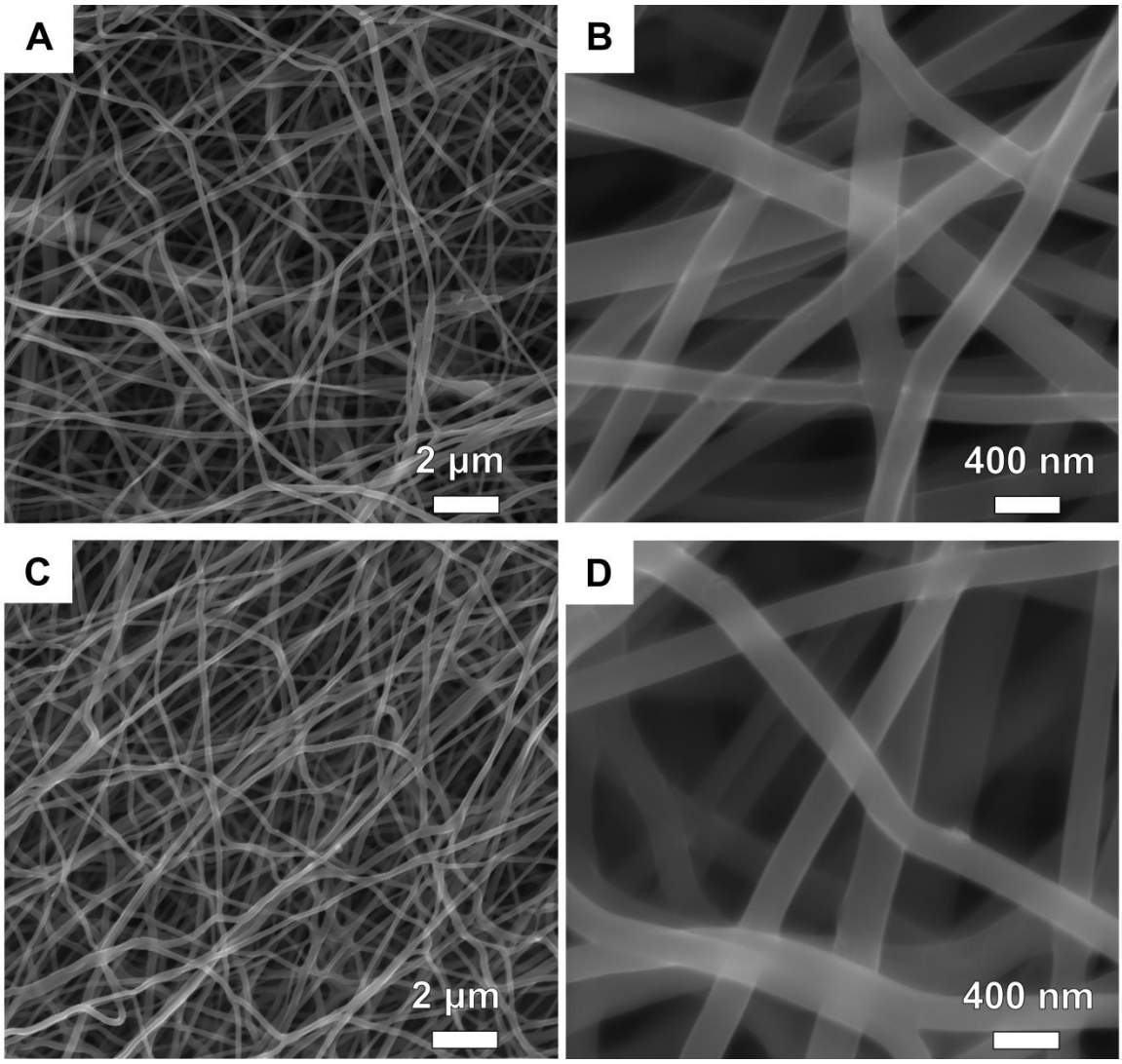

Figure 6.6 SEM images fibers electrospun from lignin/PVA solution pyrolized at 600 °C (A,B) and 900 °C (C,D) and low magnification (A,C) and high magnification (B,D).

In terms of relative peak intensity, the pyrolysis process seems to reduce the Na and S content in the carbon fibers. This is consistent with the observed additional mass loss after rinsing the lignin derived carbon fibers. Still, some of the pulping salts may indeed be contained inside the pyrolized carbon fibers and thus contributes to the observed EDS spectrum.

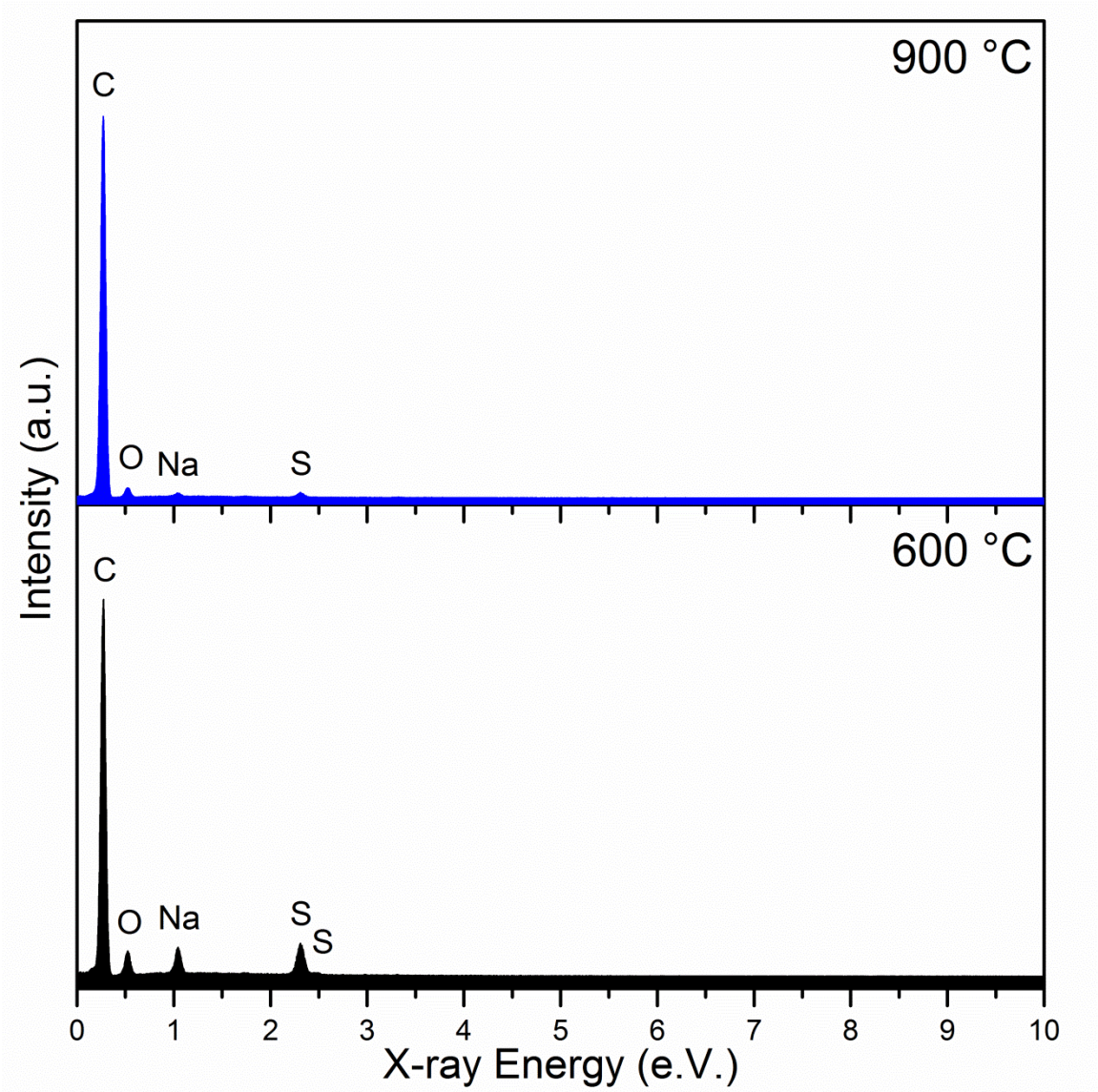

Figure 6.7 EDS of electrospun Lignin/PVA fibers after pyrolysis at 600 °C and 900 °C in nitrogen. Intensity scales are normalized relative to the C Kα peak at 0.277 eV.

Table 6.2 compares the various physical parameters of the electrospun fibers before and after pyrolysis. Both polymer types show an increase in mass loss with increasing pyrolysis temperature, however an obvious jump is observed for the PAN fibers in which the mass loss more than doubles between 600 °C and 900 °C. While several volatile organic species containing carbon are evolved during pyrolysis, the PAN and lignin monomers are 68% and 64% carbon by mass, respectively, which gives some indication of expected carbon yields. Previous reports of thermal analysis conducted on PAN fibers during thermal oxidation and pyrolysis shows that properties such as electronic conductivity, morphology, mass loss and fiber strength are all dependent on the heat treatment conditions used. Pyrolysis is expected to begin at temperatures above 300 °C with the observed mass loses here being roughly consistent with previous reports of stabilized PAN fibers after pyrolysis to temperatures in the range of 600 °C to 900 °C [182, 183].

Compared to the PAN fibers, the lignin/PVA fibers show a significantly increased mass loss at both pyrolysis temperatures studied, resulting in only 30 wt% of the original electrospun fiber mass remaining after pyrolysis at 900 °C. Lignin has a wide variety types based on the pulping process used and as a result there are not many examples of pyrolysis conditions for Kraft lignin and PVA blends, however similar works describing the pyrolysis of lignin report pyrolysis temperatures beginning in the range of 300 °C to 400 °C with residual masses of approximately 60 wt% and 40 wt% when pyrolized to 600 °C and 900 °C respectively [184, 185]. It is unclear whether any of the PVA content in the lignin/PVA fibers was also converted to carbon. Several studies have reported that PVA only fibers combust entirely under pyrolysis conditions leaving only a small amount (<5 wt%) of residual mass, while certain inorganic additives which favor the formation of cyclic carbon rings dramatically increase this value, allowing for the formation of intact carbon fibers by pyrolysis of PVA fibers including these additives [186, 187]. One study conducted low temperature thermal analysis (<350 °C) in air and reported that

mechanical mixtures of PVA and lignin led to an increased residual mass content with certain concentrations and variants of PVA, suggesting that such an interaction in the present study might be possible [188]. If PVA is assumed to completely volatilize during the pyrolysis procedure, then only about two-thirds of the pre-pyrolysis mass can be converted to carbon. This factor, along with the inorganic salts which were removed by rinsing (about 7 wt% for both pyrolysis conditions), may explain the relatively low apparent carbon yields in the lignin/PVA fibers compared to the PAN fibers. Both of the electrospun fiber types show a decreased density relative to CFP (0.58 g/cm^3), and interestingly density seems to be invariant with pyrolysis temperature.

Table 6.2 Comparison of diameters, mass loss and density of electrospun fibers before and after pyrolysis

	Diameter (nm)		Mass loss (wt. %)		Density (g/cm^3)	
Sample	**PAN**	**Lignin/PVA**	**PAN**	**Lignin/PVA**	**PAN**	**Lignin/PVA**
Pre-Pyrolysis	503 (80)	142 (19)	N/A	N/A	0.244	0.460
600 °C	378 (18)	161 (37)	22	62 (55 pre-rinsed)	0.243	0.375
900 °C	339 (46)	151 (30)	51	70 (63 pre-rinsed)	0.236	0.387

6.3.2 Structure and conductivity of pyrolized carbon fibers

Raman spectra for the pyrolized electrospun fibers, as well as the commercially produced CFP, shows both the D and G peaks associated with sp^2 hybridization in disordered carbons occurring at 1340 cm^{-1} and 1580 cm^{-1} respectively[190, 191]. The ratio in relative intensity of the D and G band (denoted herein as I_D and I_G), or I_D/I_G is inversely proportional to the crystallite size in graphitic carbons and is therefore used to express relative degrees of graphitization in disordered carbons[189]. In general, the relative intensity of the G band has been reported to increase with increasing pyrolysis

temperature, indicating a greater degree of graphitization occurring in the carbon fibers[167, 190, 191]. Thus, larger values of I_D/I_G indicate a greater degree of disorder in the carbon structure. The full-width at half-maximum of the D band is also an important parameter. For a given excitation energy (i.e. photon wavelength) a larger FWHM of the D band indicates a greater inhomogeneity in local carbon-carbon bonding. Greater graphitic domain size and greater homogeneity are hallmarks of highly ordered carbons, which is usually only obtained with very high pyrolysis temperatures.

Raman spectra for CFP shows two relatively sharp peaks with comparable height. Compared to CFP, the pyrolized PAN fibers show a significantly broader D band at both pyrolysis temperatures. However, an obvious increase in G band intensity is observed when comparing the fibers pyrolized at 600 °C and 900 °C. This change indicates a dramatic increase in graphitic content occurs between the lower and higher pyrolysis temperatures.

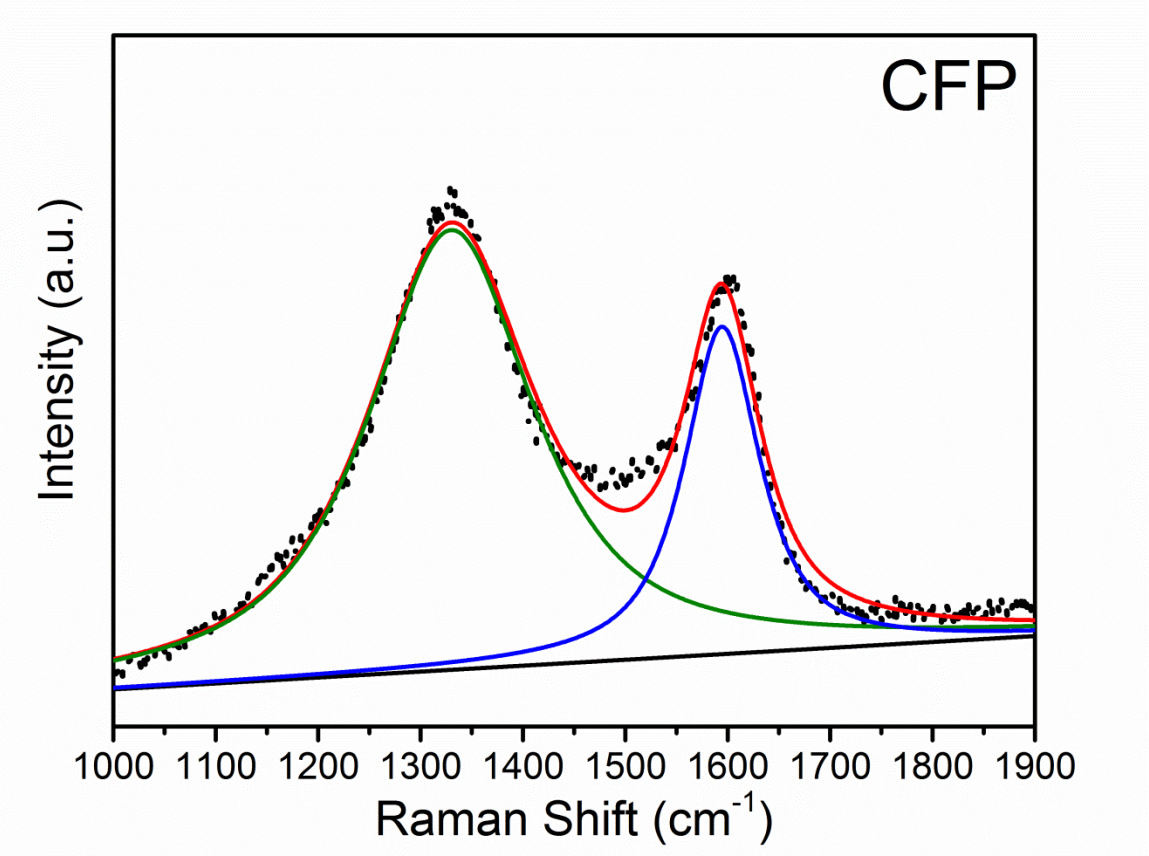

Figure 6.8 Raman spectroscopy for commercially obtained carbon fiber paper. Peak fitting is indicated by the blue D band, green G band and red total fit curves. Raw data is indicated with a dotted line.

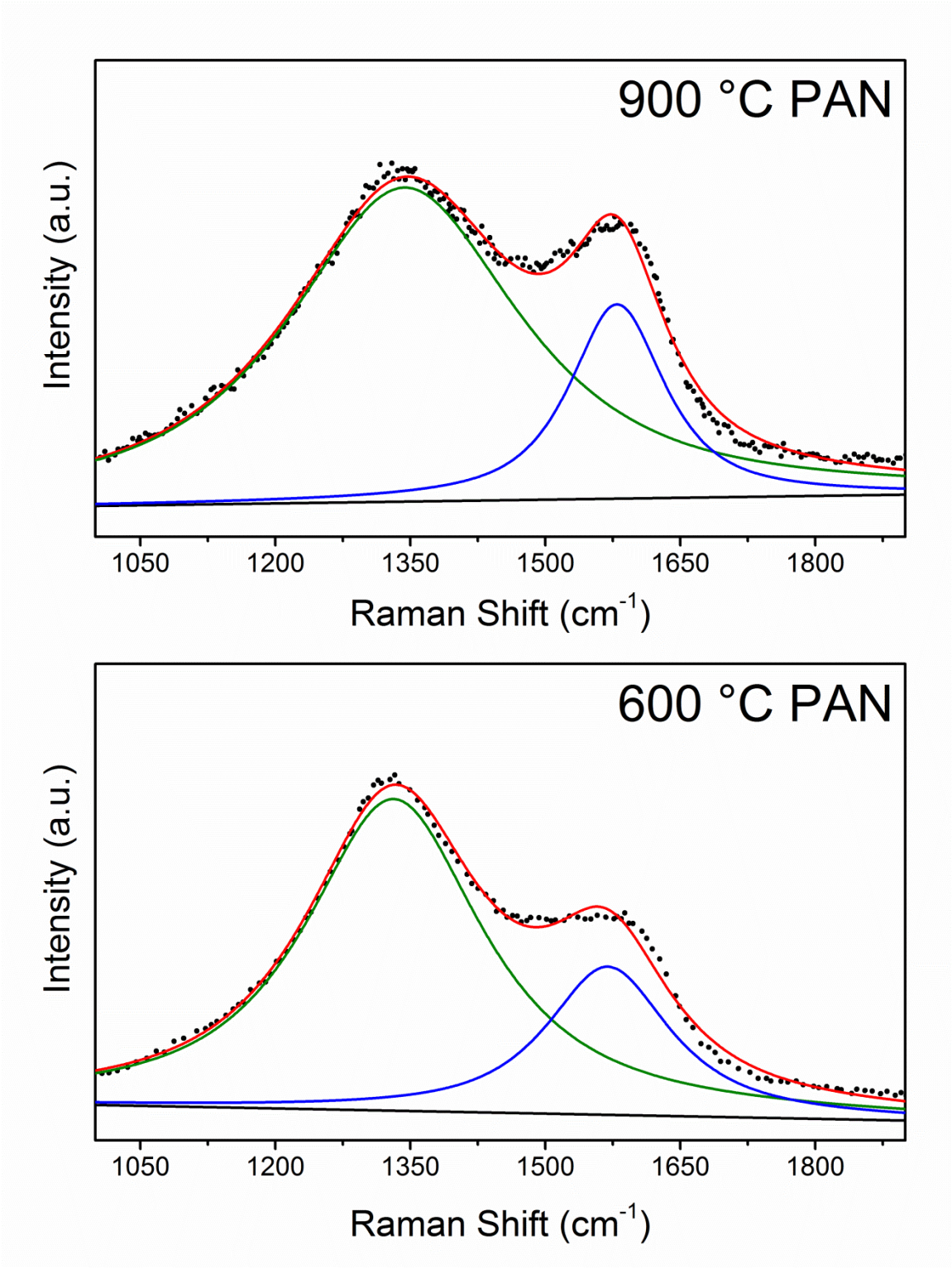

Figure 6.9 Raman spectroscopy for carbon fibers derived from electrospun PAN pyrolized at 600 °C and 900 °C. Peak fitting is indicated by the green D band, blue G band and red total fit curves. Raw data is indicated with a dotted line.

Meanwhile, Raman spectra of the pyrolyized Ligin/PVA fibers show minimal differences between the two pyrolyiss temperautres utilized. Both the FWHM of the D band, as well as the relativele intensity of the two bands, is fairly constant. In fact, for the samples analyized here the I_D/I_G ratio is slightly higher for the 600 °C pyrolized Lignin/PVA sample, thought is likely due to an intrinsic measurement error.

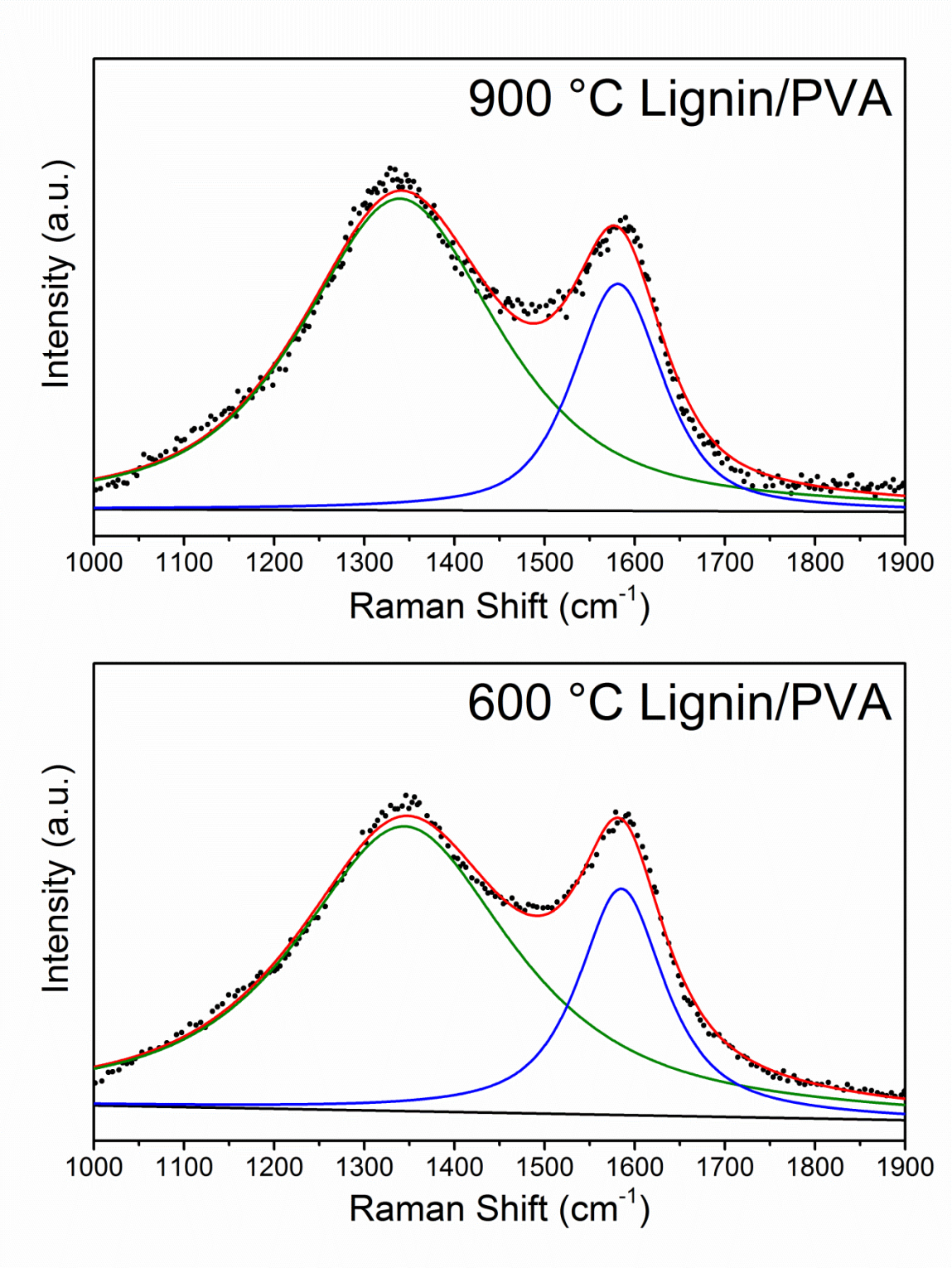

Figure 6.10 Raman spectroscopy for carbon fibers derived from electrospun Lignin/PVA pyrolized at 600 °C and 900 °C. Peak fitting is indicated by the green D band, blue G band and red total fit curves. Raw data is indicated with a dotted line.

As summarized in Table 6.3, CFP has the lowest bulk resistivity, as well as the lowest I_D/I_G ratio and smallest D peak width, indicating a larger content of graphitic domains compared to the other samples. While the 900 °C pyrolized Lignin/PVA fibers had a bulk resistivity on the same order of magnitude as the CFP, the PAN fibers were an order of magnitude higher even for the same pyrolysis temperature. Furthermore, both the I_D/I_G ratio and $FWHM_D$ of the 900°C PAN fibers were noticeably larger than either the 900 °C Lignin/PVA fibers or the CFP, which indicates a lower degree of graphitization. The resistivity and Raman results for the 600 °C pyrolized fibers support this conclusion, as while both the Lignin/PVA and PAN fibers show increased resistivity, this increase is five orders of magnitude for the PAN fibers while only three for the Lignin/PVA fibers.

Table 6.3 Electronic resistivity and Raman spectroscopy derived peak parameters for carbon fibers pyrolized at different temperatures.

Sample	Bulk resistivity (Ω m)	I_D/I_G	$FWHM_D$
600 °C Lignin/PVA	$1.0\text{-}2.6\text{x}10^{-1}$	1.26	288
600 °C PAN	$1.6\text{-}8.5\text{x}10^{2}$	2.10	237
900 °C Lignin/PVA	$3.6\text{-}6.5\text{x}10^{-4}$	1.37	258
900 °C PAN	$1.6\text{-}1.71\text{x}10^{-3}$	1.62	306
CFP	$1.4\text{-}1.9\text{x}10^{-4}$	1.34	192

6.3.3 Morphology and structure of $LiMn_2O_4$ on electrospun carbon fibers

$LiMn_2O_4$ was deposited onto electrospun fiber mats in a process identical to the technique described in previous chapters. The hydrothermal coating produced by coating 900 °C pyrolized PAN fiber is conformal but shows a morphology reminiscent of the 5:2 Li:Mn coating on CFP produced without NH_4Cl (Figure 4.13). Rather than a single morphology consisting of discrete crystallites expected for $LiMn_2O_4$, a combination of ultrafine nano-needles with the occasional faceted crystallite.

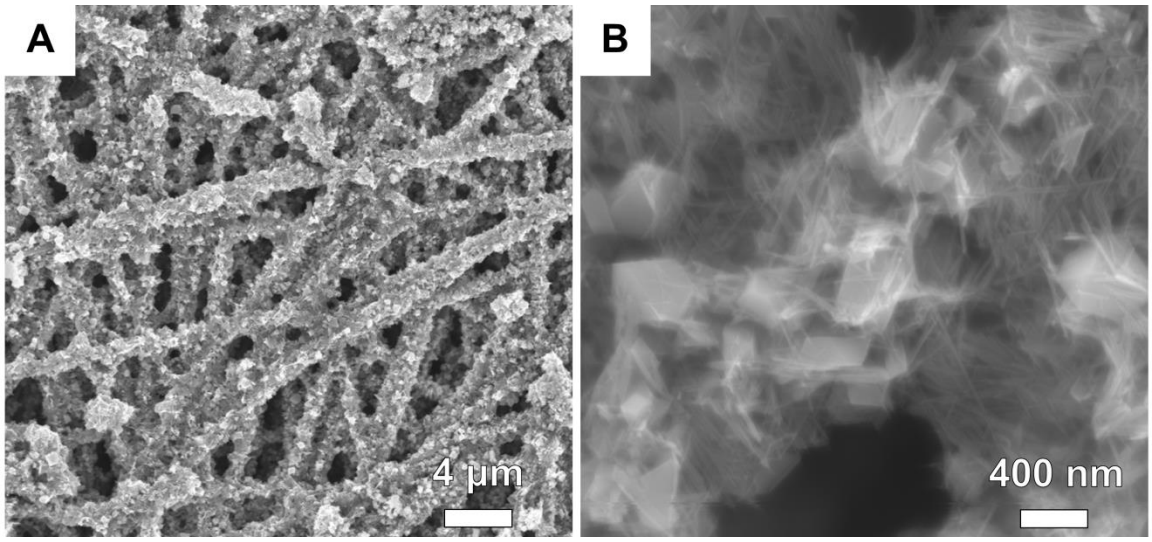

Figure 6.11 SEM images of hydrothermal coating on electrospun PAN fibers pyrolized at 900 °C at low magnification (A) and high magnification (B).

When PAN derived carbon fibers pyrolized at 600 °C are used, the coating produced by the hydrothermal process is further manipulated away from the desired morphology associated with phase pure $LiMn_2O_4$. No large crystallites are observed and the predominant coating morphology resembles the birnessite phases produced on CFP.

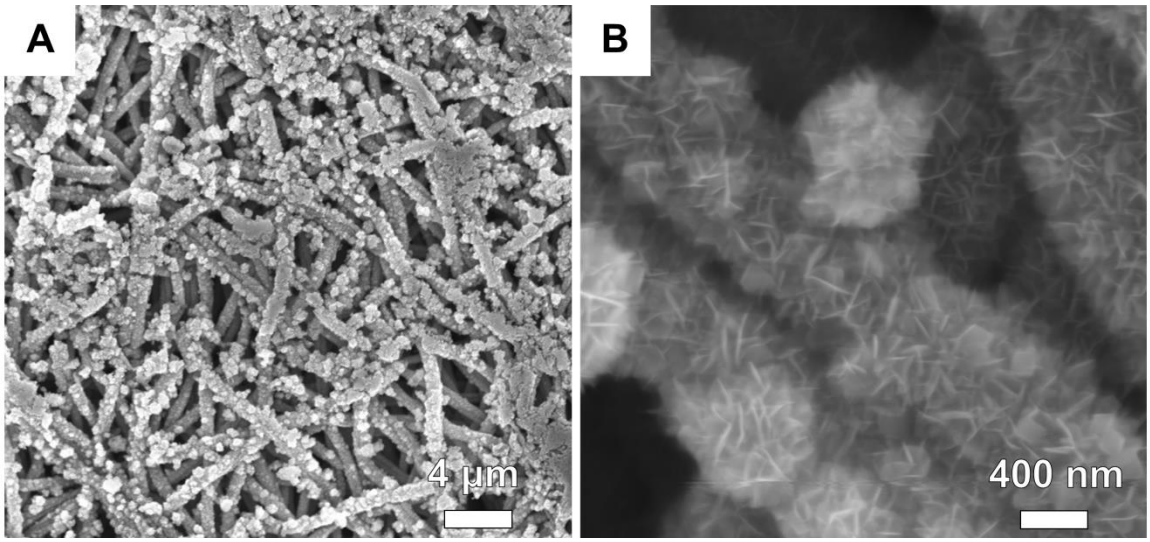

Figure 6.12 SEM images of hydrothermal coating on electrospun PAN fibers pyrolized at 600 °C at low magnification (A) and high magnification (B).

EDS testing shows that consistent with the observed morphology, the hydrothermal coatings on electrospun PAN contain some fraction of K, suggesting that the produced phase is not exclusively $LiMn_2O_4$. Furthermore, the relative concentration of K is reduced in the hydrothermal coating of 900 °C pyrolized PAN fibers, suggesting that the needle-like phase contains the observed K content.

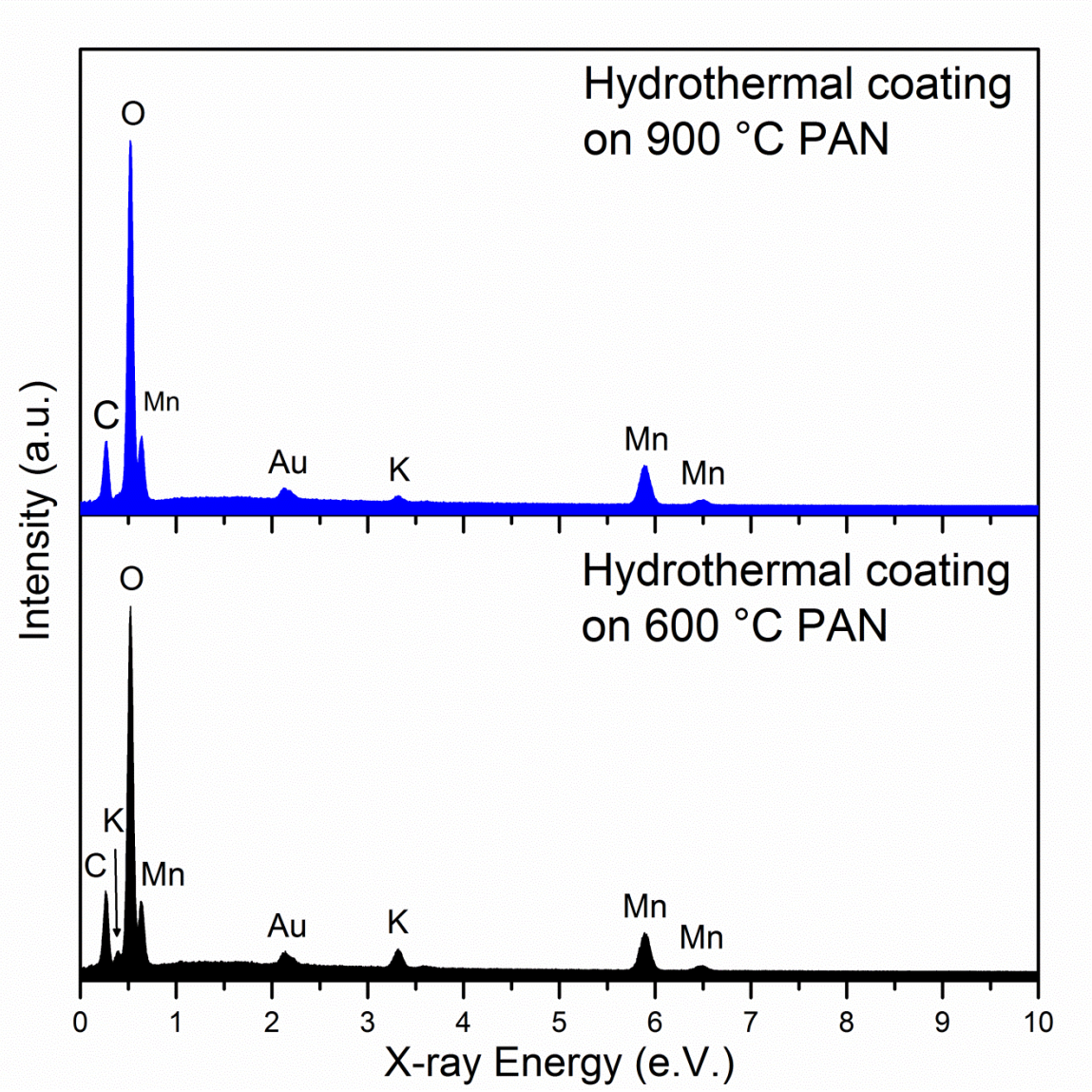

Figure 6.13 EDS hydrothermal coating from solution containing $LiOH•H_2O$, $KMnO_4$ and NH_4Cl onto PAN fibers pyrolized at 600 °C and 900 °C. Intensity scales are normalized relative to the O Kα peak at 0.525 eV.

XRD analysis of the hydrothermal coatings onto pyrolized PAN fibers confirms that the K containing phase is indeed birnessite, which is present in both the coatings on 600 °C and 900 °C pyrolized fibers. As was observed with SEM and EDS, the K containing birnessite phase becomes more intense in the coating on the lower pyrolysis temperature fibers. Meanwhile, the peaks associated with $LiMn_2O_4$ show the opposite trend and are significantly more intense in the coated 900 °C PAN fibers.

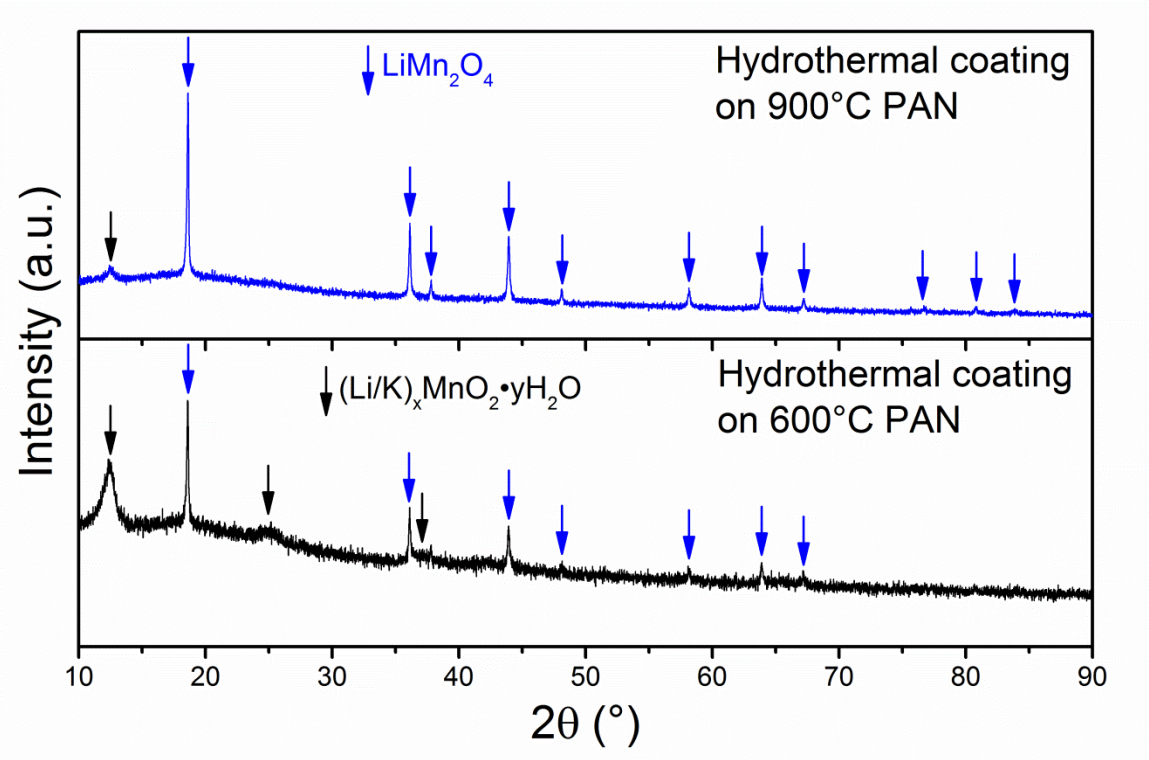

Figure 6.14 XRD patterns for hydrothermal coatings onto electrospun PAN fibers pyrolized at 600 °C and 900 °C.

The morphology of the hydrothermal coatings on pyrolized lignin/PVA fibers reveals that the carbon fibers are completely obscured by particulates. For the 900 °C pyrolized fibers the particulates are uniform and reminiscent of the phase pure $LiMn_2O_4$ coatings produced on CFP.

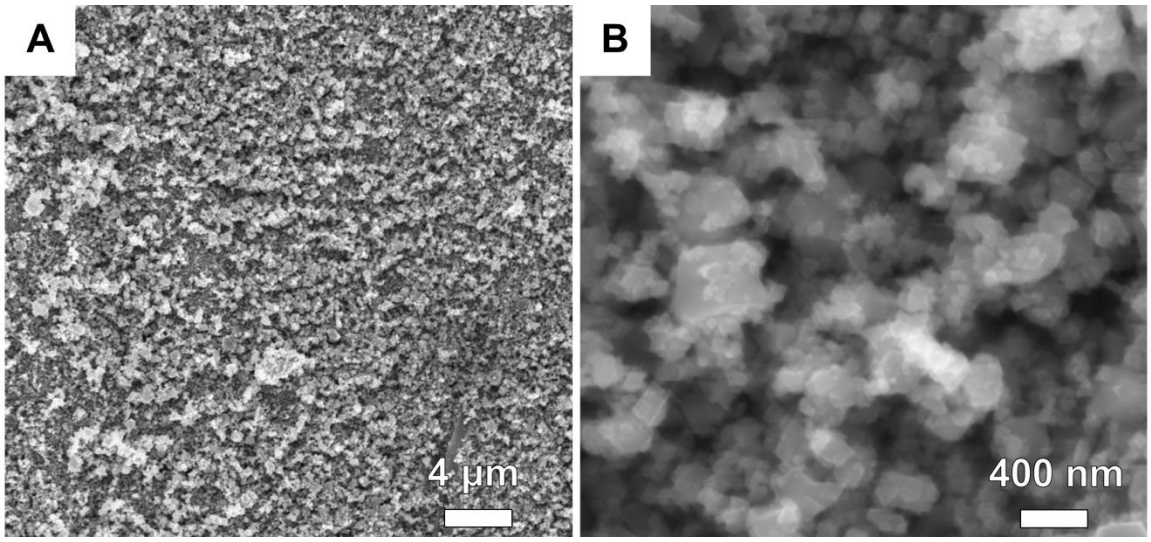

Figure 6.15 SEM images of hydrothermal coating on electrospun lignin/PVA fibers pyrolized at 900 °C at low magnification (A) and high magnification (B).

Hydrothermal coatings on 600 °C pyrolized lignin/PVA fibers appear similar to the coatings produced onto the 900 °C pyrolized fibers at low magnifications. Meanwhile, nanorod features are visible under higher magnification, suggesting that like the PAN derived fiber pyrolysis temperature may have some influence on the phases formed during the hydrothermal coating process.

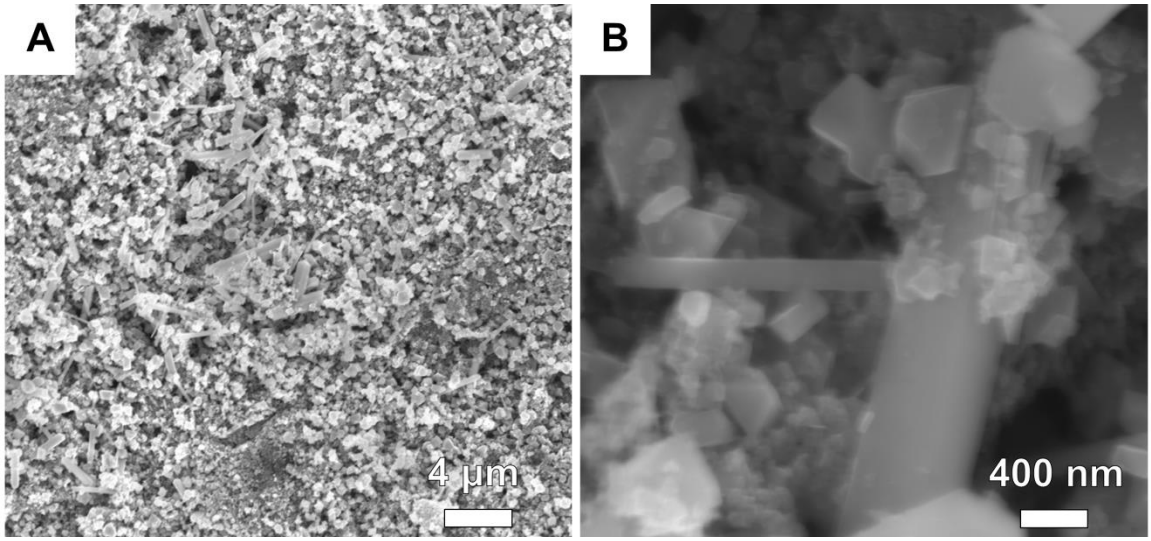

Figure 6.16 SEM images of hydrothermal coating on electrospun lignin/PVA fibers pyrolized at 600 °C at low magnification (A) and high magnification (B).

Elemental analysis of the hydrothermal coatings on lignin/PVA fibers does not detect K for either of the pyrolysis temperatures studied. Instead, Mn, O and C appear in nearly identical ratios indicating that the coatings have quite similar compositions.

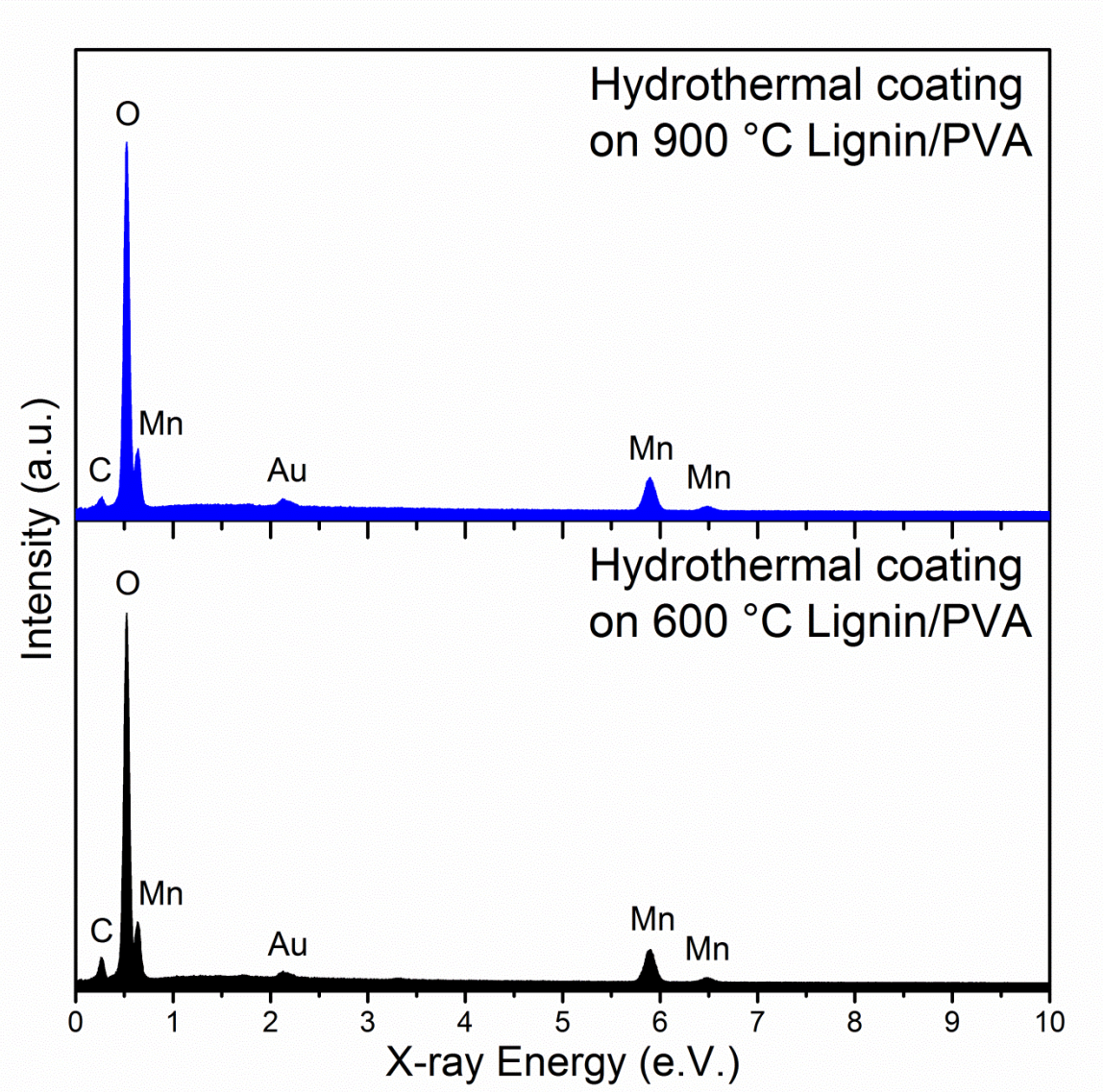

Figure 6.17 EDS hydrothermal coating from solution containing $LiOH{\bullet}H_2O$, $KMnO_4$ and NH_4Cl onto lignin/PVA fibers pyrolized at 600 °C and 900 °C. Intensity scales are normalized relative to the O Kα peak at 0.525 eV.

XRD confirms that while a small impurity phase of MnO(OH) is present in coatings produced on the 600 °C pyrolized lignin/PVA fibers, $LiMn_2O_4$ is the predominant phase formed.

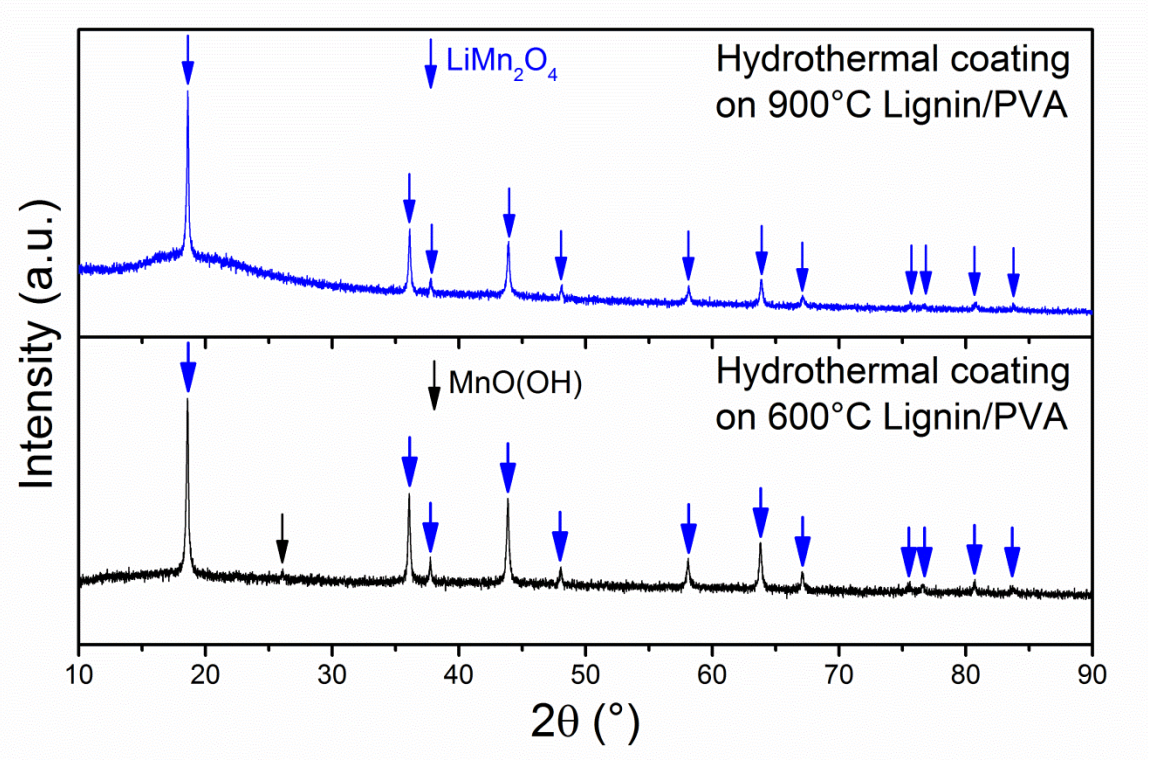

Figure 6.18 XRD patterns for hydrothermal coatings onto electrospun lignin/PVA fibers pyrolized at 600 °C and 900 °C.

Crystallite sizes for the $LiMn_2O_4$ phase deposited on the above discussed electrospun carbon fibers, as well as the typical mass loadings for each type is summarized in Table 6.4. Observed crystallite sizes are slightly larger than for the CFP based coatings, which under identical hydrothermal conditions had an average crystallite size of 38 nm (Table 4.2). Despite having larger diameter fibers and pore sizes, the PAN derived fibers had a higher mass loading of oxide after the hydrothermal coating. Meanwhile, the PAN derived fibers had the lowest density among all of the carbon fiber types tested, which may be the dominating factor determining maximum mass loading

during hydrothermal experiments. However, it is difficult to determine the relative contents of crystalline $LiMn_2O_4$ and amorphous birnessite in the hydrothermal coated PAN fibers which makes this conclusion somewhat misleading. For both substrate types the mass loading is significantly higher than the average value for CFP, though in all cases the standard deviation is relatively large. Variations in carbon fiber sheet thickness and hydrothermal conditions are likely the source of these deviations. Note that for the 600 °C pyrolized fibers, no standard deviation is provided due to limited experimental repetitions.

Table 6.4 Crystallite sizes and mass loading for $LiMn_2O_4$ coatings on electrospun carbon fibers

Carbon Fiber substrate	Average crystallite size (nm)	Mass loading (wt%)
600 °C PAN	46.7 (4.7)	57 (-)
900 °C PAN	56.1 (3.4)	64.9 (5.7)
600 °C lignin/PVA	41.5 (4.9)	45.9 (-)
900 °C lignin/PVA	45.8 (2.7)	53.1 (7.1)

6.3.4 Electrochemical testing of $LiMn_2O_4$ on electrospun carbon fibers

Galvanostatic testing shows a large dependence of specific capacity on pyrolysis temperature. While both the 600 °C and 900 °C pyrolized fibers showed evidence of crystalline $LiMn_2O_4$ by XRD with similar morphologies to the CFP based electrodes, all of the 600 °C pyrolized fiber electrodes show increased overpotential resulting in decreased capacity, even at a low rate of C/10. It seems very probable that this overpotential is due to the significantly increased bulk resistivity observed for the lower temperature pyrolized carbon fibers. Because the 600 °C pyrolized lignin/PVA fibers have lower resistivity, produced a mostly phase-pure $LiMn_2O_4$ coating, and have lower

mass loading, the specific capacity for these electrodes it over triple that of the hydrothermal coated 600 °C PAN fibers.

For the 900 °C pyrolized samples the specific capacities at lower current densities are much closer regardless of carbon precursor and are comparable to the $LiMn_2O_4$@CFP electrodes discussed in previous chapters. With the increase in oxide mass loading, this significantly enhances the overall gravimetric energy density of carbon fiber based electrodes.

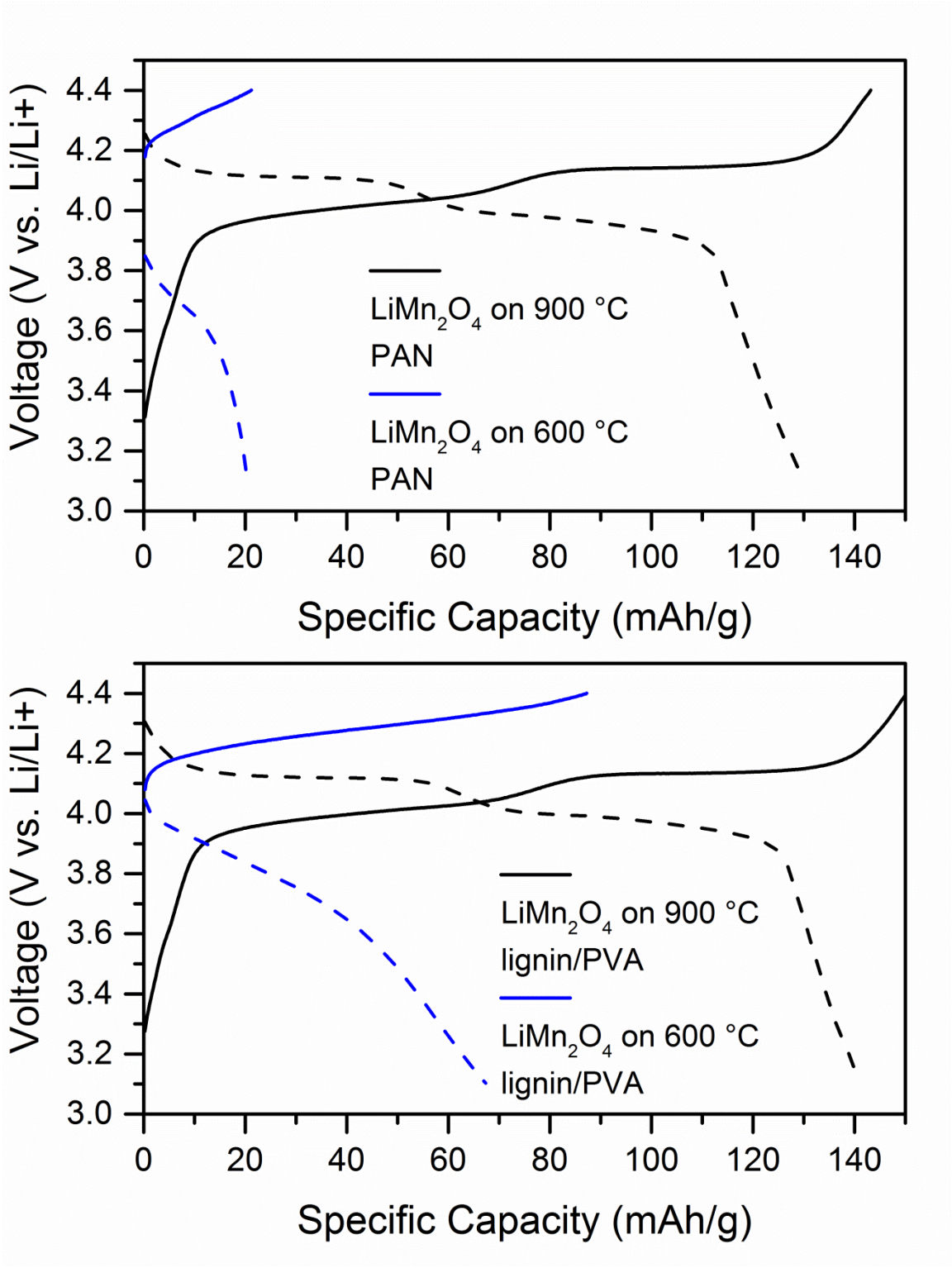

Figure 6.19 Charge and discharge testing at a rate of C/10 for $LiMn_2O_4$ on PAN and Lignin/PVA fibers at difference pyrolysis conditions. Current density and specific capacities are normalized by the assumed mass of $LiMn_2O_4$ in the electrode.

Increasing the current density during galvanostatic testing reveals a huge discrepancy between the PAN based and lignin/PVA based fibers. Like with the 600 °C pyrolized fibers, a combination of resistivity, mass loading and phase purity could be contributing to the decreased capacity and rate capability for the hydrothermal coated 900 °C pyrolized PAN fibers. While the 900 °C pyrolized lignin/PVA fibers show capacities and rate capabilities comparable to the uncoated $LiMn_2O_4$ on CFP shown in Chapter 5, the 900 °C PAN fibers demonstrate near-zero reversible capacity at rates above 1C. Meanwhile, the lignin/PVA fibers show rate capabilities comparable to the CFP and tape cast electrodes demonstrated in previous chapters.

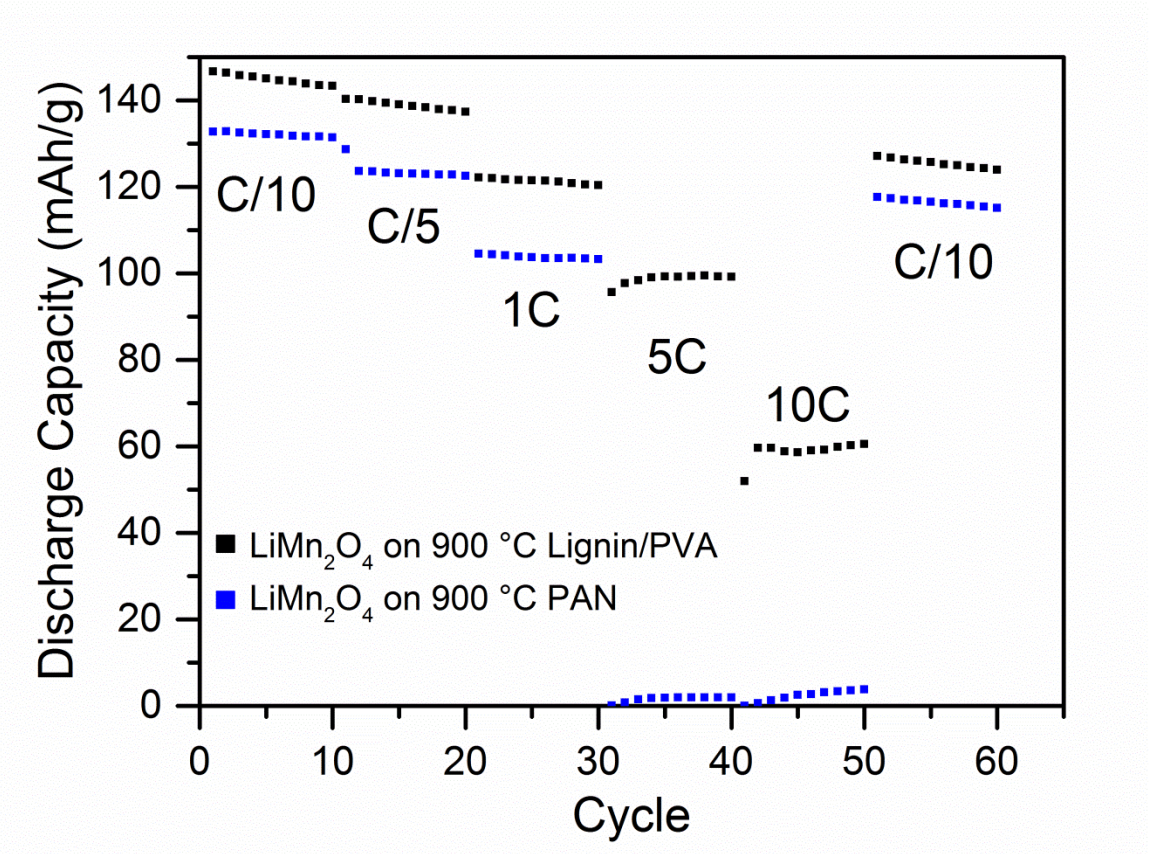

Figure 6.20 Rate capability of $LiMn_2O_4$ coated carbon nanofibers derived from electrospun lignin/PVA and PAN pyrolized at 900 °C. Rate current densities and capacities are normalized by the assumed mass of $LiMn_2O_4$ in the electrode.

Rate capabilities of the two carbon nanofiber based electrodes were further characterized by conducting cycling voltammetry and multiple rates. Consistent with the observed poor high-rate capability, the PAN derived electrodes show a transition from quasi-reversible to irreversible behavior at a much lower voltage sweep rate than either CFP or lignin/PVA based fibers.

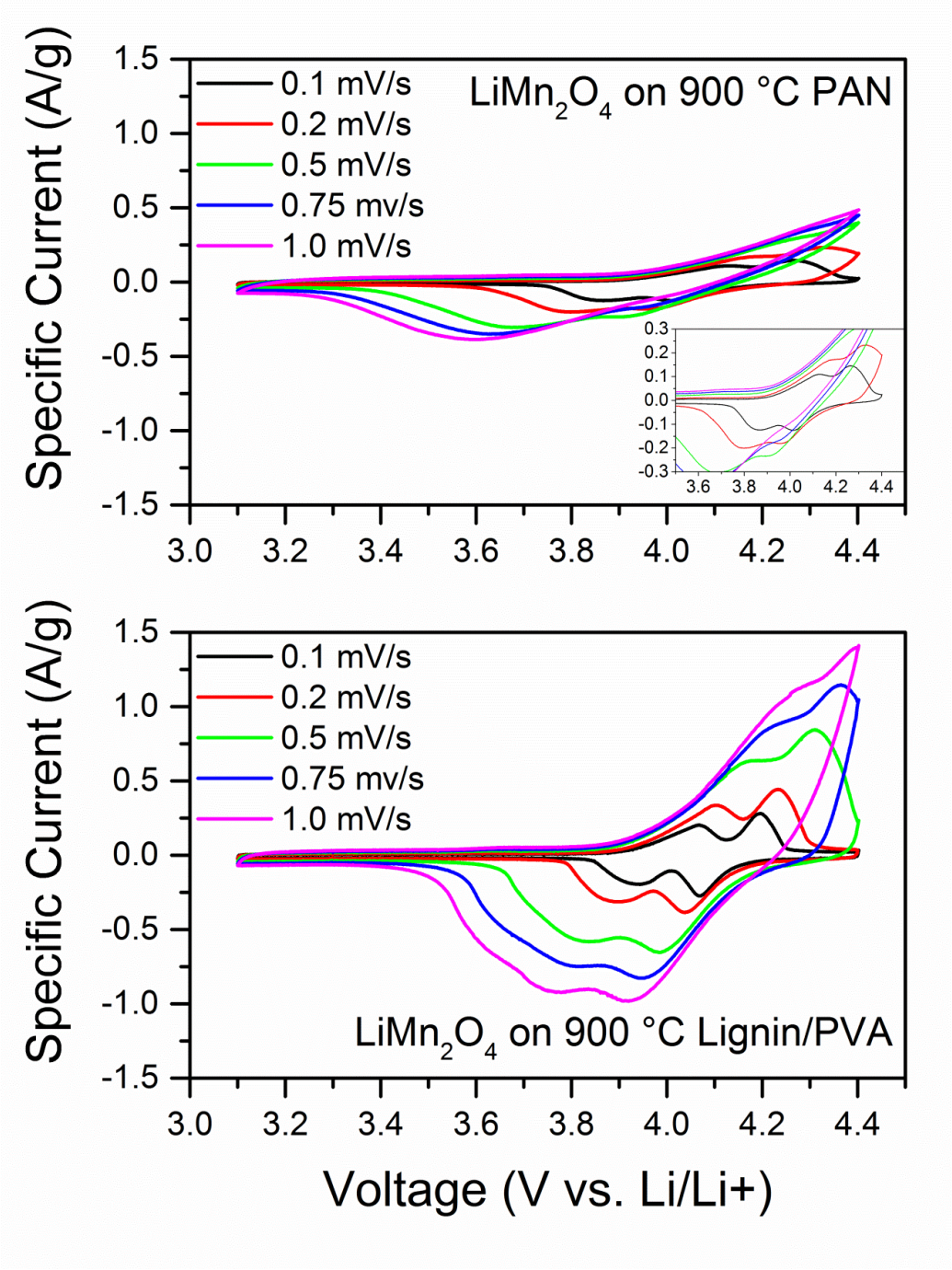

Figure 6.21 Cyclic voltammograms conducted on $LiMn_2O_4$ coated carbon nanofibers derived from electrospun lignin/PVA and PAN pyrolized at 900 °C.

While the PAN derived fibers had the highest mass loading of oxide after the hydrothermal treatment, which is desirable, the combination of factors described in this chapter that led to poor performance make the lignin/PVA fibers a clearly superior

choice. One obvious method to improve the performance of the PAN derived fibers is to simply increase the pyrolysis temperature to improve the graphitic quality, and in turn the electronic conductivity, of the composite electrodes. Still, it seems plausible that the higher mass loading of oxide was in some way due an intrinsically higher reactivity of the PAN derived fibers towards the hydrothermal solution. This higher reactivity could result in a preferential formation of amorphous oxide species, which as seen for the CFP electrodes result in higher overall mass loading of the hydrothermal coating (Table 4.3).

To further compare the carbon nanofiber based electrodes with the CFP based electrodes described in the previous chapters, $LiMn_2O_4$ on lignin/PVA electrospun fibers pyrolized at 900 °C were cycled 250 times at room temperature at a rate of 1C. The nanofiber based electrodes show slightly lower rates of capacity loss to the as-prepared $LiMn_2O_4$ on CFP electrodes, which maintain on average about 89 mAh/g of an initial 133 mAh/g (67 %) (Figure 5.9) compared to 76 mAh/g of an initial 132 mAh/g (58%) respectively.

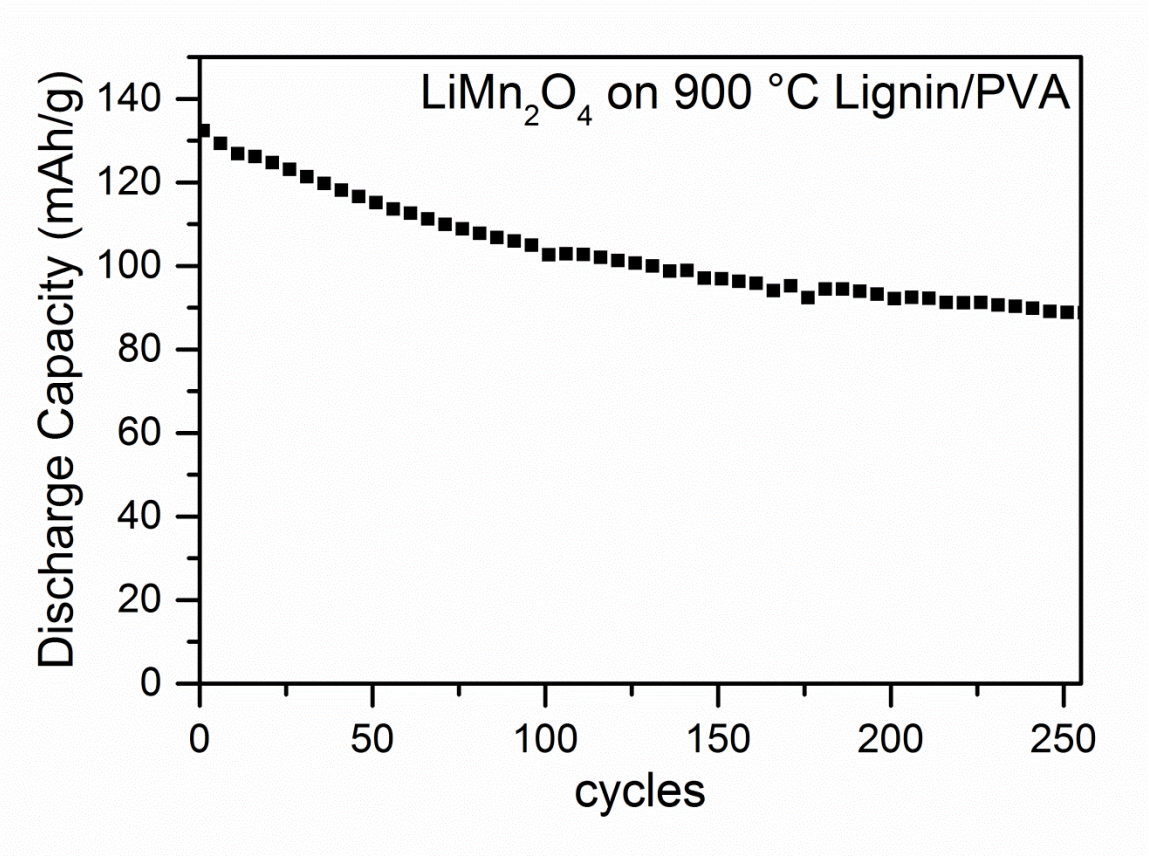

Figure 6.22 Extended cycling of $LiMn_2O_4$ on electrospun lignin/PVA fibers pyrolized at 900 °C. Cycling was conducted at a rate of 1C at room temperature.

6.4 Conclusions

In this chapter electrospun fibers were pyrolized to produce non-woven mats of interconnected carbon fibers with similar overall morphology to the CFP used in the previous chapters. Despite similar electrospinning conditions and identical pyrolysis procedures carbon fibers derived from lignin/PVA blends showed superior properties, both as bare carbon fibers and as composite electrodes, compared to fibers derived from PAN. The ultimate goal of this approach was to improve the overall mass loading, and thus energy density of carbon fiber based composite electrodes. At an initial 1C capacity of 133 mAh/g and an average mass loading of 53 wt%, the effective capacity of composite electrodes using hydrothermal coatings on 900 °C pyrolized lignin/PVA is

70.5 mAh/g. This is a large improvement over the 33 mAh/g based on the total weight of the CFP electrode (Chapter 4), but still inferior to the 82 mAh/g total weight capacity of tape cast electrodes. Another important parameter which has not yet been discussed is volumetric capacity. For the ~150 micrometer thick lignin/PVA samples, the volumetric capacity is about 45 mAh/cm^3. The same tape cast electrodes mentioned above have volumetric capacities of nearly 200 mAh/cm^3. While increases in mass loading seem plausible, improving the volumetric capacity of porous carbon fiber based electrodes, especially when using nano-particulate coatings, is more challenging. Combined with the rapid capacity fading, poor energy density, and uncertain scalability of electrospinning and hydrothermal precipitation the possibility of carbon fiber based LIB electrodes outperforming traditional tape cast electrodes seems slim.

7 ANALYSIS OF SURFACE-MODIFIED LIMN2O4 THIN FILM MODEL ELECTRODES

In the following chapter, the porous coatings of nanocrystalline $LiMn_2O_4$ on carbon fibers used in the previous chapters are replaced by dense $LiMn_2O_4$ films on conductive substrates. No binders or conductive additives are included, thus allowing for an unadulterated platform from which to study the $LiMn_2O_4$/electrolyte interface, particularly after modification by ALD. These model electrodes both remove any structural or chemical signature from the carbon fibers or other passive additives as well as the possibility for side reactions involving such additives. Thus, dense film electrodes enable an evaluation of the conclusions drawn regarding the structural and chemical changes resulting from electrochemical cycling of carbon fiber based electrodes which have much more complex geometries. In addition to the electrochemical and materials characterization techniques relied on in the previous chapters, *in situ* Raman spectroscopy is utilized in this chapter to gain some additional insight. The specific goal of this approach is to confirm the formation of a new phase by reaction of the electrolyte with the ALD aluminum oxide which results in both suppression of Mn dissolution and increases overall lithium diffusivity in the electrode.

7.1 Background on thin-film $LiMn_2O_4$ and Raman Spectroscopy

Films of $LiMn_2O_4$ have been researched extensively both for application in rechargeable microbatteries as well as to study fundamental interfacial effects governing the rate capability and capacity loss in lithium-ion battery electrodes [192-198]. Physical

vapor deposition techniques, specifically pulsed laser deposition (PLD) and radio-frequency (RF) sputtering are perhaps the most common approaches used to prepare thin films of $LiMn_2O_4$ and produce extremely uniform, smooth and dense films [48, 193-195, 197, 199]. Another popular technique involves depositing solutions containing metal-salt precursors by drop-coating, spin coating or spraying, though this technique usually produces lower quality films than physical vapor deposition [45, 47, 196, 200, 201].

Because of the simplified interfacial geometry and lack of inactive additives films have been used extensively to study the electrode-electrolyte interface. This property is particularly useful for Raman spectroscopy, which is limited for composite electrodes as inactive components can be degraded by the high energy laser. This degradation leads to artificial signatures not associated with native electrode species[202]. *Ex situ* Raman spectroscopy has been used extensively to characterize $LiMn_2O_4$ and these works provide important reference for the present study. In particular, several reports have highlighted the sensitivity of Raman spectroscopy to the lithium-content in $LiMn_2O_4$ [147, 202, 203]. In an example from early work in this area by Julien and Massot (Figure 7.1) a clear distinction is observed between the fully-lithiated $LiMn_2O_4$ and de-lithiated λ-MnO_2. In all of the spinel structured magnates the strongest vibrational mode (A_{1g}) occurring around 600-650 cm^{-1} is associated with stretching of the Mn-O bond, and as such is sensitive to the oxidation state of Mn. McLarnon and co-workers took advantage of this sensitivity to observe spontaneous λ-MnO_2 formation along with several electrolyte decomposition products after storing $LiMn_2O_4$ films in an $LiPF_6$ containing carbonate electrolyte at elevated temperatures [47]. By monitoring the formation of λ-MnO_2 through a reaction with the electrolyte, the researchers were able to infer that Mn dissolution had occurred. A few works have used *ex situ* Raman spectroscopy to characterize surface-modified electrodes, but only to determine whether the film had altered the near-surface structure of the underlying $LiMn_2O_4$ active material[204, 205].

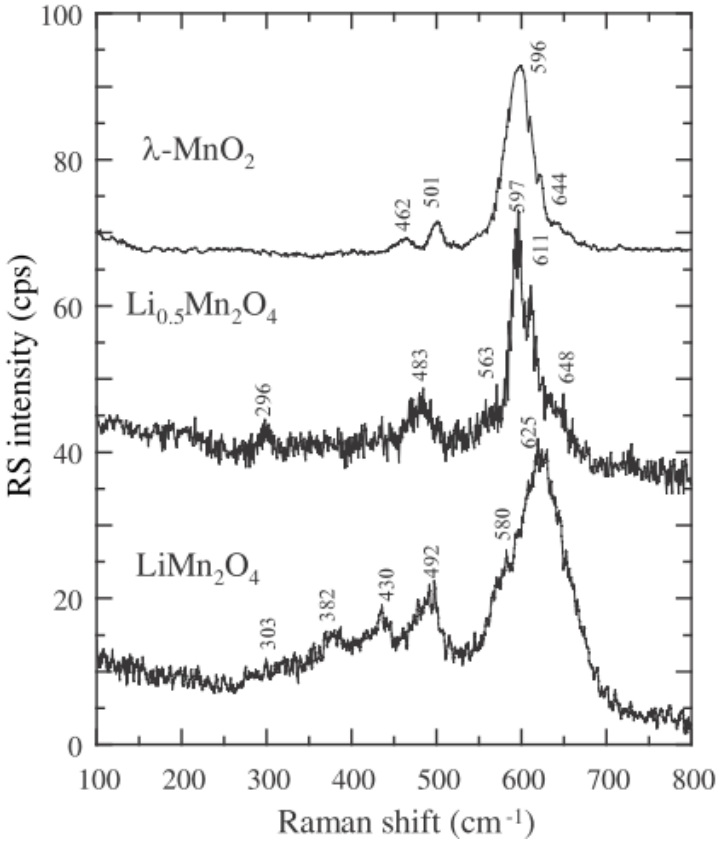

Figure 7.1 *Ex situ* Raman spectrum for $LiMn_2O_4$ with varying lithium contents (From Ref. 202).

For space groups which have a center of inversion (including the $Fd\bar{3}m$ structure belonging to $LiMn_2O_4$) only molecular vibrations which have "Gerade" symmetry, indicating no change in phase occurs after an inversion operation, are Raman-active. Five Raman bands are expected for ideal $LiMn_2O_4$ (A_{1g}, E_g, and three F_{2g} modes). Occasionally "extra" bands are detected, like the small band identified at 303 cm^{-1} in Figure 7.1, which are attributed to deviations from ideal structure. These features can be exceedingly difficult to differentiate from contaminants and new phases.

In situ testing of $LiMn_2O_4$ electrodes has also been demonstrated in a few cases to monitor the bulk structural changes which occur during lithiation and de-lithiation.

Scherson and co-workers used Raman spectroscopy with a single crystal $LiMn_2O_4$ microelectrode pressed against a piece of optical glass to observe these structural changes [206]. A noticeable contribution of the electrolyte is also observed for Raman spectrum collected *in situ*, which generally results in lower observed intensities for the underlying electrode or additional signal from fluoresce or Raman active electrolyte species [207]. The Scherson work avoided this by minimizing the electrode-electrolyte interface through cell design, while in the present study this interface is a prerequisite. In the Liu lab, a laser wavelength of 633 nm was found to minimize fluorescence from a 1M $LiPF_6$ in 1:1 EC:DMC electrolyte. Coincidently, this wavelength may also enhance the intensity of the A_{1g} band in λ-MnO_2, which was reported to resonate at a wavelength of approximately 620 nm [203].

7.2 Experimental Methods

7.2.1 Preparation of $LiMn_2O_4$ films by drop coating

Electrodes were prepared by drop coating a sol-gel solution of 100 mM Manganese Acetylacetonate and 55 mM Lithium Acetylacetonate in a solvent of 3:1 by volume 1-butanol:acetic acid, in a procedure derived from Park et. Al [201]. The substrates used were 1.1 cm diameter, 50.8 micron thick discs of 304 stainless-steel punched from a sheet of foil which were pressed flat under a load of 10 tons and then cleaned by sonication in ethanol and acetone. After cleaning, the flat foil discs were sputtered with a 100 nm layer of Pt by DC sputtering prior to spin coating to prevent reaction between the $LiMn_2O_4$ precursors with the steel substrate during calcination, as well as limit the contribution of Fe-oxides to the observed Raman spectrum. Sputtering conditions for the Pt layer were

45 minutes with a DC power of 20 W, a working pressure of $2.5e^{-2}$ mBar flowing Ar, and a substrate to target distance of approximately 15 cm.

The sol-gel solution was stirred in a sealed vial for a period of 4-5 hours and used within 24 hours of mixing, after which time significant solute precipitation was observed. Multiple layers were deposited sequentially to increase the film thickness, with each layer consisting of a 10 μL droplet. After each droplet was applied the wet sol was allowed to dry for a period of 20 minutes at room temperature in a fume hood to begin gelation. After drying at room temperature the gels were converted to thin, dense layers by rapidly heating to approximately 80 °C on a hot plate which evaporated residual solvent. This temperature was held for 20 minutes, following which the substrates were further heated on a hotplate to approximately 150 °C and held for a period of 20 minutes and finally 300 °C for 20 minutes. At this point the films darkened indicating an initial decomposition of the Li and Mn precursors. The entire process was repeated five times, after which the films were calcined at 700 °C for one hour with a heating and cooling rate of 1°C/min. Some electrodes were further modified via ALD using identical parameters to those described in Chapter 5. Based on the concentration of the precursor solute and the molecular weight of stoichiometric $LiMn_2O_4$ (180.8 g/mol), the five 10 μL droplets are expected to produce 0.452 mg of $LiMn_2O_4$. The thickness of the films (assuming they are produced perfectly flat) can be estimated by considering the theoretical density of $LiMn_2O_4$ (4.3 g/cm^3), which combined with the electrode area (0.969 cm^2) and theoretical mass yield, a minimum theoretical thickness of 1.02 microns is obtained. Another technique, RF Sputtering was also used to prepare $LiMn_2O_4$ films but provided poor electrochemical results. These attempts are summarized in Appendix B.

7.2.2 Electrochemical testing and physical characterization

Electrochemical testing was performed in both Swagelok style cells consistent with previous chapters, as well as in specialty cells for *in situ* Raman spectroscopy featuring a

transparent window. A schematic of the Raman cell used is shown in Figure 3.6. In both cases the working electrode was a 0.969 cm^2 sol-gel $LiMn_2O_4$ film, the counter electrode was lithium metal, and the electrolyte was 1 M $LiPF_6$ in 1:1 EC:DMC soaked into a glass fiber separator. For the Raman measurements a 0.16 cm (3/32") hole was punched into the glass fiber separator while a 0.24 cm (1/16") hole was punched into the lithium counter electrode. Keeping a minimum hole size in both the separator and counter electrode was critical to ensure good electrolyte wetting of the working electrode and as non-tortuous an ionic pathway as possible. Rate capability and galvanostatic testing was conducted with the Swagelok cells, while only cyclic voltammetry was used for the *in situ* Raman hardware with maximum scan rates of 200 μV/s.

Ex-situ testing was conducted on the thin film electrodes before and after electrochemical cycling. XRD, SEM and XPS analysis was conducted under identical conditions described in previous chapters. Raman measurements were conducted under identical conditions for both *in situ* and *ex situ* testing using a Renishaw RM 1000 spectromicroscopy system. A laser wavelength of 633 nm and total power of 8 mW was coupled with a 20x objective to achieve minimum a laser spot size of approximately 2 μm. To avoid damaging the samples, the microscope objective was deliberately defocused when collecting Raman spectrum. While this protects the sample from structural changes due to laser heating (demonstrated later in this chapter) defocusing the laser spot prevents the ability to achieve any appreciable amount of lateral resolution on the sample surface. Thus, multiple regions were analyzed and the thin film samples were generally found to be homogeneous.

7.3 Results and Discussion

7.3.1 Physical characterization of as-prepared sol-gel films

SEM analysis of the calcined, sol-gel films shows that they are relatively uniform featuring nanosized grains on the sample surface when deposited on stainless steel. A cross section image for a calcined film deposited on Si (without a sputtered Pt layer) shows a thickness which varies between 900 nm and 1.3 microns, close to the calculated thickness for a completely uniform film with theoretical density.

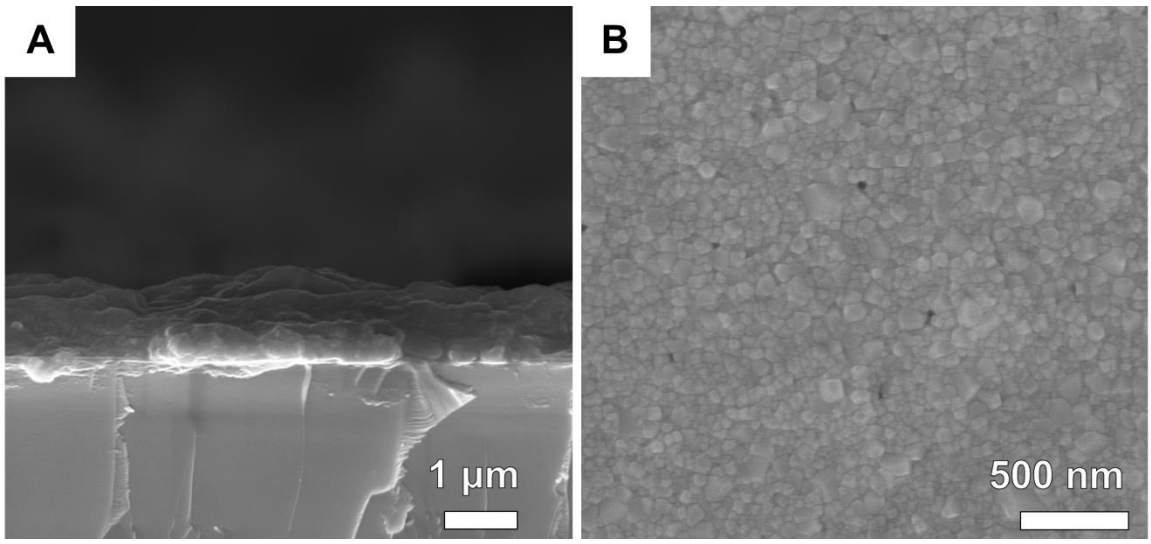

Figure 7.2 SEM images of drop-coated sol-gel $LiMn_2O_4$ film after calcining at 700 °C for 1 hour. A cross-section image of a film deposited on Si (A) shows a total thickness of approximately 1 µm, while a top down image for a film deposited on Pt coated stainless steel (B) shows a relatively dense polycrystalline surface.

While elemental analysis shows only minimal traces of carbon, suggesting a complete decomposition of the organic precursor compounds, the relative intensity of the Mn and O Kα x-rays at 5.894 eV and 0.525 eV respectively is nearly half that of the values observed for $LiMn_2O_4$ on carbon fibers (Table 4.3) at only 7.8%. This could imply a non-stoichiometry in the sol-gel film, or that x-rays from other oxide phases are being detected. In some regions (not shown) Fe from the substrate, along with the Pt detected

throughout, is also observed. “Matrix effects” which influence the ability of x-rays to escape from samples with varying stoichiometry, densities and morphology may be the main cause for this apparent decrease in Mn:O ratio.

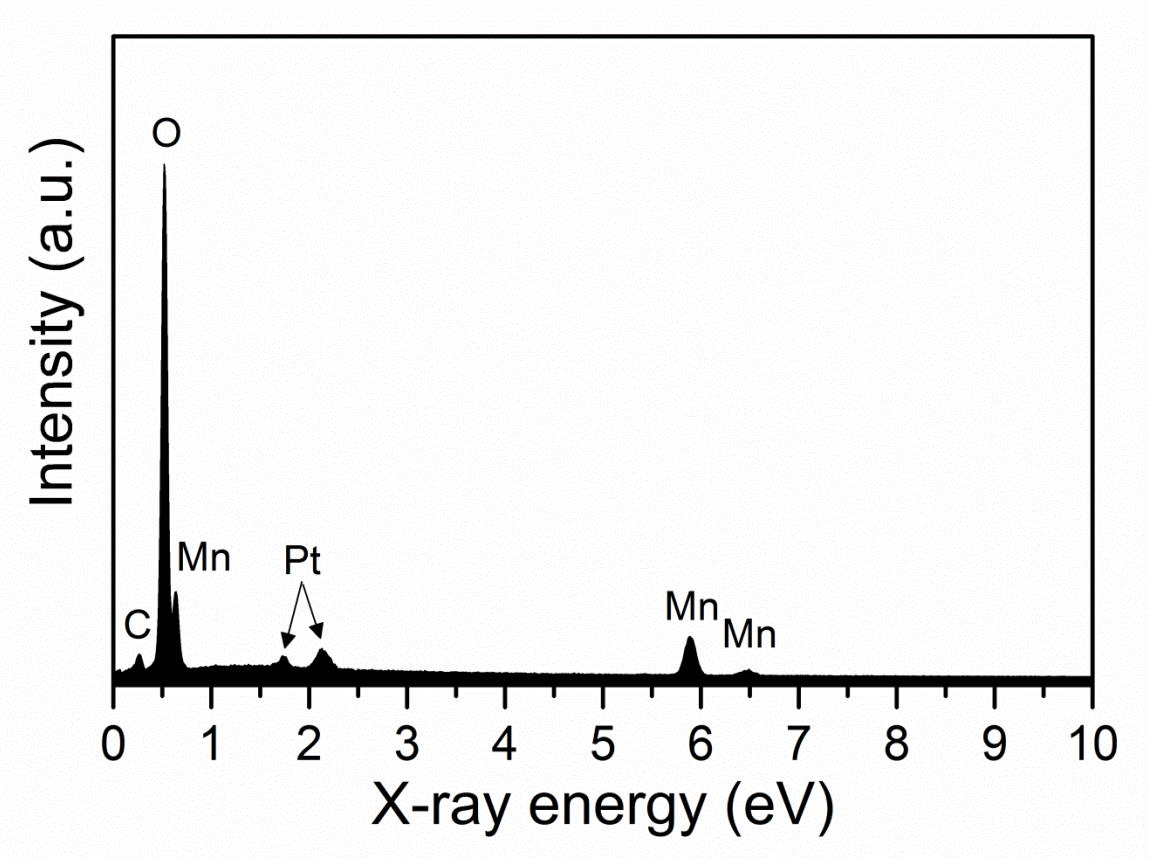

Figure 7.3 EDS of spin-coated $LiMn_2O_4$ film on Pt coated stainless steel after calcining at 700 °C for 1 hour.

XRD shows that in addition to peaks assignable to Pt and the stainless steel substrate, six peaks are assignable to $LiMn_2O_4$ are also found. Based on the lattice position calculated from the most intense $LiMn_2O_4$ peak occurring at approximately 18.6 ° 2θ, the as-prepared film has a lattice constant identical to stoichiometric $LiMn_2O_4$.

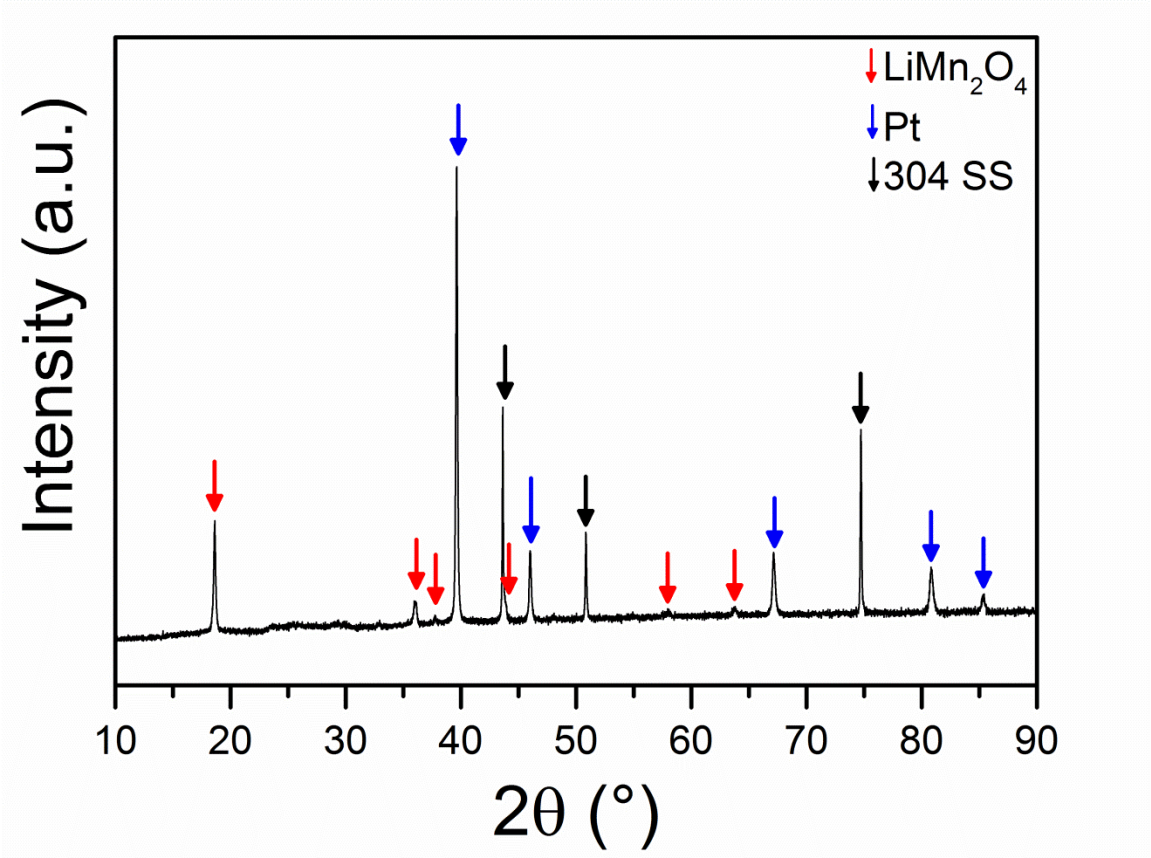

Figure 7.4 X-ray diffraction pattern for drop-coated sol-gel $LiMn_2O_4$ on Pt coated stainless steel after calcination at 700 °C for 1 hour.

Ex situ Raman spectroscopy shows that the as-prepared sol-gel films, both with and without ALD films, have detectable A_{1g} (625 cm^{-1}) and $F_{2g}^{(1)}$ (~580 cm^{-1}) modes (Figure 7.5A), while none of the other Raman bands attributed to $LiMn_2O_4$ occurring at lower wavenumbers (Figure 7.1) could be identified. An additional shoulder peak at higher wavenumber is also observed for the sol-gel films. Reference samples of commercial powder $LiMn_2O_4$ and LMO@CFP show nearly identical Raman bands to each other (Figure 7.5B), while the relative intensity and position of the A_{1g} and $F_{2g}^{(1)}$ bands is slightly shifted for the films. This, along with the higher wavenumber band, suggests that the films have some slight deviation from an ideal structure or composition of $LiMn_2O_4$. The sol-gel films also show a broad region of higher intensity from 300 cm^{-1}

to 400 $^{-1}$ which is not attributed to any specific molecular vibration, but may indicate some structural variation in the films relative to the reference samples.

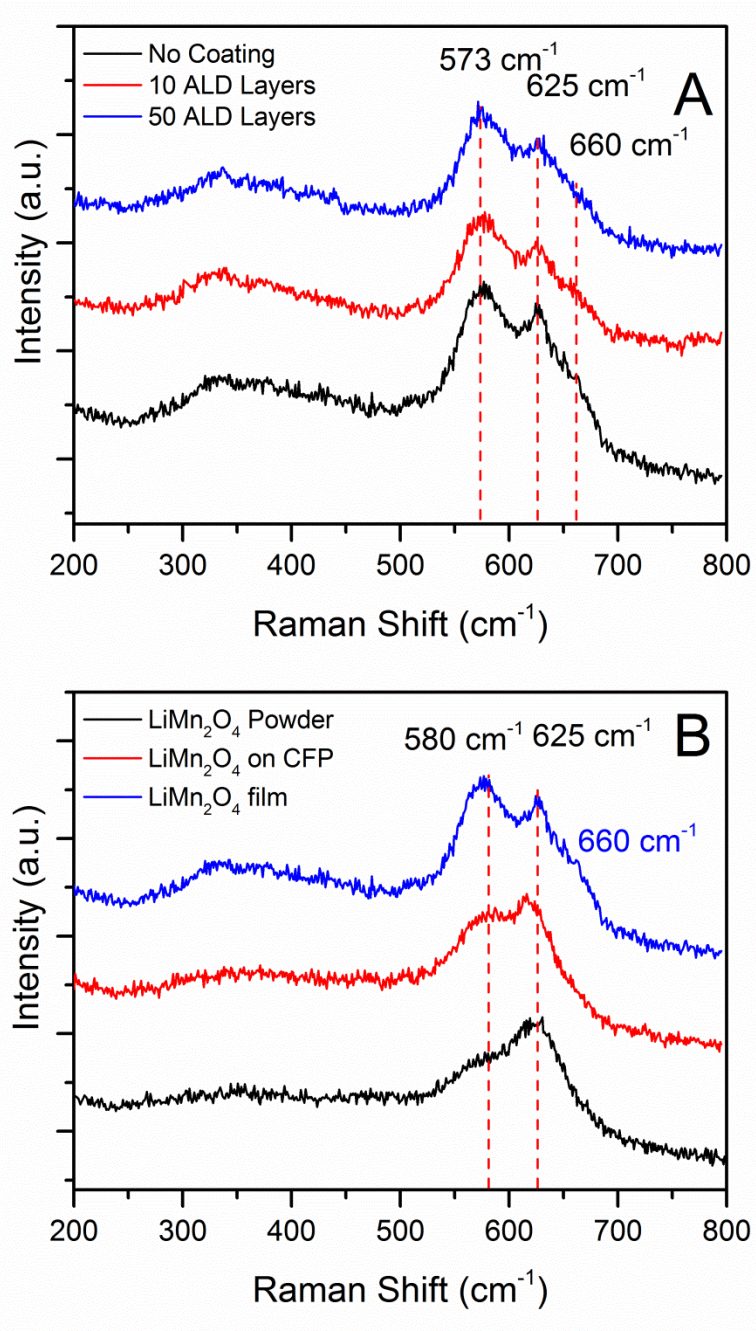

Figure 7.5 Comparison of *Ex Situ* Raman spectrum for sol-gel film electrodes with and without ALD coatings (A) and comparison of sol-gel $LiMn_2O_4$ film to reference samples including store-bought $LiMn_2O_4$ powder and LMO@CFP (B).

Literature reports have highlighted that the Raman bands observed for $LiMn_2O_4$ are extremely sensitive to structure and stoichiometry, which may be the origin of the deviations in the sol-gel film electrodes. However, heating due to the focused laser is also a considerable factor. Figure 7.6 shows that focusing the Raman laser on the sample surface can introduce significant distortion of the observed Raman spectrum. For the commercial powder reference sample, a shift toward smaller wave numbers is observed along with the appearance of a higher-wavenumber shoulder peak when the Raman laser is focused to a minimum spot size. Meanwhile, massive changes are observed in both the total background intensity as well as Raman band position for the LMO@CFP sample when using a focused laser point. In addition to the high background intensity and shift in Raman band position, the damage caused on LMO@CFP due laser heating is apparent under the 20x magnification of the optical microscope objective. For the CFP containing electrodes the laser heating may be sufficient to enable oxidation of the carbon fibers which as observed in Chapter 5 can be catalyzed by $LiMn_2O_4$. Despite the apparent deviation from the reference samples, the film electrodes show no variation between a focused or defocused condition other than a decreased intensity for the A_{1g} and $F_{2g}^{(1)}$ peaks. It is unclear whether this is because they are highly resistant to laser heating, or so susceptible that even defocusing the spot size cannot prevent laser heating from occurring. To avoid possible complications in spectrum analysis due to sample heating, a "defocused" condition was used for all subsequent Raman measurements.

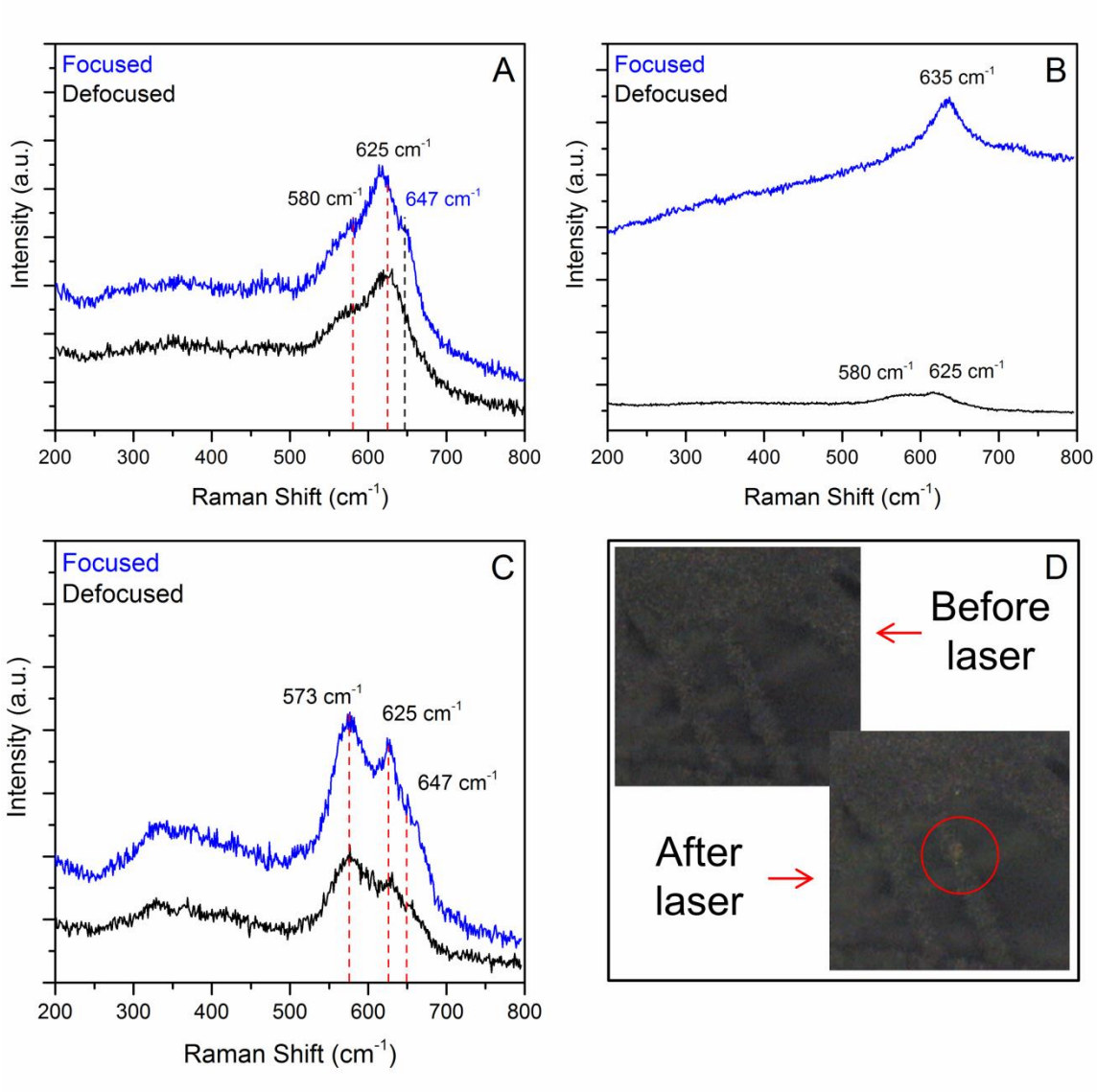

Figure 7.6 Influence of laser focus on commercial $LiMn_2O_4$ (A) LMO@CFP(B), and sol-gel $LiMn_2O_4$ film (C). In (A,B) red dashed lines indicate the position of common Raman bands, while the black dashed line indicates the shoulder band only observed in the laser-heated sample. An optical image showing the region damaged by the Raman laser on LMO@CFP is shown in (D).

7.3.2 Electrochemical testing of surface-modified films

Cyclic voltammetry testing of the ALD modified thin film electrode shows similar results with the ALD modified LMO@CFP electrodes in that the highest current density is observed for the 10 ALD layer electrode. As with the CFP and carbon nanofiber based

electrodes, two pairs of oxidation and reduction peaks are observed for the sol-gel film electrodes at approximately 4.04 V vs. Li/Li+ and 4.17 V vs. Li/Li+ during charge and 4.09 V vs. Li/Li+ and 3.97 V vs. Li/Li+ during discharge.

Galvanostatic testing conducted at a rate of C/10 shows a voltage profile consistent with the CV measurements shown in Figure 7.7, but with a noticeably reduced specific capacity (less than 100 mAh/g) compared to the carbon fiber based electrodes, which is typical of thin-film $LiMn_2O_4$ electrodes. Similar to the carbon fiber electrodes however, the uncoated and 10 ALD layer coated electrodes have comparable discharge capacities, while the 50 ALD layer coated electrode has slightly less capacity but with identical redox peak positions.

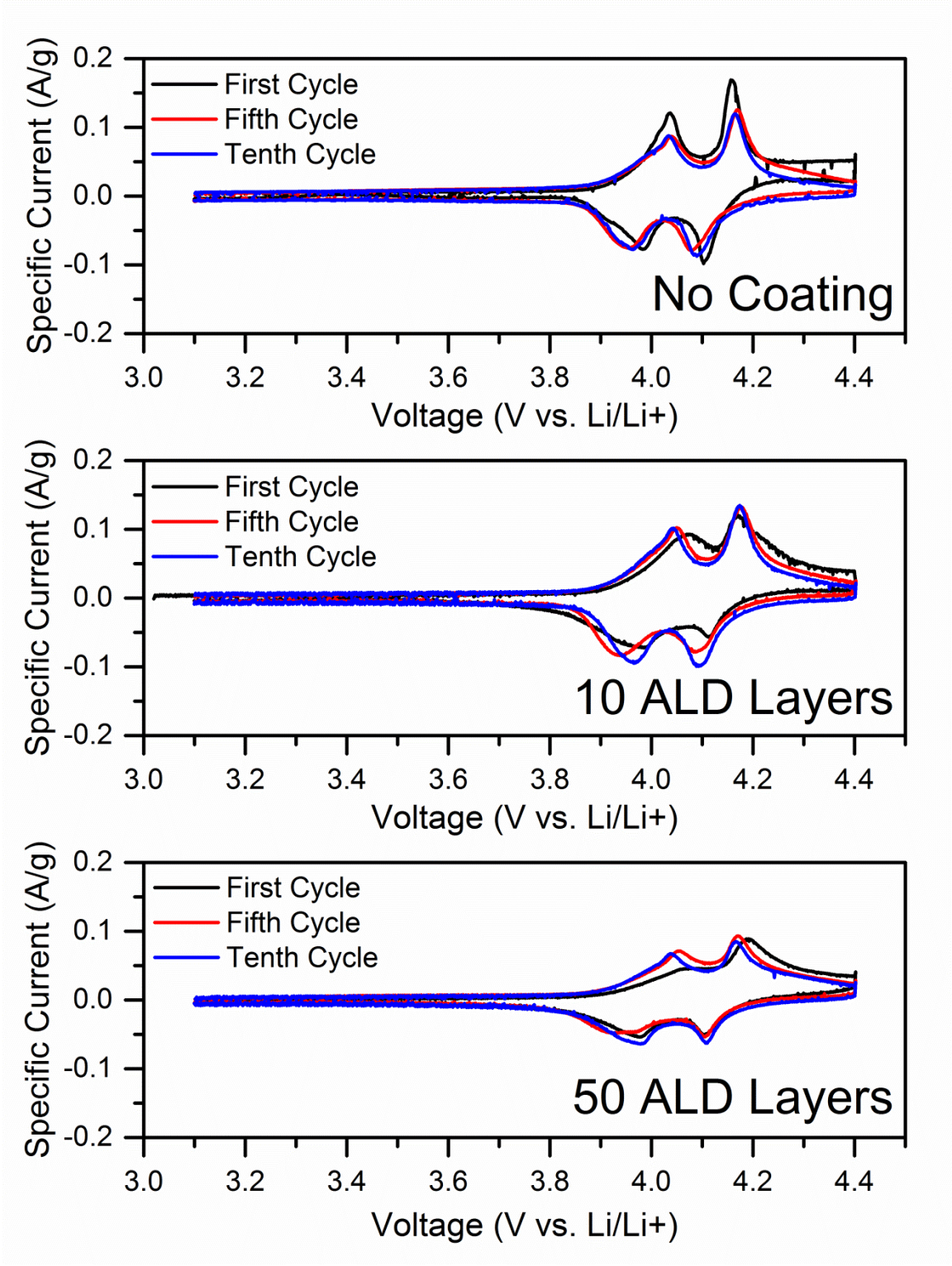

Figure 7.7 Cyclic voltammograms at a scan rate of 50 μV/s for sol-gel $LiMn_2O_4$ films with and without ALD coatings.

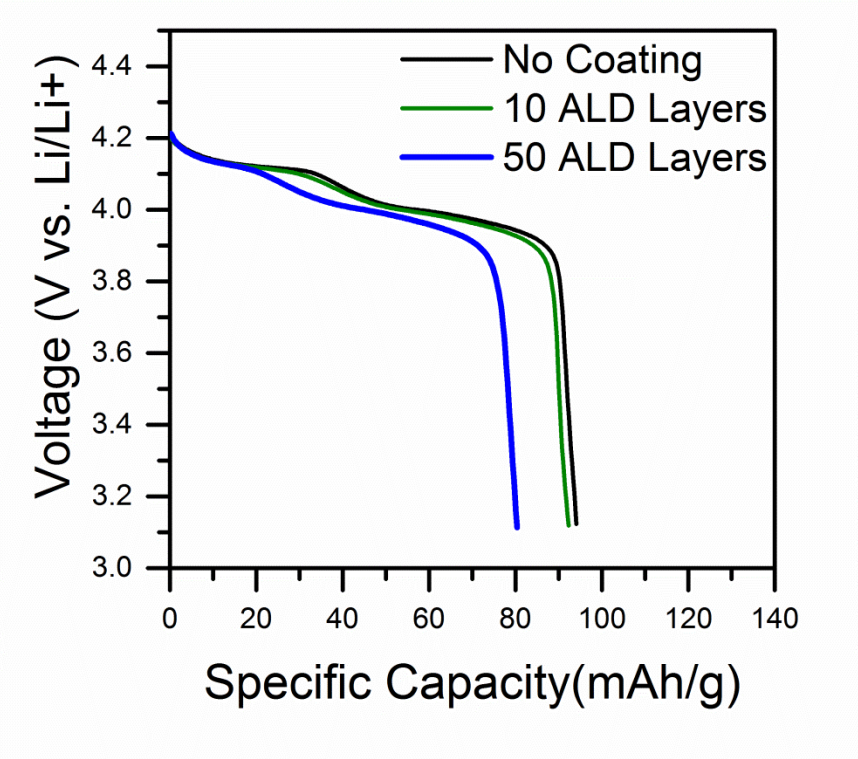

Figure 7.8 Specific discharge capacity for sol-gel thin film $LiMn_2O_4$ electrodes with and without ALD. Current density of C/10 defined based on assumed $LiMn_2O_4$ mass loading of 0.452 mg.

Increasing scan rate CV testing was used to determine the apparent Li+ diffusivity in the thin film electrodes. Compared to the CFP and carbon nanofiber based electrodes, the dense sol-gel films show much better overall reversibility as evidenced by minimal warping of the voltammograms shape and peak positions with increasing scan rate. While the uncoated and 10 ALD layer CFP based electrodes had peak separation of over 300 mV at a scan rate of 1 mV/s the corresponding film electrodes are below 200 mV of separation, indicating good electrochemical reversibility in the films. Similar comparisons can be made at all scan rates. Contradicting this observation however is the relatively lower ratio of peak currents for the films, which were slightly higher for the CFP based electrodes. A deviation from a completely reversible 1.0 ratio for CFP based electrodes was attributed in Chapter 5 to side reactions such as irreversible reaction of a minority phase or electrolyte oxidation. While an impurity phase seems less likely for the

sol-gel films which were calcined at 700 °C, the small mass of active material may make the overall current contribution from electrolyte oxidation more apparent. Values of peak current ratio and peak separation were derived from these plots and are summarized in Table 7.1.

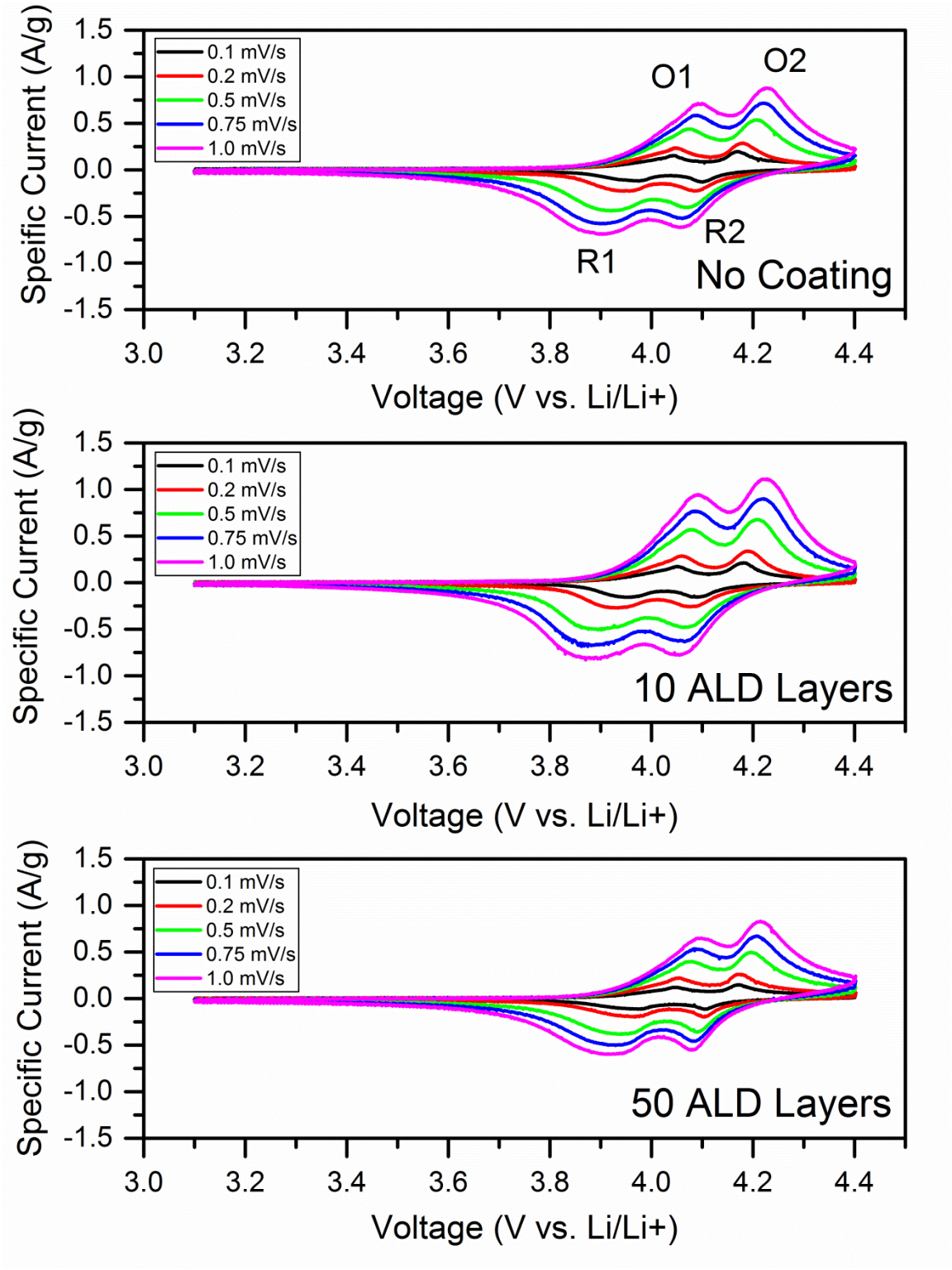

Figure 7.9 Cyclic voltammograms for $LiMn_2O_4$ thin film electrodes with and without ALD coatings.

Table 7.1 Summary of values derived from CV measurements for $LiMn_2O_4$ thin films with and without ALD coatings.

Scan rate (mV/s)	I_{R1}/I_{O1}	I_{R2}/I_{O2}	$\Delta V_{(O1-R1)}$ (mV)	$\Delta V_{(O2-R2)}$ (mV)
No Coating				
0.1	0.83	0.60	69	70
0.2	0.96	0.80	102	96
0.5	0.92	0.82	155	135
0.75	0.89	0.81	179	161
1	0.87	0.79	188	169
10 ALD Layers				
0.1	0.90	0.74	97	91
0.2	0.90	0.80	126	106
0.5	0.84	0.75	184	139
0.75	0.82	0.75	195	149
1	0.82	0.74	197	162
50 ALD layers				
0.1	0.94	0.77	73	62
0.2	0.88	0.75	87	76
0.5	0.90	0.77	138	106
0.75	0.86	0.75	156	123
1	0.85	0.72	161	135

Like with the CFP based electrodes, plots of peak current versus the square root of scan rate (Figure 7.10) show a linear relationship. Thus, the Randles-Sevchik equation is again applied to calculate lithium diffusivity. The 10 ALD layer coated electrodes are again observed to have slightly higher apparent lithium diffusivity than the uncoated electrodes, while the 50 ALD layer coated electrodes are slightly lower. All of the film samples show diffusivity values approximately two orders of magnitude lower than the CFP counterparts; however all of the calculated values are consistent with literature reports for $LiMn_2O_4$. Because the Randles-Sevhick equation assumes a planar, infinitely thick diffusion region, the porous CFP electrodes have an effectively higher electrode area than the superficial surface area used for the calculation, leading to a higher apparent diffusivity.

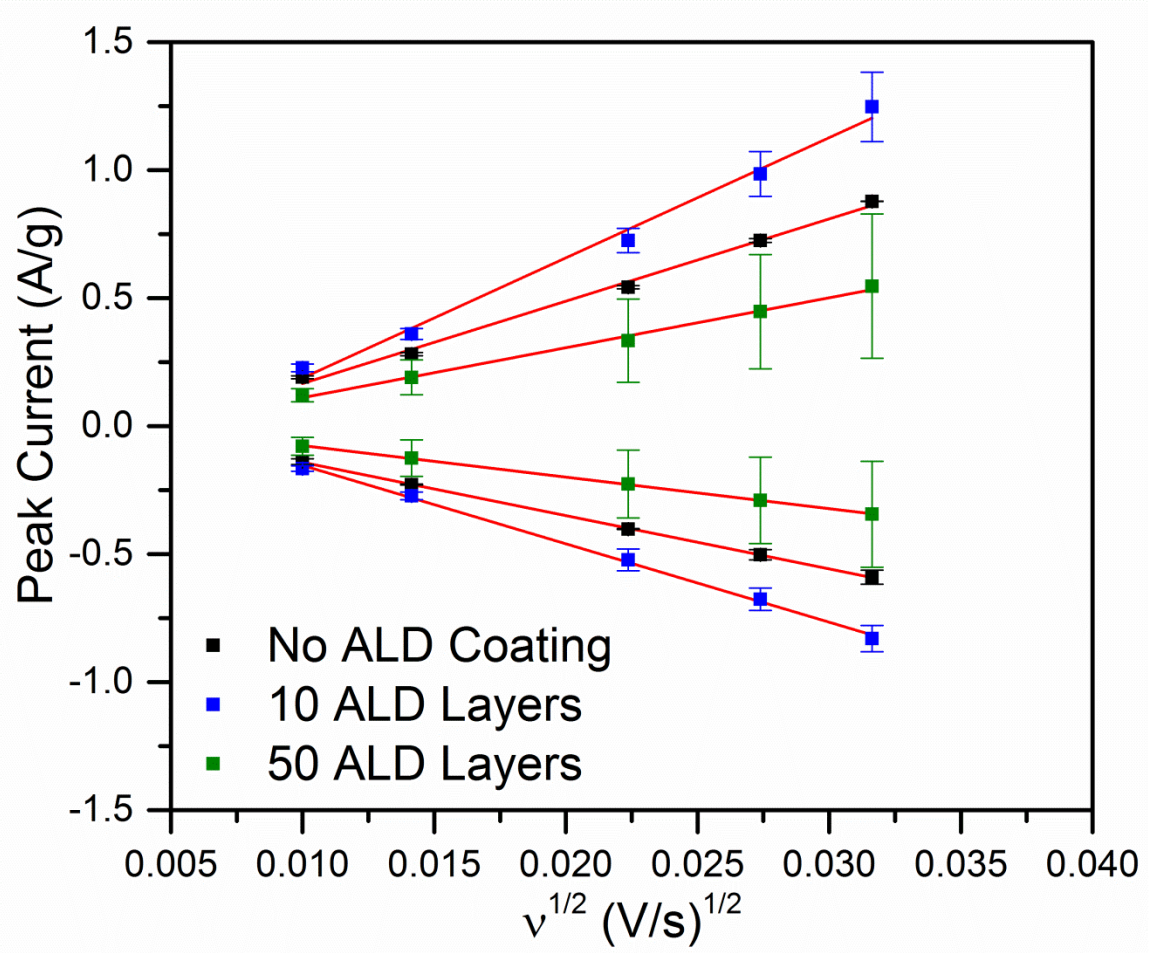

Figure 7.10 Peak current vs. square root of scan rate for sol-gel $LiMn_2O_4$ thin films with and without ALD coatings.

Table 7.2 Calculated values of lithium diffusivity sol-gel $LiMn_2O_4$ thin films derived from second oxidation and reduction peaks observed by CV.

Sample	D_{Li}, O2 (cm^2/s)	D_{Li}, R2 (cm^2/s)
No ALD coating	$2.05\text{-}4.16 \times 10^{-12}$	$0.87\text{-}2.03 \times 10^{-12}$
10 ALD Layers	$2.78\text{-}8.28 \times 10^{-12}$	$1.46\text{-}3.67 \times 10^{-12}$
50 ALD Layers	$0.78\text{-}1.59 \times 10^{-12}$	$3.26\text{-}6.29 \times 10^{-13}$

7.3.3 Characterization of surface-modified films by *ex situ* XPS and Raman spectroscopy

Analysis of the Mn 2p and Al 2p photoelectron lines for the surface modified films is completely consistent with the observations made with surface modified CFP based electrodes. Using the same peak shape constraints described in Chapter 5, and average manganese oxidation state of 3.51+ was determined for the uncoated electrode, while decreased oxidation states of 3.42+ and 3.40+ were calculated for the 10 and 50 ALD layer coated electrodes, respectively. This decreased oxidation state, which was also observed for the CFP electrodes, indicates that the alumina precursor (TMA) is very likely acting as a reducing agent at the outer surface of the $LiMn_2O_4$ electrodes. Also like the CFP based electrodes, the 50 ALD layer coated electrode shows a significant decrease in Mn 2p intensity relative to the other samples, indicating that the thickness of the ALD coating on the sol-gel film electrodes is comparable to the CFP based electrodes. Meanwhile peak fitting for the Al 2p photoelectron line was accomplished with a single peak with binding energies and FWHM values comparable to that of the ALD coated CFP electrodes, indicating that a single bond type of Al-O is present in the as-prepared thin film samples.

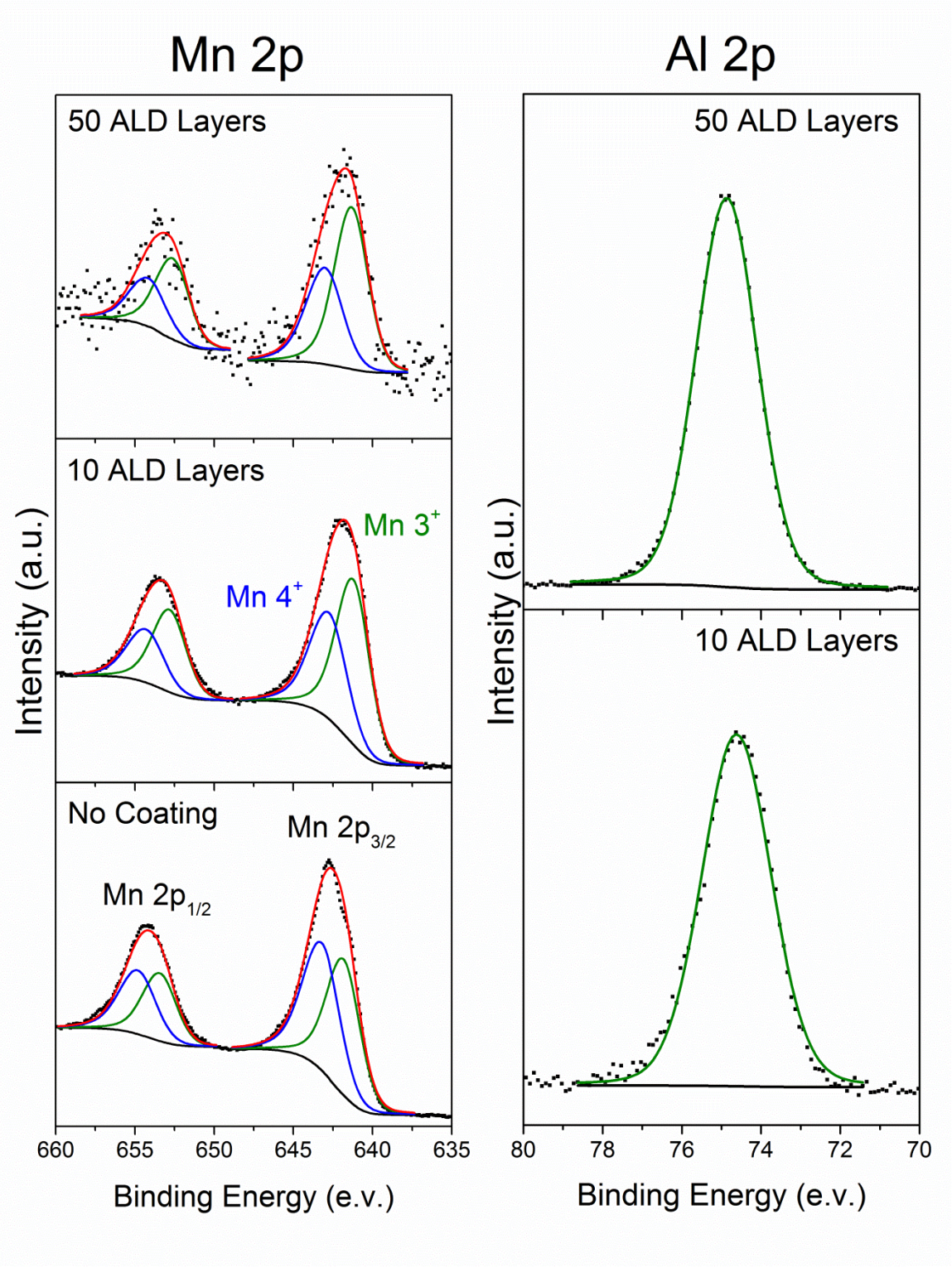

Figure 7.11 XPS characterization of Mn 2p and Al 2p photoelectron lines for as-prepared sol-gel films.

In addition to monitoring the changes of Mn and Al photoelectrons after electrochemical cycling, analysis of the F1s peak was added to confirm the formation of Al-F concluded from the CFP based electrodes. Furthermore, samples were also analyzed after simple exposure to electrolyte at room temperature for 24 hours, without the inclusion of Li metal or current flow. All of the reactions suggested between the Al_2O_3 layer and HF in the electrolyte are independent of the cathode state of charge or potential, thus similar reactions are expected to occur even under *in vitro* conditions.

Both after electrolyte exposure and electrochemical cycling, the Mn 2p peak shows similar trends with the CFP electrodes. Specifically, a slight reduction in Mn oxidation state is observed for the uncoated electrode, while the 10 ALD electrode maintains an oxidation state close to 3.5+. One major deviation in the sol-gel films compared to the CFP electrodes is found in the Mn 2p photoelectrons for the 50 ALD layer sample. Unlike the CFP electrodes, the thin-film electrodes do not show a significant increase in Mn 2p signal to noise ratio after electrochemical cycling. Instead, fitting of the Mn 2p photoelectron lines for the 50 ALD layer coated electrodes is inconclusive for all of the thin film samples, leading to inconsistent separations between Mn $2p_{3/2}$ and Mn $2p_{1/2}$ (usually around 11.6 eV for $LiMn_2O_4$) peaks and low values of calculated oxidation state.

In the CFP based electrodes, the increased signal to noise ratio in the Mn 2p peak for the 50 ALD layer electrodes was attributed to redistribution of Mn from the electrode interior to the surface of the ALD coating, which was supported by TEM analysis of these electrodes after electrochemical cycling. While this process cannot be ruled out for the sol-gel electrodes it seems based on the XPS analysis to be less significant in comparison to the CFP based electrodes, possibly due to the more consistent morphology of the dense electrodes which would be assumed to have a more homogenous coating by ALD.

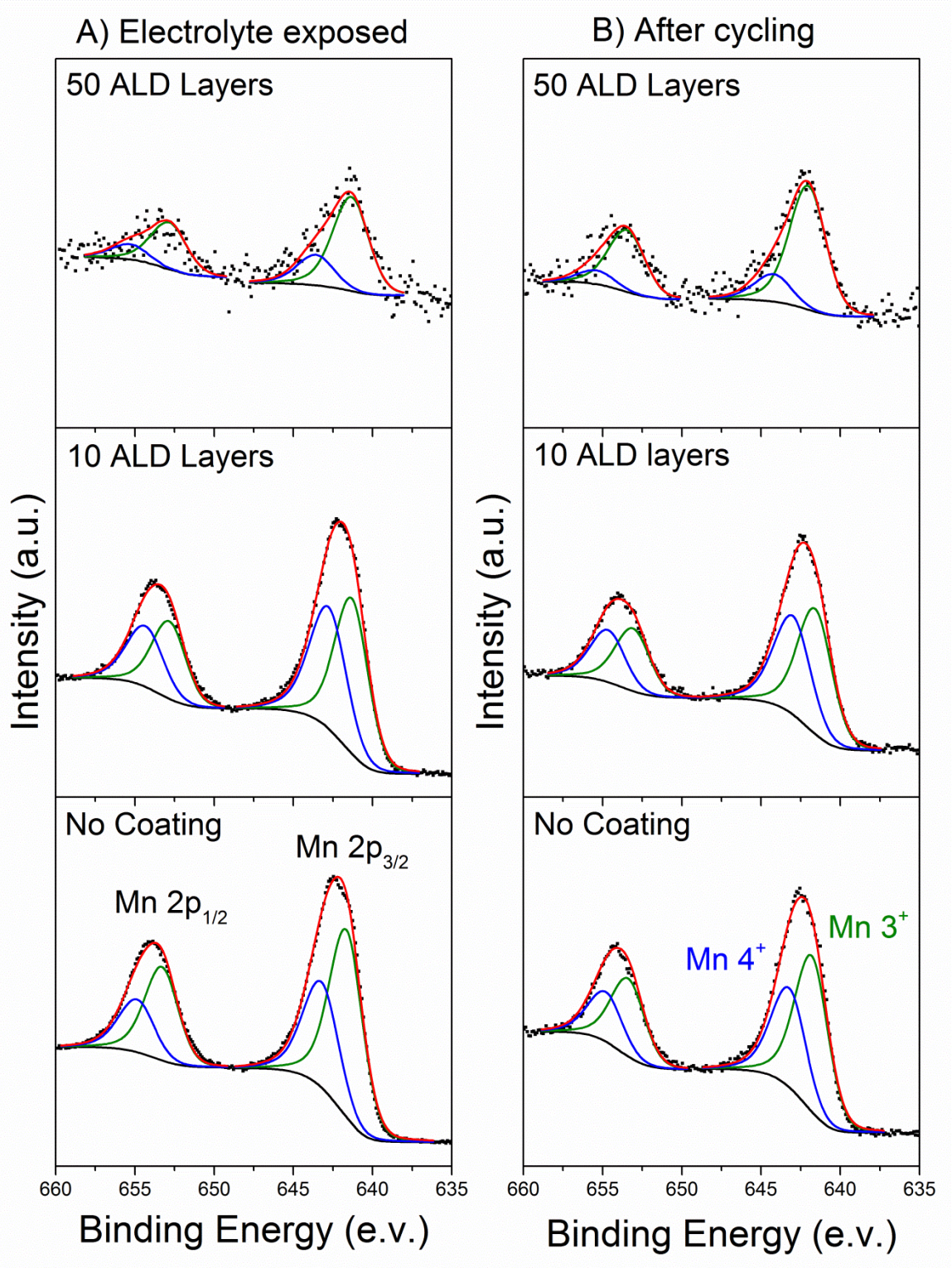

Figure 7.12 XPS characterization of Mn 2p after 24 hour electrolyte exposure and electrochemical cycling.

Table 7.3 Summary of XPS fitting results for Mn 2p. Binding energies (B.E.) are corrected relative to adventitious carbon on each sample.

Sample	Mn 3+			Mn 4+			
	Mn 2p3/2 B.E. (eV)	Mn 2p1/2 B.E. (eV)	ΔB.E. (eV)	Mn 2p3/2 B.E. (eV)	Mn 2p1/2 B.E. (eV)	ΔB.E. (eV)	Mn Ox.
Before Cycling							
No Coating	641.4	653.1	11.6	642.8	654.4	11.6	3.51
10 ALD Layers	641.4	653.0	11.6	642.9	654.5	11.6	3.42
50 ALD Layers	641.5	652.8	11.3	643.2	654.3	11.2	3.40
Electrolyte Exposed							
No Coating	641.6	653.3	11.6	643.2	654.8	11.6	3.38
10 ALD Layers	641.3	652.8	11.5	642.8	654.3	11.6	3.47
50 ALD Layers	641.3	652.8	11.5	643.6	655.3	11.7	3.25
After Cycling							
No Coating	641.8	653.4	11.6	643.2	654.8	11.6	3.40
10 ALD Layers	641.4	652.9	11.5	642.8	654.4	11.6	3.47
50 ALD Layers	642.0	653.5	11.4	642.0	655.4	11.1	3.19

After electrolyte exposure the ALD coated sol-gel films, a new peak is observed in the Al 2p region indicative of Al-F bond formation. This observation confirms the spontaneous fluorination of Al-F in the presence of HF, which was the suspected mechanism for Al-F formation in the CFP based electrodes. For the cycled electrodes, disassembling the Swagelok cells used for electrochemical testing led to some mechanical exfoliation (electrodes are squeezed against the glass fiber separator during assembly). Because the film was damage a large signal associated with Pt 4f was observed in the Al 2p region (not shown), making analysis difficult. To compensate for this the Al 2s photoelectron line was used for the electrochemically cycled samples, which at the photon energy used for these experiments (1486.3 eV for Al Kα) has a similar photoionization cross-section, and thus similar photoelectron yield, to Al 2p but is well removed from the Pt 4f region. Consistent with the CFP samples and electrolyte

exposed films, the cycled sol-gel films show two peaks attributed to Al-O and Al-F bonding, which for both thicknesses of ALD coating show an increase in relative Al-F content after cycling. This increase could be due simply to an increased duration of time spent in the electrolyte which was approximately one week for the cycled samples and 24 hours for the electrolyte exposed films. In both cases Al-O bonding is still present and the peak attributed to Al-F is not at a high enough binding energy to expected a pure Al-F bonding as would be expected for AlF_3 (121-122 eV for Al 2s and 76.9-77.1 eV for Al 2p), indicating that like with the CFP samples an aluminum-oxygen-fluorine compound is likely present.

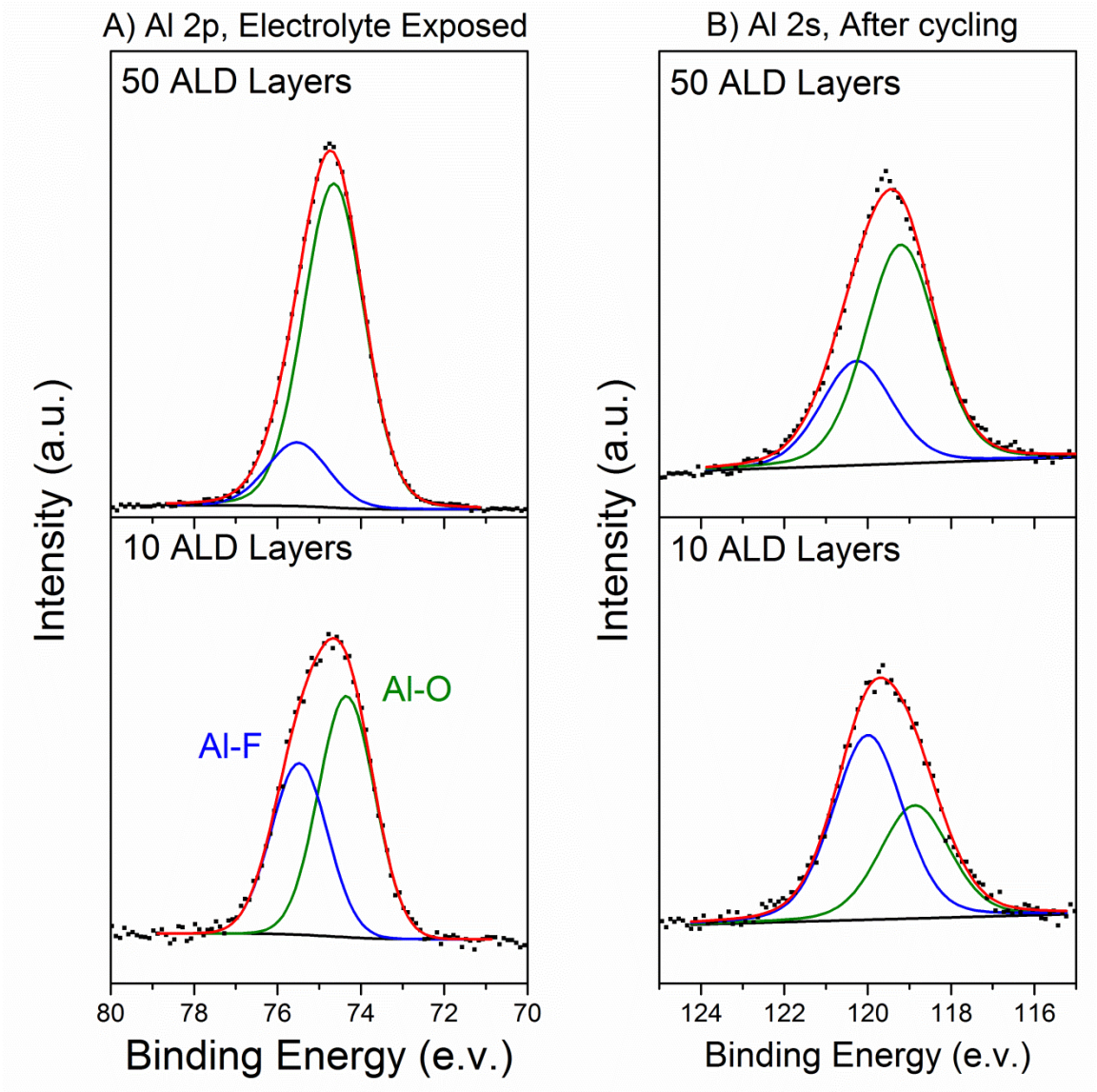

Figure 7.13 Al 2p for electrolyte exposed sol-gel films with ALD coatings (A) and Al 2s for electrochemically cycled sol-gel films with ALD coatings (B).

Table 7.4 Summary of XPS fitting results for Al 2p and Al 2s (cycled electrodes only) peaks.

Sample	Al-O B.E. (eV)	Al-F B.E. (eV)	Al 2p FWHM (eV)
Before Cycling			
10 ALD Layers	74.62	-	2.06
50 ALD Layers	74.87	-	1.82
Electrolyte exposed			
10 ALD Layers	74.3	75.5	1.59
50 ALD Layers	74.9	75.9	1.72
After Cycling			
10 ALD Layers	118.9	120.0	1.98
50 ALD Layers	119.2	120.3	2.01

XPS analysis of the F1s peak was conducted to confirm the formation of Al-F, and to investigate whether any other fluorine containing phases are also formed. After electrolyte exposure both the 10 ALD layer and 50 ALD layer coated electrodes show a single strong peak with a binding energy near 685.7 eV and a small shoulder peak at a higher binding energy of approximately 688 eV. For the uncoated electrode three peaks are observed, with a high binding energy peak in approximately the same region as was observed for the ALD coated electrodes, an additional small peak is observed in the region of 686.6 eV between the highest intensity peak and the highest binding energy shoulder peak.

For the ALD coated electrodes after electrolyte exposure it seems obvious that one of the two peaks should be assigned to Al-O-F type bonding, but with overlapping ranges of Li-F (685 to 686.5 eV for LiF), Mn-F (684.8 to 686.1 eV for MnF_2) and Al-F (682.8 to 686.3 eV for AlF_xH_2O and 687.5 to 687.8 eV for AlF_3) casual assignments should be avoided. Meanwhile, the highest binding energy peak can be assigned with some confidence to derivatives of the $LiPF_6$ electrolyte salt, which despite rinsing in dimethyl carbonate is still present on the electrode surface and has a reported binding energy of 688.3 to 688.8 eV[198]

After electrochemical cycling the assignment of F1s peaks becomes somewhat clarified. For the uncoated electrode, a large increase in the middle peak indicates the addition of new material to the sample surface, which therefore seems likely to come from electrolyte decomposition. Meanwhile, the position and relative intensity of the highest intensity peak for both ALD coated samples is relatively invariant. As a result of these observations, the two peaks in addition to Li_xPF_y observed in the uncoated electrode are assigned as Li-F and Mn-F, with the Li-F bonding increasing as electrolyte is decomposed on the sample surface.

These observations not only support the conclusion that Al_2O_3 coatings can react remove HF from an $LiPF_6$ containing electrolyte by forming Al-O-F compounds, but also provide some indication as to why a higher rate capability and greater apparent lithium diffusivity is observed for the ALD coated electrodes. While AlF_xH_2O type compounds are not expected to have particularly high electronic or ionic conductivity, formations Mn-F and Li-F have been previously reported to increase cell polarization and thus decrease electrochemical performance[198]. By avoiding the formation of these compounds the electrode-electrolyte interface is protected from progressive electrolyte decomposition.

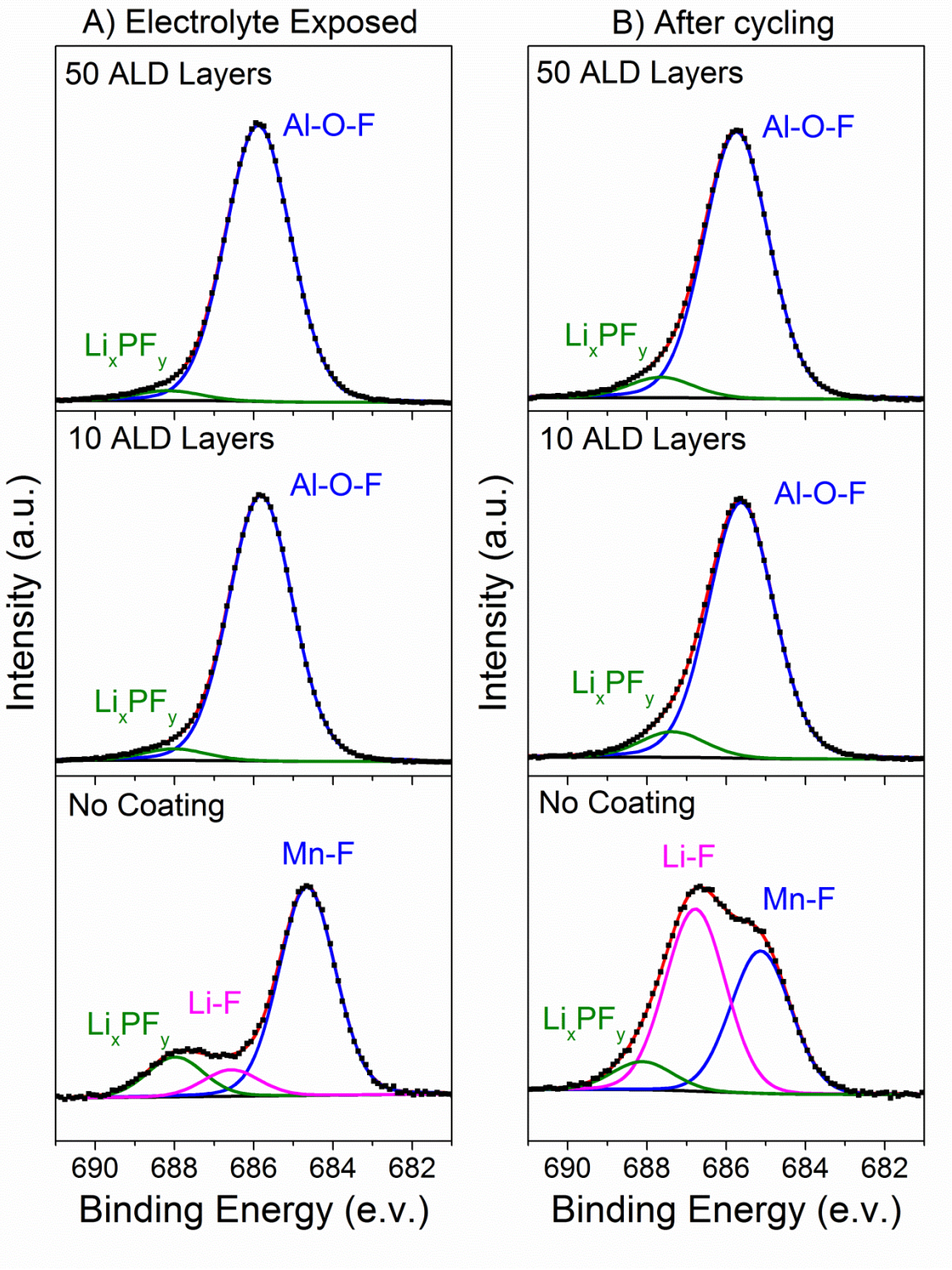

Figure 7.14 F1s XPS spectrum for sol-gel $LiMn_2O_4$ with and without ALD coatings after electrolyte exposure (A) and electrochemical cycling (B).

Table 7.5 Summary of XPS fitting results for F1s peak.

Sample	Al-O-F, Mn-F B.E. (eV)	LiF B.E. (eV)	Li_xPF_y B.E. (eV)	FWHM (eV)
Electrolyte exposed				
No Coating	684.7	686.6	687.9	1.68
10 ALD Layers	685.8	-	688	1.90
50 ALD Layers	685.9	-	688.2	1.95
After Cycling				
No Coating	685.1	686.8	688.1	1.79
10 ALD Layers	685.6	-	687.4	1.94
50 ALD Layers	685.7	-	687.7	1.93

Ex situ Raman analysis conducted after electrolyte exposure and electrochemical cycling shows very slight changes to the three Mn-O vibration peaks ($A1_g$ at ~625 cm^{-1}, $F_{2g}^{(2)}$ at~580 cm^{-1} and a shoulder peak at 660 cm^{-1}) identified in Figure 7.5. However, all of the samples in Figure 7.15 show reduced overall intensity in the Mn-O region making peak assignment more difficult. In addition to the vibration modes known to be attributable to $LiMn_2O_4$, a much wider range of wavenumbers was analyzed to investigate the formation of new bands at higher wavenumbers. Three peaks, indicated by black arrows in Figure 7.15 at 975 cm^{-1}, 1259 cm^{-1} and 1370 cm^{-1} are attributable to the dried electrolyte as shown in Figure 7.16 however none of the other spectral features seen in the dried electrolyte are apparent in the sol-gel films.

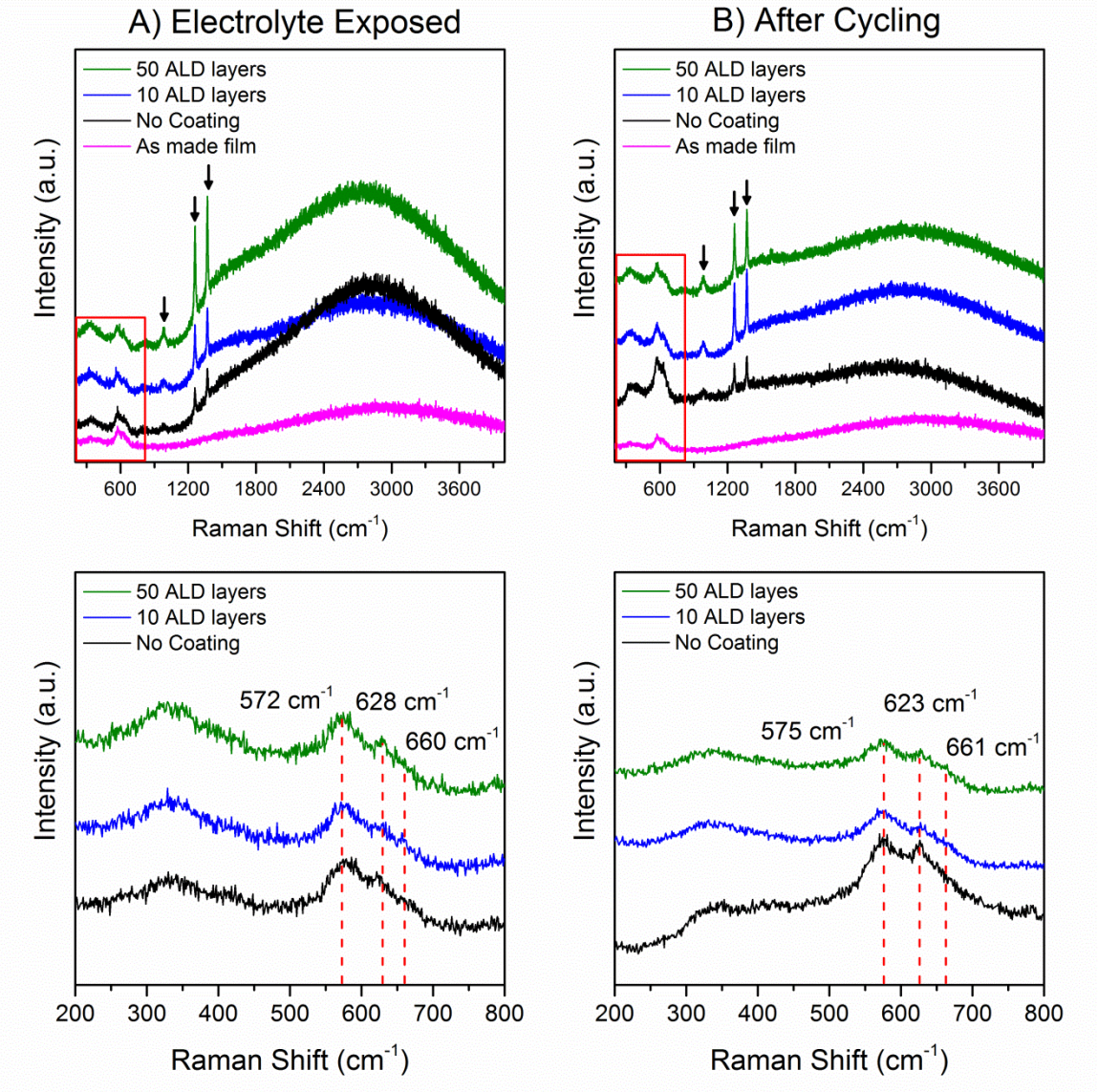

Figure 7.15 Comparison of *Ex Situ* Raman spectrum for sol-gel film electrodes with and without ALD coatings after overnight electrolyte exposure (A) and electrochemical cycling (B). Black arrows indicate peaks assigned to the electrolyte and red boxes show the wavenumber region associated with Mn-O molecular vibrations.

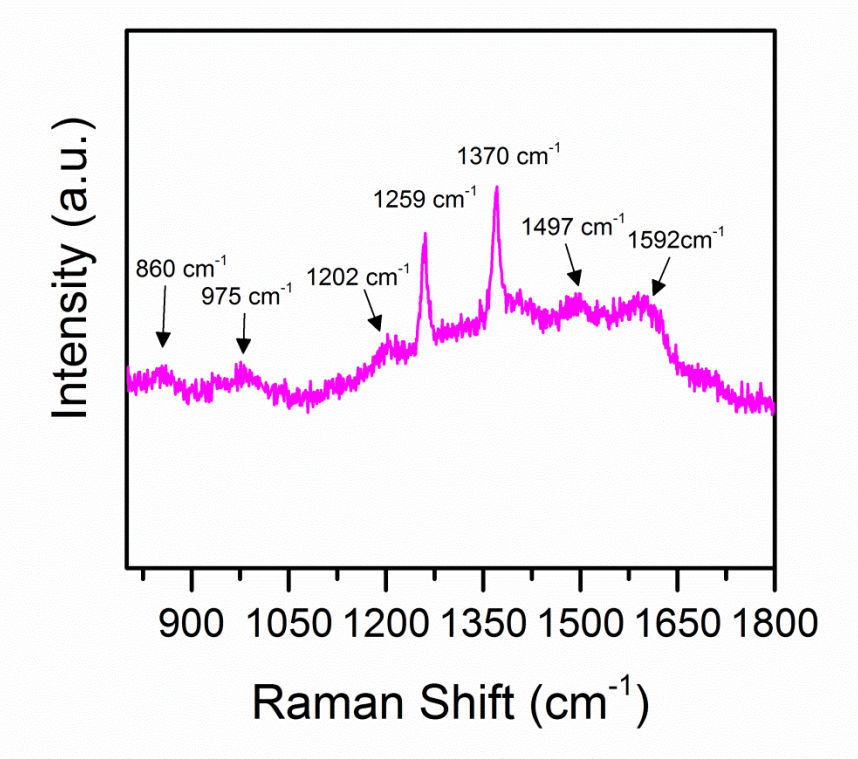

Figure 7.16 Ex situ Raman spectrum of dried electrolyte on Pt coated SS.

7.3.4 Characterization of surface-modified films by *in situ* Raman spectroscopy

In situ Raman analysis was conducted on unmodified and ALD coated thin film electrodes to determine whether any additional phases could be detected by avoiding exposure to air and without the solvent rinsing step used prior to *Ex Situ* measurements. For Figures 7.17, 7.18 and 7.19, cells were assembled with uncoated, 10 ALD layer coated and 50 ALD layer coated working electrodes as described in section 7.2.2. Upon assembly weak Raman bands associated with $LiMn_2O_4$ can be detected, while several additional peaks attributable to the DMC solvent (which had evaporated before the Ex Situ measurement of the electrolyte in Figure 7.16) are also apparent. Upon charging several new peaks with a massive intensity increase are observed. These peaks are all assignable to the fully de-lithiated spinel λ-MnO_2, which as mentioned previously resonates strongly near the wavelength used in the current analysis.

After collecting the Raman spectrum in the as-assembled discharged and fully charged states, the cells were cycled ten times by cyclic voltammetry at a rate of 200 μV/s between 3.5 V vs. Li/Li+ and 4.5 V vs. Li/Li+. Raman spectrum were then collected again under identical conditions as the initial discharged and charged measurements. While Raman measurements were collected during the duration of the cycling process, the persistent laser energy led to electrolyte evaporation even under defocused conditions and the region being analyzed became electrochemically isolated from the rest of the electrode. For this reason the measurements collected before and after cycling were taken in two different regions within the 1/16" diameter area visible by the microscope objective.

For every electrode, regardless of surface coating, the discharged state becomes virtually undetectable (and in fact was barely detectable for the ALD coated electrodes to begin with), while in the charged state the same high intensity λ-MnO_2 peaks could be resolved but with a decreased signal to noise ratio. This could indicate the formation of surface phases which block the Raman signal after electrochemical cycling, but without additional Raman features it is difficult to support this conclusion. All of the peaks identified during the *In Situ* measurements are summarized in Table 7.6.

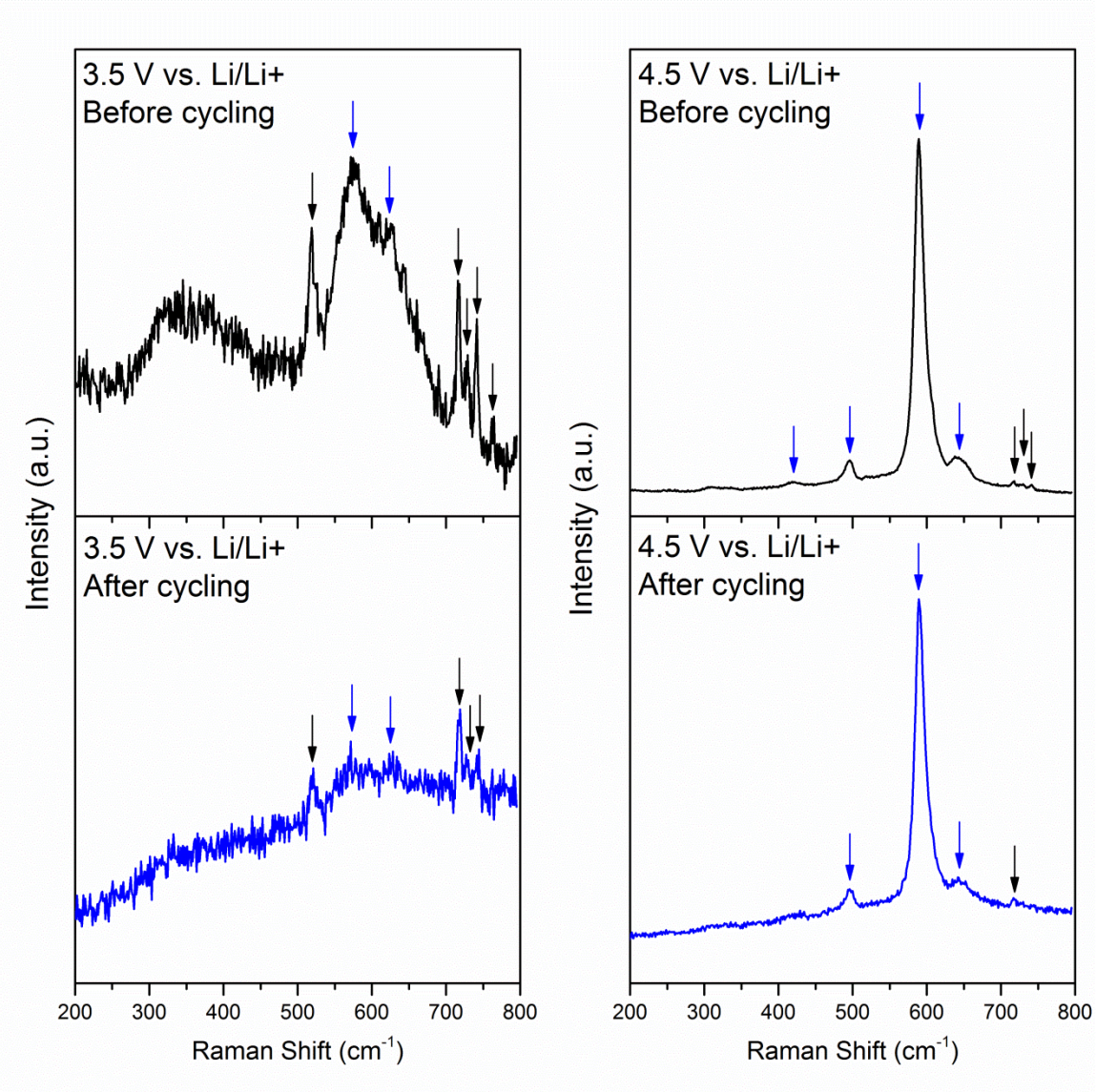

Figure 7.17 *In Situ* Raman spectroscopy of uncoated sol-gel $LiMn_2O_4$ film in region of Mn-O vibration at full charge and discharge state before and after electrochemical cycling. Black arrows indicate electrolyte peaks while blue arrows indicate electrode peaks.

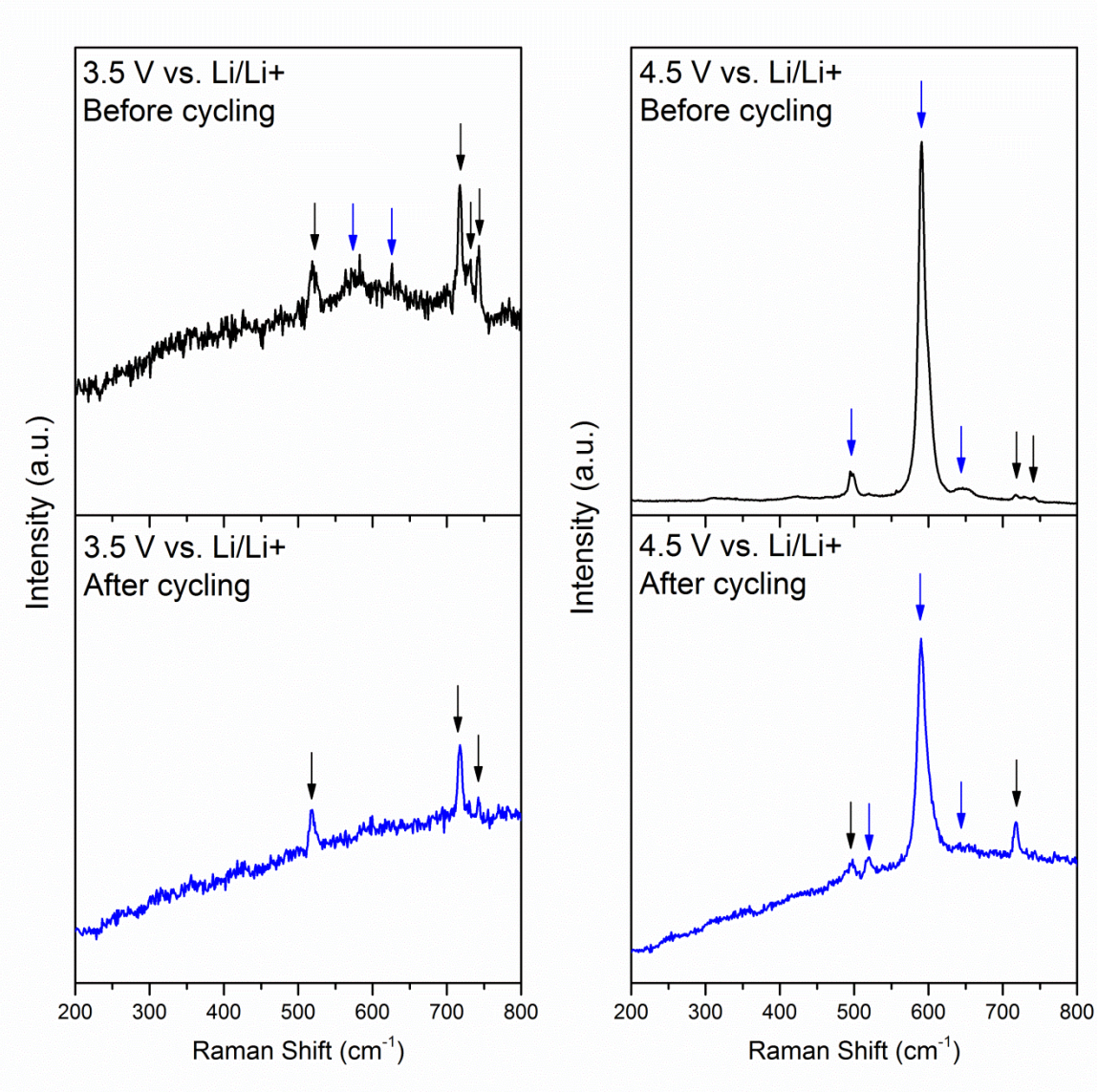

Figure 7.18 In Situ Raman spectroscopy of 10 ALD layer coated sol-gel $LiMn_2O_4$ film in region of Mn-O vibration at full charge and discharge state before and after electrochemical cycling. Black arrows indicate electrolyte peaks while blue arrows indicate electrode peaks.

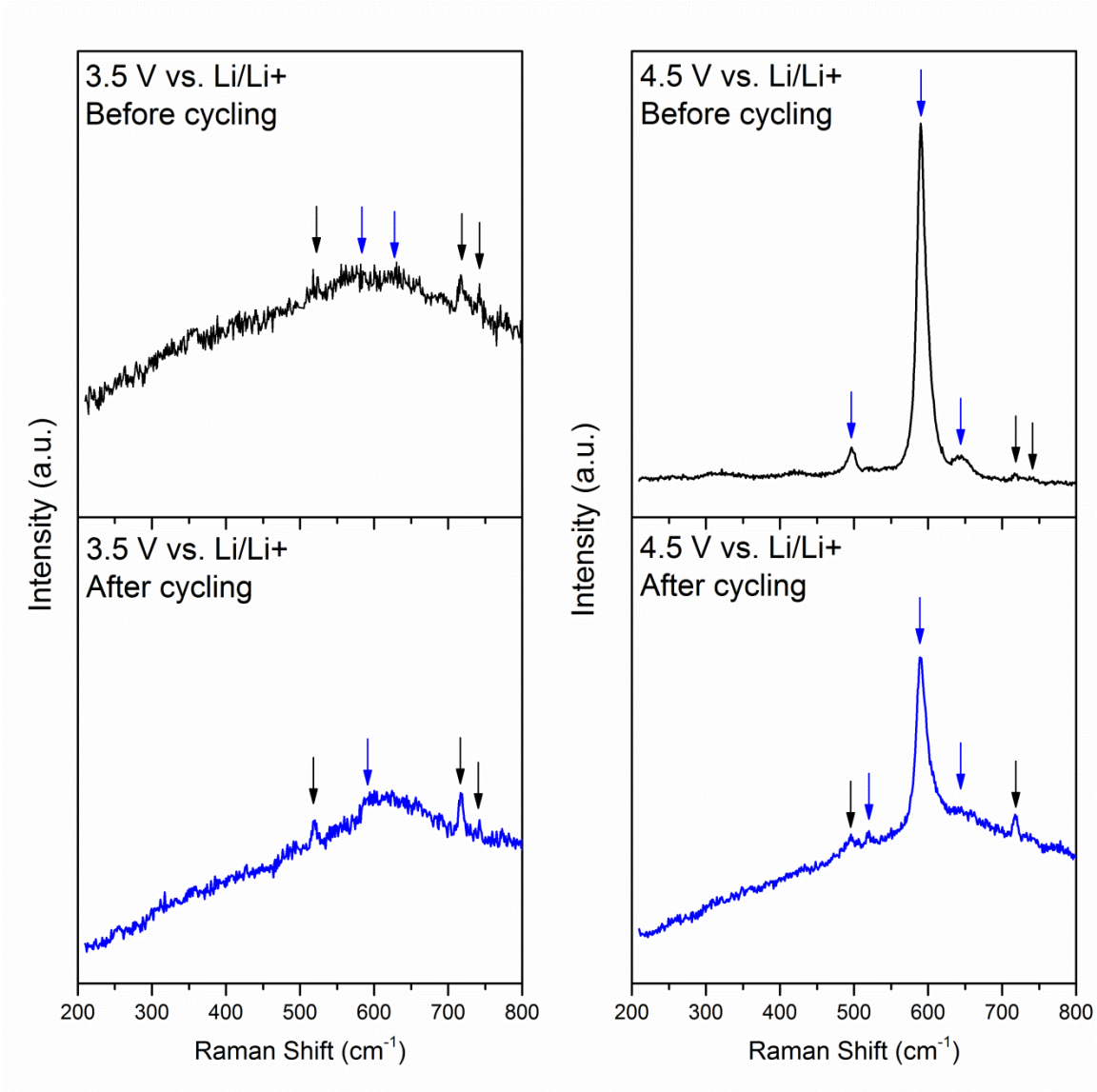

Figure 7.19 In Situ Raman spectroscopy of 50 ALD layer coated sol-gel $LiMn_2O_4$ film in region of Mn-O vibration at full charge and discharge state before and after electrochemical cycling. Black arrows indicate electrolyte peaks while blue arrows indicate electrode peaks.

Table 7.6 Features identified during *In Situ* Raman spectroscopy measurements of sol-gel $LiMn_2O_4$ films

Sample	After assembly (cm^{-1})	First Charge (cm^{-1})	After cycling, discharged (cm^{-1})	After cycling, charged (cm^{-1})
No ALD Coating	**$LiMn_2O_4$:** 573, 625 **DMC:** 519, 717, 730, 742, 763	**λ-MnO_2:** 420,496, 589, 643 **DMC:** 717, 730, 742	**$LiMn_2O_4$:** 573, 625 **DMC:** 519, 717, 730, 742	**λ-MnO_2:** 420,496, 589, 643 **DMC:** 717, 730, 742
10 ALD Layers	**$LiMn_2O_4$:** 573, 625 **DMC:** 519, 717, 731, 742	**λ-MnO_2:** 496, 590, 643 **DMC:** 717, 730, 742	**$LiMn_2O_4$:** - **DMC:** 717, 730, 742	**λ-MnO_2:** 494, 590, 643 **DMC:** 519,717
50 ALD Layers	**$LiMn_2O_4$:** 581, 630 **DMC:** 717, 741	**λ-MnO_2:** 496, 590, 643 **DMC:** 717, 741	**$LiMn_2O_4$:** 592 **DMC:** 519, 719, 741	**λ-MnO_2:** 494, 589, 644 **DMC:** 521, 719

A potential improvement over the *In Situ* measurements present above could be achieved by surface-enhanced Raman spectroscopy, or SERS. Standard Raman spectroscopy typically measures structural changes occurring within ~1 micrometer of the electrode surface, which limits the ability to characterize the electrode/electrolyte interface in detail as the desired signals may be lost as noise in the larger bulk signal or fluorescence contribution. The SERS effect is achieved by applying noble metallic nanoparticles (e.g. silver or gold) to the sample surface which enhances the signal of Raman active phases in the immediate vicinity of the SERS particles produce greater signal intensity, whereas Raman signals generated from deeper in the sample are not enhanced. In a typical experiment SERS particles are applied to the sample surface by a technique such as sputtering; however the bare metal particles are not suitable for electrochemical cycling at the highly oxidizing potentials of the positive electrode, which would lead to a buildup of electrolyte decomposition products or direct oxidation of the SERS particles. Both cases would preclude the SERS effect. At least one example of oxide coated SERS particles for *in situ* Raman on positive electrodes has also been

recently published, while uncoated SERS particles have been demonstrated for negative electrodes in which oxidation is less of a concern [208, 209].

7.4 Conclusions

In this chapter, sol-gel model electrodes were used to successfully confirm the influence of ALD coatings on both the rate capability and surface chemistry for $LiMn_2O_4$ in an $LiPF_6$ containing electrolyte. Like was observed for $LiMn_2O_4$ coated CFP, uncoated electrodes showed a decrease in Mn oxidation state, while ALD coatings (at least for the 10 layer ALD electrode) did not. Furthermore, Al-F bond formation was observed both for electrochemical cycling and simple electrolyte exposure, confirming the spontaneous nature in which Al_2O_3 coatings passivate the $LiMn_2O_4$ from HF attack. New understanding was gained by analysis of the F 1s photoelectron line, which revealed that in addition to the expected Al-F formation in the ALD coated electrodes, the uncoated electrodes formed Li-F and Mn-F compounds, the relative content of which increased with electrochemical cycling.

These conclusions support much of the empirical evidence surrounding surface-modified electrodes, however they also conflict with some of the commonly reported assumptions regarding Mn dissolution. Specifically, the process through which Mn^{3+} disassociates to form electrolyte soluble Mn^{2+} and insoluble Mn^{4+} compounds (Reaction 3 in Chapter 5) should lead to an increase of near-surface Mn oxidation states and potentially give rise to a detectable λ-MnO_2 signal with Raman spectroscopy. Neither of these events are supported by the current analysis, and instead it seems that after dissolution new Mn compounds with lower oxidation states are formed on the electrode surface. Future work should focus on testing this hypothesis with surface coatings that have tailored reactivity towards species such as HF, and with cathode materials of varying Mn oxidation state.

8 CONCLUSIONS AND RECOMMENDATIONS FOR FUTURE WORK

8.1 Conclusions

The following key conclusions were determined from each chapter:

Chapter 4: Development of $LiMn_2O_4$ coated carbon fiber electrodes

1. Electrochemically active $LiMn_2O_4$ can be deposited on carbon fiber substrates from a hydrothermal solution containing 20 mM $KMnO_4$, 20 mM NH_4Cl and 50 mM $LiOH{\bullet}H_2O$ with a range of solution temperatures from 140 °C to 180 °C. Increasing temperatures led to a decreased $LiMn_2O_4$ mass loading and emergence of impurity phases, which was maximized at approximately 30 wt%.
2. Various phases of Mn oxide (K/Li birnessite and λ-MnO(OH)) could be produced by manipulating the hydrothermal conditions. While these phases show minimal reactivity toward Li+, they may be useful as electrochemical active materials in other electrolytes.

Chapter 5: Improving lifetime of $LiMn_2O_4$ on carbon fiber electrodes with ALD coatings

1. Approximately 1 nm coatings of Al_2O_3 led to greater than 100% increase in capacity retention for $LiMn_2O_4$ electrodes cycled at room temperature.
2. Increasing thickness of the ALD coating to approximately 5 nm led to a large decrease in specific capacity, however no corresponding increase in overpotential at low current densities.
3. Compared to the uncoated electrodes, a small increase in polarization resistance was observed for the electrodes with the thickest ALD coatings, while a small decrease in polarization was observed for the thinnest ALD coatings. Lithium

diffusivity followed the same trend with thinnest ALD coatings > No ALD coating > thickest ALD coatings.

4. A change in binding energy for the Al 2p photoelectron implied the formation of Al-F bonding after electrochemical cycling.

Chapter 6: Carbon nanofiber based electrodes prepared by electrospinning

1. Decreasing carbon fiber diameter can increase oxide mass loading and overall energy density by up to 100%.
2. Lower pyrolysis temperatures led to an expected decrease in electronic conductivity and graphitic content, but also manipulated the phases formed by hydrothermal precipitation.

Chapter 7: Analysis of surface-modified $LiMn_2O_4$ thin film model electrodes

1. Thin films prepared by a sol-gel drop coating method show identical trends in lithium diffusivity and Al photoelectron binding energy to those observed for CFP based electrodes.
2. Analysis of F1s photoelectron revealed formation of Li-F and Mn-F for the electrodes without ALD coatings.

8.2 Recommendations for Future Work

In this dissertation, $LiMn_2O_4$ was investigated as a positive electrode material for lithium-ion batteries. An alternative electrode design featuring a porous carbon fiber current collector was implemented to determine the feasibility of adopting this approach over the conventional tape casting method. Both micron-scale, commercially available carbon fibers as well as nanosized electrospun carbon fibers were utilized for this purpose. The hydrothermal method was used to deposit the $LiMn_2O_4$ active material onto the carbon fiber current collectors, and while under certain conditions this approach was

effective at producing a phase-pure active material, minimal control over morphology, crystallite size, or mass loading was realized. As a direct consequence significant variation was observed between experimental batches. Much of this variation is likely due to the experimental conditions employed which relied on a high-temperature box furnace and unstirred hydrothermal solution. Commercial hydrothermal systems are available which offer much greater precision in temperature control and solution convection which would enable significant optimization of the conditions presented in this dissertation.

The carbon fiber substrates themselves could be further improved with a deeper understanding of the extent to which graphitic and disordered carbons interact with the hydrothermal solution. At low pyrolysis temperatures for the electrospun carbon fibers new phases were observed under identical hydrothermal conditions, suggesting that the carbon fibers are not simply serving as heterogeneous nucleation sites but rather as active participants in the hydrothermal reaction. Increasing the pyrolysis temperature is the logical progression of this topic as it would further increase graphitic content and electronic conductivity, and could also provide additional benefits to the negative electrode work presented in Appendix A.

Regardless of possible improvements made to either the carbon fiber substrate or oxide coating conditions it is important to emphasize the even under the best performing, highest mass loading of active material conditions presented in this dissertation (900°C pyrolized Lignin/PVA fibers), carbon fiber based electrodes are at least by some metrics insufficient compared to conventional tape cast electrodes. Specifically, maximum rate capability and volumetric energy density are limited by replacing a metallic current collector with the porous network of relatively low electrical conductivity carbon fibers. For this reason, future research in this area should begin with an assessment of the "competing" technologies or approaches using every relevant metric before proceeding with a lengthy optimization procedure.

Capacity retention was addressed by atomic layer deposition of aluminum oxide directly onto both carbon fiber composite and thin film electrodes and while several reports have suggested that Al_2O_3 is an extremely effective surface coating material, transition metal oxides such as TiO_2 and ZrO_2 have also been investigated and in some instances demonstrate superior results to Al_2O_3 and could be applied here. Like with Al_2O_3 coatings, very few studies have focused on assessing changes in chemistry and structure of the protective coatings, rather than the electrode material being protected. Comparisons between dense coatings with similar thicknesses and morphologies but varying chemistries or crystal structures would provide some additional insight into the mechanism with which the protective coatings influence the electrode/electrolyte interface. Specifically, reactivity of various coating chemistries towards the presumed compounds responsible for electrode degradation (i.e. HF and electrolyte decomposition products) could be investigated. These studies would be critical in order to optimize the beneficial influence of surface coatings, which as demonstrated in this dissertation can include both improved capacity retention and increased lithium ion diffusivity.

Thin film electrodes provide the greatest opportunity for future research based on the present work. Unlike the hydrothermal method which requires case by case optimization, sol-gel thin film electrodes can be produced with greater homogeneity and process control using a generic solution approach making the investigation of a wide variety of cathode materials possible. Issues of film adhesion, which complicated the post-electrochemical cycling characterization of thin film electrodes, could also be improved by utilizing a physical vapor deposition technique, substrate choice or more elaborate electrochemical testing setup. Specifically, use of Swagelok cells in this work required a conducting substrate, and thus stainless steel was used; however many other works use Si substrates with patterned electrodes.

This dissertation focused on one electrolyte, $LiPF_6$ in EC/DMC, which is used as a “general purpose” electrolyte for the overwhelming majority of lithium-ion battery

studies, however many other salts and solvents exist (e.g. salts like $LiClO_4$, $LiB(C_2O_4)_2$ or solvents such as propylene carbonate) which would likely produce varying interactions with electrode materials and surface coatings. $LiPF_6$ in EC/DMC is the preferred electrolyte due to high ionic conductivity and good electrochemical stability (particularly for anode SEI formation), but decomposition products of this electrolyte are directly responsible for Mn dissolution. Thus while surface coatings can address the symptom of Mn dissolution, they do not prevent the root cause. Further studies focused on benefits versus drawbacks of surface modification or electrode choice, as opposed to simply changing the electrolyte, could be conducted.

It is important to emphasize the interaction between cathode and anode surface layers, which was not investigated in this study. Mn dissolution is known to lead to destruction of the SEI layer on graphitic anodes, which further accelerates capacity loss in $LiMn_2O_4$ vs. graphite full cells. Some studies have shown that cathode coatings do indeed improve capacity retention in full cells; however optimization of half-cell performance could produce misleading results. Thus, future studies focusing on cathode protective coatings using half-cells should also include an evaluation of full-cell performance.

Finally, *in situ* experiments such as the *in situ* Raman spectroscopy applied in this dissertation are necessary to understand both cathode degradation and protection mechanisms under the conditions in which they occur. In this dissertation, *in situ* Raman spectroscopy was only cable of determining that significant changes in Mn-O occurred as a function of ALD coatings. New bands associated with electrode degradation may be present but were concealed by their intrinsically low intensities and high background intensity due to fluorescence. SERS is one possible avenue to improve sensitivity to near-surface minority phases, but would require extensive optimization.

APPENDIX A NEGATIVE ELECTODES USING CARBON FIBERS

In order to create a full cell without any tape cast electrodes, electrospun carbon fibers were tested electrochemically to determine their feasibility as negative electrodes. Electrodes made of 900 °C pyrolized lignin/PVA fibers show a typical voltage profile and reversible capacity of amorphous carbon. A major limitation of amorphous carbons is the huge irreversible capacity on the first cycle and very steep voltage profile, which reduces overall cell energy density.

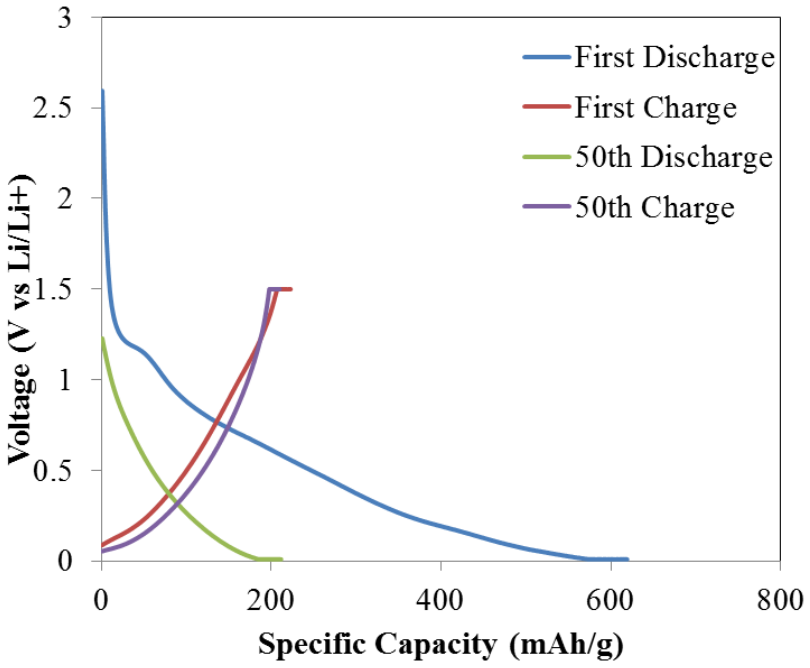

Figure A.1 Galvanostatic testing of carbon fiber negative electrode at a current density of 30 mA/g.

After the initial irreversibly capacity loss, carbon fiber negative electrodes are quite stable and show a reversible capacity of about 200 mAh/g.

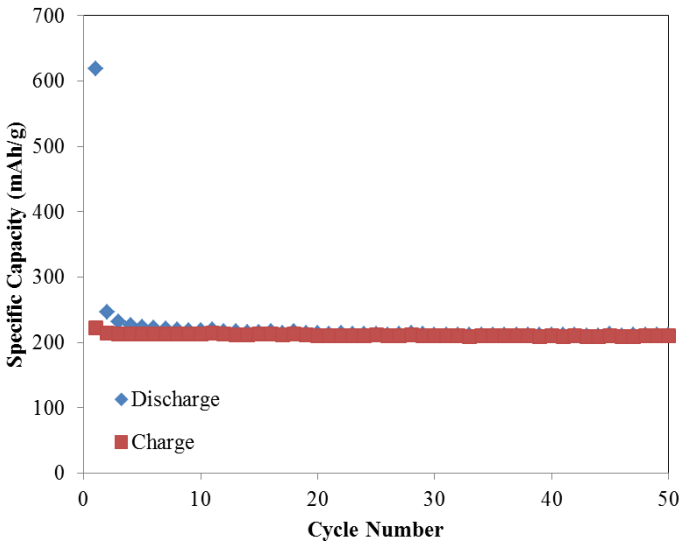

Figure A.2 Galvanostatic cycling of lignin/PVA carbon fibers at 60 mA/g.

Several attempts were made to increase the overall reversible capacity by including additional phases, such as Sn and Sn intermetallic by electrodeposition and reduce the initial irreversible capacity loss, such as increasing the pyrolysis temperature (max temperature available was 1500 °C) however none of these routes were effective.

APPENDIX B LIMN2O4 THIN FILMS BY RF SPUTTERING

Thin films were initially prepared by RF sputtering, but with poor results. For the sputtering experiments attempted, powders of $LiMn_2O_4$ were mixed with a polymeric binder (e.g. polyvinyl propylene or polyvinyl alcohol) and pressed into a green body using a uniaxial powder press. This is first fired at a low temperature (400-600°C) to burn out the binder, and then sintered at high temperature (800-1300°C depending on the materials) to form a dense ceramic disc which can be used as a target for RF sputtering. Store-bought $LiMn_2O_4$ targets were also utilized.

Utilizing a sputtering power of 5 W/cm^2 (the maximum value for our system) and a working pressure of $2x10^{-2}$ mbar of Ar, the film shown in A1 was obtained after 30 hours a total thickness is about 370 nm, which corresponds to a sputter rate of roughly 12 nm per hour. This value is considerably smaller than the rates reported by previous researchers, which are usually on the order of 30-100 nm per hour with identical working conditions. Control of sputtering parameters such as RF power, working pressure, target to substrate distance can be used to optimize the morphology, composition and growth rate during the sputtering process and were all varied in an attempt to increase the sputtering growth rate [193, 194, 210].

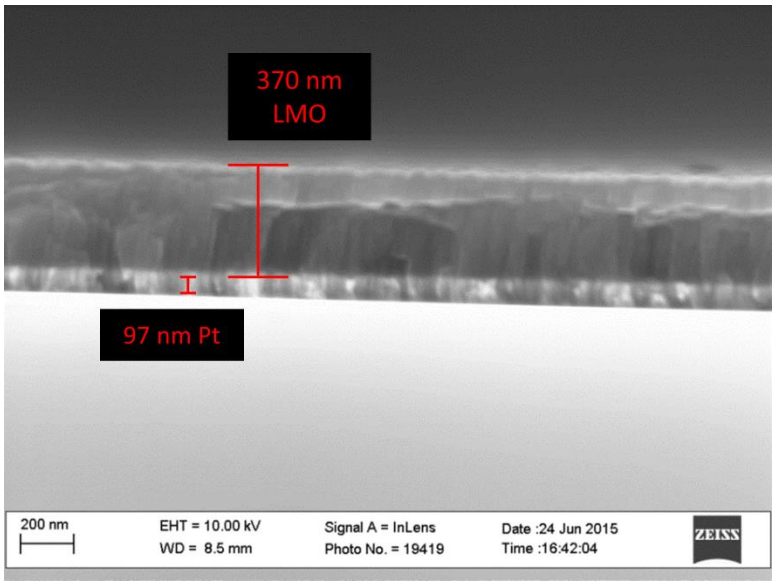

Figure B.1 Cross section electron micrograph of RF sputtered LiMn2O4 film

While most of the literature reports for RF sputtering of $LiMn_2O_4$ used larger diameter targets (2" or 3" vs. 1" used here), the sputtering system in the Liu lab is capable of high sputtering rates for some materials. Figure A2.2 shows a film deposited from a CeO_2 target produced in our lab. The CeO_2 film was deposited under identical conditions as the $LiMn_2O_4$ film with the only difference being the target material. A layer of gold which has a known sputter rate was also deposited to calibrate the growth rate of the CeO_2 film. The ceria target was sputtered for 9 hours, corresponding to a deposition rate of 690 nm per hour – fifty times the rate observed for the $LiMn_2O_4$ target.

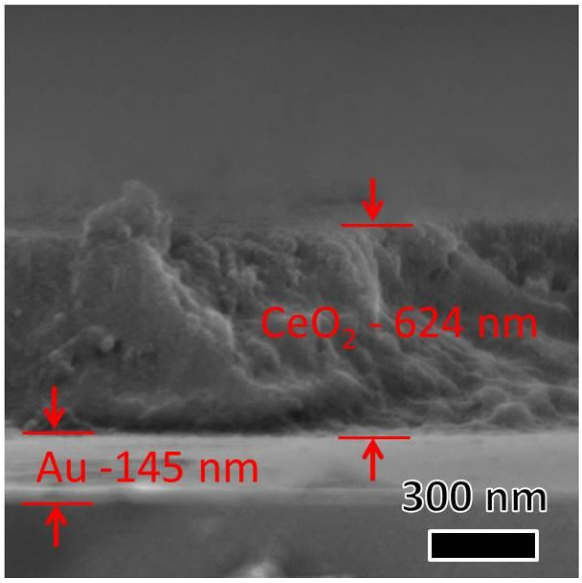

Figure B.2 Cross-section electron micrograph of RF sputtered CeO_2 on Au thin film

Very weak peaks were observable by XRD for the ~400 nm film show in Figure A2.1 after annealing at various temperatures.

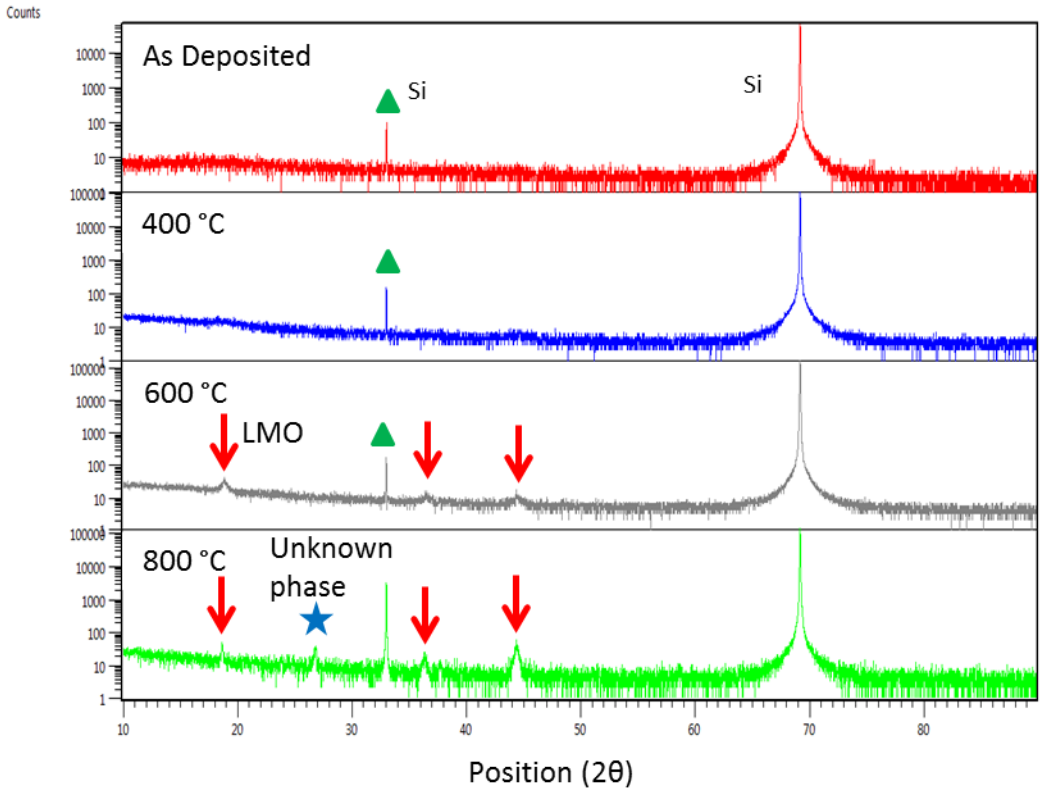

Figure B.3 XRD of RF sputtered $LiMn_2O_4$ film on Si

Further difficulty was also encountered when attempting to conduct electrochemical testing on the sputtered LMO films. Figure A2.4 shows a CV test on a 600 °C annealed $LiMn_2O_4$ sputtered onto stainless steel. After an initial oxidation peak, the observed current density drops significantly indicating a loss in electrochemical activity.

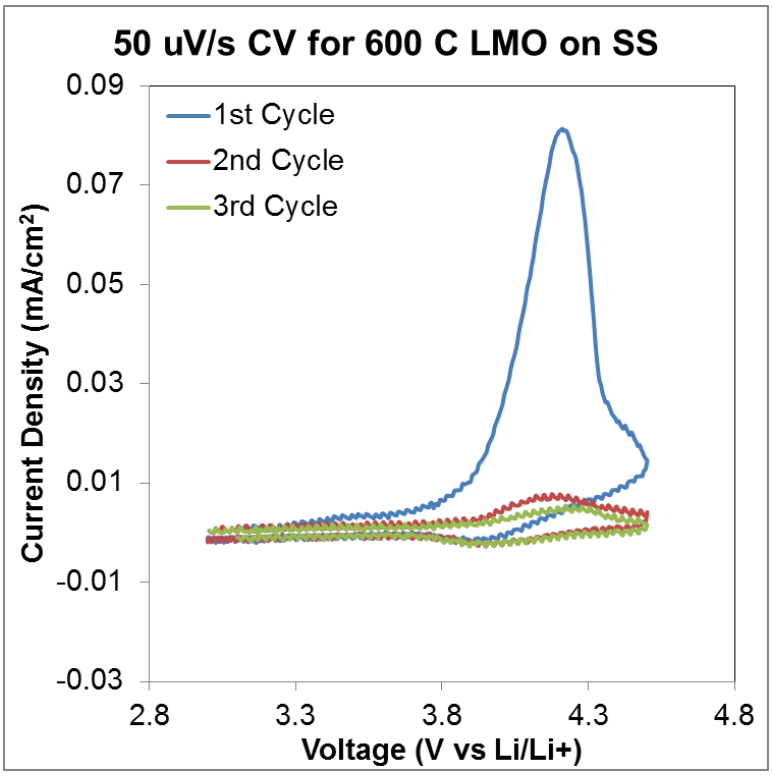

Figure B.4 CV testing of 600 °C annealed RF sputtered $LiMn_2O_4$ (LMO) film on stainless steel (SS).

Due to the factors of low growth rate that decreased the ability of the films to be easily characterized or electrochemically cycled, the sol-gel method was implemented instead.

REFERENCES

1. J. M. Tarascon and M. Armand, *Nature*, 2001, **414**, 359-367.

2. B. Dunn, H. Kamath and J. M. Tarascon, *Science*, 2011, **334**, 928-935.

3. O. K. Park, Y. Cho, S. Lee, H. C. Yoo, H. K. Song and J. Cho, *Energy Environ. Sci.*, 2011, **4**, 1621-1633.

4. U. S. D. o. Energy, *Grid Energy Storage*, 2013.

5. E. P. R. Dan Doughty, *The Electrochemical Society's Interface*, 2012, **21**.

6. P. A. Nelson, K. G. Gallagher, I. Bloom and D. W. Dees, 2012, **ANL-12/55**.

7. G. Amatucci, A. Du Pasquier, A. Blyr, T. Zheng and J. M. Tarascon, *Electrochim. Acta*, 1999, **45**, 255-271.

8. G. Amatucci and J. M. Tarascon, *J. Electrochem. Soc.*, 2002, **149**, K31-K46.

9. R. A. Huggins, *Advanced Batteries: Materials Science Aspects*, Springer, New York, NY, 2009.

10. M. Winter and R. J. Brodd, *Chem. Rev.*, 2004, **104**, 4245-4269.

11. R. E. Garcia and Y. M. Chiang, *J. Electrochem. Soc.*, 2007, **154**, A856-A864.

12. J. L. Li, C. Daniel and D. Wood, *J. Power Sources*, 2011, **196**, 2452-2460.

13. J. C. Lytle, J. M. Wallace, M. B. Sassin, A. J. Barrow, J. W. Long, J. L. Dysart, C. H. Renninger, M. P. Saunders, N. L. Brandell and D. R. Rolison, *Energy Environ. Sci.*, 2011, **4**, 1913-1925.

14. M. Roberts, P. Johns, J. Owen, D. Brandell, K. Edstrom, G. El Enany, C. Guery, D. Golodnitsky, M. Lacey, C. Lecoeur, H. Mazor, E. Peled, E. Perre, M. M. Shaijumon, P. Simon and P. L. Taberna, *J. Mater. Chem.*, 2011, **21**, 9876-9890.

15. D. R. Rolison, J. W. Long, J. C. Lytle, A. E. Fischer, C. P. Rhodes, T. M. McEvoy, M. E. Bourga and A. M. Lubers, *Chem. Soc. Rev.*, 2009, **38**, 226-252.

16. S. K. Martha, N. J. Dudney, J. O. Kiggans and J. Nanda, *J. Electrochem. Soc.*, 2012, **159**, A1652-A1658.

17. A. H. Whitehead and M. Schreiber, *J. Electrochem. Soc.*, 2005, **152**, A2105-A2113.

18. H. X. Ji, L. L. Zhang, M. T. Pettes, H. F. Li, S. S. Chen, L. Shi, R. Piner and R. S. Ruoff, *Nano Lett.*, 2012, **12**, 2446-2451.

19. O. Toprakci, H. A. K. Toprakci, L. W. Ji, G. J. Xu, Z. Lin and X. W. Zhang, *ACS Appl. Mater. Interfaces*, 2012, **4**, 1273-1280.

20. S. Luo, K. Wang, J. P. Wang, K. L. Jiang, Q. Q. Li and S. S. Fan, *Adv. Mater.*, 2012, **24**, 2294-2298.

21. A. K. Kercher, J. O. Kiggans and N. J. Dudney, *J. Electrochem. Soc.*, 2010, **157**, A1323-A1327.

22. B. Liu, J. Zhang, X. F. Wang, G. Chen, D. Chen, C. W. Zhou and G. Z. Shen, *Nano Lett.*, 2012, **12**, 3005-3011.

23. M. S. Wu, J. T. Lee, P. C. J. Chiang and J. C. Lin, *J. Mater. Sci.*, 2007, **42**, 259-265.

24. S. K. Martha, J. O. Kiggans, J. Nanda and N. J. Dudney, *J. Electrochem. Soc.*, 2011, **158**, A1060-A1066.

25. W. H. Woodford, W. C. Carter and Y. M. Chiang, *Energy Environ. Sci.*, 2012, **5**, 8014-8024.

26. K. S. Kang, Y. S. Meng, J. Breger, C. P. Grey and G. Ceder, *Science*, 2006, **311**, 977-980.

27. M. Gateshki, Central Michigan University X-ray Diffraction Laboratory website, 2006.

28. M. M. Thackeray, *J. Am. Ceram. Soc.*, 1999, **82**, 3347-3354.

29. M. M. Thackeray, W. I. F. David, P. G. Bruce and J. B. Goodenough, *Mater. Res. Bull.*, 1983, **18**, 461-472.

30. C. Y. Ouyang, S. Q. Shi and M. S. Lei, *J. Alloy. Compd.*, 2009, **474**, 370-374.

31. J. Liu and A. Manthiram, *J. Phys. Chem. C*, 2009, **113**, 15073-15079.

32. M. Park, X. C. Zhang, M. D. Chung, G. B. Less and A. M. Sastry, *J. Power Sources*, 2010, **195**, 7904-7929.

33. E. Hosono, T. Kudo, I. Honma, H. Matsuda and H. S. Zhou, *Nano Lett.*, 2009, **9**, 1045-1051.

34. B. Kang and G. Ceder, *Nature*, 2009, **458**, 190-193.

35. H. W. Lee, P. Muralidharan, R. Ruffo, C. M. Mari, Y. Cui and D. K. Kim, *Nano Lett.*, 2010, **10**, 3852-3856.

36. T. F. Yi, X. Y. Li, H. P. Liu, J. Shu, Y. R. Zhu and R. S. Zhu, *Ionics*, 2012, **18**, 529-539.

37. H. G. Zhang, X. D. Yu and P. V. Braun, *Nat. Nanotechnol.*, 2011, **6**, 277-281.

38. D. Aurbach, *J. Power Sources*, 2000, **89**, 206-218.

39. J. B. Goodenough and Y. Kim, *Chem. Mat.*, 2010, **22**, 587-603.

40. K. A. Walz, C. S. Johnson, J. Genthe, L. C. Stoiber, W. A. Zeltner, M. A. Anderson and M. M. Thackeray, *J. Power Sources*, 2010, **195**, 4943-4951.

41. J. C. Hunter, *Journal of Solid State Chemistry*, 1981, **39**, 142-147.

42. D. H. Jang, Y. J. Shin and S. M. Oh, *J. Electrochem. Soc.*, 1996, **143**, 2204-2211.

43. R. Benedek and M. M. Thackeray, *Electrochem. Solid State Lett.*, 2006, **9**, A265-A267.

44. M. Mohamedi, D. Takahashi, T. Itoh and I. Uchida, *Electrochim. Acta*, 2002, **47**, 3483-3489.

45. K. Y. Chung, W. S. Yoon, K. B. Kim, B. W. Cho and X. Q. Yang, *J. Appl. Electrochem.*, 2011, **41**, 1295-1299.

46. K. Edstrom, T. Gustafsson and J. O. Thomas, *Electrochim. Acta*, 2004, **50**, 397-403.

47. Y. Matsuo, R. Kostecki and F. McLarnon, *J. Electrochem. Soc.*, 2001, **148**, A687-A692.

48. M. Hirayama, H. Ido, K. Kim, W. Cho, K. Tamura, J. Mizuki and R. Kanno, *J. Am. Chem. Soc.*, 2010, **132**, 15268-15276.

49. D. H. Jang and S. M. Oh, *J. Electrochem. Soc.*, 1997, **144**, 3342-3348.

50. K. Amine, J. Liu, S. Kang, I. Belharouak, Y. Hyung, D. Vissers and G. Henriksen, *J. Power Sources*, 2004, **129**, 14-19.

51. J. Q. Zhao and Y. Wang, *J. Phys. Chem. C*, 2012, **116**, 11867-11876.

52. L. J. Fu, H. Liu, C. Li, Y. P. Wu, E. Rahm, R. Holze and H. Q. Wu, *Solid State Sci.*, 2006, **8**, 113-128.

53. H. Sahan, H. Goktepe, S. Patat and A. Ulgen, *Solid State Ion.*, 2008, **178**, 1837-1842.

54. S. Bin Park, S. M. Lee, H. C. Shin, W. Il Cho and H. Jang, *J. Power Sources*, 2007, **166**, 219-225.

55. S. B. Park, H. C. Shin, W. G. Lee, W. I. Cho and H. Jang, *J. Power Sources*, 2008, **180**, 597-601.

56. C. Daniel, *Jom*, 2008, **60**, 43-48.

57. P. G. Balakrishnan, R. Ramesh and T. P. Kumar, *J. Power Sources*, 2006, **155**, 401-414.

58. T. M. Bandhauer, S. Garimella and T. F. Fuller, *J. Electrochem. Soc.*, 2011, **158**, R1-R25.

59. L. Wang, T. Maxisch and G. Ceder, *Chem. Mat.*, 2007, **19**, 543-552.

60. N. S. Choi, Z. H. Chen, S. A. Freunberger, X. L. Ji, Y. K. Sun, K. Amine, G. Yushin, L. F. Nazar, J. Cho and P. G. Bruce, *Angewandte Chemie-International Edition*, 2012, **51**, 9994-10024.

61. W. L. R. Suchanek, R.E., *Advances in Science and Technology*, 2006, **45**, 184-193.

62. C. S. Cundy and P. A. Cox, *Chem. Rev.*, 2003, **103**, 663-701.

63. B. L. Cushing, V. L. Kolesnichenko and C. J. O'Connor, *Chem. Rev.*, 2004, **104**, 3893-3946.

64. S. H. Feng and R. R. Xu, *Accounts Chem. Res.*, 2001, **34**, 239-247.

65. X. L. Jia, C. Z. Yan, Z. Chen, R. R. Wang, Q. Zhang, L. Guo, F. Wei and Y. F. Lu, *Chemical Communications*, 2011, **47**, 9669-9671.

66. J. F. von Bulow, H. L. Zhang and D. E. Morse, *Adv. Energy Mater.*, 2012, **2**, 309-315.

67. H. J. Yue, X. K. Huang, D. P. Lv and Y. Yang, *Electrochim. Acta*, 2009, **54**, 5363-5367.

68. K. Kanamura, S. Koizumi and K. Dokko, *J. Mater. Sci.*, 2008, **43**, 2138-2142.

69. X. Qin, X. Wang, H. Xiang, J. Xie, J. Li and Y. Zhou, *The Journal of Physical Chemistry C*, 2010, **114**, 16806-16812.

70. J. J. Chen, M. J. Vacchio, S. J. Wang, N. Chernova, P. Y. Zavalij and M. S. Whittingham, *Solid State Ion.*, 2008, **178**, 1676-1693.

71. L. Kavan, M. Kalbac, M. Zukalova, I. Exnar, V. Lorenzen, R. Nesper and M. Graetzel, *Chem. Mat.*, 2004, **16**, 477-485.

72. C. Wang, Y. Zhou, M. Y. Ge, X. B. Xu, Z. L. Zhang and J. Z. Jiang, *J. Am. Chem. Soc.*, 2010, **132**, 46-+.

73. C. Liu, Z. Wang, C. Shi, E. Liu, C. He and N. Zhao, *ACS Appl. Mater. Interfaces*, 2014, **6**, 8363-8368.

74. G. A. G. Mansoori, T.F.;Assoufid, L.;Zhang, G., Topics in Applied Physics, 2007.

75. G. Cao, *Nanostructures & Nanomaterials*, Imperial College Press, 2004.

76. D. A. Porter, K. E. Easterling and K. E. Sherif, *Phase Transformations in Metals and Alloys*, CRC Press, 2008.

77. D. Li and Y. N. Xia, *Adv. Mater.*, 2004, **16**, 1151-1170.

78. B. Lu, Y. Wang, Y. Liu, H. Duan, J. Zhou, Z. Zhang, Y. Wang, X. Li, W. Wang, W. Lan and E. Xie, *Small*, 2010, **6**, 1612-1616.

79. F. Yener and O. Jirsak, *Journal of Nanomaterials*, 2012, **2012**, 6.

80. D. Dhakal, Self-terminating Chemiabsorption of TMA of the Substrate followed by the Ligand Exchange during Al2O3 ALD on Si-substrate., http://www.dileepnanotech.com/ALD_Saturating__Chemical_Reaction.htm.

81. W. C. (Claudionico), 2013.

82. R. Nave, 2015.

83. A. J. Bard, *Electrochemical methods : fundamentals and applications*, New York, Wiley, 2001.

84. N. Yabuuchi and T. Ohzuku, *J. Power Sources*, 2003, **119**, 171-174.

85. M. H. Lee, Y. Kang, S. T. Myung and Y. K. Sun, *Electrochim. Acta*, 2004, **50**, 939-948.

86. Y. K. Sun, Z. H. Chen, H. J. Noh, D. J. Lee, H. G. Jung, Y. Ren, S. Wang, C. S. Yoon, S. T. Myung and K. Amine, *Nat. Mater.*, 2012, **11**, 942-947.

87. K. M. Shaju and P. G. Bruce, *Chem. Mat.*, 2008, **20**, 5557-5562.

88. S. H. Kang, J. B. Goodenough and L. K. Rabenberg, *Electrochem. Solid State Lett.*, 2001, **4**, A49-A51.

89. H. M. Wu, J. P. Tu, Y. F. Yuan, X. T. Chen, J. Y. Xiang, X. B. Zhao and G. S. Cao, *J. Power Sources*, 2006, **161**, 1260-1263.

90. C. H. Jiang, S. X. Dou, H. K. Liu, M. Ichihara and H. S. Zhou, *J. Power Sources*, 2007, **172**, 410-415.

91. B. J. Liddle, S. M. Collins and B. M. Bartlett, *Energy Environ. Sci.*, 2010, **3**, 1339-1346.

92. H. Xia, K. R. Ragavendran, J. P. Xie and L. Lu, *J. Power Sources*, 2012, **212**, 28-34.

93. R. Moshtev and B. Johnson, *J. Power Sources*, 2000, **91**, 86-91.

94. B. Lawson, Woodbank Communications Ltd, http://www.mpoweruk.com, 2014.

95. M. Yao, K. Okuno, T. Iwaki, M. Kato, S. Tanase, K. Emura and T. Sakai, *J. Power Sources*, 2007, **173**, 545-549.

96. C. G. Yang, D. W. Zhang, Y. B. Zhao, Y. H. Lu, L. Wang and J. B. Goodenough, *J. Power Sources*, 2011, **196**, 10673-10678.

97. M. Yao, K. Okuno, T. Iwaki, T. Awazu and T. Sakai, *J. Power Sources*, 2010, **195**, 2077-2081.

98. L. Yang, S. Cheng, Y. Ding, X. B. Zhu, Z. L. Wang and M. L. Liu, *Nano Lett.*, 2012, **12**, 321-325.

99. M. K. Song, S. Cheng, H. Y. Chen, W. T. Qin, K. W. Nam, S. C. Xu, X. Q. Yang, A. Bongiorno, J. Lee, J. M. Bai, T. A. Tyson, J. Cho and M. L. Liu, *Nano Lett.*, 2012, **12**, 3483-3490.

100. M. J. Zhi, A. Manivannan, F. K. Meng and N. Q. Wu, *J. Power Sources*, 2012, **208**, 345-353.

101. Y. S. Luo, J. Jiang, W. W. Zhou, H. P. Yang, J. S. Luo, X. Y. Qi, H. Zhang, D. Y. W. Yu, C. M. Li and T. Yu, *J. Mater. Chem.*, 2012, **22**, 8634-8640.

102. K. L. Holland and J. R. Walker, *Clays and Clay Minerals*, 1996, **44**, 744-748.

103. Q. T. Qu, L. Li, S. Tian, W. L. Guo, Y. P. Wu and R. Holze, *J. Power Sources*, 2010, **195**, 2789-2794.

104. X. Lou, X. Wu and Y. Zhang, *J. Alloy. Compd.*, 2013, **550**, 185-189.

105. Z. Guo, G. Zhu, Z. Qiu, Y. Wang and Y. Xia, *Electrochemistry Communications*, 2012, **25**, 26-29.

106. L. Zhang, X. Zhang, Z. Wang, J. Xu, D. Xu and L. Wang, *Chemical Communications*, 2012, **48**, 7598-7600.

107. H. Fang, S. Zhang, X. Wu, W. Liu, B. Wen, Z. Du and T. Jiang, *J. Power Sources*, 2013, **235**, 95-104.

108. Y. Y. Liang, S. J. Bao, B. L. He, W. J. Zhou and H. L. Li, *J. Electrochem. Soc.*, 2005, **152**, A2030-A2034.

109. Y. Q. Gao, Z. G. Wang, J. X. Wan, G. F. Zou and Y. T. Qian, *Journal of Crystal Growth*, 2005, **279**, 415-419.

110. Z. C. Qiu, J. P. Zhou, G. Q. Zhu, X. M. Chen, R. L. Yang, Y. H. Song and P. Liu, *Journal of Nanoscience and Nanotechnology*, 2012, **12**, 6552-6557.

111. H. Y. Chen, J. Wang, S. C. Hou and L. Xiang, *Journal of Nanomaterials*, 2015.

112. M. Nakayama, T. Kanaya, J.-W. Lee and B. N. Popov, *J. Power Sources*, 2008, **179**, 361-366.

113. Y. C. Chen, K. Xie, Y. Pan and C. M. Zheng, *J. Power Sources*, 2011, **196**, 6493-6497.

114. R. J. Gummow, A. Dekock and M. M. Thackeray, *Solid State Ion.*, 1994, **69**, 59-67.

115. G. H. Li, H. Ikuta, T. Uchida and M. Wakihara, *J. Electrochem. Soc.*, 1996, **143**, 178-182.

116. Y. S. Lee, N. Kumada and M. Yoshio, *J. Power Sources*, 2001, **96**, 376-384.

117. Y. J. Shin and A. Manthiram, *J. Electrochem. Soc.*, 2004, **151**, A204-A208.

118. A. Antonini, C. Bellitto, M. Pasquali and G. Pistoia, *J. Electrochem. Soc.*, 1998, **145**, 2726-2732.

119. L. Xiong, Y. Xu, T. Tao and J. B. Goodenough, *J. Power Sources*, 2012, **199**, 214-219.

120. G. G. Amatucci, A. Blyr, C. Sigala, P. Alfonse and J. M. Tarascon, *Solid State Ion.*, 1997, **104**, 13-25.

121. J. P. Cho and G. Kim, *Electrochem. Solid State Lett.*, 1999, **2**, 253-255.

122. W.-S. Yoon, K. Y. Chung, K.-W. Nam and K.-B. Kim, *J. Power Sources*, 2006, **163**, 207-210.

123. J. S. Kim, C. S. Johnson, J. T. Vaughey, S. A. Hackney, K. A. Walz, W. A. Zeltner, M. A. Anderson and M. M. Thackeray, *J. Electrochem. Soc.*, 2004, **151**, A1755-A1761.

124. Y. K. Sun, K. J. Hong and J. Prakash, *J. Electrochem. Soc.*, 2003, **150**, A970-A972.

125. Y. M. Lin, H. C. Wu, Y. C. Yen, Z. Z. Guo, M. H. Yang, H. M. Chen, H. S. Sheu and N. L. Wu, *J. Electrochem. Soc.*, 2005, **152**, A1526-A1532.

126. A. M. Kannan and A. Manthiram, *Electrochem. Solid State Lett.*, 2002, **5**, A167-A169.

127. Y. S. Jung, A. S. Cavanagh, A. C. Dillon, M. D. Groner, S. M. George and S. H. Lee, *J. Electrochem. Soc.*, 2010, **157**, A75-A81.

128. D. S. Guan, J. A. Jeevarajan and Y. Wang, *Nanoscale*, 2011, **3**, 1465-1469.

129. B. Xiao, J. Liu, Q. Sun, B. Wang, M. N. Banis, D. Zhao, Z. Wang, R. Li, X. Cui, T.-K. Sham and X. Sun, *Advanced Science*, 2015, **2**, n/a-n/a.

130. X. Li, J. Liu, M. N. Banis, A. Lushington, R. Li, M. Cai and X. Sun, *Energy Environ. Sci.*, 2014, **7**, 768-778.

131. X. Li, J. Liu, X. Meng, Y. Tang, M. N. Banis, J. Yang, Y. Hu, R. Li, M. Cai and X. Sun, *J. Power Sources*, 2014, **247**, 57-69.

132. S. C. Jung and Y. K. Han, *J. Phys. Chem. Lett.*, 2013, **4**, 2681-2685.

133. X. Meng, X.-Q. Yang and X. Sun, *Adv. Mater.*, 2012, **24**, 3589-3615.

134. Y. S. Jung, A. S. Cavanagh, L. A. Riley, S.-H. Kang, A. C. Dillon, M. D. Groner, S. M. George and S.-H. Lee, *Adv. Mater.*, 2010, **22**, 2172-2176.

135. M. B. Sassin, S. G. Greenbaum, P. E. Stallworth, A. N. Mansour, B. P. Hahn, K. A. Pettigrew, D. R. Rolison and J. W. Long, *J. Mater. Chem. A*, 2013, **1**, 2431-2440.

136. J. Xie, K. Kohno, T. Matsumura, N. Imanishi, A. Hirano, Y. Takeda and O. Yamamoto, *Electrochim. Acta*, 2008, **54**, 376-381.

137. J. Xie, T. Tanaka, N. Imanishi, T. Matsumura, A. Hirano, Y. Takeda and O. Yamamoto, *J. Power Sources*, 2008, **180**, 576-581.

138. Q. Zhang, J. Mei, X. Wang, J. Guo, F. Tang and W. Lu, *J. Alloy. Compd.*, 2014, **617**, 326-331.

139. K. Dokko, M. Mohamedi, M. Umeda and I. Uchida, *J. Electrochem. Soc.*, 2003, **150**, A425-A429.

140. J. Lu, C. Zhan, T. P. Wu, J. G. Wen, Y. Lei, A. J. Kropf, H. M. Wu, D. J. Miller, J. W. Elam, Y. K. Sun, X. P. Qiu and K. Amine, *Nat. Commun.*, 2014, **5**.

141. D. C. Tang, L. B. Ben, Y. Sun, B. Chen, Z. Z. Yang, L. Gu and X. J. Huang, *J. Mater. Chem. A*, 2014, **2**, 14519-14527.

142. W. K. Kim, D. W. Han, W. H. Ryu, S. J. Lim and H. S. Kwon, *Electrochim. Acta*, 2012, **71**, 17-21.

143. R. L. Patel, H. Xie, J. Park, H. Y. Asl, A. Choudhury and X. H. Liang, *Advanced Materials Interfaces*, 2015, **2**.

144. T. Eriksson, T. Gustafsson and J. O. Thomas, *Electrochem. Solid State Lett.*, 2002, **5**, A35-A38.

145. D. W. Shin, J. W. Choi, W. K. Choi, Y. S. Cho and S. J. Yoon, *Electrochemistry Communications*, 2009, **11**, 695-698.

146. H. W. Nesbitt and D. Banerjee, *Am. Miner.*, 1998, **83**, 305-315.

147. C. V. Ramana, M. Massot and C. M. Julien, *Surf. Interface Anal.*, 2005, **37**, 412-416.

148. R. P. Pohanish and S. A. Greene, *Wiley Guide to Chemical Incompatabilities*, Wiley, 2009.

149. A. C. Dillon, A. W. Ott, J. D. Way and S. M. George, *Surface Science*, 1995, **322**, 230-242.

150. S. M. George, *Chem. Rev.*, 2010, **110**, 111-131.

151. M. M. Biener, J. Biener, A. Wichmann, A. Wittstock, T. F. Baumann, M. Bäumer and A. V. Hamza, *Nano Lett.*, 2011, **11**, 3085-3090.

152. F. Lin, I. M. Markus, D. Nordlund, T.-C. Weng, M. D. Asta, H. L. Xin and M. M. Doeff, *Nat Commun*, 2014, **5**.

153. A. Jarry, S. Gottis, Y.-S. Yu, J. Roque-Rosell, C. Kim, J. Cabana, J. Kerr and R. Kostecki, *J. Am. Chem. Soc.*, 2015, **137**, 3533-3539.

154. D. S. Guan and Y. Wang, *Ionics*, 2013, **19**, 1-8.

155. S. T. Myung, K. Izumi, S. Komaba, Y. K. Sun, H. Yashiro and N. Kumagai, *Chem. Mat.*, 2005, **17**, 3695-3704.

156. Z. H. Chen, Y. Qin, K. Amine and Y. K. Sun, *J. Mater. Chem.*, 2010, **20**, 7606-7612.

157. I. Barin, *Thermochemical Data of Pure Substances*, *Thermochemical Data of Pure Substances*, Wiley-VCH, 1997.

158. M. W. Chase, *JANAF thermochemical tables*, 1986, **1**.

159. Y. Oh, D. Ahn, S. Nam and B. Park, *Journal of Solid State Electrochemistry*, 2010, **14**, 1235-1240.

160. S. Jayaraman, V. Aravindan, P. S. Kumar, W. C. Ling, S. Ramakrishna and S. Madhavi, *Chemical Communications*, 2013, **49**, 6677-6679.

161. N. Yu, C. L. Shao, Y. C. Liu, H. Y. Guan and X. H. Yang, *J. Colloid Interface Sci.*, 2005, **285**, 163-166.

162. Z. W. Fu, J. Ma and Q. Z. Qin, *Solid State Ion.*, 2005, **176**, 1635-1640.

163. Y. H. Ding, P. Zhang, Z. L. Long, Y. Jiang and D. S. Gao, *J. Alloy. Compd.*, 2008, **462**, 340-342.

164. X. W. Mao, T. A. Hatton and G. C. Rutledge, *Curr. Org. Chem.*, 2013, **17**, 1390-1401.

165. S. Park, *Carbon Fibers*, Springer Series in Materials Science, 2015.

166. C. Kim, K. S. Yang, M. Kojima, K. Yoshida, Y. J. Kim, Y. A. Kim and M. Endo, *Advanced Functional Materials*, 2006, **16**, 2393-2397.

167. Y. Wang, S. Serrano and J. J. Santiago-Aviles, *Synth. Met.*, 2003, **138**, 423-427.

168. S. Y. Gu, J. Ren and Q. L. Wu, *Synth. Met.*, 2005, **155**, 157-161.

169. Y. Wang, J. J. Santiago-Aviles, R. Furlan and I. Ramos, *Ieee Transactions on Nanotechnology*, 2003, **2**, 39-43.

170. E. J. Ra, E. Raymundo-Pinero, Y. H. Lee and F. Beguin, *Carbon*, 2009, **47**, 2984-2992.

171. C. Kim and K. S. Yang, *Appl. Phys. Lett.*, 2003, **83**, 1216-1218.

172. S. Kubo, Y. Uraki and Y. Sano, *Carbon*, 1998, **36**, 1119-1124.

173. C. D. Warren, F. L. Paulauskas, F. S. Baker, C. C. Eberle and A. Naskar, *Sampe Journal*, 2009, **45**, 24-36.

174. M. Lallave, J. Bedia, R. Ruiz-Rosas, J. Rodríguez-Mirasol, T. Cordero, J. C. Otero, M. Marquez, A. Barrero and I. G. Loscertales, *Adv. Mater.*, 2007, **19**, 4292-4296.

175. W. E. Tenhaeff, O. Rios, K. More and M. A. McGuire, *Advanced Functional Materials*, 2014, **24**, 86-94.

176. C. Lai, Z. Zhou, L. Zhang, X. Wang, Q. Zhou, Y. Zhao, Y. Wang, X.-F. Wu, Z. Zhu and H. Fong, *J. Power Sources*, 2014, **247**, 134-141.

177. S.-X. Wang, L. Yang, L. P. Stubbs, X. Li and C. He, *ACS Appl. Mater. Interfaces*, 2013, **5**, 12275-12282.

178. S. Hu, S. Zhang, N. Pan and Y.-L. Hsieh, *J. Power Sources*, 2014, **270**, 106-112.

179. T. Wang and S. Kumar, *Journal of Applied Polymer Science*, 2006, **102**, 1023-1029.

180. D. Choi, J.-N. Lee, J. Song, P.-H. Kang, J.-K. Park and Y. Lee, *Journal of Solid State Electrochemistry*, 2013, **17**, 2471-2475.

181. H. Tavanai, R. Jalili and M. Morshed, *Surf. Interface Anal.*, 2009, **41**, 814-819.

182. F. Agend, N. Naderi and R. Fareghi-Alamdari, *Journal of Applied Polymer Science*, 2007, **106**, 255-259.

183. Cho C, Cho D, Ko Y, Kwon O and K. I, *Carbon Letters*, 2007, **8**, 313-320.

184. H. Yang, R. Yan, H. Chen, D. H. Lee and C. Zheng, *Fuel*, 2007, **86**, 1781-1788.

185. S. X. Hu and Y. L. Hsieh, *J. Mater. Chem. A*, 2013, **1**, 11279-11288.

186. U. K. Fatema, A. J. Uddin, K. Uemura and Y. Gotoh, *Textile Research Journal*, 2011, **81**, 659-672.

187. A. Y. Shaulov, S. M. Lomakin, T. S. Zarkhina, A. D. Rakhimkulov, N. G. Shilkina, Y. B. Muravlev and A. A. Berlin, *Dokl Phys Chem*, 2005, **403**, 154-158.

188. E. Corradini, E. A. G. Pineda and A. A. W. Hechenleitner, *Polym. Degrad. Stabil.*, 1999, **66**, 199-208.

189. F. Tuinstra and J. L. Koenig, *Journal of Chemical Physics*, 1970, **53**, 1126-&.

190. A. Ramos, I. Cameán and A. B. García, *Carbon*, 2013, **59**, 2-32.

191. E. Zussman, X. Chen, W. Ding, L. Calabri, D. A. Dikin, J. P. Quintana and R. S. Ruoff, *Carbon*, 2005, **43**, 2175-2185.

192. H.-S. Moon, S. W. Lee, Y.-K. Lee and J.-W. Park, *J. Power Sources*, 2003, **119–121**, 713-716.

193. K. Jayanth-Babu, P. Jeevan-Kumar and O. M. Hussain, *Proceeding of International Conference on Recent Trends in Applied Physics & Material Science*, 2013, **1536**, 1177-1178.

194. B. J. Hwang, C. Y. Wang, M. Y. Cheng and R. Santhanam, *J. Phys. Chem. C*, 2009, **113**, 11373-11380.

195. M. Hirayama, N. Sonoyama, M. Ito, M. Minoura, D. Mori, A. Yamada, K. Tamura, J. Mizuki and R. Kanno, *J. Electrochem. Soc.*, 2007, **154**, A1065-A1072.

196. J. L. Lei, L. J. Li, R. Kostecki, R. Muller and F. McLarnon, *J. Electrochem. Soc.*, 2005, **152**, A774-A777.

197. F. Simmen, A. Foelske-Schmitz, P. Verma, M. Horisberger, T. Lippert, P. Novak, C. W. Schneider and A. Wokaun, *Electrochim. Acta*, 2011, **56**, 8539-8544.

198. L. Baggetto, N. J. Dudney and G. M. Veith, *Electrochim. Acta*, 2013, **90**, 135-147.

199. H.-S. Moon and J.-W. Park, *J. Power Sources*, 2003, **119–121**, 717-720.

200. X. Wu, S. Chen, F. Mai, J. Zhao, C. Li and W. Liu, *Journal of Solid State Electrochemistry*, 2013, **17**, 707-711.

201. Y. J. Park, J. G. Kim, M. K. Kim, H. T. Chung and H. G. Kim, *Solid State Ion.*, 2000, **130**, 203-214.

202. C. M. Julien and M. Massot, *J. Phys.-Condes. Matter*, 2003, **15**, 3151-3162.

203. B. Ammundsen, G. R. Burns, M. S. Islam, H. Kanoh and J. Rozière, *The Journal of Physical Chemistry B*, 1999, **103**, 5175-5180.

204. S. Zhao, Q. Chang, K. Jiang, Y. Bai, Y. Yang and W. Zhang, *Solid State Ion.*, 2013, **253**, 1-7.

205. M. Michalska, B. Hamankiewicz, D. Ziółkowska, M. Krajewski, L. Lipińska, M. Andrzejczuk and A. Czerwiński, *Electrochim. Acta*, 2014, **136**, 286-291.

206. Q. F. Shi, Y. Takahashi, J. Akimoto, I. C. Stefan and D. A. Scherson, *Electrochem. Solid State Lett.*, 2005, **8**, A521-A524.

207. R. Baddour-Hadjean and J. P. Pereira-Ramos, *Chem. Rev.*, 2010, **110**, 1278-1319.

208. S. Hy, F. Felix, J. Rick, W.-N. Su and B. J. Hwang, *J. Am. Chem. Soc.*, 2014, **136**, 999-1007.

209. R. Hu, D. Chen, G. Waller, Y. Ouyang, Y. Chen, B. Zhao, B. Rainwater, C. Yang, M. Zhu and M. Liu, *Energy Environ. Sci.*, 2016.

210. K. Jayanth-Babu, P. Jeevan-Kumar, O. M. Hussain and C. M. Julien, *Journal of Solid State Electrochemistry*, 2012, **16**, 3383-3390.